Die approbierte gedruckte Originalversion dieser Diplomarbeit ist an der TU Wien Bibliothek verfügbar.
The approved original version of this thesis is available in print at TU Wien Bibliothek.

Master Thesis

Optimization of iron-based Master Alloys for liquid phase sintering of PM steels

submitted in fulfilment of the requirements for the degree

Diplom-Ingenieur/in

within the framework of the study

Technical Chemistry

submitted by

Stefan Geroldinger
Matriculation number 00642034

carried out at the Institute for Chemical Technologies and Analytics (CTA) at TU Wien in the Research Group Powder Metallurgy

Supervisors: Assistant Prof.Raquel De Oro Calderon,PhD MSc

Associate Prof. Dipl.-Ing. Dr.techn.Christian Gierl-Mayer

Univ.Prof. Dipl.-Ing. Dr.techn. Dr.h.c.mult.Herbert Danninger

Wien, TT.MM.JJJJ

(Signature author) (Signature supervisor)

Die approbierte gedruckte Originalversion dieser Diplomarbeit ist an der TU Wien Bibliothek verfügbar.
The approved original version of this thesis is available in print at TU Wien Bibliothek.

TECHNISCHE UNIVERSITÄT WIEN

Diplomarbeit

Optimierung von Eisen-basierten Master Alloys für die Flüssigphasensinterung von PM Stählen

Eingereicht zum Erwerb des Titels

Diplom-Ingenieur/in

im Rahmen des Studiums

Technische Chemie

eingereicht von

Stefan Geroldinger
Matrikelnummer 00642034

Durchgeführt am Institut für chemische Technologien und Analytik (CTA) der TU Wien
In der Forschungsgruppe Pulvermetallurgie

Betreuer: Assistant Prof.Raquel De Oro Calderon,PhD MSc

Associate Prof. Dipl.-Ing. Dr.techn.Christian Gierl-Mayer

Univ.Prof. Dipl.-Ing. Dr.techn. Dr.h.c.mult.Herbert Danninger

Wien, TT.MM.JJJJ

(Unterschrift Autor) (Unterschrift Betreuer)

Die approbierte gedruckte Originalversion dieser Diplomarbeit ist an der TU Wien Bibliothek verfügbar.
The approved original version of this thesis is available in print at TU Wien Bibliothek.
TU Bibliothek Your knowledge hub WIEN

Die approbierte gedruckte Originalversion dieser Diplomarbeit ist an der TU Wien Bibliothek verfügbar.
The approved original version of this thesis is available in print at TU Wien Bibliothek.

Acknowledgements

It was a great opportunity that I got the chance to carry out my master thesis within the framework of a topic I was fascinated in from the very moment I first heard about it: powder metallurgy.

Gaining insight and understanding in this field feels like an adventure to me which is astonishing and exciting likewise.

I especially wanted to thank Univ.Prof. Dipl.-Ing. Dr.techn. Dr.h.c.mult. Herbert Danninger for the opportunity to carry out this work at the CTA and guiding me with patience and his expertise.

I am very grateful that I had the chance to work with Assistant Prof. Raquel De Oro Calderon,PhD MSc as my direct supervisor. Thank you for your patience, your knowledge and your cheerful personality despite personal setbacks.

I as well wanted to thank Associate Prof. Dipl.-Ing. Dr.techn.Christian Gierl-Mayer that he always shared his wises if I felt stuck.

I am very thankful to Ao.Univ.Prof. Dipl.-Chem. Dr.rer.nat Matthias Weil for the help in crystallographic matters.

I wanted to thank Project Assistant Dipl.-Ing Dr.techn. Johannes Zbiral, Dipl.-Ing Werner Artner and OR Dipl.-Ing. Dr.techn. Susanne Strobl for supporting my work with measurements and advices.

Of course, I also want to thank my colleagues for providing a unique working atmosphere, enjoyable time spent together and enlightening scientific discussions.

I wanted to thank my husband for the love and affection he provides me every day of my life.

Love and thanks to my parents for their love and support to make my studies possible and always encouraged me to go my own way.

Die approbierte gedruckte Originalversion dieser Diplomarbeit ist an der TU Wien Bibliothek verfügbar.
The approved original version of this thesis is available in print at TU Wien Bibliothek.
TU Bibliothek Your knowledge hub WIEN

Die approbierte gedruckte Originalversion dieser Diplomarbeit ist an der TU Wien Bibliothek verfügbar.
The approved original version of this thesis is available in print at TU Wien Bibliothek.

Abstract

In the context of Powder Metallurgy (PM) steels, a master alloy can be defined as a powder which contains a high amount of alloying elements in a combined form. It is designed to be admixed in small amounts to a base powder, so that the final steel composition is achieved after sintering. The application of “master alloys” (MA) as alloying carriers in PM steels gives the possibility of enhancing sintering by using liquid phases with tailored compositions. In addition, it allows the use of highly oxygen sensitive alloying elements well known from standard ingot metallurgy. The characteristics of the liquid and its interaction with the iron base powder can play a highly relevant role for the final microstructure and the dimensional behaviour of the components. This work presents a thorough study of the master alloy systems Fe-Mn-Si-C, Fe-Cr-Si-C and Fe-Mn-Cr-Si-C that is based on both theoretical calculations and experimental findings. The systems were optimized to provide low melting temperatures, meaning standard sintering temperatures for PM steels (1120°C / 1250°C) and narrow melting temperature intervals. The modified systems were characterized by differential thermal analysis (DTA), powder diffraction (XRD), X-ray fluorescence analysis (XRF), electronic and light microscopy in terms of composition, phases and melting behaviour. The interaction with Fe was studied by wetting, infiltration and DTA experiments. It was found that by adjusting the C and Si content in the master alloy, liquids with widely varying properties could be obtained. This might be a key for tailoring microstructures, properties and dimensional stability of sintered steels.

Die approbierte gedruckte Originalversion dieser Diplomarbeit ist an der TU Wien Bibliothek verfügbar.
The approved original version of this thesis is available in print at TU Wien Bibliothek.

Content

Die approbierte gedruckte Originalversion dieser Diplomarbeit ist an der TU Wien Bibliothek verfügbar.
The approved original version of this thesis is available in print at TU Wien Bibliothek.
TU Bibliothek Your knowledge hub WIEN

Die approbierte gedruckte Originalversion dieser Diplomarbeit ist an der TU Wien Bibliothek verfügbar.
The approved original version of this thesis is available in print at TU Wien Bibliothek.

1. Introduction

1.1 Powder metallurgy

Powder metallurgy (PM) is a well-developed alternative route to conventional metalworking such as casting, rolling and machining, having several advantages like near-net-shape products, reduced numbers of steps to produce a part and an efficient raw material use. The raw material can be produced out of up to 80% recycled scrap. Another advantage is the possibility of introducing high-melting-point alloying elements such as Mo, Ta and Nb. In comparison to ingot metallurgy a higher flexibility in alloy design and composition control is possible by avoiding segregation problems. On the other hand, sintered steel parts typically contain ~10% porosity which can cause property limitations for some high-performance applications. In terms of weight reduction, the porosity of PM products is not always considered as a disadvantage. Some porous materials such as e.g. filters or self-lubricating bearings cannot be realised with conventional metalworking. [1],[2] Dimensional control and secured properties of the raw material is a must for PM steels. [3],[4],[5] Properties of the powders are significantly dependant on their particle size and shape.

Powders used for PM techniques can be produced from several approaches:

- **Milling:** Powder production by mechanical disintegration of a stock of material, where size reduction is achieved due to mechanical energy. This method is easy to realize with the disadvantage of high energy consumption. Depending on the material milled, oxidation can take place rather easily even under controlled atmosphere, so it is not suitable for high oxygen affine materials.[3], [4], [6], [7]
- **Atomization**: This is the most common powder production method for PM powders. The powder is produced by melting and afterwards disintegrating the melt into fine droplets with high pressure water jets or gas streams. [3], [4]
    - **Water atomization:** Water atomized powders are usually fully covered by oxide layers which need to be reduced after the atomization. It is typically done for iron and low alloyed steel powders and results in irregular particle shapes, which is suitable for die compaction due to better interlocking of the particles and thus sufficient green strength. [3], [4]
    - **Gas atomization:** This atomization method is chosen for manufacturing powder that is sensitive to oxidation such as high alloy steels, stainless steels, master alloys which contain oxygen sensitive elements, superalloys, Ti and its alloys etc. These powders have a spherical shape showing a good flowability but cannot be compacted by uniaxial pressing. [3], [4]
- **Reduction of metal oxide:** Reducing an oxide with a reducing agent such as CO, H_2 produce a metal sponge which can be crushed and separated over several steps. [3]
- **Electrolysis:** Raw material is provided as anode in an electro-chemical cell. Next to purification the desired material is precipitated as fine, in part highly porous sheets which can be crushed and milled to a fine, very pure oxide free powder.
- **Gas phase reactions:** Bringing metal complexes (e.g carbonyl or iodide) complexes to reaction in the gas phase. This results in a very fine powder. [3]

1.2 Sintered steel:

In standard PM processing the powder is compacted, usually with pressing lubricants (e.g. zinc stearate) where again different methods of pressing and shaping methods can be used. The

Die approbierte gedruckte Originalversion dieser Diplomarbeit ist an der TU Wien Bibliothek verfügbar.
The approved original version of this thesis is available in print at TU Wien Bibliothek.
TU Bibliothek Your knowledge hub WIEN

resulting component is called a green body. "*To densify powder compacts elevated temperature processing is needed, which is called sintering. Porosity is minimized and interparticle contacts are created. This process can be proceeded completely without melting of any constituent or by melting of material*" [3]. "*Sintering is one single step during which the compact is transformed from a fairly fragile green body to a specimen that in many cases already possesses the strength properties required for a respective application.*" [8] *"The main driving force for sintering is to minimise the excess free energy by reducing the surface area, which is dominant for fine powders. In solid state sintering of PM steels utilising coarse powders, surface diffusion is dominant for the atoms to migrate through points of contact forming inter-particle necks. Densification will only happen over bulk transport of atoms, not through surface diffusion of atoms. The degree of the sintering is determined by the number and strength of the established sinter necks. Formation and growth of inter-particle necks are enabled by early and efficient reduction of the surface oxide layers covering the powder particles. This is either achieved due to a reducing atmosphere (CO, H_2) or extra C (Graphite)*" [4]. The main densification occurs during the heating stage, while the isothermal stage provides temperature and time for alloying element diffusion. [8] Some elements require a strict dew point and atmosphere control, due to a high oxygen affinity. [3],[4],[9]. Sintering temperatures are dependent on the material, mostly at 2/3 to 4/5 of the base material melting temperature. [1] Sintering goes usually along with densification and due to that with the improvement of all mechanical properties. [1] For ferrous precision parts, dimensional stability is much more desired than pore removal resulting in shrinkage,[8] which is a clear difference to hard metals or metal injection molding. Material property improvement through sintering is an effect of strong sintering contacts, coming from strong sintering necks and rounded pores.[8] Typical sintering temperatures for PM steels are 1120°C or 1250°C, depending on the furnace used.

Solid state sintering is the standard PM process. Material transport works only via solid state diffusion [1]. The driving force is the reduction of the Gibbs free enthalpy due to surface area reduction which can be achieved through densification and pore rounding [1], which are usually desired, and pore coarsening [1], which is undesired in most cases because bigger pores means bigger weak points for the material.

A special approach in sintering is liquid phase sintering (LPS). Basically, there are two different types of liquid phases which can occur during the sintering:

1. **Persistent liquid phase**: A liquid phase is formed and from that point on is stable over the whole sintering process. The liquid phase might change the composition but does not disappear during the rest of the sintering stage. [10]
2. **Transient liquid phase**: A liquid phase is formed during the sintering process, but it disappears due to dissolutive effects during the sintering stage. [10]

It is conventionally accepted that three different stages take place during persistent LPS [4], [11],[12]:

1. **Particle rearrangement:** *Primary rearrangement*: Depends on the contact angle of the liquid. With low contact angles the liquid will spread over the particles favouring

Die approbierte gedruckte Originalversion dieser Diplomarbeit ist an der TU Wien Bibliothek verfügbar.
The approved original version of this thesis is available in print at TU Wien Bibliothek.
TU Bibliothek Your knowledge hub WIEN

densification. High contact angles will lead to swelling due to the retreat of the liquid from the solid. The composition of the liquid phase and the particle surface determines the wettability. *Secondary rearrangement*: Determined by liquid penetration of intraparticle grain boundaries and clustering of powder particles.
In this stage kinetics of densification are the most intense, while solubility and diffusion play a minor role. [12]

2. **Intermediate solution reprecipitation:** Three phenomena occur at the same time. Grain growth, meaning smaller particles get dissolved, while re-precipitation takes place on larger particles, which leads to grain coarsening, the so called Ostwald-gripening. [12],[13],[14]. Grain shape accommodation, like the Kingery mechanism [12], [14] leads to densification due to flattening of the solid particle contacts. Densification mainly is determined by pore filling by the liquid.
3. **Solid state sintering:** In this final stage pore elimination, grain coarsening and strengthening of the inter-particle necks take place without significant densification. A solid "skeleton" is formed which prevents particle rearrangement. [4], [11],[12]

"*The liquid phase can coexist with the solid phase at the sintering temperature. The liquid then can penetrate the interparticle channels, which decreases the interfacial energy. Internal forces are set up by capillary pressure equivalent to large external pressure. Properties of the liquid phase such as wetting and spreading determine how beneficial the liquid phase is. Wetting represents the solid liquid, solid vapour and liquid vapour interaction and can be characterized with contact angle measuring. 90° angle is the border between good and poor wettability.* "[3] The smaller the contact angles and dihedral angles are, the better is the densification. Dihedral angles change during the sintering stage reaching an equilibrium state. "*The desired function of the liquid phase is enhancing the sintering and a homogeneous distribution of the alloying elements*."[15] LPS accelerates sintering and has a beneficial effect on homogenization and diffusion rates [5],[6],[7],[10],[11],. A liquid phase can enhance the reduction of oxides during the sintering process. [16] In some cases, LPS can enhance densification [4],[5],[6] but it can lead to swelling as well [17]. LPS can also cause extreme dimensional changes and distortion and can lead to secondary porosity. Primary porosity means pores already existing in the green compact, while secondary porosity is formed during the sintering process due to liquid phase penetration of the matrix grain boundaries, leaving voids at the original sites of the liquid-forming additive. [18] The secondary pores can be considerably larger than the primary ones. [18] Dimensional changes are a big challenge in PM, and for some applications it is essential to inhibit dimensional instability for achieving excellent dimensional control during the sintering process [4]. Shrinkage and swelling are mostly determined over liquid phase behaviour such as solubility of the liquid in the base material and solubility of the base material in the liquid [4],[17],[19] . Parameters such as green density of the compact, particle sizes, internal particle porosity, number of additives, volume fraction of the liquid phase and viscosity of this phase are additional parameters known to influence shrinkage. Sintering conditions such as atmosphere heating and cooling rates also determine properties and dimensional stability. [4]
In some systems e.g. Fe + Ti (3.5 or 7%) during the heating stage a liquid phase occurs which is transient and disappears before the sintering temperature of 1300°C is reached. This system shows another liquid phase formed at the sintering temperature with completely different

Die approbierte gedruckte Originalversion dieser Diplomarbeit ist an der TU Wien Bibliothek verfügbar.
The approved original version of this thesis is available in print at TU Wien Bibliothek.
TU Bibliothek Your knowledge hub WIEN

properties than the first one during. [20] Different liquid phases can occur during the sintering stage, changing their properties with composition and temperature.

1.3 Alloying route

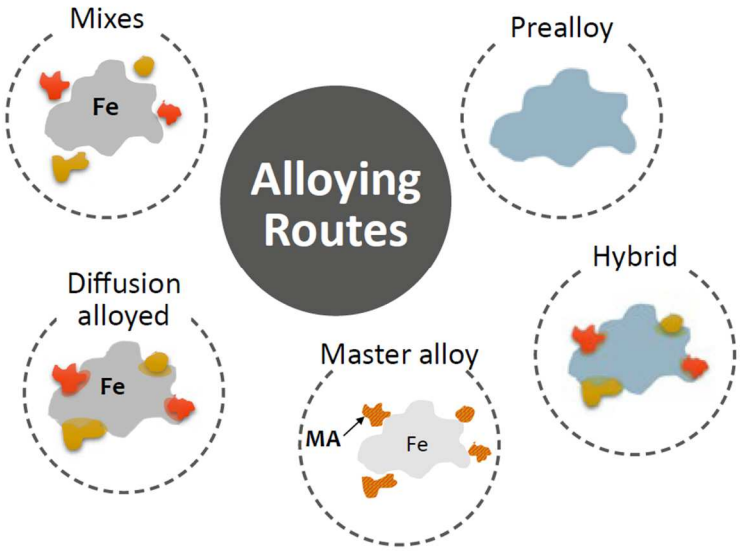

Figure 1 Graphical representation of powders from different alloying routes. Picture from [21]

According to Youseffi [22] alloying additives in PM can be divided mainly into groups: They are either ferrite stabilizers or austenite stabilizers and in the presence of carbon they can either form carbides or not [22]. Introducing alloying elements into steels leads to clear benefits of the steel properties. The question is more how alloying elements are introduced into a PM system, facing some challenging problems especially with oxygen affine elements. Figure 1 shows how powder mixes from different alloying routes look alike.

- **Blended elemental (powder mixture):** This method is easy and cheap to realise, however has some disadvantages such as huge oxidation problems with oxygen affine elements like Cr, Mn and Si. [22], [23], [24] It can be used for all elements and additions. Usually it is employed for graphite, boron, additives and lubricant [4] but also for the most widely used PM steel Fe-Cu-C. Segregation problems are another disadvantage that can occur, possibly leading to unwanted inhomogeneity.
    - **Process:** Simply mixing elemental powders together. [4]
- **Prealloyed:** This method allows a homogeneous distribution of alloying elements which leads to more consistent dimensional change during sintering compared to other alloying routes. It is suitable for oxygen sensitive alloying elements such as Cr, Si, Mn and V. [4],[25],[26],[27] Creating a pre-alloyed powder determines its alloying element content, thus eliminating compositional flexibility. Prealloyed powders are more difficult to compact[8] due to solid solution hardening in every particle.
    - **Process:** Producing a base powder with a certain amount of alloying element, usually by atomizing a melt of suitable composition.
- **Diffusion bonded:** This method bypasses segregation problems occurring in other alloying routes, so homogeneity is guaranteed [28], [29]
    - **Process:** Pure iron or pre-alloyed powder is mixed with fine elemental powder (Cu, Ni, etc.) and heat treated in a reducing atmosphere. The fine particles will

Die approbierte gedruckte Originalversion dieser Diplomarbeit ist an der TU Wien Bibliothek verfügbar.
The approved original version of this thesis is available in print at TU Wien Bibliothek.
TU Bibliothek Your knowledge hub WIEN

bond to the bigger base powder due to diffusion, but without solid solution hardening [4]

- **Master alloy:** "*A master alloy is a pre-alloyed concentrate or mixture of alloying elements. They are used to add all the major alloying elements in one form to the base material*." [30]

  This route offers the following benefits: Introducing of oxygen sensitive alloying elements such as Cr, Si, Mn and V. [5],[6],[27] Reducing or bypassing compressibility problems caused by e.g. B, Si, Mn, Cr and Ni if added in prealloyed powder [7],[31]. Achieving dimensional stability with tailored MA [4],[24]. Generating a liquid phase with different properties due to elemental compositions and / or amounts of the added MA. The MA approach can either lead to homogeneity or to heterogeneous microstructure, as desired or tailored. Depending on the phases contained, the MA may cause excessive die wear, which can be a problem. The MA route is sometimes a possible solution for elemental-specific problems such as Mn loss during sintering through evaporation [27]

  - **Process:** Melting a certain composition with relatively high amounts of alloying elements combined and producing powder out of this melt usually through gas atomization.

    Use: MA are used as addition to Fe base powders in low amounts, e.g. ~4 mass% containing enough alloying elements to achieve the desired composition. The route enables a higher flexibility in terms of introduced alloying elements than pre-alloyed powders. Compressibility is not affected very much due to this low amount of additives, the mix thus benefiting from the high compressibility of plain Fe powder. MA can be used to introduce oxygen sensitive alloying elements and/ or achieving liquid phases with tailored features.

1.4 Master alloy approach

Fe-based master alloys for sintered steels first came up in the late seventies. MCM, MVM and MM are prominent representatives from this time, being experimentally used until the 1990's.[28] Since they showed an improvement in properties, several studies were carried out to understand the properties of different elements in MA and their interactions.

- **B:** B is a sintering enhancer and promotes densification significantly [12],[31],[32]. Fe-B eutectic is at 1149°C which is quite low but no activated sintering with B at 1120°C is possible.[12] B has a very low solubility in Fe, while Fe has a very good solubility in B [12] . It forms boride networks along the grain boundaries, improving the hardness. These boride networks cause embrittlement [4],[12],[32], and the significant densification goes along with extreme shrinkage, [31] which is even more enhanced by additional C or Mo [31]. This makes B challenging in terms of dimensional control and mechanical properties but very interesting for reaching high densities.[12] Another challenging aspect of B is the different behaviour under different sintering atmospheres. Vassileva, V., et al. [32] studied Fe-B systems under Ar, H_2 and N_2. Under Ar 0.15 – 0.2% B increases the density and other mechanical properties going along with increased density, of the specimens, facing "Ar trapping" issues. [32] Sintering under H_2 increases

Die approbierte gedruckte Originalversion dieser Diplomarbeit ist an der TU Wien Bibliothek verfügbar.
The approved original version of this thesis is available in print at TU Wien Bibliothek.
TU Bibliothek Your knowledge hub WIEN

densification up to 0.3% B [32], facing deboronizing effects due reactions between B and H_2 [12],[32],[33] leading on the other hand to less embrittlement [32] N_2 as sintering atmosphere leads to a full inactivation of the B activity. [32], [33] "*There is neither a significant effect on the density, nor on the impact energiy – in positive or negative direction*" [32]. "*In general, the activation of sintering by boron is reasonably controllable in carbon-free materials while in the case of Fe-C-B the "window" for "usefull" boron contents – those that are effective towards activation of sintering while still avoiding embrittlement – is narrow and very difficult to control, esp. when rearding the reactivity of B with atmospheric constituents*." [32]

- **Cu:** Cu shows a very good wettability of Fe metal allowing a penetration of inter particle contacts and grain boundaries. [34],[35] Wettability of Fe oxide from Cu is not given, so an oxygen free surface is necessary for Cu applications. [35],[36] The wettability as well depends on the sintering atmosphere. [34] In combination as a MA, Cu can be used as a vehicle for distribution of elements with low diffusion rates such as Ni. Cu oxides are easily reduced, and standard atmospheres can be used [3]. Cu allows transient LPS [8],[11],[18] at relatively low temperatures, improving the tensile strength [28], the hardenability [22] and improving properties of the sintered bodies formed from Fe base powder and Fe-Mo pre-alloyed powders [27]. Besides these beneficial aspects, Cu is expensive and is subject to price fluctuations [28]. Cu causes swelling during sintering because of the penetration of the iron grain boundaries [3],[37]. This phenomenon can be decreased by addition of C [3],[37]. There are several described effects of C in Fe-Cu system. [37] "*C reduces the solubility of Cu in Fe. C increases the volume fraction of molten phase by forming a low melting iron phase*." [37] C increases the solubility of Fe in molten Cu. [34] C is supposed to increase the dihedral angle of the liquid phase in Fe-C-Cu system inhibiting grain boundary penetration of Cu. [34],[37] The C content in Fe-C-Cu seem to mainly influence the process kinetics. [34] Grain boundary penetration is supposed to be the major reason for Cu swelling. [37] "*Every element increasing the dihedral angle reduces swelling and vice versa.*" [37] This general statement from Berner et. al. [37] seems to be controversial to findings of Huppmann et. al [38] with Fe_Mn_Sn systems. "*The addition of P to the system Fe-Cu-C decreases dimensional changes and makes the system insensitive to both the Cu and/or C concentrations.*" [3] Fe can dissolve ~9% Cu, so infiltration with <9% form a transient liquid phase while higher amounts of Cu lead to a persistent liquid phase during the sintering process. [18]
- **C:** Although in steels C is not considered as an "alloying element" it is the element having the best influence on improving the tensile strength in PM application. [28],[27] C has a much higher solubility in γ-Fe (Austenite) than in α-Fe (Ferrite). [1] C has an adverse influence on α-sintering, meaning sintering at temperatures where α-Fe is stable, since it lowers the ferrite-austenite transformation temperature [1],[2]. Adding C to MA helps to reduce oxides, can lower melting temperatures and protects oxygen-sensitive alloying elements from being oxidized [7,14]. Admixed C plays a huge role in reducing surface oxides during the sintering process through direct or indirect carbothermal reduction, especially when sintering in an inert atmosphere [4]. Formation of CO and CO_2 could be obtained ~30 – 40 K below the α-γ-

Die approbierte gedruckte Originalversion dieser Diplomarbeit ist an der TU Wien Bibliothek verfügbar.
The approved original version of this thesis is available in print at TU Wien Bibliothek.
TU Bibliothek Your knowledge hub WIEN

transformation. [1],[2],[8],[39] CO might have a carburizing effect, delivering the first C via gas phase and having a promoting influence on the α-γ-transformation which results in a better solubility of C in the Fe matrix [1]. C diffusion starts at low temperatures, long before a first liquid would be formed, it diffuses into the Fe lattice.[5],[8] C diffusion seems to be affected by the sintering atmosphere. [8, 39] Gierl C. [1] associates the dissolution of C, added as graphite, in the Fe matrix with a sudden increase of hardness in the specimens investigated in this work obtained around 950°C. C diffusion seems to happen in very fast in a narrow temperature interval [1],[2],[39]. Wolfsgruber E. [2] obtained pearlitic "islands" in Fe-C samples sintered at 900°C even after a short time, while he could not find pearlitic structures in samples sintered at 750°C, even after sintering for longer times. [2] The temperature interval seems to be dependent on the graphite used, obtaining differences between natural (UF4) and artificial (F10) graphite. [1] At standard sintering temperatures there is no significant difference between UF4 and UF10. [39] In combination with Si, C leads to high sintered densities [22] C is usually added as fine grade powders expecting a rapid and complete dissolution[39]

- **Cr:** Cr stabilizes α -Fe [2]. This element is well established in conventional metallurgy. For PM, Cr increases the hardenability and mechanical properties e.g. tensile strength as well [15,31,33]. The major challenge with Cr is its oxygen sensitivity [28, 40, 41],[42] . "*The main reducing agent in the Cr prealloyed steels is carbon, even when sintering under H_2.*" [42] It raises the temperature for liquid phase formation and needs protective sintering atmosphere [4]. "*Cr_3C_2 is the first carbide formed as a layer on the Cr_2O_3 layer or around the Cr_2O_3 particles. The carbothermal reduction process of Cr_2O_3 consists of two subprocesses, firstly, the CO/CO_2 transport reactions and, secondly, the reaction of the primarily formed Cr_3C_2 with Cr_2O_3.*" [9] "*With Cr steels, deoxidation is shifted to markedly higher temperatures, taking place above 1000°C. CO formation is observed even at T > 1250°C, indicating the necessity of high temperature sintering.*" [8] Another problem of Cr is its fairly slow diffusion in Fe, needing either time or higher temperatures to distribute. [5] Cr has a low hardening effect on ferrite and therefore is easily introduced through pre-alloying [42]
- **P**: P as an alloying element is undesired in wrought steels due to its tendency of segregation and resulting embrittlement. [16],[43] P seems beneficial for PM steels regarding tensile strength even in very small amounts (0.15 mass% P). [22],[28],[43] Adding elemental red P or Fe_2P can lead to agglomeration problems resulting in inhomogeneity. [16] It is a liquid phase former [3],[11],[16],[43] and forms an eutectic with Fe at 1048°C [3],[4],[43]. P stabilizes α -Fe [28,47,50,65], in which phase Fe has a 100 times higher self-diffusion rate compared to γ-Fe. [3],[16],[43] This effect results in higher sintering rates [2],[3], lower porosity and in the end promotes rounded pores. [3] Hardness and density of Fe-P systems increase at least up to 1 mass% P [43]. The increased density goes along with quite remarkable dimensional changes. [43] Impact energy increases up to 0.15 mass% P but, significantly decreases with higher P content. [43] Higher amounts of P can lead to brittle phase formation, even in well homogenised powders, due to the tendency of segregation of P to the sintering necks [16],[28],[43]. In presence of Mn, the segregation effect is enhanced for Mn and for P. The effect of P +

Die approbierte gedruckte Originalversion dieser Diplomarbeit ist an der TU Wien Bibliothek verfügbar.
The approved original version of this thesis is available in print at TU Wien Bibliothek.
TU Bibliothek Your knowledge hub WIEN

C brings up controversial opinions if diffusion and segregation is enhanced or repulsed due to P – C interaction. [3]

- **Mn:** Another challenging alloying element is the inexpensive Mn [6],[28],[40],[42]. Its benefits are solid solution hardening and ferrite strengthening, even better than Cu and Ni [5],[22],[27],[42],[44]. This effect is further enhanced in combination with Si and/or C, increasing the tensile strength but reducing elongation [40] as the amount of martensite increases with Mn [7],[27]. Due to its high vapour pressure, Mn forms Mn vapour during sintering [41],[45]. This vapour formation is beneficial for alloy element distribution but can lead to Mn loss during sintering which can be bypassed using the MA alloying technique [5],[41]. A side effect of Mn vapour is the reducing ability for Cr, Fe and Mo. [9] and a unique gas phase transport mechanism. [42],[45] A. Salak postulates in [45] that sublimation of Mn from fine particles (15 µm) takes place in 130 s at 700°C and almost instantaneously at 1100°C. The Mn vapour formed even from Fe_1Mn is supposed to have a several time higher volume than the pore volume of the powder compact, leading to a homogenized condensation over all Fe particles and a "forcing out" of the initial atmosphere of the pores through the Mn vapour. [45] The Mn vapour is supposed to react with oxygen from the sintering atmosphere, forming Mn oxides in a gas phase reaction which are carried away by the flowing gas, establishing an oxygen-protecting atmosphere for the powder compact even at standard purity of the sintering atmosphere [45]. "*The manganese vapours, which may also be a function of other factors, condense predominantly upon the free surfaces of iron powder particles in the compacts or loosely filled state, and are partially removed by the protective gas*". [45] *Mn concentrates during sintering around Fe particles and penetrates along the austenite grain boundaries along with Ni*" **[5]**. "*Some Mn loss through evaporation from the compacts may occur but this seems to be much less critical in industrial practice than in the laboratory.*" [42] One challenge with Mn is its oxygen sensitivity, which is slightly higher than that of Cr [44], especially with H_2O, requiring reducing conditions and high temperature for reduction [9],[22],[28],[40],[41],[42],[45], but also CO/CO_2 from carbothermal reduction as well as the oxygen content of the base powder has to be taken into account when using Mn. [44]

  When adding Mn through the mixing route, e.g. as ferromanganese, homogenization is quite fast through gas phase transport at first place. Final homogenization is challenged due to the fact that the oxygen from the reduced base powder surfaces is not removed but just transferred to the Mn and concentrated there. [44] Danninger, H., et al. [44] describe this effect as an "internal getter" effect. Taking the difference of Mn and Fe amount into account, a quite significant oxidation of Mn occurs. *"… the resulting oxides are much more difficult to reduce, requiring high sintering temperatures at which however Mn loss at the surfaces due to evaporation becoming significant, with resulting drop of surface hardness and strength*". [44] Mn, introduced as ferromanganese, showed either volume diffusion or the three times faster grain boundary diffusion depending on the characteristics of the iron base powder. [40] When introducing Mn via the prealloying route, Mn shows a lower and a more constant chemical activity [44]. Higher sintering temperatures to reduce the very stable oxides are not such a big problem since less evaporation problems of Mn come from

Die approbierte gedruckte Originalversion dieser Diplomarbeit ist an der TU Wien Bibliothek verfügbar.
The approved original version of this thesis is available in print at TU Wien Bibliothek.
TU Bibliothek Your knowledge hub WIEN

prealloyed powders, resulting in more beneficial surface properties compared to the mixing route. [44] The difference in compressibility is only slightly lower than from the mixing route and better than commonly assumed, at least at Mn levels <2 mass%. [44]

- **Mo:** Mo stabilizes α -Fe [2]. Mostly introduced through a pre-alloyed powder, Mo is one of the common alloying elements in PM. Mo shows a good effect on hardenability of PM steels, further enhanced with additional Ni or B [4],[22],[28]. Mo with B lowers the liquid phase formation temperature, increasing the volume fraction of the liquid phase at sintering temperatures [4]. B has a huge attraction to Mo leading to Mo segregation even out of pre-alloyed powders to form borides at the grain boundaries, which induce massive embrittlement. [4] PM steels with Mo have medium strength, are easy to produce and have no critical sintering condition requirements due to the low oxygen affinity of Mo. [27] These steels can easily be processed at standard sintering temperatures. [9] Mo is a slow diffusion species in Fe, but still faster than Mn or Ni. [5]
- **Ni:** Ni provides a good combination of strength and ductility suited for high performance applications. [4],[28] Ni promotes B and C diffusion in γ-Fe [2],[4] and is itself a γ-Fe stabilizing alloying element, meaning a lowering of the α-γ-transformation temperature. [2] Ni does not promote a liquid phase formation. [2] The strengthening effect of Ni is improved by the presence of Mo, and Ni itself has a low oxygen affinity, making it sinterable at standard sintering temperatures without strict dewpoint control. [9] The biggest disadvantage of Ni is the price and the price fluctuation [28]. Large amount of Ni must be added to reach competitive properties of the PM steel. [28] Ni is a strong allergen which leads to several worker protection regulations for EU countries as well as strict control of high purity Ni powder as so-called “dual use material” 1C240. [46]
- **Si:** Si has indisputable positive effects on steel, l for PM as well as for conventional metallurgy steels being inexpensive in addition [6],[7],[19],[11],[22],[27]. Si improves tensile strength, hardness due to martensite formation, density due to its α-Fe stabilizing effects and it activates diffusion[2],[7],[22],[24]. ~3% Si is considered as an optimum amount in PM [22]. The beneficial effects of Si go along with shrinkage [11],[19]. To compensate shrinkage and increase the beneficial properties of Si, C additions turned out to be very effective in low amounts (~0.5% C) [22]. Si has a well-known oxygen affinity making higher temperatures and a clean protective atmosphere necessary for the sintering process. [22],[28] Shrinkage due to very good densification causes problems with dimensional stability. This problem can be countered with Mn and / or C achieving dimensional stability for certain compositions. [22] Adding Cu or Al did not lead to dimensional stability [7]. Si can reduce Fe and even Mn and Cr oxides due to its higher oxygen affinity. [9]

Die approbierte gedruckte Originalversion dieser Diplomarbeit ist an der TU Wien Bibliothek verfügbar.
The approved original version of this thesis is available in print at TU Wien Bibliothek.

Die approbierte gedruckte Originalversion dieser Diplomarbeit ist an der TU Wien Bibliothek verfügbar.
The approved original version of this thesis is available in print at TU Wien Bibliothek.

Table 1 shows a list of MAs used for LPS in PM steels as given in the literature

Table 1 List of MA in the literature for liquid phase sintering in PM steels

Nr.	MA Composition	Sintering temperature	Properties	Source
1	Fe_45Mn_20Si [7%]	1100°C 1150°C 1200°C 1250°C	Optimum properties with the composition Fe–3.2%Mn–1.2%Si–0.35%C, sintered at 1473 K for 90 min under Ar/5H_2. Achieved tensile strength of 900 MPa and an elongation of 4.8%.	[6]
2	Fe_2Mn_1.5Si + C Fe_3Mn_1.5Si + C Fe_4Mn_1.5Si + C Fe_1.4Si_3.2Mn_0.4C	1150°C 1250°C	Early researches on Fe-Mn-Si MA systems. In contrast to the binary Fe-Si and Fe-Mn alloys the MA show small dimensional change during sintering combined with remarkably high strength.	[7]
3	Fe_38Mn_11Si Fe_39Mn_11Si_0.3C	1250°C	MAs form liquid phases below standard sintering temperatures e.g. <1020 °C for Fe38Mn_11Si. DTA experiments showed that extra C, added as UF4, did only affect the MA without C reducing the melting point of this MA. Reducing effects of the base powder surface through highly oxygen affine alloying elements in the MA could be obtained with these MA.	[15]
4	Fe_25Si (Ferrosilicon) + 0.6% UF4	1120°C 1150°C	Appearance of a liquid phase at 1200°C which accelerates the diffusivity of Si in Fe. Ferrosilicon deteriorates the compatibility. Adding 5% Si to Cr or Mo pre-alloyed base powders lead to better densification going along with shrinkage. 1250°C still does not show a homogeneous distribution of the Si.	[19]
5	a. Fe_35Mn_14Si b. Fe_35Mn_20Si c. Fe_45Mn_20Si	1090 – 1170°C 1115– 1225°C 1110 – 1215°C	MA combined with prealloyed base powder. The best tensile strength and smallest dimensional expansion have been obtained for Fe_0.85Mo_1.4Mn_0.8Si_0.5C steel with Fe_35Mn_20Si master alloy sintered in H_2 as N_2/10%H_2.	[27]

Die approbierte gedruckte Originalversion dieser Diplomarbeit ist an der TU Wien Bibliothek verfügbar.
The approved original version of this thesis is available in print at TU Wien Bibliothek.

	d. Fe_60Mn_14Si	1085 – 1125°C		
6	Fe_5Ni_4.5Cu Fe_1.5Cu_XNi + Disaloy Fe_4Mn_2Cu Fe_4Cu_XCr Fe_20Mn_20Cr_20Mo_7C [7%] Fe_20Mn_20V_20Mo_5C [7%]	1200°C 1120°C 1000°C 1150°C 1250°C	Basic research comparing MVM and MCM MA with new MA in properties and especially in price. Finding Mn and Si containing MA as promising figuring out problems of the high oxygen sensitivity.	[28]
7	Ni_46Mn_7.9B	1000°C 1100°C 1140°C	MA enhances the density of the compact by 2 – 4% through liquid phase formation. The MA melts at 1000°C. Additional Mo and C lower the melting point and two different types of liquid phases could be obtained during the sintering process. Adding 2.5% MA led to boride networks causing embrittlement, lower MA contents lead to a strengthening due to discontinuous boride networks.	[31]
8	Cu_3Mn_9Si	1050°C 1150°C 1350 °C	Adding 10% of the Cu_3Mn_9Si MA to a Fe-Cu pre-alloyed base powder and sinter for 1h under H_2 tensile strength of 7.58 $^{g}/_{cm^3}$ could be achieved.	[36]
9	Ni_28Fe_3.7B	1250°C 1300°C	1 or 2 % of this MA was added to Fe or Fe_1.5Mo. 0.8% C was added to all mixes. The samples were sintered in technically pure H_2 atmosphere with getter boxes Al_2O_3 to avoid decarburisation. Using the relatively low melting point of the Ni-B eutectic was the major intent of this work. With this MA enhancement in hardness and impact energy especially for low C contents could be obtained. Mentioning ~32 J/cm^2 with ~240 HV for Fe_1.5Mo +2 %MA + 0.8 %C This enhancement does not go along with densification but with the strengthening of the sintering necks. Embrittlement due to B could not be obtained for these systems.	[33]

Die approbierte gedruckte Originalversion dieser Diplomarbeit ist an der TU Wien Bibliothek verfügbar.
The approved original version of this thesis is available in print at TU Wien Bibliothek.

10	Fe_Mn_C	1120°C	High C containing Ferromanganese (75%Mn7.75%C) added in amounts of 2.5 – 5% to two different types of iron powders. Investigating the effect of Mn on tensile strength, elongation, hardness and its effect on green and sintered density. For single pressed and sintered and hot forged specimens. Findings of the effect of different iron base powders on the mechanical properties of the specimens are well discussed. In a second study with the same systems the vapour formation of Mn during sintering and its effects are investigated.	[40, 41]
11	Cu_2Ni_1.5Si [2%]	1120°C	Achieved a better dimensional stability during the heating stage using the MA compared to elemental Cu by realising a continuous formation of liquid phase.	[47]
12	a. Fe_3.94C_3.35B b. Fe_4.37C_1.75B	1150°C	Interaction with B from MA and Mo from a prealloyed base powder in terms of shrinkage and densities up to 7.58 $^{g}/_{cm^3}$ going along with 3.18% shrinkage.	[48]
13	Cu_2Si Cu_2.1Ni_1.2Si Ni_3.9Cu_11.6Si Fe_40Mn_15Si_1C_10Ni	1120°C 1150°C	Study of Cu based, Ni based and Fe based MA, showing their wettability and liquid solid interaction between the liquid MA on different substrates. Pointing out the differences between high and low dissolutive conditions on liquid phase behaviour. In addition, the effect of high oxygen sensitive alloying elements on the reduction of surface oxides is discussed.	[49]
14	Fe_6.5P_1.5C Fe_5P_3C Fe_5P_3C_5Cu Fe_2.7P_2.7C_2.6Cu	1120°C 1150°C 1300°C	Full densification and microstructures without brittle grain boundaries could be achieved with these MA.	[50]
15	Cu_2Ni_1Si	1080°C 1085°C 1090°C 1120°C	The different MA showed different dissolutive conditions, which determines infiltration and wettability and in a consequence of that the	[51]

Die approbierte gedruckte Originalversion dieser Diplomarbeit ist an der TU Wien Bibliothek verfügbar.
The approved original version of this thesis is available in print at TU Wien Bibliothek.

	Ni_4Cu_12Si Fe_40Mn_15Si_1C	1250°C	formation of heterogeneous or more homogeneous microstructures. A special attention was given to Fe_40Mn_15Si_1C and its surface reducing abilities due to the high amount of oxygen sensitive alloying elements. The dissolutive ability of this MA is sensitive to the atmosphere as well so the liquid phase ability of this MA changes with atmosphere and oxygen transfer from the base powder to the MA surface.	
16	Fe_52Mn_8Cr_8Mo_4Ni_3.5C Fe_36Mn_22Cr_10Mo_8Ni_3.5C Fe_58Mn_8Mo_10Ni_4C	1150°C 1280°C 1300°C	At 1280°C temperatures slightly increased strength but not significantly better. At 1300°C more than 80% of the MA formed a liquid phase showing a noticeable improvement in the tensile rupture strength compared to traditional alloys.	[52]
17	Fe_Cr_C Fe_Mo_C Fe_Mn_C Fe_Cr_Mo_C	1280°C	Transient liquid phase sintering with diffusion of the alloying elements from the liquid phase into the Fe matrix. General discussion about acceleration and homogenisation of the sinter process due to the presence of a liquid phase. Fe gets dissolved leading to an increasing of liquid phase amount and to a further increase in diffusion. Produced materials are considered to have a very high tensile strength potential.	[53]

1.5 Properties of liquid phase from MA

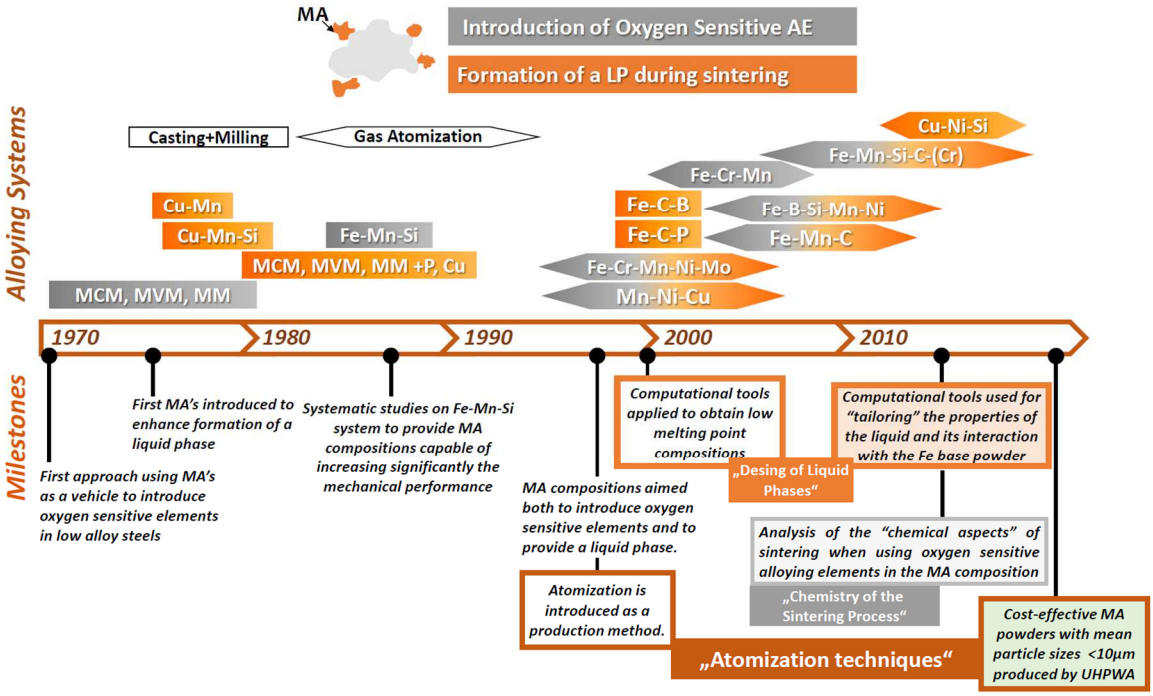

Figure 2 Timetable with different approaches of MA use. Picture from [21]

Figure 2 shows two different approaches for MA applications. First the introduction of oxygen-sensitive alloying elements was intended. Another approach was LPS made possible with MA. Using standard atomization techniques, MAs with much higher purity could be realized, but the yield of desirable particle sizes, at least <45 or <63 µm was poor. A new technology UHPWA (ultra-high-pressure water atomization) allows a cost-efficient MA powder production with particle sizes <10 µm. Designed liquid phases for LPS can come from MA additions to the base powders. With different properties of the formed liquid phases different properties in the steel can be achieved.

Liquid phases can have different properties e.g. in terms of appearance during the sintering process, their infiltration and wetting of the base material and the solubility of the liquid in the solid and the solubility of the solid in the liquid phase.

Appearance of the liquid phase during the sintering process:

The formation of liquid phases depends on the phase diagrams the MA and the base powder show. [10] So called **transient liquid phases** appear for a short time and disappear during the sintering stage. Another possibility is a **persistent liquid phase** which is stable over the whole sinter process. If the liquid phase is persistent or transient is mainly depends on the miscibility of the components and the type of phase diagram. Having a major component, A, e.g. an iron base powder and a minor component B, e.g. a MA. [10]

- If **A and B are completely immiscible** in solid and liquid state, only steady state LPS is possible in the range from the melting of component B until the melting of component A. [10]

Die approbierte gedruckte Originalversion dieser Diplomarbeit ist an der TU Wien Bibliothek verfügbar.
The approved original version of this thesis is available in print at TU Wien Bibliothek.
TU Bibliothek Your knowledge hub WIEN

- In case of **eutectic systems between A and B with limited miscibility** the liquid phase is transient if the concentration of B is lower than the solubility limit at the sintering temperature or persistent if the solubility limit is exceeded. [10]

With persistent state LPS high density can be achieved, while homogenization is the desired effect with transient LPS. [8, 12] *"Systems sintered with transient liquid phase can in principle also be sintered without any liquid phase e.g. by extremely slow heating"* [10]
The stages of **transient liquid phase** are briefly described in three steps: [10],[20]

1. Forming a liquid phase between matrix and alloying element(s) e.g. the MA.
2. Penetration of the liquid phase into primary pores leaving behind a secondary pore instead of the MA particle, which can have the same size as the MA particle or be even bigger due to dissolving of the matrix material.
3. The final stage is the interdiffusion of the liquid phase into the grains of the matrix and homogenisation due to solid state diffusion. [12]

Infiltration:
If the liquid phase can penetrate the open porosity of the green body the alloying elements can be distributed in realistic times, leading to a homogeneous microstructure comparable to pre-alloyed powders. Non-infiltrating liquid phases lead to heterogeneous microstructures comparable to diffusion bonded powders. [35],[15],[51]

Wetting: Contact angles < 90° are regarded as a good wetting and therefore help to distribute the liquid within the channels. A good wetting is necessary for a homogeneous distribution but on its own no guarantee to achieve it. Liquids with wetting angles > 90° are poor in wetting leading to high concentration zones of certain elements. [3]

- **Complete miscible and peritectic systems:** This means that the initially formed liquid phase has the composition of the MA. In this case all liquid phase is formed during the first moment of liquid phase sintering. All MA particles melt and in **case of a sufficient wetting** LPS for these systems can be separated into 3 steps occurring one after another according to Danninger [10]:
  1. *Melting of all MA particles*
  2. *Capillary and grain boundary penetration and formation of pores at the sites of the MA particles ("intergranular" homogenization)*
  3. Diffusion of MA alloying elements into the base powder "*…grains from the boundaries and progressive "intragranular" homogenization"*

  These phenomena are described for binary systems, but in this special case where the MA shows eutectic behaviour for itself, it should behave the same way, besides the homogenization step. In this last step the alloying elements which formed the MA diffuse differently into the base powder, accelerated or inhibited from each other depending on the MA system. [10]

  "*In **case of insufficient wetting** , no capillary and grain boundary penetration occurs and for every MA particle there remains a pool of liquid phase in the solid matrix which, through solution of base material in the melt, is progressively enriched with the base material until the melt solidifies from the boundaries towards the center*" [10]

Die approbierte gedruckte Originalversion dieser Diplomarbeit ist an der TU Wien Bibliothek verfügbar.
The approved original version of this thesis is available in print at TU Wien Bibliothek.
TU Bibliothek Your knowledge hub WIEN

- **Eutectic systems:** In this case the MA forms a eutectic melt with the base powder and the eutectic melting temperature is lower than the liquidus temperature of the MA. The liquid phase can only be formed at a sintering temperature above the eutectic temperature and below the MA liquidus temperature when there is a contact zone between the MA and the base powder. The formation of the liquid phase depends on the diffusivity of the base material into the MA and the MA components into the base material. In this case the liquid phase is continuously formed as long as there is a contact area between base material and MA. The liquid phase can penetrate the grain boundaries which removes the liquid phase from the original site. Due to the fact that base material is needed for the formation of the liquid phase, secondary pores occurring for these systems are larger than the initial MA particles. The smaller the particles are, the bigger is their relative surface going along with more contacts with the base powder. This leads to better liquid phase formation and of course to smaller secondary pores. [10]

Note: Above the MA liquidus temperature there is no more contact to the base powder required for forming a liquid phase, but with that it is no longer a eutectic system.

"With eutectic systems, formation and consumption of liquid phase overlap, and only a fraction of the total liquid phase is present at any moment of sintering. This leads to enrichment of the alloying element near its original sites, necessitating more intense sintering. The pores generated are larger in size than the original alloying powder particles, the more, the higher the content of the major constituent in the eutectic melt. Thus, the necessity of using fine alloying powders to keep secondary pores small […]. Homogenization in eutectic systems can be promoted by adding (component) B not as elemental powder but as a pre-alloyed powder of eutectic composition (meaning a MA)*, by which measure the desired rapid formation of liquid phase and thus fast homogenization can be attained"* [10]

Solubility of liquid in the solid: High solubility of the liquid-forming component in the solid promotes swelling [3],[4]. Diffusion of alloying elements (e.g. Si) out of a persistent liquid phase into base powder particles leads to homogenization and densification [22]. The liquid phase shortens diffusion length delivering the alloying element to the particles.

Solubility of solid in the liquid: High solubility of the (solid) main component in the liquid enables a high mass transport via the liquid. If the solubility is low, solid-state sintering is the dominant densification mechanism. Controlled solubility of the solid in the liquid promotes densification due to re-precipitation. Solidification due to dissolving base material in the liquid phase is used as application e.g. in reactive sinter brazes. [54] Unbalanced solubility of the solid in the liquid along with incorporation of atoms by diffusion causes swelling. [3],[4],[5]

"*Liquid phase transport via grain boundary attack can be regarded as the fastest of the processes involved. Consumption of the melt depends on MA diffusion into the base material matrix and of solution of base material in the melt"* [10]

Die approbierte gedruckte Originalversion dieser Diplomarbeit ist an der TU Wien Bibliothek verfügbar.
The approved original version of this thesis is available in print at TU Wien Bibliothek.
TU Bibliothek Your knowledge hub WIEN

Note: The desired effect of the liquid phase is a homogeneous distribution of the alloying elements, which can only occur if they are evenly distributed in the compact.

2.4 Motivation and objectives

The undisputed benefits of Si, Mn and Cr as alloying elements in PM steels bring along some challenges. This work faces these challenges by finding modifications of Fe-based MA containing Si and C as well as Mn and/or Cr. The MA used here powders were produced through the UHPWA technique [21] where a certain amount of Si and C is needed for the production process. Starting from three prototype powders criteria of improvement were the following:

- Liquid phase formation at standard sintering temperatures (1120°C / 1250°C)
- Narrow melting ranges
- Improved content of alloying elements
- Improvement of the liquid phase behaviour in terms of wetting and infiltration

Using ThermoCalc for theoretical calculations as a good approach for new systems made it possible to find several promising new compositions. The most promising ones were prepared in the lab based on the original compositions (H45: Fe_32Cr_8Si_4C, H46: Fe_42Mn_6Si_0.4C and H47: Fe_28Mn_27Cr_6Si_3.7C). Master Alloy powders with these compositions were still available as UHPWA powders from previous studies described by de Oro Calderon et al. [21] and were modified by adding elemental powders to achieve the desired composition. These modifications were tested if the desired behaviour could be achieved, and the modifications were characterized in terms of phases, melting temperatures, composition, liquid phase formation and behaviour of the liquid phase. Afterwards the modifications were classified and investigated to get information about possible reactions between MA and base powder compacts. The final goal was finding optimized modifications of the MA for further studies on property enhancement of PM steels with these modified MAs.

Die approbierte gedruckte Originalversion dieser Diplomarbeit ist an der TU Wien Bibliothek verfügbar.
The approved original version of this thesis is available in print at TU Wien Bibliothek.
TU Bibliothek Your knowledge hub WIEN

2. Materials and experimental procedure

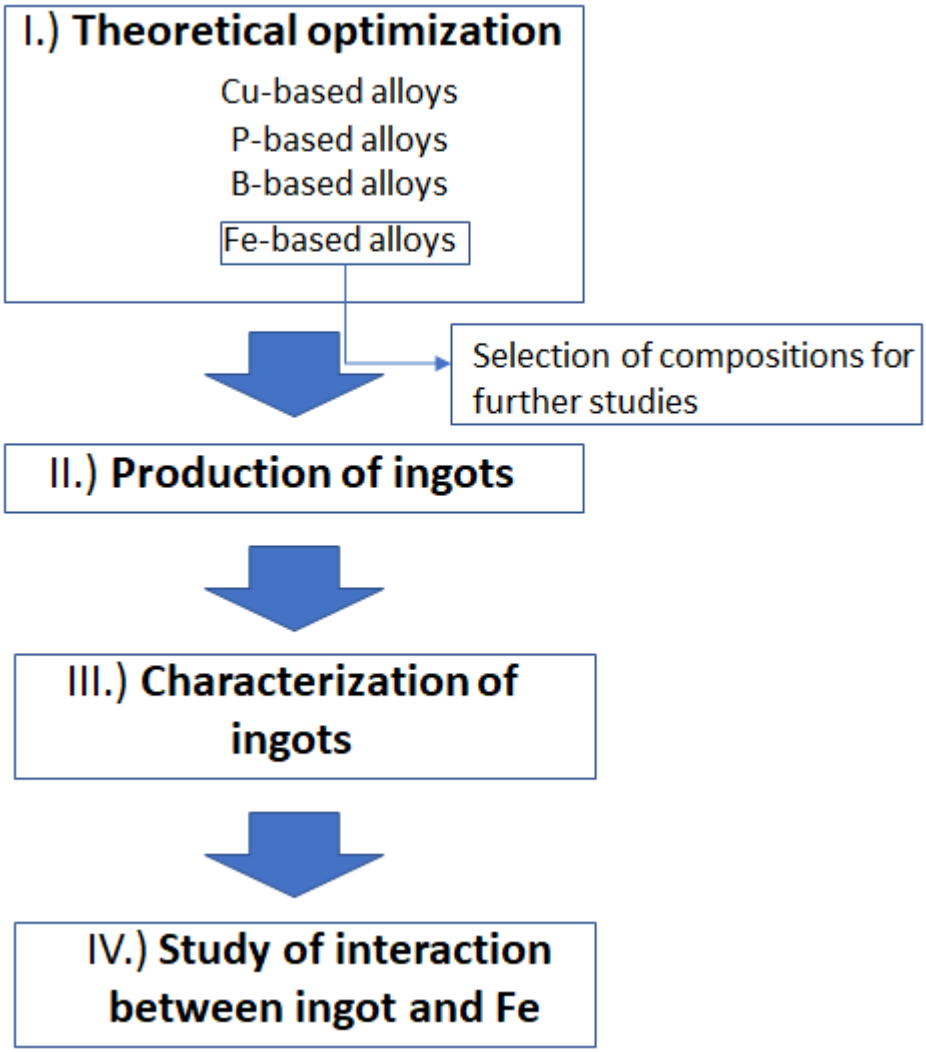

2.1 Theoretical optimization

Theoretical optimization was carried out with ThermoCalc. For this, the following criteria were set to optimize the alloys in terms of melting temperature, amount of alloying elements in the master alloy and a narrow melting window. First, lowering the temperature for sintering processes is beneficial for energy saving, going along with cost reduction and practicability of sintering processes. Second, as the master alloy is used as an alloying element delivery, the amount of necessary master alloy can be decreased if it is possible to introduce more of the desired elements into the system. Third, a narrow melting window or showing up as much liquid at a certain temperature as possible was considered as a major criterion for improving infiltration behaviour.

ThermoCalc offers several tools such as the possibility to calculate the evolution of the phases (EoP) shown in Figure 3, isothermal cuts shown in Figure 4 and phase diagrams shown in Figure 5. Next to graphic information it is possible to get theoretical information about phase composition in a table. All calculations carried out were equilibrium calculations.

Die approbierte gedruckte Originalversion dieser Diplomarbeit ist an der TU Wien Bibliothek verfügbar.
The approved original version of this thesis is available in print at TU Wien Bibliothek.

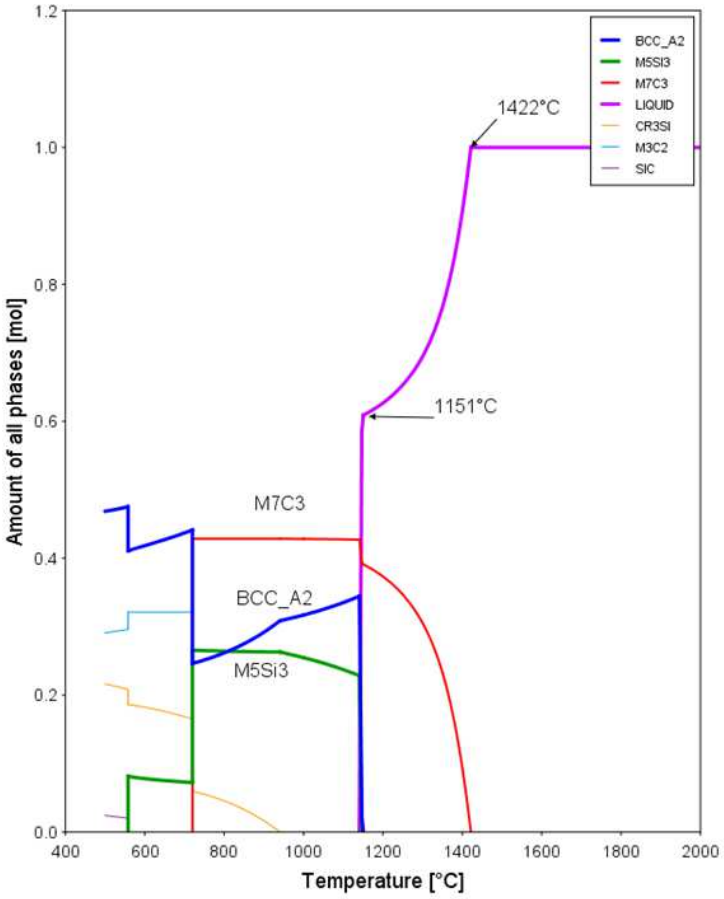

Figure 3 Example for an evolution of phases over the temperature

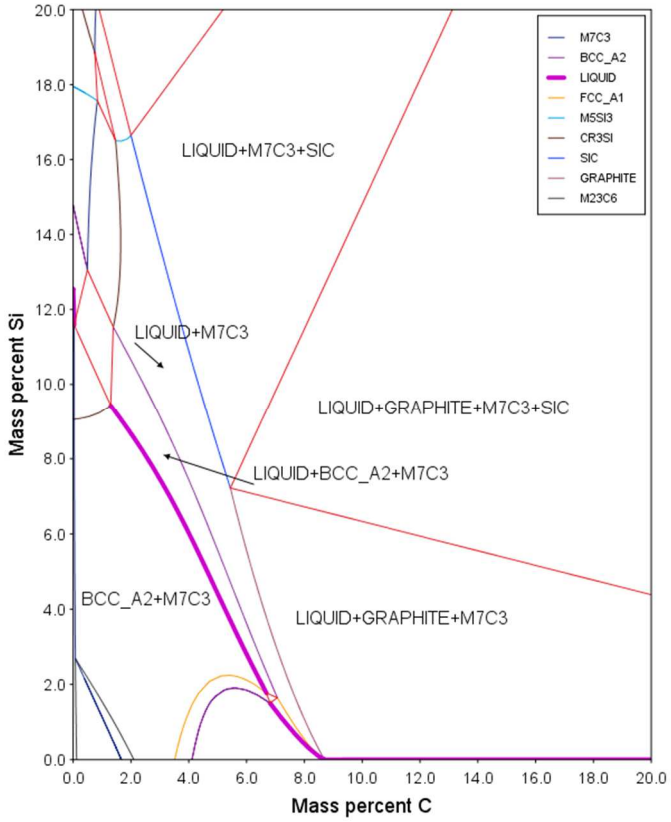

Figure 4 Example for isothermal section for C vs Si at 1250°C

Die approbierte gedruckte Originalversion dieser Diplomarbeit ist an der TU Wien Bibliothek verfügbar.
The approved original version of this thesis is available in print at TU Wien Bibliothek.

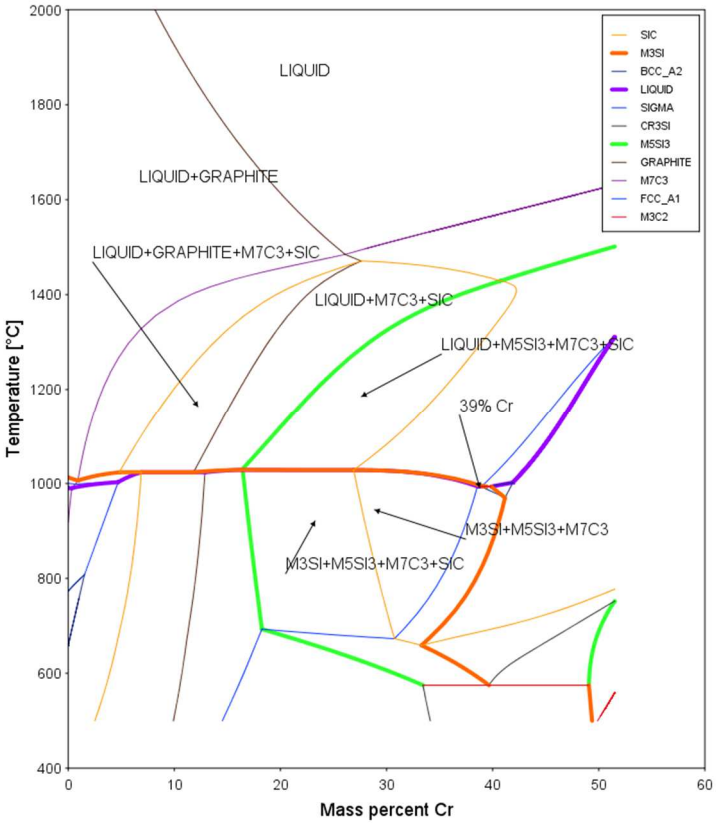

Figure 5 Example phase diagram Cr content vs temperature

2.1.1 Optimization criteria

Starting criteria considered to be beneficial for MA in LPS were the following:

- **Lower melting temperatures:** Melting temperatures/range at standard sintering temperatures for industrial furnaces (1120°C / 1250°C) or even lower was a critical criterion for the MA to be useable in the PM process.
- **Narrow melting window:** Forming a liquid phase in a certain temperature range, as narrow as possible, in best case a eutectic melting point, was considered to be beneficial for infiltration.
- **Increasing the alloying element content:** The more alloying element the MA contains the less percent of MA have to be added to achieve a desired alloying element concentration, which makes the MA more cost efficient.
- **Infiltration and wetting behaviour:** Finding MA systems with infiltrating behaviour were considered to be beneficial for a homogeneous distribution of the alloying elements.

2.1.2 Optimized systems

Theoretical optimizations were carried out for Cu- based and Fe-based B or P containing MAs from the literature. The major work was carried out for Fe-Si-C based MA containing Mn and / or Cr in addition. These MA were prototype powders produced with a new UHPWA technique. For these systems theoretical optimization with ThermoCalc was carried out, and based on these calculations new modifications were produced and characterized.

Die approbierte gedruckte Originalversion dieser Diplomarbeit ist an der TU Wien Bibliothek verfügbar.
The approved original version of this thesis is available in print at TU Wien Bibliothek.

2.2 Production of ingots

To produce the ingots, powder mixtures were prepared from existing base MA powders with the compositions **Fe_32Cr_8Si_4C**, **Fe_42Mn_6Si_0.4C** and **Fe_28Mn_27Cr_6Si_3.7C,** adding C, Cr, Fe, Mn and / or Si as necessary to modify the compositions accordingly.

Table 2 Starting materials used to produce powder mixes

Element	Starting material
C	UF 4 Carbon
Cr	266299-100G Aldrich chromium powder ~325 mesh ≤ 99%
Fe	ASC 100.29 Höganäs
Mn	266132 Aldrich manganese powder ~325 mesh ≤ 99%
Si	215619-250G Aldrich Silicon powder ~325 mesh ≤ 99%
MA	**Prototype powder**
H45	Fe_32Cr_8Si_4C (O_2 = 0.14%) (d_{10} =3.21, d_{50} = 7.84, d_{90} = 18.4)
H46	Fe_42Mn_6Si_0.4C (O_2 = 0.10%) (d_{10} =2.33 d_{50} = 6.70, d_{90} = 16.1)
H47	Fe_28Mn_27Cr_6Si_3.7C (O_2 = 0.12%) (d_{10} =2.92, d_{50} = 8.09, d_{90} = 22.6)

After mixing the powder batches in a tubular mixer for 45 min the fully homogenized powders were filled into LECO ceramic crucibles and placed into a steel boat as shown in Figure 6.

Figure 6 LECO crucibles filled with powder mixes

The boat was pushed into the high temperature zone of a furnace set at 1300°C under Ar flow. Then a H_2/Ar atmosphere was set and the samples were kept for 1 h in the furnace. Afterwards the boat was pushed to a cooling zone to cool from 1300°C to approximately room temperature within 45 min. After the furnace run the powder mixes were fully molten to ingots as shown in Figure 7.

Die approbierte gedruckte Originalversion dieser Diplomarbeit ist an der TU Wien Bibliothek verfügbar.
The approved original version of this thesis is available in print at TU Wien Bibliothek.
TU Bibliothek Your knowledge hub WIEN

Figure 7 Powder mixes molten to ingots after furnace run

The crucibles were smashed with a hammer to release the ingot. Modifications of **Fe_40Cr_11Si_3.5C** have been melted at 1450°C in a vacuum furnace to achieve a fully molten homogeneous ingot. These ingots were cooled in vacuum just by switching off the heating overnight.

2.3 Characterization of the ingots

2.3.1 Scanning electron microscopy (SEM) [55]

SEM scanning over the sample detecting backscattered electrons (BSE) was done. The primary electron beam was set at 20 keV, BSE electrons are in ranges of ~1 keV depending on their mean atomic number. Detected BSE electrons result in a grey scaled picture giving a contrast between phases with different average atomic mass (an example is shown in Figure 8.

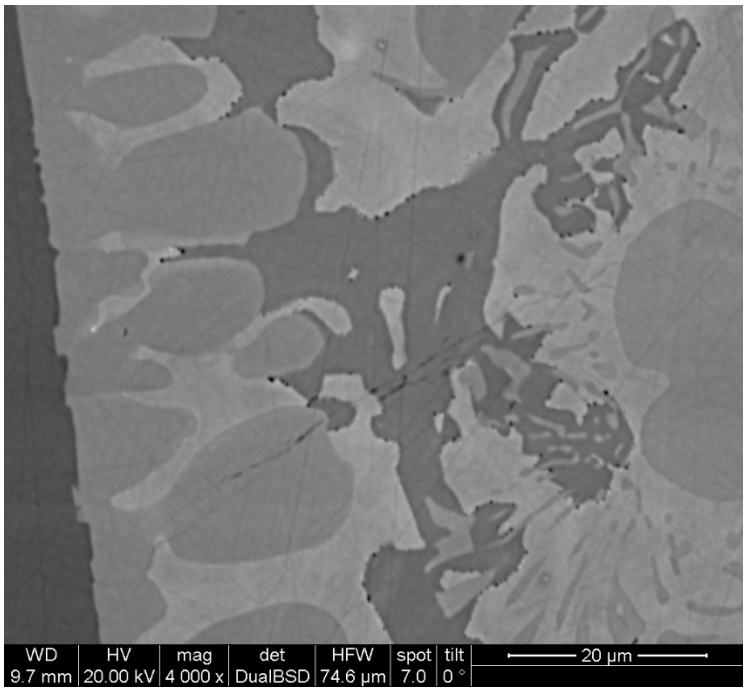

Figure 8 Example BSE picture H45_E2: Fe_40Cr_14Si_4C

Die approbierte gedruckte Originalversion dieser Diplomarbeit ist an der TU Wien Bibliothek verfügbar.
The approved original version of this thesis is available in print at TU Wien Bibliothek.

The primary electron beam ejects core electrons out of their orbitals. Other electrons in higher orbitals will drop down to this empty place, releasing X-rays characteristic for the respective element which can be detected by energy dispersive X-ray detection (EDX). EDX is giving a specific distribution of the elements either in analysing a single spot or in mapping over a bigger area. The EDX method is more sensitive to heavier atoms, having problems in accurate detection of light elements such as carbon or boron.
For SEM investigation, ingots wetting and infiltration samples were metallographically prepared, i.e. embedded in bakelite resin and polished.

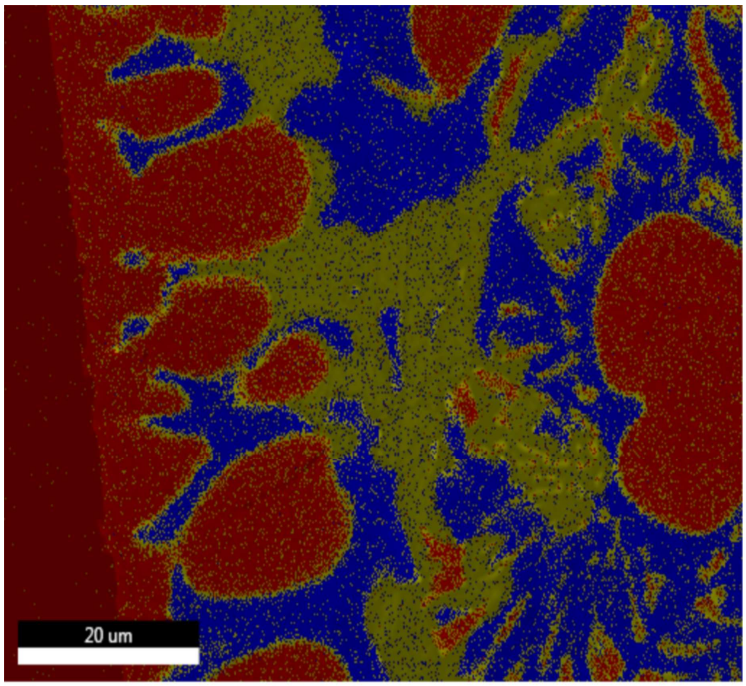

Figure 9 Example of EDX mapping over the same area as Figure 8 H45_E2: Fe_40Cr_14Si_4C.

Figure 9 shows a coloured version of Figure 8. These colours are generated by the software, which tries to identify phases automatically - a helpful tool which is not always accurate.

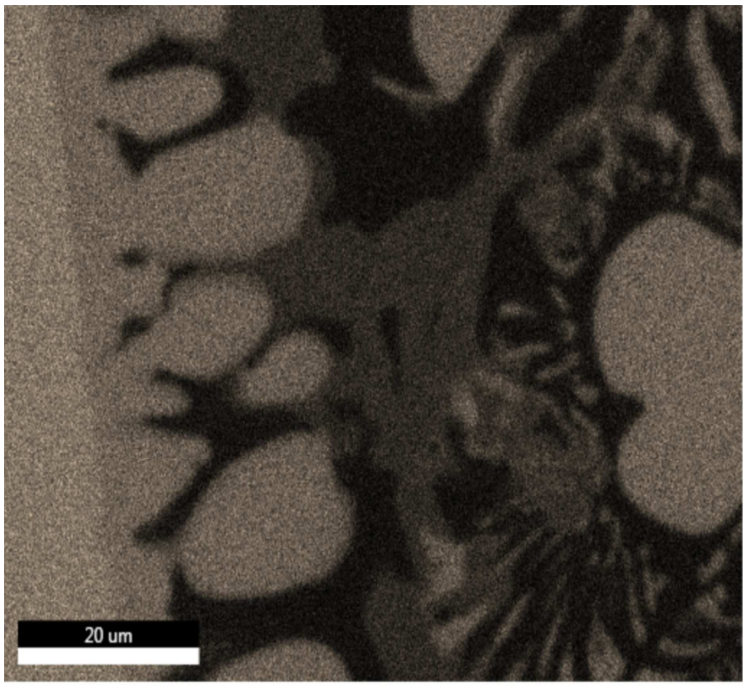

Figure 10 Cr Kα mapping of the area shown in Figure 8.

Die approbierte gedruckte Originalversion dieser Diplomarbeit ist an der TU Wien Bibliothek verfügbar.
The approved original version of this thesis is available in print at TU Wien Bibliothek.
TU Bibliothek Your knowledge hub WIEN

Figure 10 is a third version of the same image, only showing the amount of Cr in this area of the sample. These pictures help a lot to find out elemental distribution and phase identification.

2.3.2 Powder X-ray diffraction (XRD) [56]

For powder X-ray diffraction analysis (P-XRD) the ingot was milled into a fine powder. An X-ray beam (Cu Kα with λ = 1.5418 Å) is scanning the sample over a range of angles (2 theta = 20-110°). Compared with single crystal X-ray diffraction, in P-XRD all possible lattices are provided from many small crystals. Mathematical refinements like Rietveld refinement help getting a clear information out of the measurement. The peak patterns in the diffractograms are characteristic for different phases and can be identified with databases. Figure 11 shows a normalized example of an X-ray diffractogram. Normalization relates all peaks of the diffractogram to the highest pattern, considered as 100%, this is necessary to compare the different measurements with each other having percentage and no absolute values.

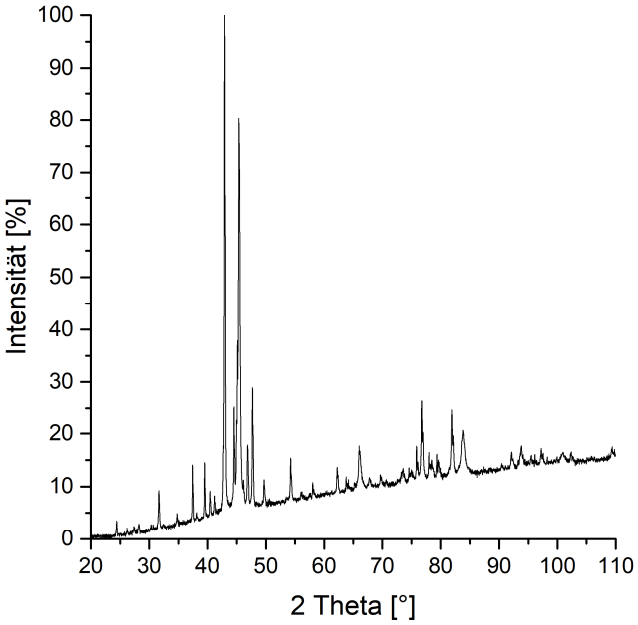

Figure 11 Example Powder XRD diffraction pattern

2.3.3 X-ray fluorescence spectrometry (XRF) [57]

With this analytical method monochromatic x-ray beams (Rh Kα with λ = 0.613 Å) are generated with 50 kV excitation voltage and 50mA tube current. The x-ray beam is focused to a small spot. The method is similar to EDX analysis; here the primary x-ray beam ejects core electrons. The empty electron spots are filled with electrons from higher orbitals. This "drop" from higher to lower energy levels releases a specific energy depending on from which spot the electron comes. The summary of all energy lines emitted result in an energy fingerprint which can be detected. This is a so-called wave length dispersive XRF (WDXRF) method which was used for this thesis. [57] The evaluation was carried out with calibration functions based on spectroscopic standards from the Institute of Spectroscopic Standards, Middlesborough U.K.

Die approbierte gedruckte Originalversion dieser Diplomarbeit ist an der TU Wien Bibliothek verfügbar.
The approved original version of this thesis is available in print at TU Wien Bibliothek.

2.3.4 Differential thermal analysis (DTA)

With differential thermal analysis (DTA), samples are measured over a certain temperature range with a defined heating and cooling rate. Their temperature is recorded continuously and compared with that of a reference sample, which is often just an empty crucible. Differences in temperature between the sample and the reference are detected. Informations from DTA are endo- or exothermic reactions such as e.g. phase transformations, like α-γ-transiton from iron, melting/solidifcation temperatures and ranges. For this study the temperature range was from room temperature to 1500°C in Ar. Heating and cooling rates were 20 K/min. DTA measurements for the ingots were carried out to identify the melting ranges and compare them with ThermoCalc calculations. An example DTA measurement is shown in Figure 12.

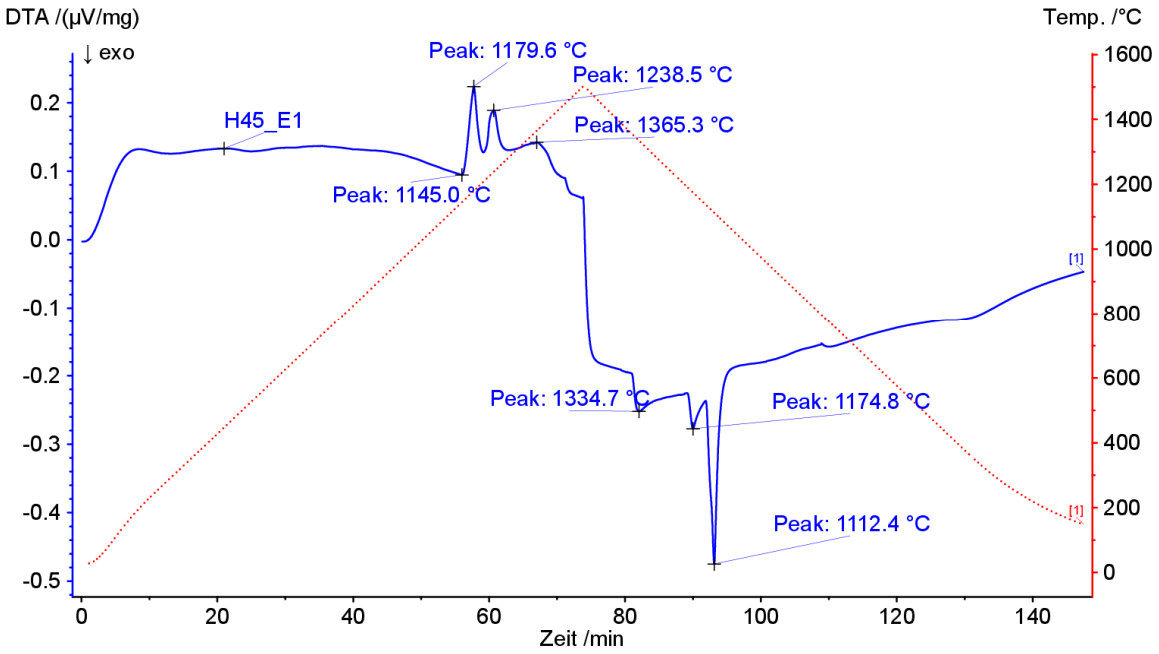

Figure 12 Example DTA analysis measured From RT to 1500°C in 75 min and cooling for 75 min

2.4 Study of the interaction between ingot and Fe

2.4.1 Wetting experiments

For wetting experiments Fe and Fe + 0.8 % C Charpy samples (bars ISO 5754) were pressed at 800 MPa using the same materials as listed in Table 2. Afterwards the Charpy specimens were sintered at 1300°C in Ar / 10 %H_2 atmosphere for 1 h. Ingot pieces, ~300 mg, simply produced by cracking the ingots with a hammer and an anvil, were glued onto the sintered Charpy samples.

Wetting tests under inert conditions were carried out on Fe Charpy samples at 1300°C in Ar atmosphere for 1 h.

Wetting tests under reducing conditions were carried out on Fe + 0.8 % C Charpy samples at 1300°C in Ar/10 %H_2 atmosphere for 1 h.

Die approbierte gedruckte Originalversion dieser Diplomarbeit ist an der TU Wien Bibliothek verfügbar.
The approved original version of this thesis is available in print at TU Wien Bibliothek.

Figure 13 shows the samples before the furnace run and Figure 14 shows the samples after the wetting experiment.

Figure 13 Wetting samples before the furnace run

Figure 14Wetting samples after the furnace run

2.4.2 Infiltration experiments

For infiltration experiments Fe and Fe + 0.6 %C Charpy samples were pressed at 600 MPa using the same material as listed in Table 2.Ingot pieces were glued on the green samples.

Infiltration experiments under inert conditions were carried out on Fe Charpy samples at 1300°C in Ar atmosphere for 1 h.

Infiltration experiments under reducing conditions were carried out on Fe + 0.6 %C Charpy samples at 1300°C in Ar/10% H_2 atmosphere for 1 h.

Figure 15 shows the ingots on the green Charpy samples for infiltration experiments. Figure 16 shows the infiltrated samples after the furnace run.

Die approbierte gedruckte Originalversion dieser Diplomarbeit ist an der TU Wien Bibliothek verfügbar.
The approved original version of this thesis is available in print at TU Wien Bibliothek.

Figure 15 Infiltration samples before the furnace run

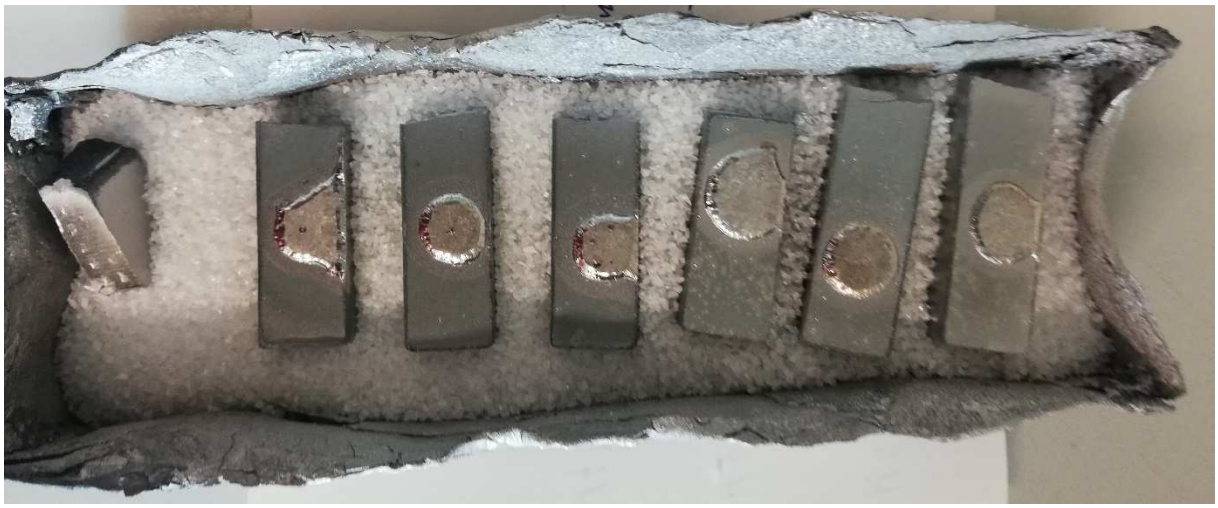

Figure 16 Infiltration samples after the furnace run

The Charpy samples from wetting and infiltration were cut as displayed in Figure 17.

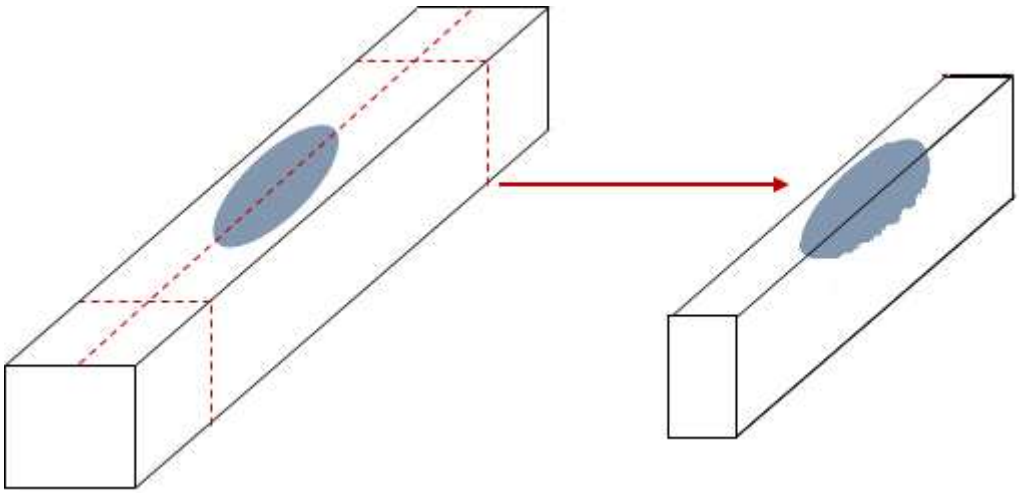

Figure 17 Ingot cutting

After the cutting, the samples were embedded in Bakelite and etched with 1% Nital, to make infiltration visible under the light microscope. An example is shown in Figure 18.

Die approbierte gedruckte Originalversion dieser Diplomarbeit ist an der TU Wien Bibliothek verfügbar.
The approved original version of this thesis is available in print at TU Wien Bibliothek.

Figure 18 1% Nital etched infiltration sample under light microscope

Note: The difference between infiltration and wetting experiments are as follows:

The Charpy samples used for **wetting experiments** were pressed at **800 MPa** and **sintered at 1300°C in Ar/10 %H_2 for 1h**. Those Charpy samples used for wetting experiments under reducing conditions had **additional 0.8 % C**. The slightly higher C content should compensate for C losses during the first sintering step.

The Charpy samples for the **infiltration experiments** were pressed at **600 MPa** and used as **porous green bodies**. The Charpy samples for the infiltration experiments under reducing conditions had **additional 0.6 % C**.

Note: The difference in the C content of the Charpy samples used in wetting and infiltration experiments under reducing conditions comes from a considered C loss during the sintering of the Charpy samples for the wetting experiments. The 0.2% extra C should compensate this loss, in order to have approximately the same C content in both types of experiments.

Both experiments were carried out with a ~300 mg MA ingot glued on the as prepared Charpy samples. The assemblies were sintered at 1300°C for 1h in Ar (inert conditions) or Ar/10 %H_2 (reducing conditions).

2.4.3 DTA measurements with ingots + Fe

For these DTA experiments, ingot and Fe + 0.6 % C powder, the same as used for infiltration Charpy samples, were mixed in a 80 : 20 (Fe+C: MA) ratio. These last studies were done for a better understanding of the influence of C and Si, and DTA measurements with iron can give a hint on the interaction between MA and Fe in terms of melting and solidification.

Figure 19 shows an example measurement of MA + Fe experiments. The blue line is the measurement from the ingot. The black line shows the measurement of the ingot and Fe + 0.6 %C in a 80 : 20 (Fe+C : MA) ratio. In the black line the α-γ- transformation occurs. The blue measurement shows only one exothermal reaction, considered as the melting of the MA. The black line shows the melting of the MA slightly shifted to lower temperatures and a second smaller reaction which probably is a eutectic reaction between the remaining solid MA and the Fe. The last peak in the black line is the melting of the Fe.

These experiments were carried out to improve the understanding of the MA in contact with the iron base powder, finding remarkably different infiltration behaviour of the MA.

Die approbierte gedruckte Originalversion dieser Diplomarbeit ist an der TU Wien Bibliothek verfügbar.
The approved original version of this thesis is available in print at TU Wien Bibliothek.
TU Bibliothek Your knowledge hub WIEN

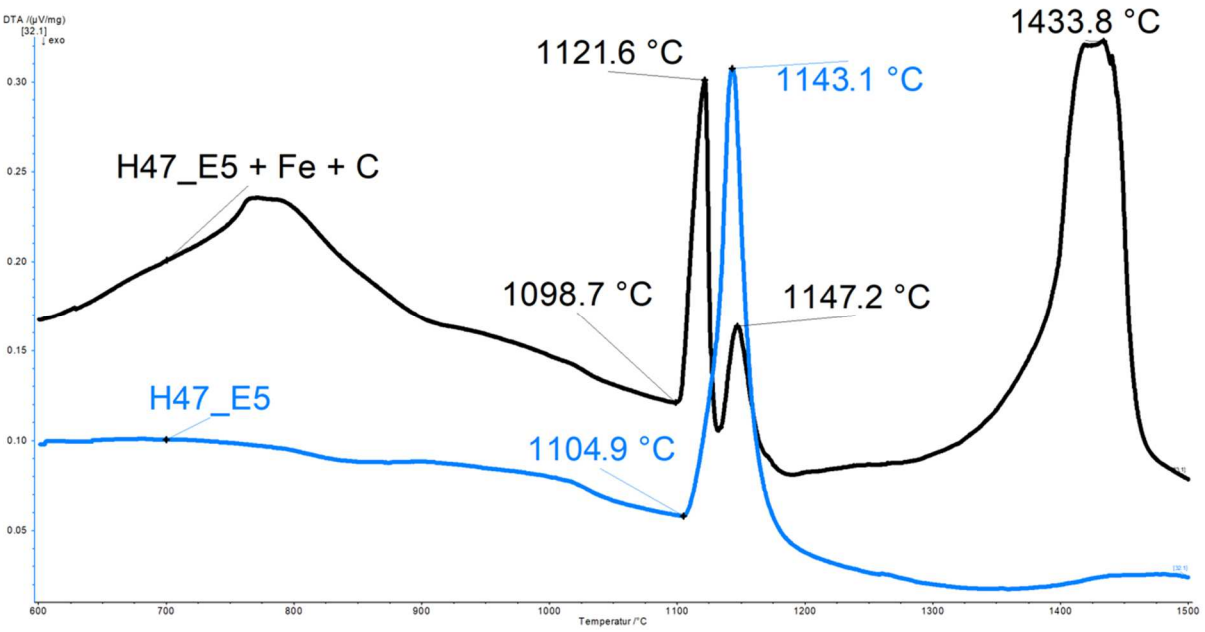

Figure 19 DTA from ingot, and ingot with Fe + 0.6 %C mixture 80 : 20 (Fe+C : MA)

Die approbierte gedruckte Originalversion dieser Diplomarbeit ist an der TU Wien Bibliothek verfügbar.
The approved original version of this thesis is available in print at TU Wien Bibliothek.

3. Results and discussion

3.1 Thermodynamic modelling of alloying systems

ThermoCalc calculations were carried out for MAs found in the literature. The aim of this theoretical study was to find modifications which are considered as "optimized" in the terms claimed in the previous chapter, by finding lower melting points, tightening the melting ranges and increasing the alloying element content as much as possible.

3.1.1 Cu based alloys

- **Cu-Ni-Si**

Cu-Ni-Si systems are known from the literature [49], such as Cu_2Ni_1Si. Starting from this composition, theoretical improvements of the systems were calculated. Achieving lower melting temperatures and higher amount of alloying elements in the MA are considered as optimization criteria.

Comparing the calculated ternary Cu-Ni-Si phase diagram with the phase diagram from the literature [58] both shown in Figure 20, it is clear to see that the prediction is not very accurate for this system. The liquid phase due to the Cu-Si eutectic is predicted at much lower Si content while the solubility of Si and Ni in Cu as a solid solution is lower in the predicted phase diagram than the experimentally determined phase diagram shows.
The differences between calculations and experimentally determined phase diagram might be related to the database used in ThermoCalc which is mainly designed for Fe and Fe based alloying systems, having probably less information about these Cu base compositions.

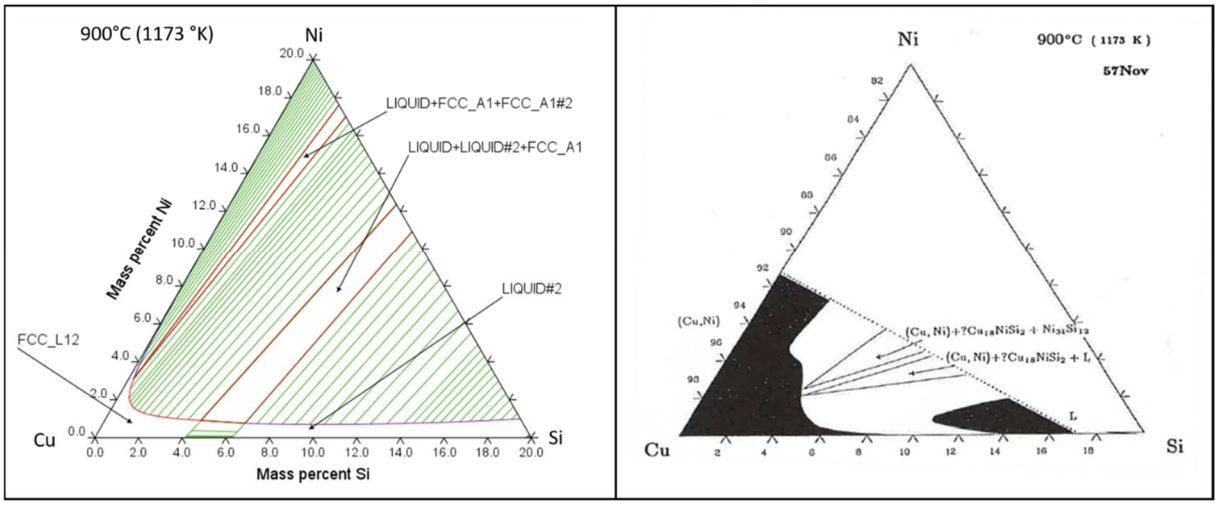

Figure 20 Ternary phase diagrams for Cu-Ni-Si calculated (left) and from the literature [58] (right). Isothermal section at 900°C

In Figure 21 an evolution of phases (EoP) is shown for the original composition, showing a melting range over 28 K at around 1078°C which is more or less the melting point of Cu T(1084°C). The first phase diagram shows the Si content vs temperature. It is clear to see that the liquidus temperature (LT) (blue line) decreases with higher Si content up to a certain amount where LT is constant. The solidus temperature (ST) decreases as well but with higher Si content. An area with two liquid phases is predicted (purple line) where the system is supposed to have eutectic points. The polythermal phase diagram Ni content vs temperature shows a constant increase of the LT and ST with increasing Ni content showing no promising

Die approbierte gedruckte Originalversion dieser Diplomarbeit ist an der TU Wien Bibliothek verfügbar.
The approved original version of this thesis is available in print at TU Wien Bibliothek.
TU Bibliothek Your knowledge hub WIEN

composition. For the first improvement step the Si content was increased to the first eutectic point.

Note: Figure 21 shows in the Si vs T phase diagram a DIAMOND_A4 phase. This predicted phase is not a Carbon Diamond, it is Si supposed to crystalize in a cubic diamond structure. This fits rather well to the binary Cu-Si phase diagram shown in Figure 177 in the attachment, where Cu can solve ~12% Si.

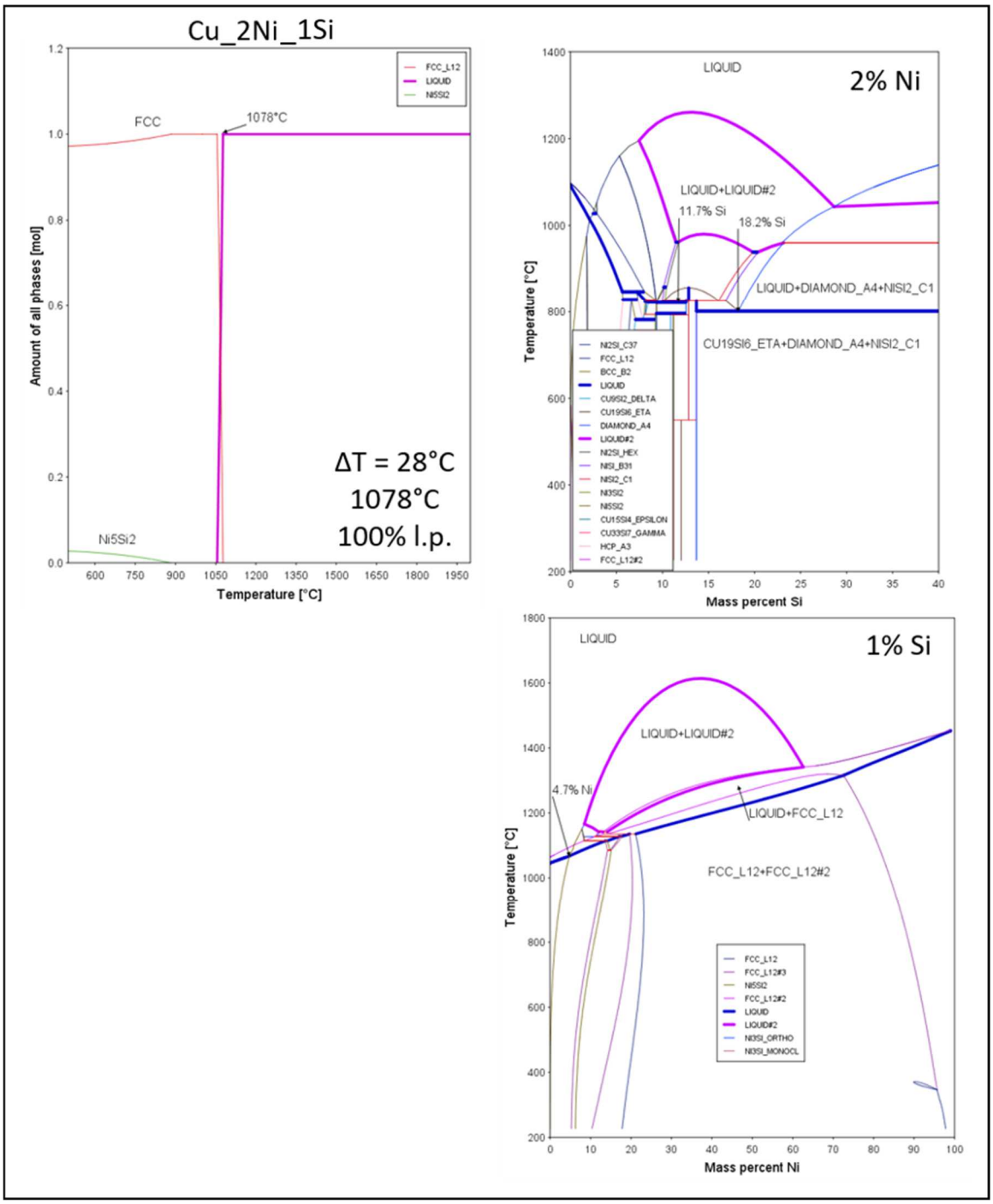

Figure 21 Evolution of phases and phase diagrams for Ni and Si vs temperature for Cu_2Ni_1Si

Figure 22 shows the first modification for the Cu-Ni-Si system by increasing the Si content. The Ni content vs. T phase diagram changes remarkably with the higher Si content. The LT is not

Die approbierte gedruckte Originalversion dieser Diplomarbeit ist an der TU Wien Bibliothek verfügbar.
The approved original version of this thesis is available in print at TU Wien Bibliothek.
TU Bibliothek Your knowledge hub WIEN

increasing anymore proportionally with the increase of the Ni content. Increasing the Ni content seems to tighten the melting window with eutectic point at ~2.3% Ni. According to ThermoCalc Cu_Si_Ni has a eutectic composition with Cu_11.7Si_2.3Ni. By increasing the Si and Ni content the melting temperature seems to be reduceable from 1078°C to 822°C. This is close to the eutectic the Cu-Si binary system forms slightly above 800°C.

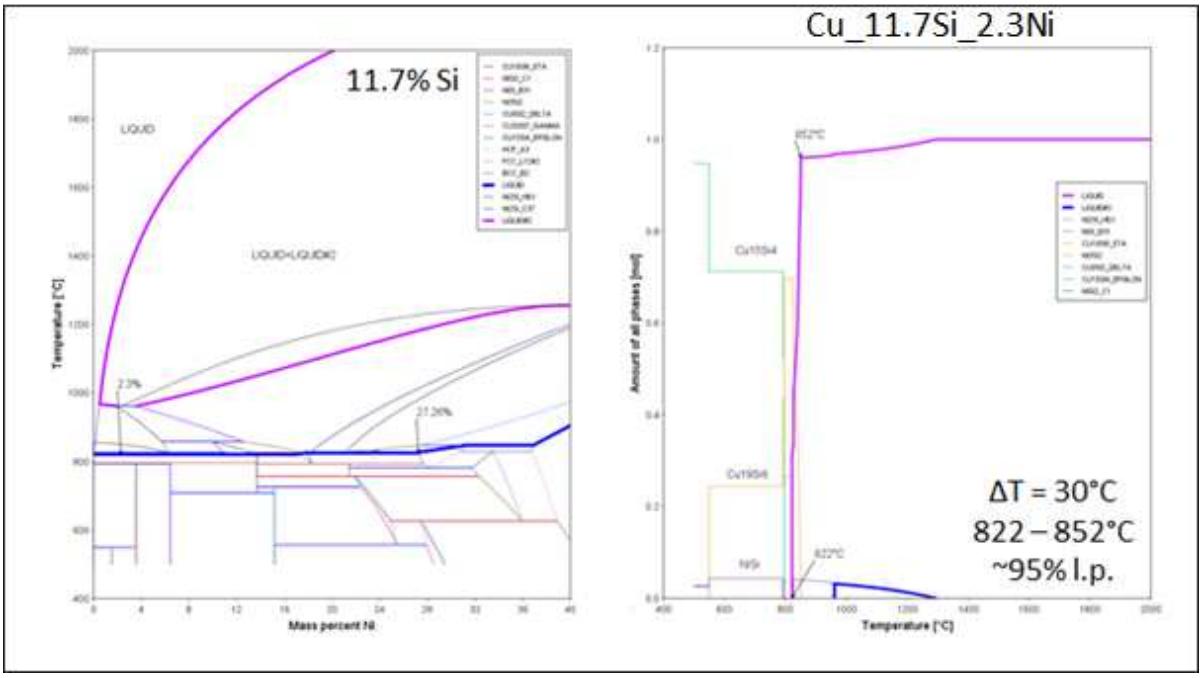

Figure 22 Ni vs temperature and Evolution of phases for Cu_11.7Si_2.3Ni

Another approach for improvement is shown in Figure 23. Not the suggested eutectic point but a peritectic point at the low LT was chosen. Again, the Ni vs T phase diagram changed remarkably with this Si content. The phase diagram shows a maximum Ni content for the lowest LT at 8.3% Ni. The EoP for Cu_18.2Si_8.3Ni shows a melting point at 826°C where $Cu_{19}Si_6$ seems to fully melt. This phase is around 85% of the MA. $NiSi_2$ transforms into NiSi by losing Si into the formed liquid. NiSi is supposed to melt at 978°C which agrees with the ASM handbook Vol. 3 [59]. This composition shows a different melting mechanism to the Cu_11.7Si_2.3Ni that forms two different liquid phases. The first liquid phase is predicted to fully melt at a certain temperature for Cu_18.2Si_8.3Ni and show a 30 K range for Cu_11.7Si_2.3Ni.

Die approbierte gedruckte Originalversion dieser Diplomarbeit ist an der TU Wien Bibliothek verfügbar.
The approved original version of this thesis is available in print at TU Wien Bibliothek.

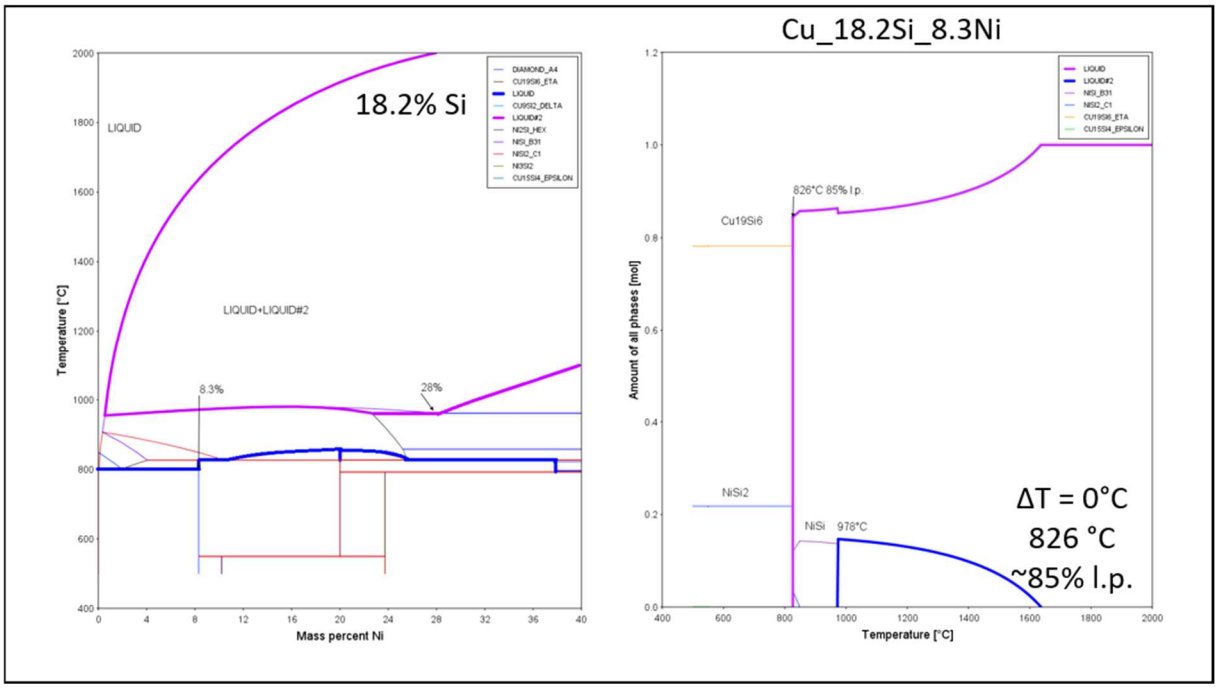

Figure 23 Ni vs temperature and Evolution of phases for Cu_18.2Si_8.3Ni

Figure 24 shows the same Ni content vs T phase diagram but the EoP for the eutectic composition at relatively high Ni content. By increasing the Ni content, the amount of the two phases changes. As the same phases seem to be formed in different amounts, no changes in the melting behaviour are expected. Only the amount of liquid phase at the melting point differs to the changed amount of phases.

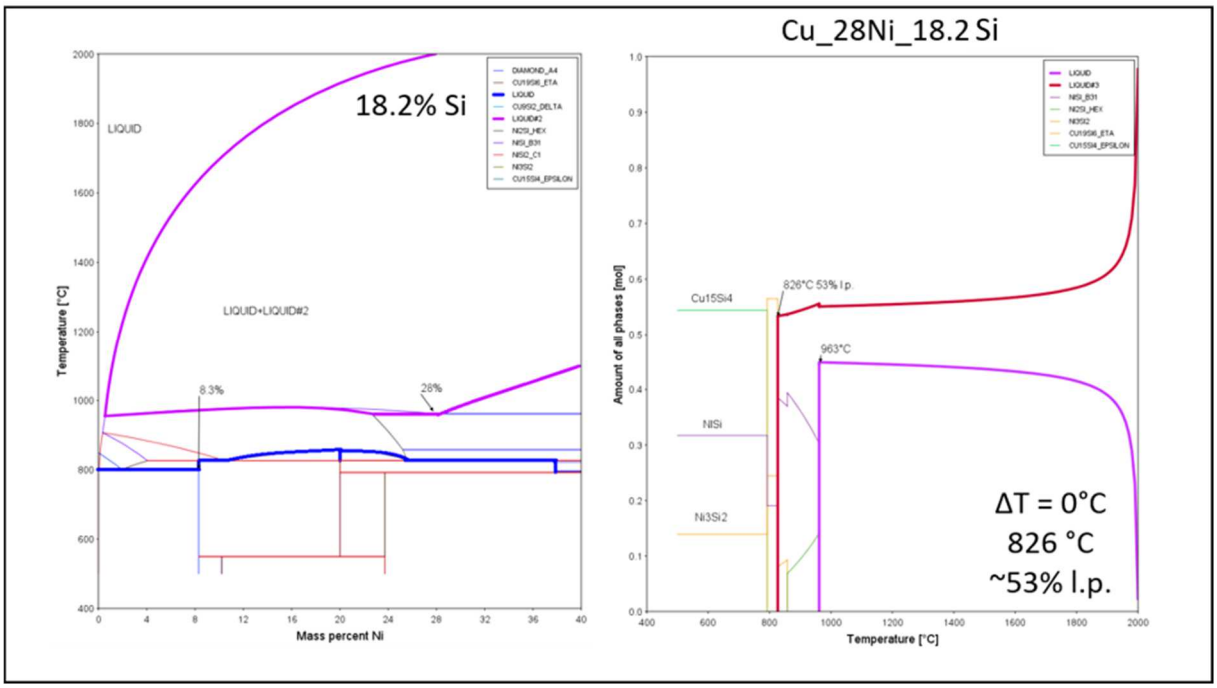

Figure 24 Ni content vs temperature and Evolution of phases for Cu_28Ni_18.2Si

Figure 25 shows that the Si vs T phase diagram changes with higher Ni contents but not as markedly as the Ni vs T phase diagram changed with increased Si content. The LT decreases

Die approbierte gedruckte Originalversion dieser Diplomarbeit ist an der TU Wien Bibliothek verfügbar.
The approved original version of this thesis is available in print at TU Wien Bibliothek.
TU Bibliothek Your knowledge hub WIEN

with increasing Si content. Eutectic compositions can be found but in comparison with the lower Ni content they are shifted to higher Si contents.

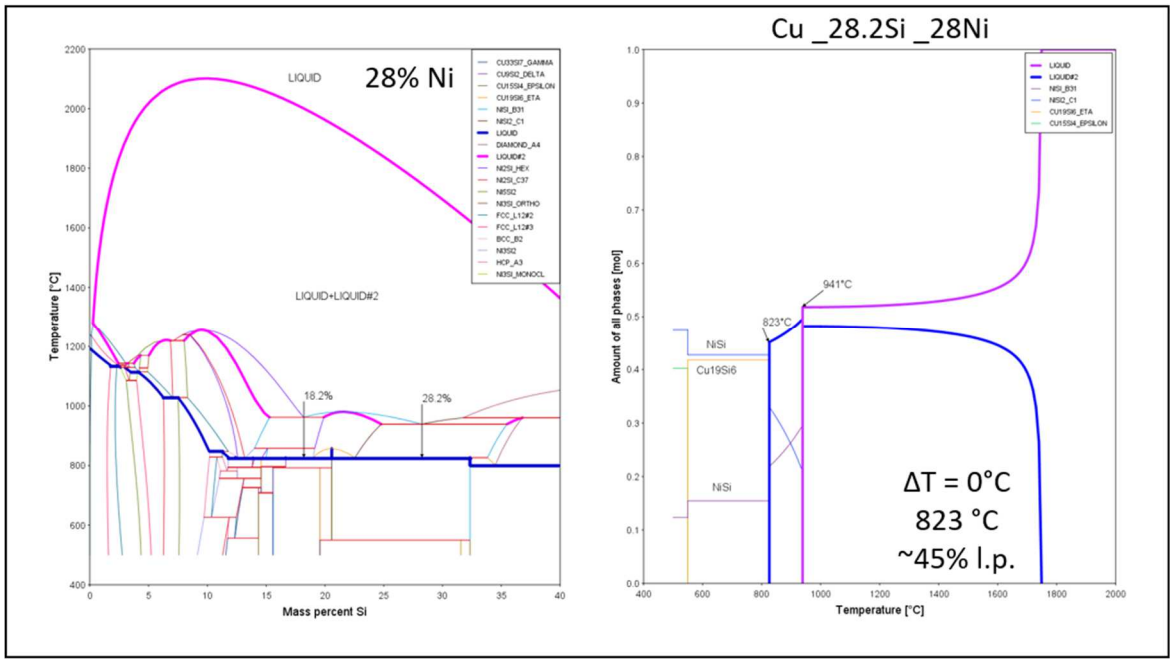

Figure 25 Si content vs temperature and Evolution of phases for Cu_28.2Si_28Ni

Summary: In case of Cu_Si_Ni it seems to be beneficial for the system to increase the Si and Ni content. Si and Ni are predicted to influence each other obtaining different phase diagrams with varying alloying element content. According to these ThermoCalc calculations Cu_Si_Ni MA with higher alloying element content and lower liquidus temperatures than the starting composition can be realized. These systems seem to be promising starting points for improvement work.

- **Cu-Mn-Si**

Cu-Mn-Si systems are well known in the literature. Compositions such as Cu_8Si_2Mn [36] are already used in powder metallurgy so it seemed to be reasonable to try to find possible improvements for this system.

Comparing the calculated ternary Cu-Mn-Si phase diagram with the experimentally determined phase diagram from the literature [58] , both shown in Figure 26, it is good to see that the phase diagrams show similarities e.g. the liquid phase window between 12 and 14 mass% Si is visible in both phase diagrams. The solubility of Mn and Si in Cu is predicted comparatively well for this system.

Die approbierte gedruckte Originalversion dieser Diplomarbeit ist an der TU Wien Bibliothek verfügbar.
The approved original version of this thesis is available in print at TU Wien Bibliothek.

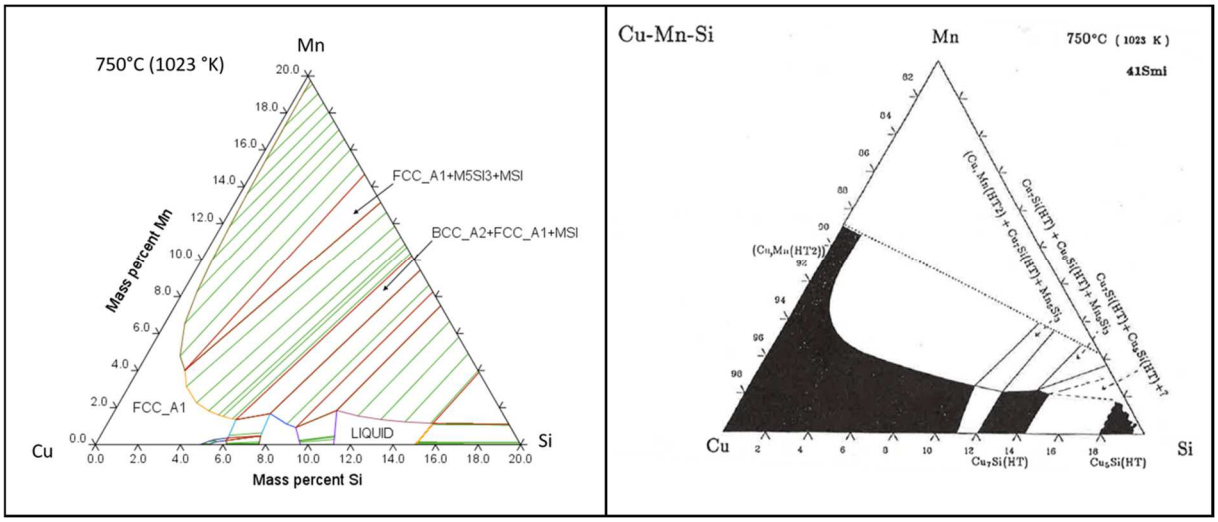

Figure 26 Ternary phase diagrams for Cu-Mn-Si calculated (left) and from the literature [58] (right). Isothermal section at 750°C

EoP for the original composition Cu_8Si_2Mn, shown in Figure 27 seems to be rather good in terms of a low melting point.

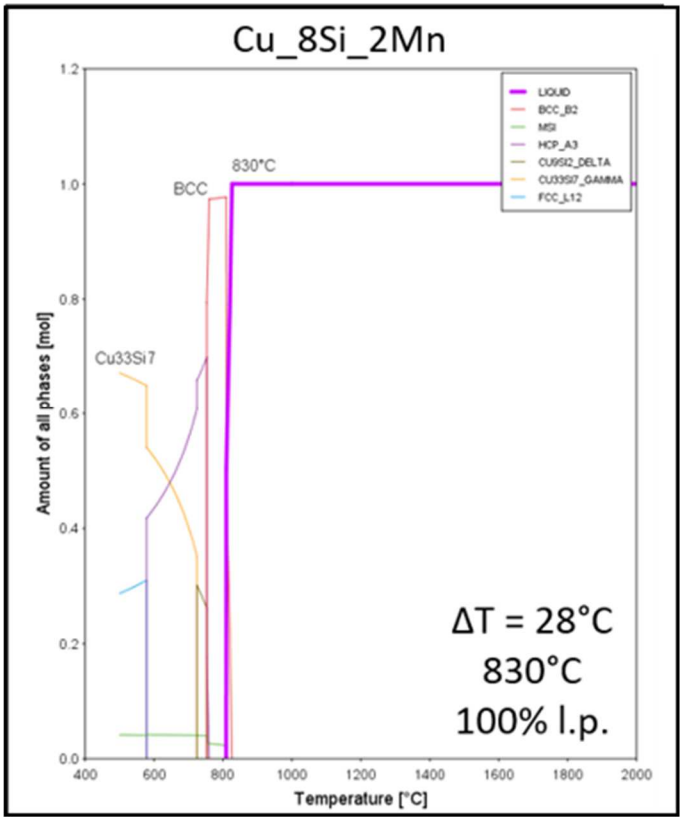

Figure 27 Evolution of phases for Cu_8Si_2Mn

Both phase diagrams shown in Figure 28 show a eutectic composition which slightly differs from the original composition.

Die approbierte gedruckte Originalversion dieser Diplomarbeit ist an der TU Wien Bibliothek verfügbar.
The approved original version of this thesis is available in print at TU Wien Bibliothek.

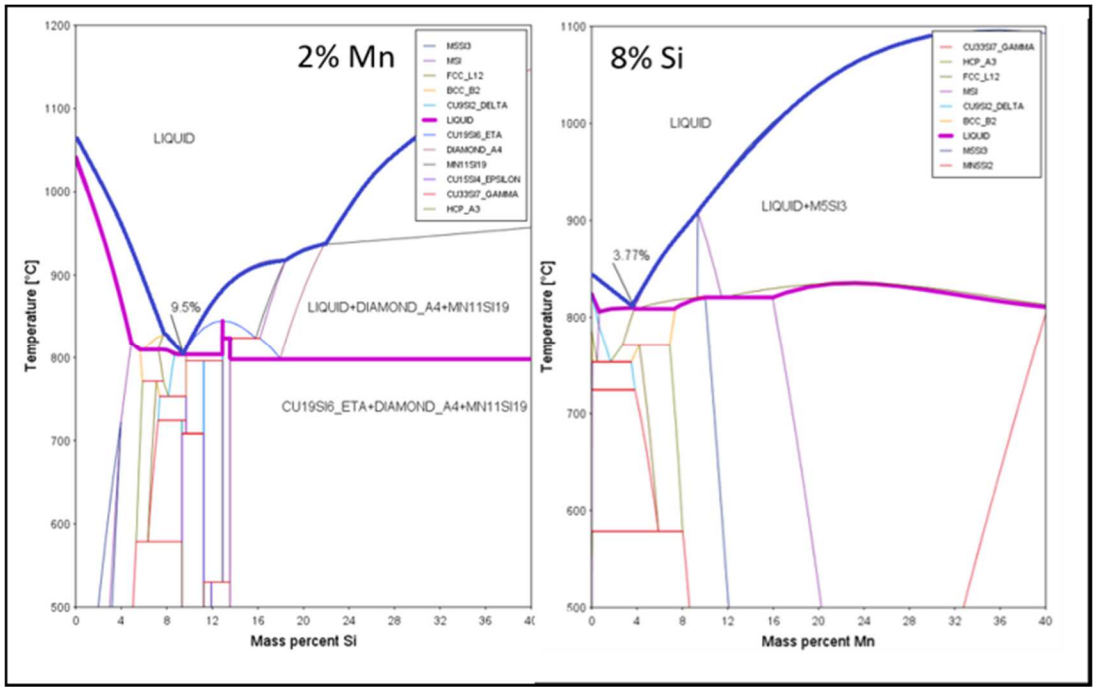

Figure 28 Evolution of phases and phase diagrams for Si and Mn vs temperature for Cu_8Si_2Mn

Figure 29 shows the step from 2% to 3.77 %Mn, achieving a predicted sharp transition instead of a melting range by adding some more Mn.

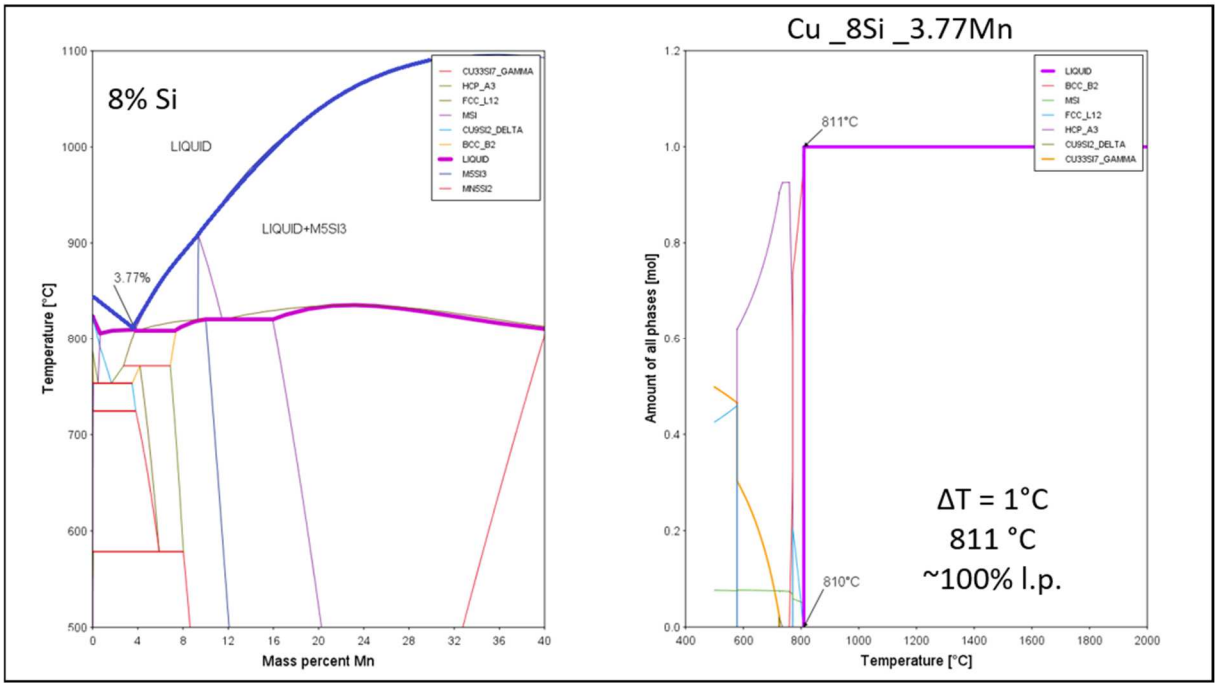

Figure 29 Mn vs temperature and Evolution of phases for Cu_8Si_3.77Mn

As shown in Figure 30 by increasing the Si content from the initial composition it was possible to find a eutectic composition that melts at 806°C, which is about 25 K lower than the initial composition.

Die approbierte gedruckte Originalversion dieser Diplomarbeit ist an der TU Wien Bibliothek verfügbar.
The approved original version of this thesis is available in print at TU Wien Bibliothek.

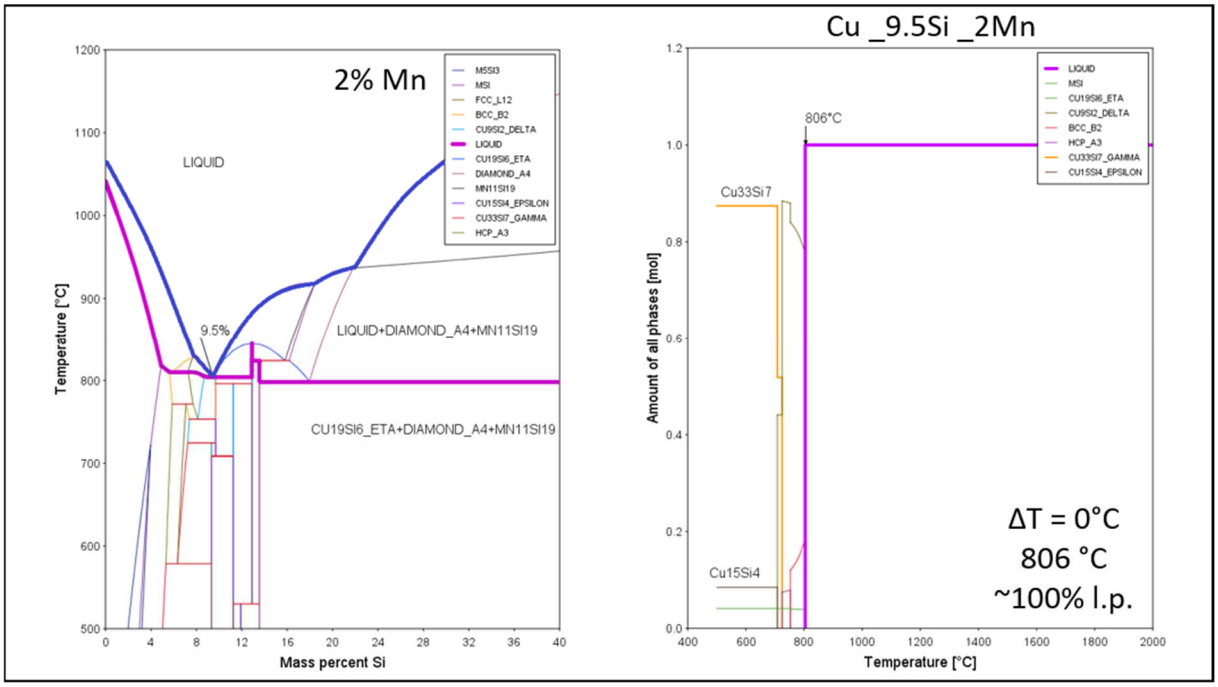

Figure 30 Si vs temperature and Evolution of phases for Cu_9.5Si_2Mn

Another approach to find an interesting system is starting from a binary eutectic. In Figure 31 the binary Cu-Mn phase diagram shows a eutectic composition at rather high Mn content. For this Mn content the Si vs T phase diagram shows a clear eutectic point. With this approach, a eutectic system with much higher alloying element content could be obtained, showing fairly the same predicted melting temperatures and behaviour but different predicted phases.

Die approbierte gedruckte Originalversion dieser Diplomarbeit ist an der TU Wien Bibliothek verfügbar.
The approved original version of this thesis is available in print at TU Wien Bibliothek.

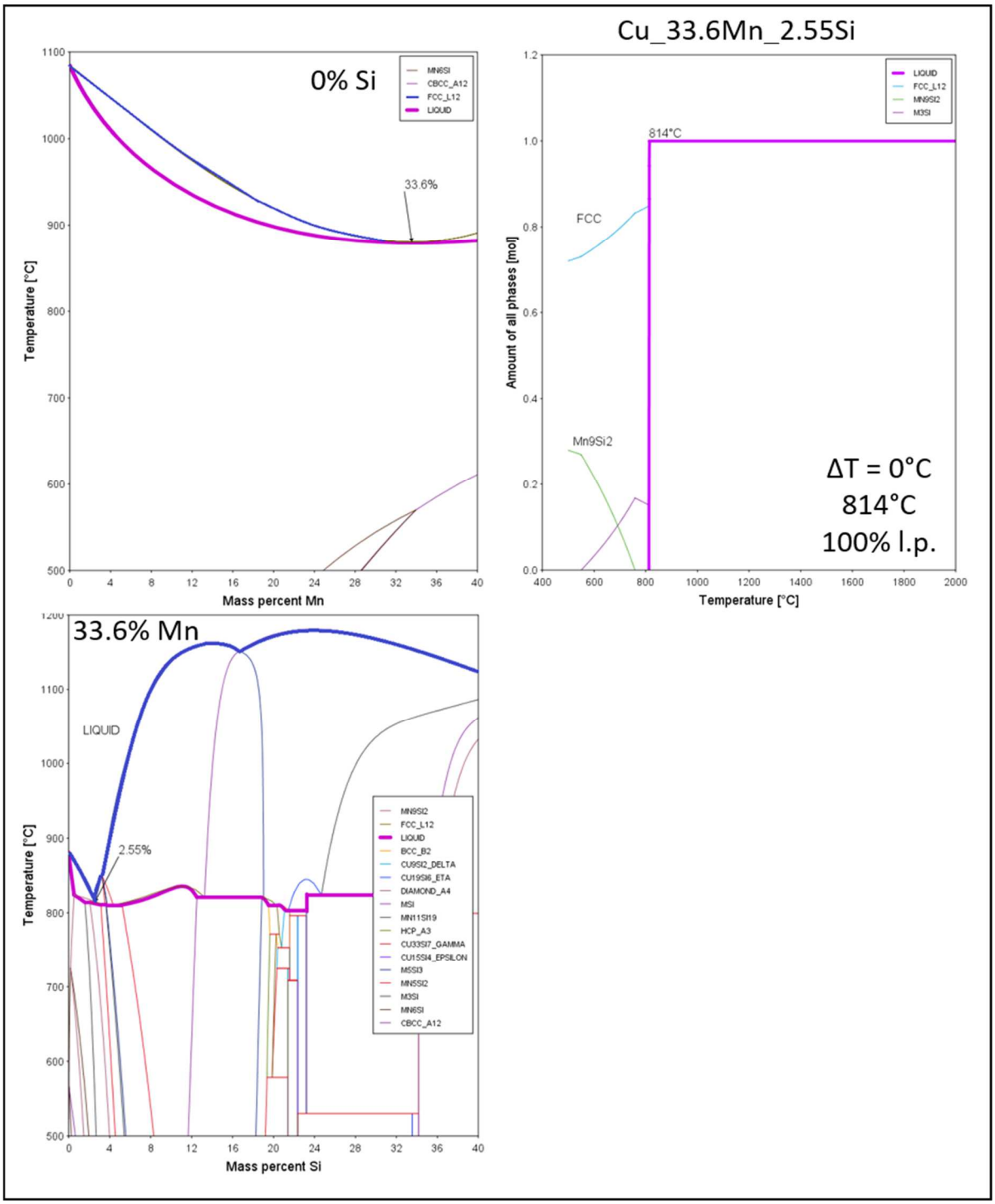

Figure 31 Mn and Si vs temperature and Evolution of phases for Cu_33.6Mn_2.55Si

Summary: For Cu_8Si_2Mn small adjustments could be beneficial in terms of melting behaviour or temperatures, while the second approach predicted a system with much higher Mn content with the same melting behaviour by increasing the alloying element content.

Die approbierte gedruckte Originalversion dieser Diplomarbeit ist an der TU Wien Bibliothek verfügbar.
The approved original version of this thesis is available in print at TU Wien Bibliothek.
TU Bibliothek Your knowledge hub WIEN

3.1.2 B containing systems

- **Fe-B-C**

B as an alloying element in Fe and Ni based master alloys has lately been described in the literature (Xiu, Salwen et al. 2003).[48] For Fe-B-C systems Fe_4.37C_1.75B was used as a starting point.

Comparing the calculated Fe-B-C shown with the experimentally determined phase diagram from the literature [60] both shown in Figure 32, it is clear to see that the database used by ThermoCalc has no detailed information about this system.

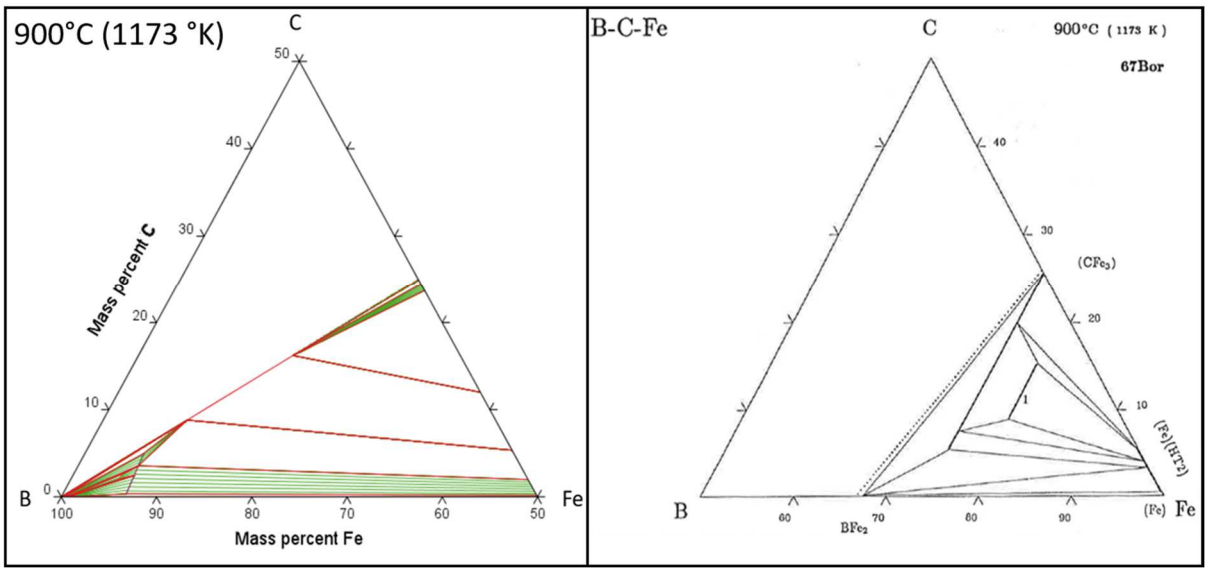

Figure 32 Ternary Fe-B-C phase diagram calculated with ThermoCalc (left) and from the literature [60] (right). Isothermal section at 900°C

In Figure 33 the EoP predicts the start of the melting of FCC phase and Cementite at 1129°C due to a eutectic reaction over a 34 K range. The C content vs T phase diagram shows a clear eutectic while the B phase diagram shows an increase of the ST with increasing B content.

Die approbierte gedruckte Originalversion dieser Diplomarbeit ist an der TU Wien Bibliothek verfügbar.
The approved original version of this thesis is available in print at TU Wien Bibliothek.

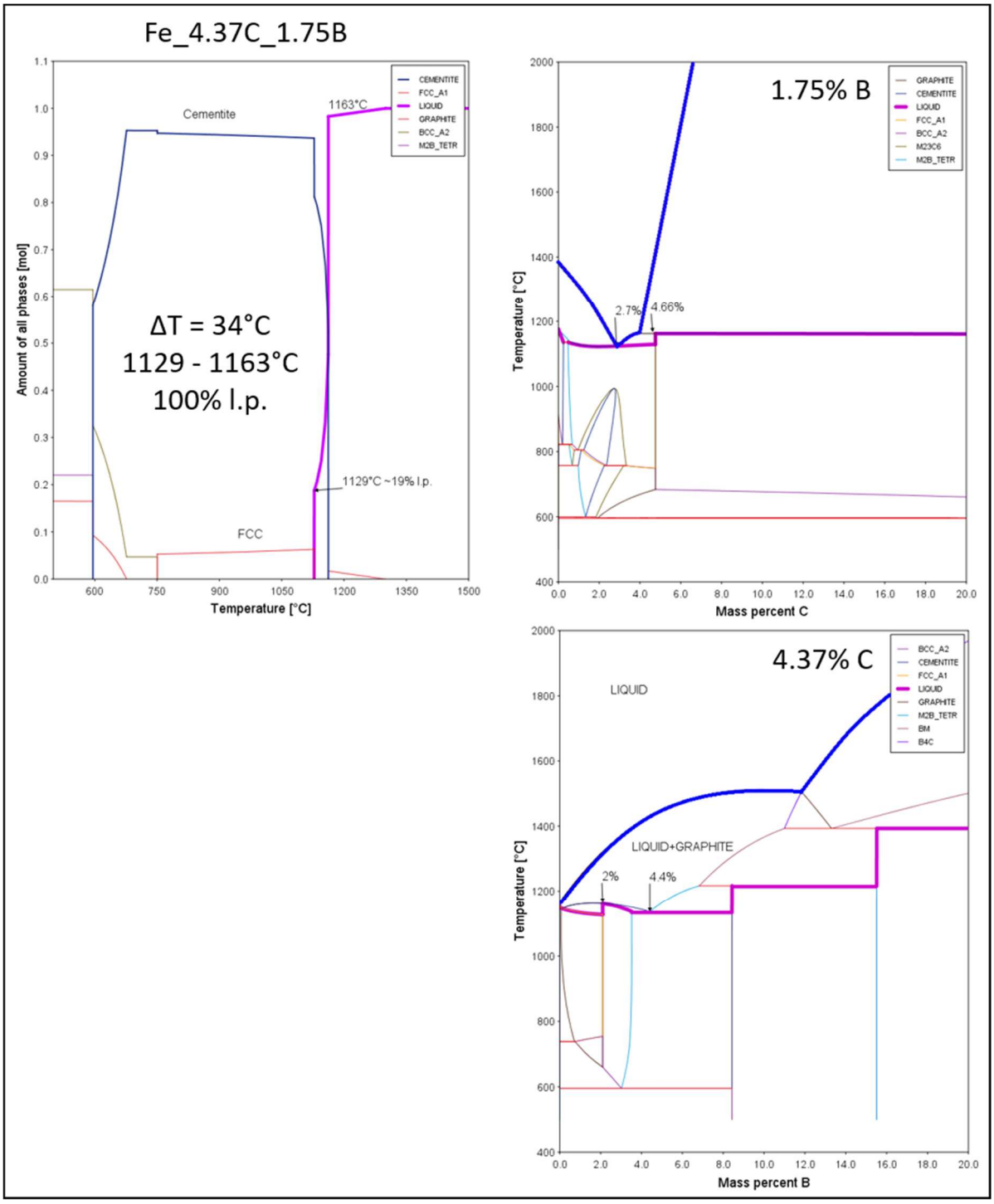

Figure 33 Evolution of phases and phase diagrams for B and C vs temperature for Fe_4.37C_1.75B

The peritectic point at 4.4% B tightened the melting window. Figure 34 shows the EoP where all the cementite is supposed to melt at a certain temperature. The C content vs T for the 4.4% B shows the eutectic point shifted to higher C contents. Adjusting the C content eliminates the graphite phase, and the system is supposed to fully melt at 1137°C. Comparatively small adjustments in the alloying element content change the melting behaviour. If a sharp transition or a continuous melting is more beneficial for the systems properties is not clear to say. Having the choice seems to be promising.

Die approbierte gedruckte Originalversion dieser Diplomarbeit ist an der TU Wien Bibliothek verfügbar.
The approved original version of this thesis is available in print at TU Wien Bibliothek.
TU Bibliothek Your knowledge hub WIEN

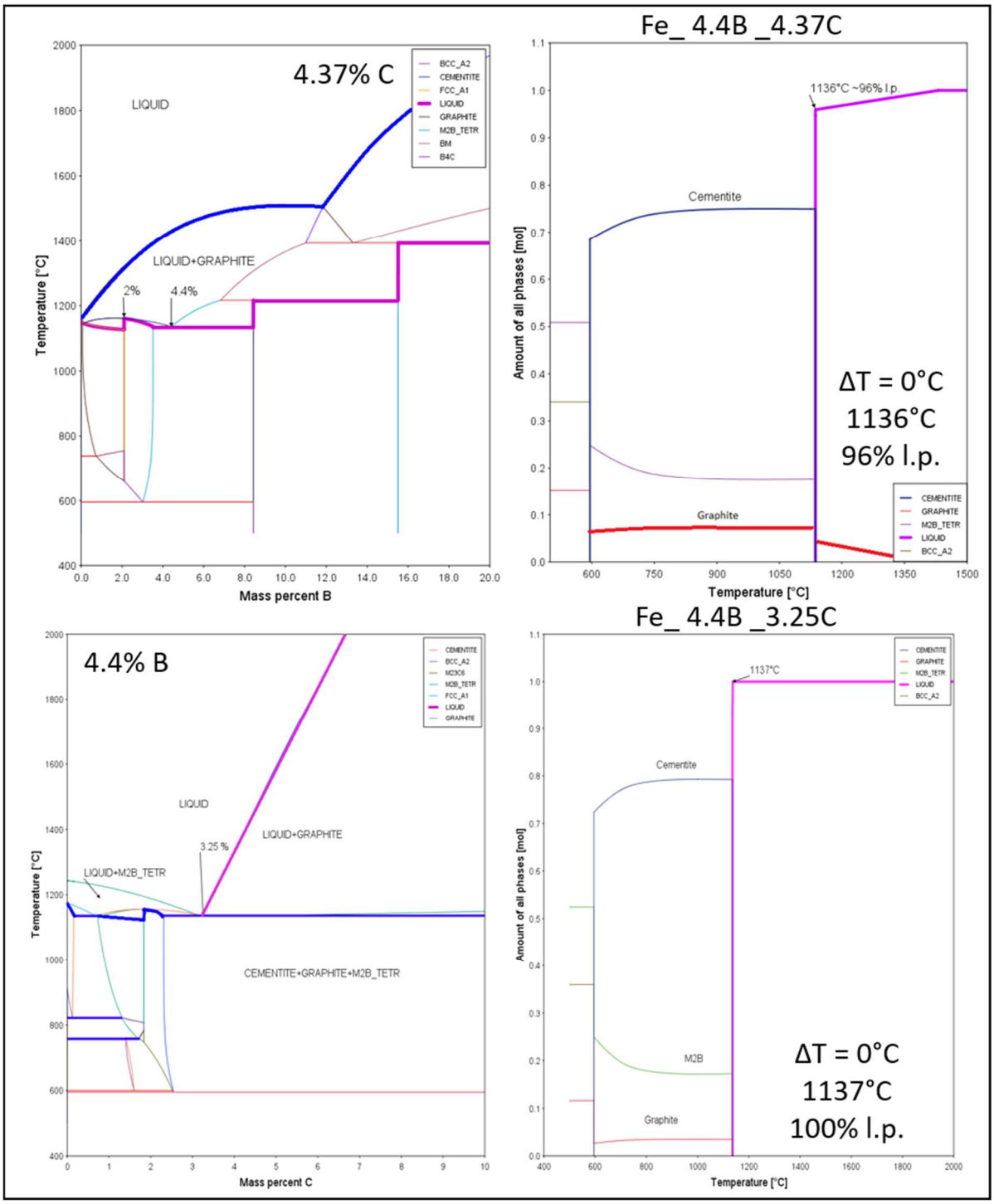

Figure 34 B and C vs temperature and evolution of phases for Fe_4.4B_4.37C and Fe_4.4B_3.25C

Figure 35 shows the eutectic composition for 1.75% B leading to a system with a defined melting point. This prediction achieves 10 K lower melting point with half the C content. This system is not considered as an improvement to the original composition.

Die approbierte gedruckte Originalversion dieser Diplomarbeit ist an der TU Wien Bibliothek verfügbar.
The approved original version of this thesis is available in print at TU Wien Bibliothek.

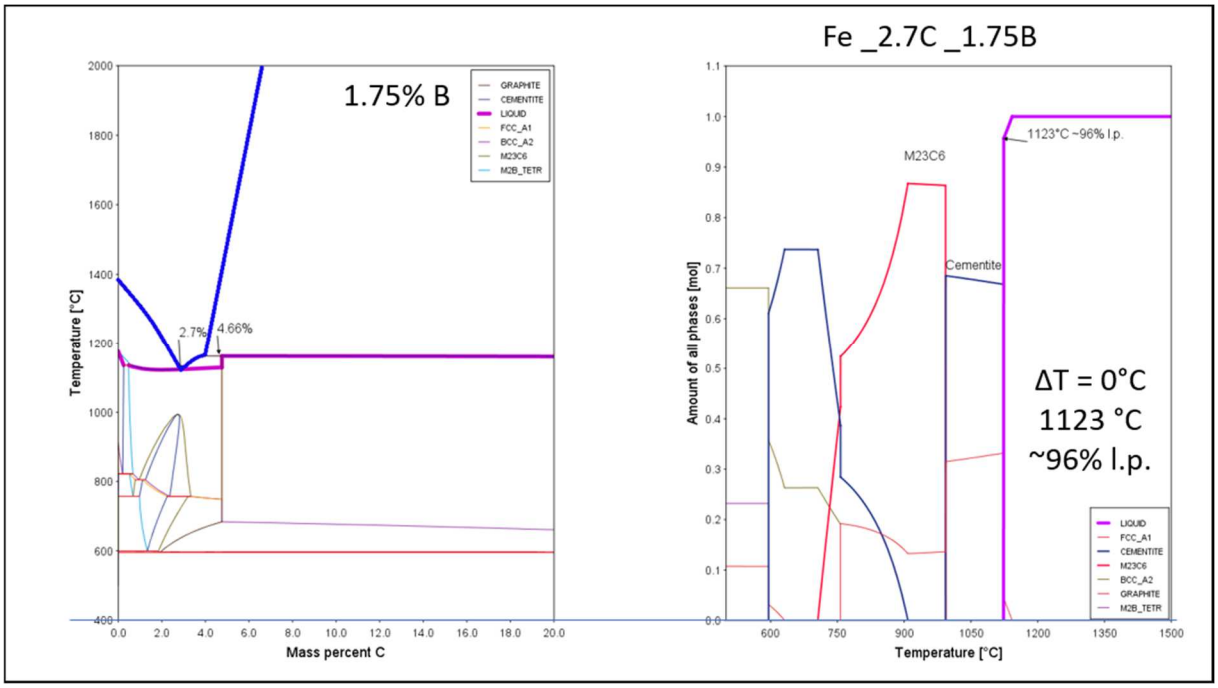

Figure 35 C vs temperature and evolution of phases for Fe_2.7C_1.75B

Summary: The original Fe_B_C system seemed to be rather optimized in terms of melting temperatures and alloying content. With adjusting of the alloying elements content, the melting behaviour is predicted to be modified in terms of melting at a defined melting point. Melting at a certain temperature might be more beneficial for infiltration properties than melting over a 34 K range.

Note: It is probably necessary to mention that for this MA, which contains elements with high diffusion rates into the Fe matrix, it is very likely that during the heating phase the composition of such a MA would continuously change its composition and with that its melting behaviour as shown in the modification path carried out in this chapter. These calculations do not consider the base powder interaction with the MA.

Die approbierte gedruckte Originalversion dieser Diplomarbeit ist an der TU Wien Bibliothek verfügbar.
The approved original version of this thesis is available in print at TU Wien Bibliothek.

- **Fe-B-Mn-Ni-Si**

The Fe-B-Mn-Ni-Si MA is a multi-alloying element example. For this system the approach through a eutectic system was taken, trying to find a system with a relatively low melting point, containing as much of alloying elements as possible. Figure 36 shows the stepwise introduction of the elements into the system, starting from the binary Fe-B eutectic and adding the maximum amount of Mn before the LT is predicted to be increased. The Si vs T phase diagram shows a eutectic point for this content of Fe, B and Mn. The Ni phase diagram seems to be remarkable, decreasing the ST with increasing Ni content.

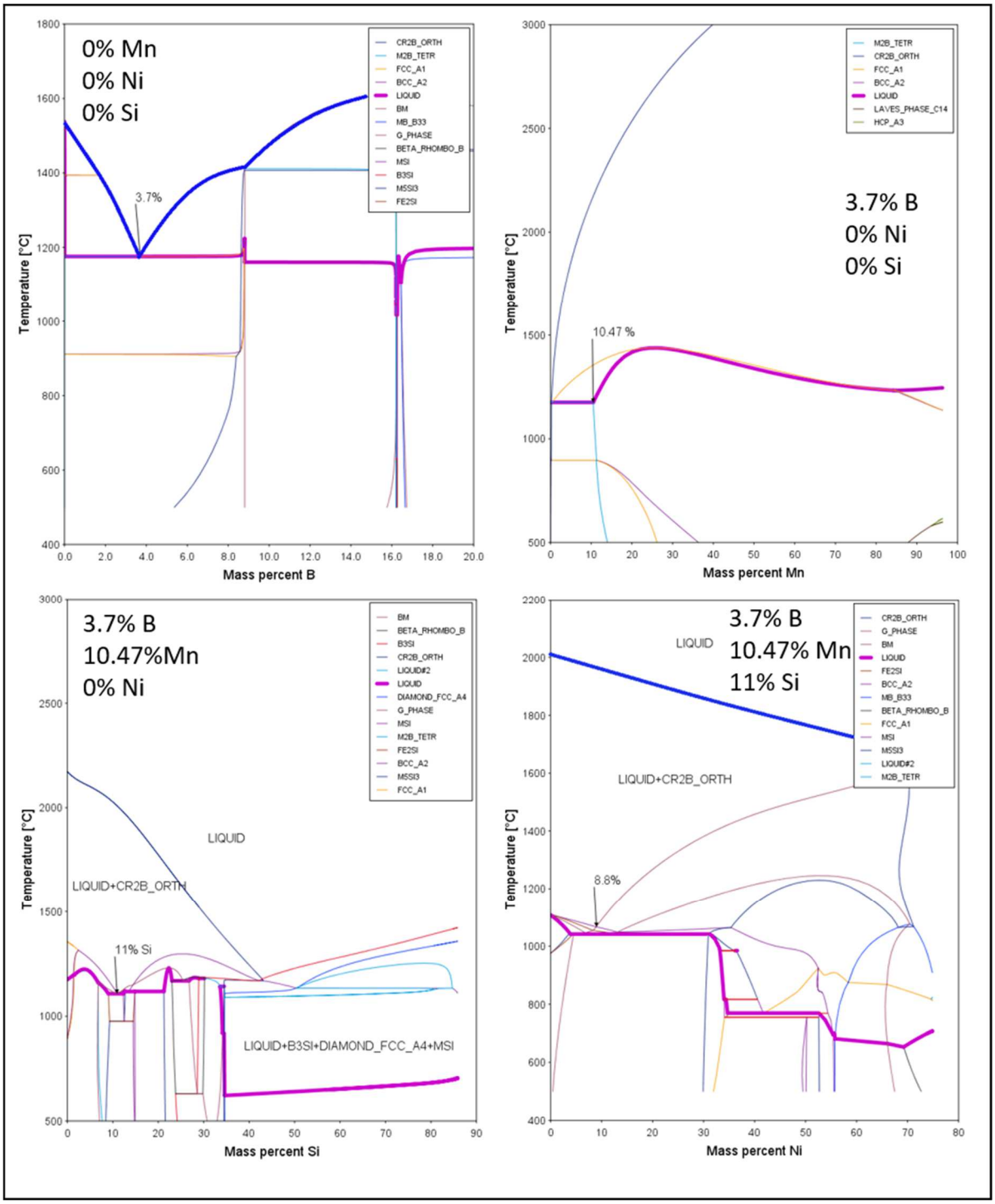

Figure 36 B, Mn, Si and Ni vs temperature. Stepwise introducing elements

Die approbierte gedruckte Originalversion dieser Diplomarbeit ist an der TU Wien Bibliothek verfügbar.
The approved original version of this thesis is available in print at TU Wien Bibliothek.

The melting temperature is supposed to decrease with increasing of Ni content. The peritectic point was chosen for a first composition. Figure 37 shows the EoP of a difficult multi component MA. The first approach seems to be reasonable. This composition was the starting point for optimization, trying especially to decrease the melting point of the system. Looking at the B vs T phase diagram, with the additional elements a tremendous change can be obtained, heavily increasing the LT by a small increase of the B content. Reducing the B content from 3.7% B to 0.16% B seems to be more beneficial for the system and more reasonable for a real approach.

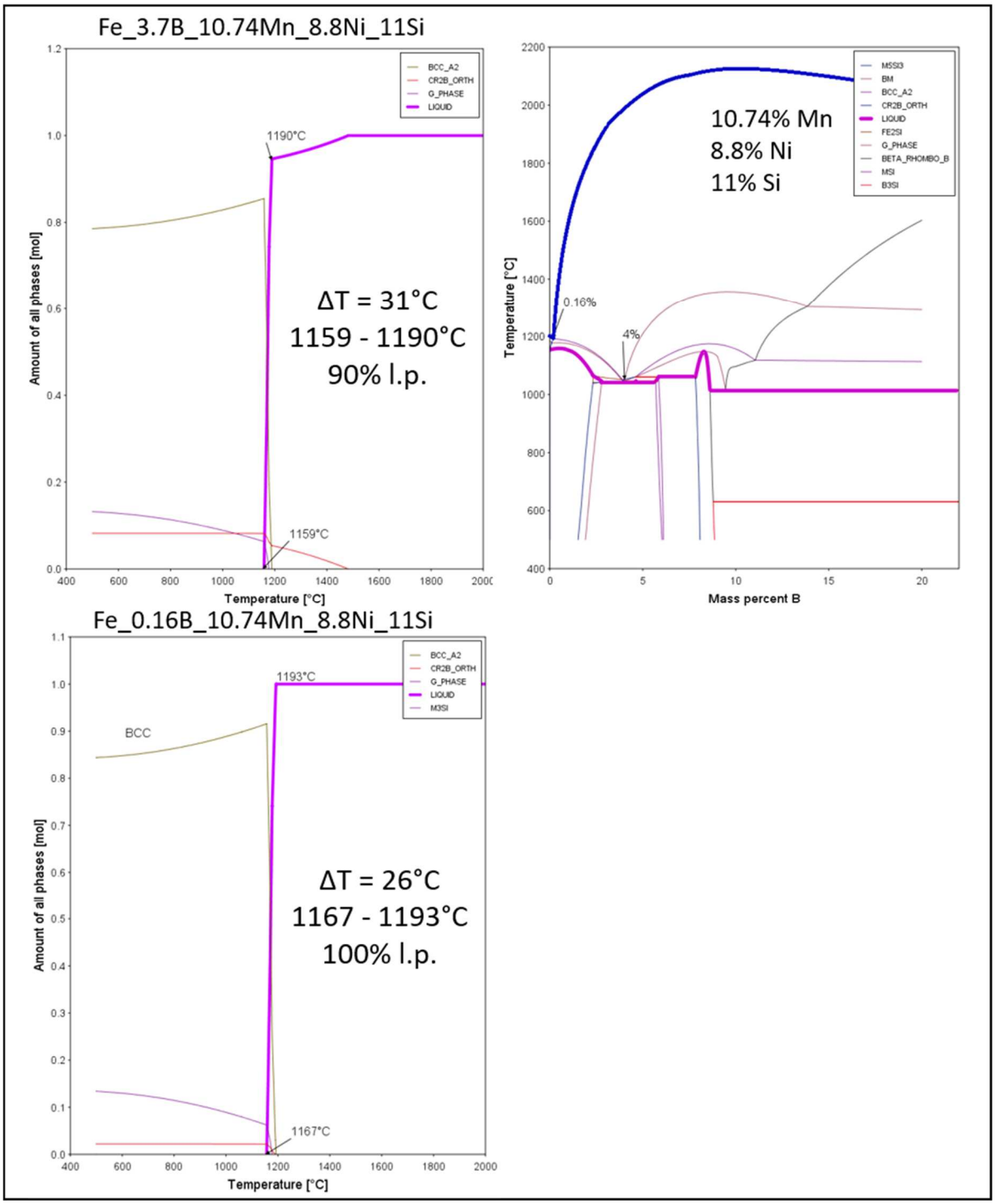

Figure 37 B vs temperature and Evolution of phases for Fe_3.7B_10.74Mn_8.8Ni_11Si and Fe-0.16B_10.74Mn_8.8Ni_11Si

Die approbierte gedruckte Originalversion dieser Diplomarbeit ist an der TU Wien Bibliothek verfügbar.
The approved original version of this thesis is available in print at TU Wien Bibliothek.
TU Bibliothek Your knowledge hub WIEN

Figure 38 shows that the adjusted B content and the Ni have a huge influence on the Si vs T phase diagram. The phase diagram shows a LT minimum between 14.5 and 21.4% Si. Increasing the Si content lowered the melting temperature but broadened the melting range.

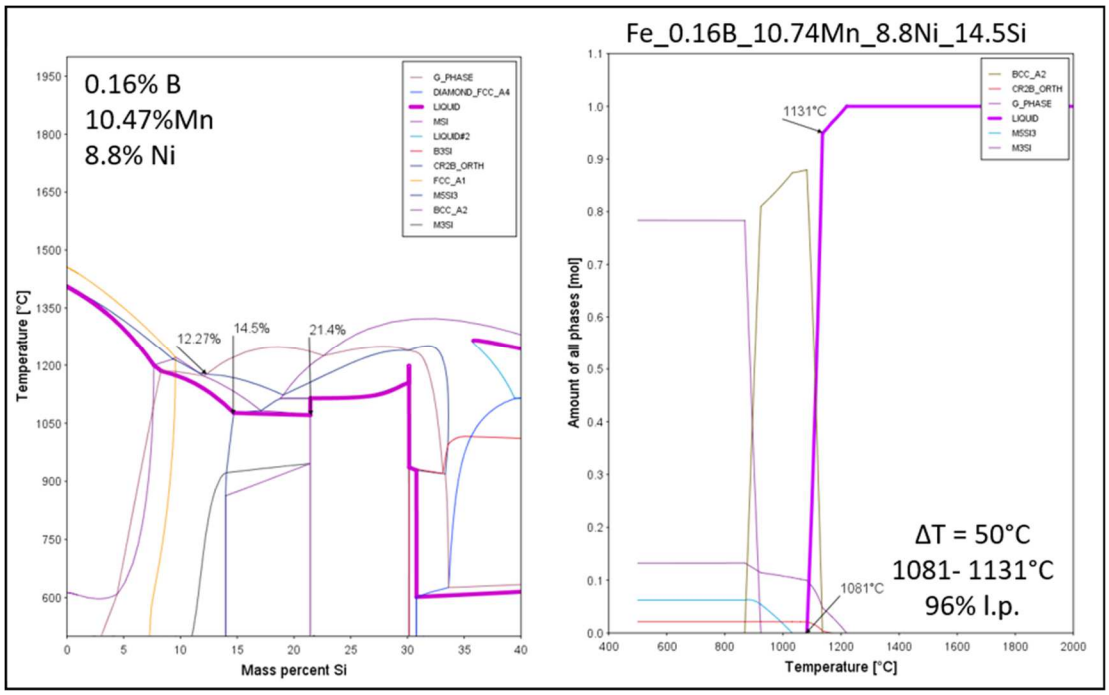

Figure 38 Si vs temperature and evolution of phases for Fe_0.16B_10.74Mn_8.8Ni_14.5Si

Figure 39 shows an adjustment which does not seem to be beneficial in the first approach, because the Ni content is decreased. The difficulty of so many alloying elements is the permanent influence on each other. The change from 8.8% Ni to the eutectic at 7% Ni had an influence on the Mn vs T phase diagram shown in Figure 40.

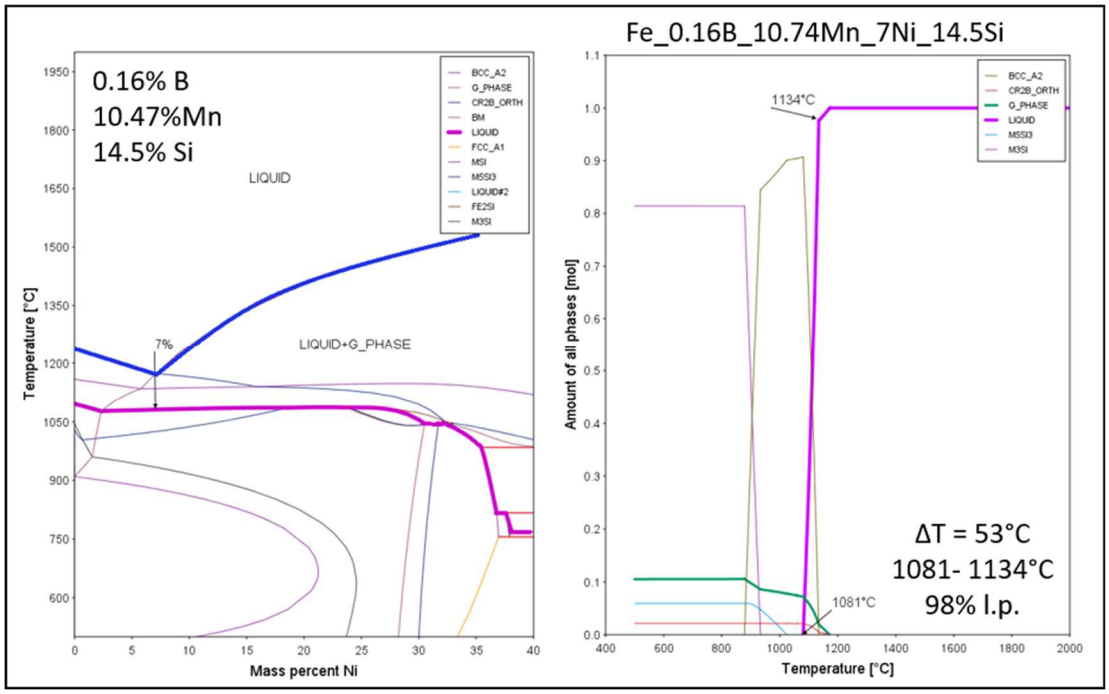

Figure 39 Ni vs temperature and evolution of phases for Fe_0.16B_10.74Mn_7Ni_14.5Si

Die approbierte gedruckte Originalversion dieser Diplomarbeit ist an der TU Wien Bibliothek verfügbar.
The approved original version of this thesis is available in print at TU Wien Bibliothek.

The Mn vs T phase diagram in Figure 40 shows a different influence of the Mn content for the Fe-B-Mn-Ni-Si system compared to the Mn vs T phase diagram for Fe-B-Mn shown in Figure 36. Figure 40 shows a decrease in ST with increasing Mn content to the eutectic point. Further increasing the Mn content would broaden up the melting range but decrease the LT. Choosing the higher Mn content tightened the melting window for the system and a lowering of the LT from 1160°C from the first composition to 1043°C could be achieved.

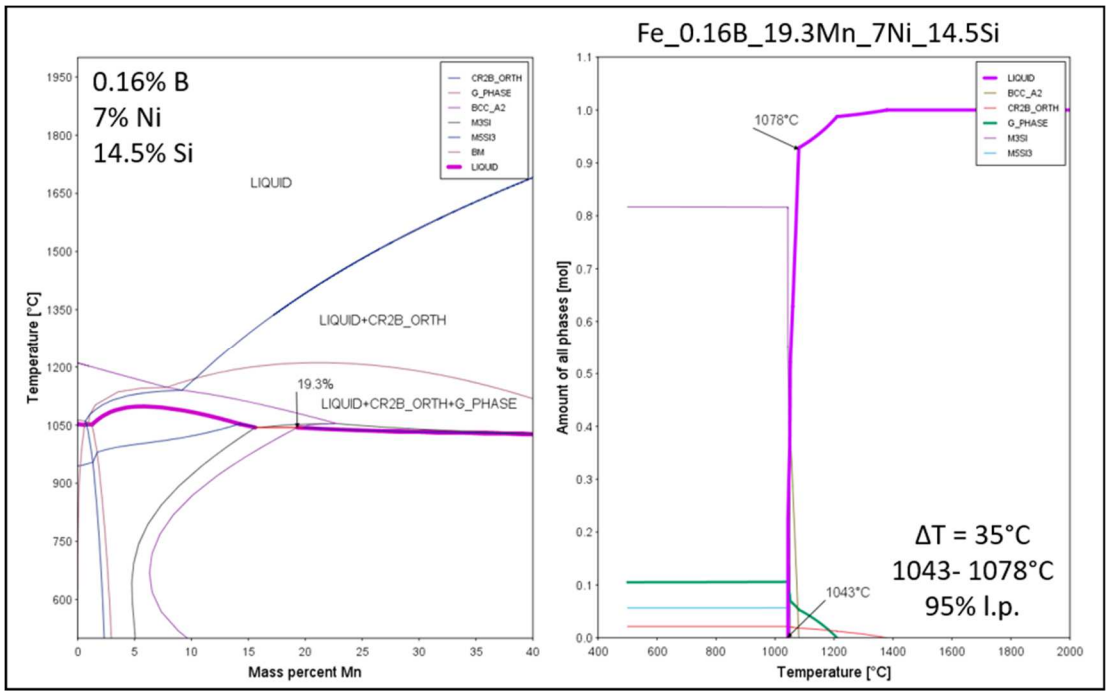

Figure 40 Mn vs temperature and evolution of phases for Fe_0.16B_19.3Mn_7Ni_14.5Si

Summary: Systems with a huge amount of different alloying elements seem to be challenging to be modified or even optimized. ThermoCalc helps a lot in giving ideas in how strongly the alloying elements can influence each other in terms of liquid phase formation and behaviour. The more complex the calculated system is, the less reliable the results might be. However, the system found could be used as a starting point for experiments which are crucial for such a complicated system.

Die approbierte gedruckte Originalversion dieser Diplomarbeit ist an der TU Wien Bibliothek verfügbar.
The approved original version of this thesis is available in print at TU Wien Bibliothek.

3.1.3 P containing systems

- **Fe-P-C**

Fe-P-C systems are described in the literature [16],[50],[61] Another approach was chosen in this chapter, starting with isothermal sections. The different approaches were chosen to give a feeling on how theoretical optimization can be carried out with the help of ThermoCalc. Figure 42 shows the Liquid window in isothermal sections for Fe-P-C. Steps in 10 K ranges were carried out to get as close as possible to the eutectic point, choosing the composition with maximum content of P and C, resulting in Fe_7.4P_1.9C as a first approach. The eutectic point lies at 977°C according to Raghavan [62]

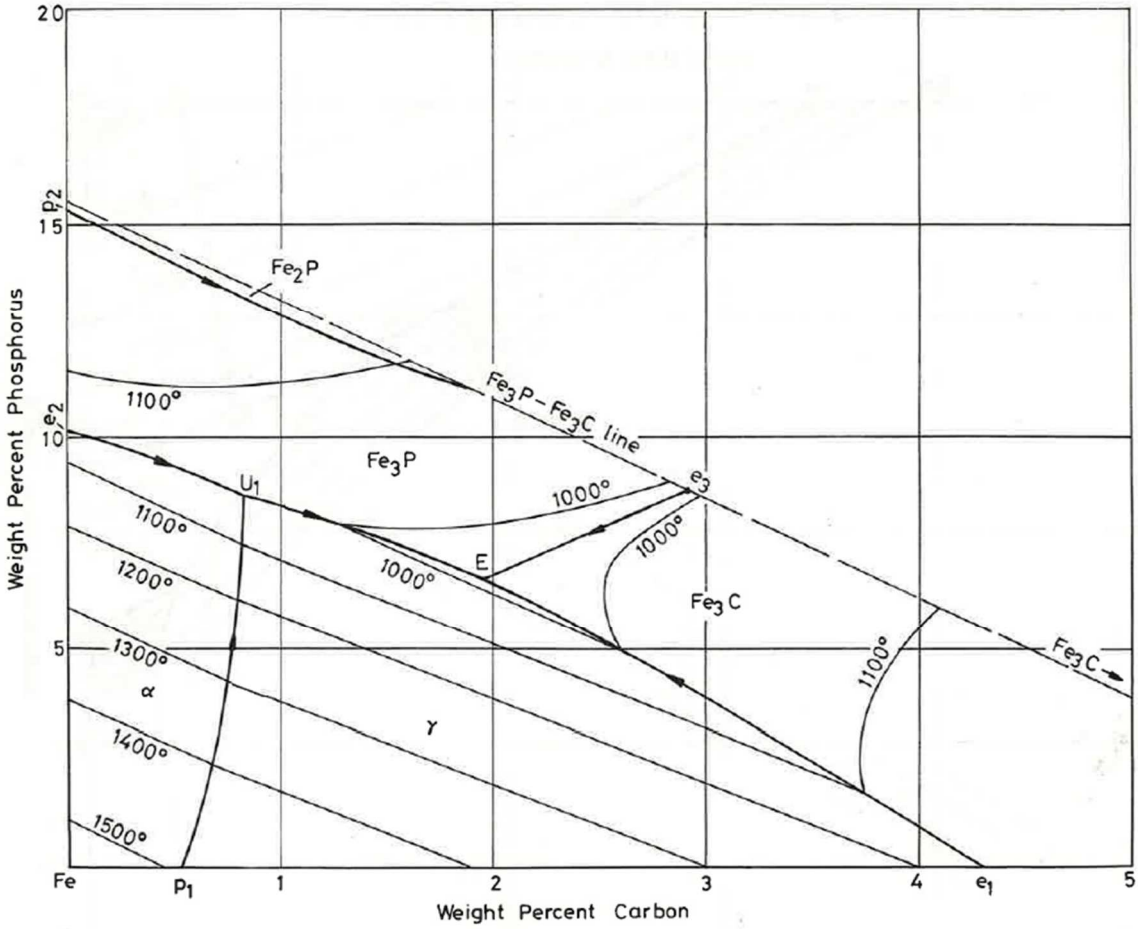

Figure 41 Experimentally determined ternary phase diagram of Fe-C-P with isothermal sections [62]

Comparing the experimentally determined Fe-P-C phase diagram shown in Figure 41 with the calculated ternary phase diagram in Figure 42 it is clear that both show a more or less triangular liquid phase area at 1000°C. Raghavan [62] shows this window between 1.3 to 2.4 wt% C and 5 to 8 wt% P while ThermoCalc shows the window between 0.8 to 2.2 wt% C and 6 to 8 wt% P. This calculation seems to be in a good range having slightly misfits with the C content.

Die approbierte gedruckte Originalversion dieser Diplomarbeit ist an der TU Wien Bibliothek verfügbar.
The approved original version of this thesis is available in print at TU Wien Bibliothek.

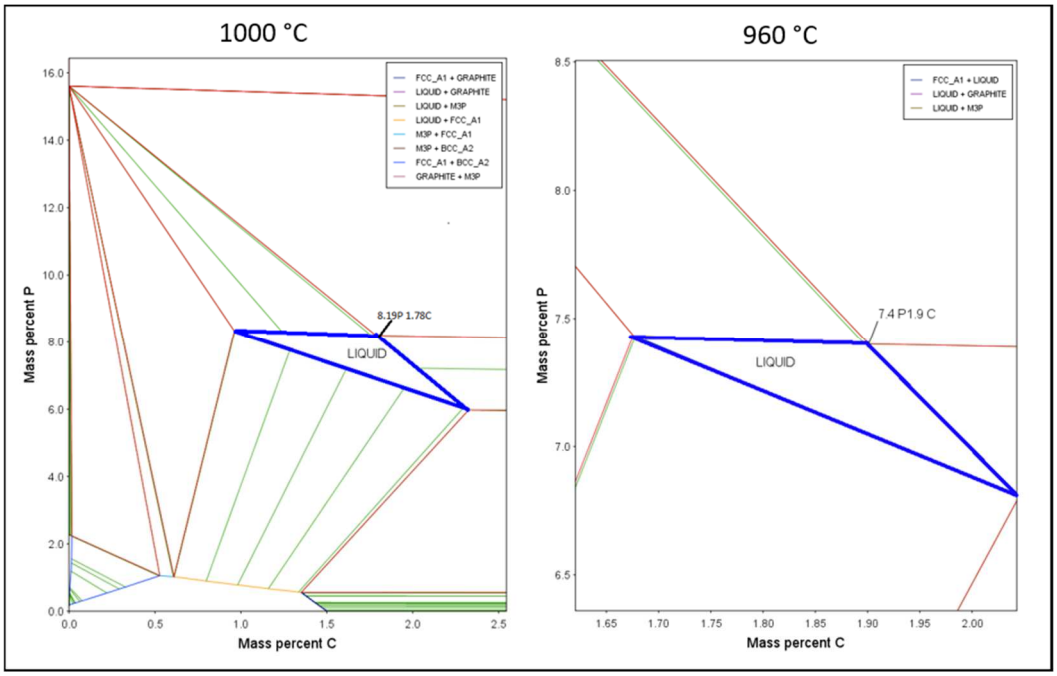

Figure 42 Isothermal sections for Fe-P-C systems at 1000°C and 960°C

Figure 43 shows the EoP for the starting composition chosen from the isothermal sections. A rather low melting temperature and a sharp liquid phase formation are proposed. The phase diagram for T vs. P shows that the chosen composition is very close to a eutectic point. The T vs. C phase diagram shows a eutectic point for slightly lower contents.

Die approbierte gedruckte Originalversion dieser Diplomarbeit ist an der TU Wien Bibliothek verfügbar.
The approved original version of this thesis is available in print at TU Wien Bibliothek.

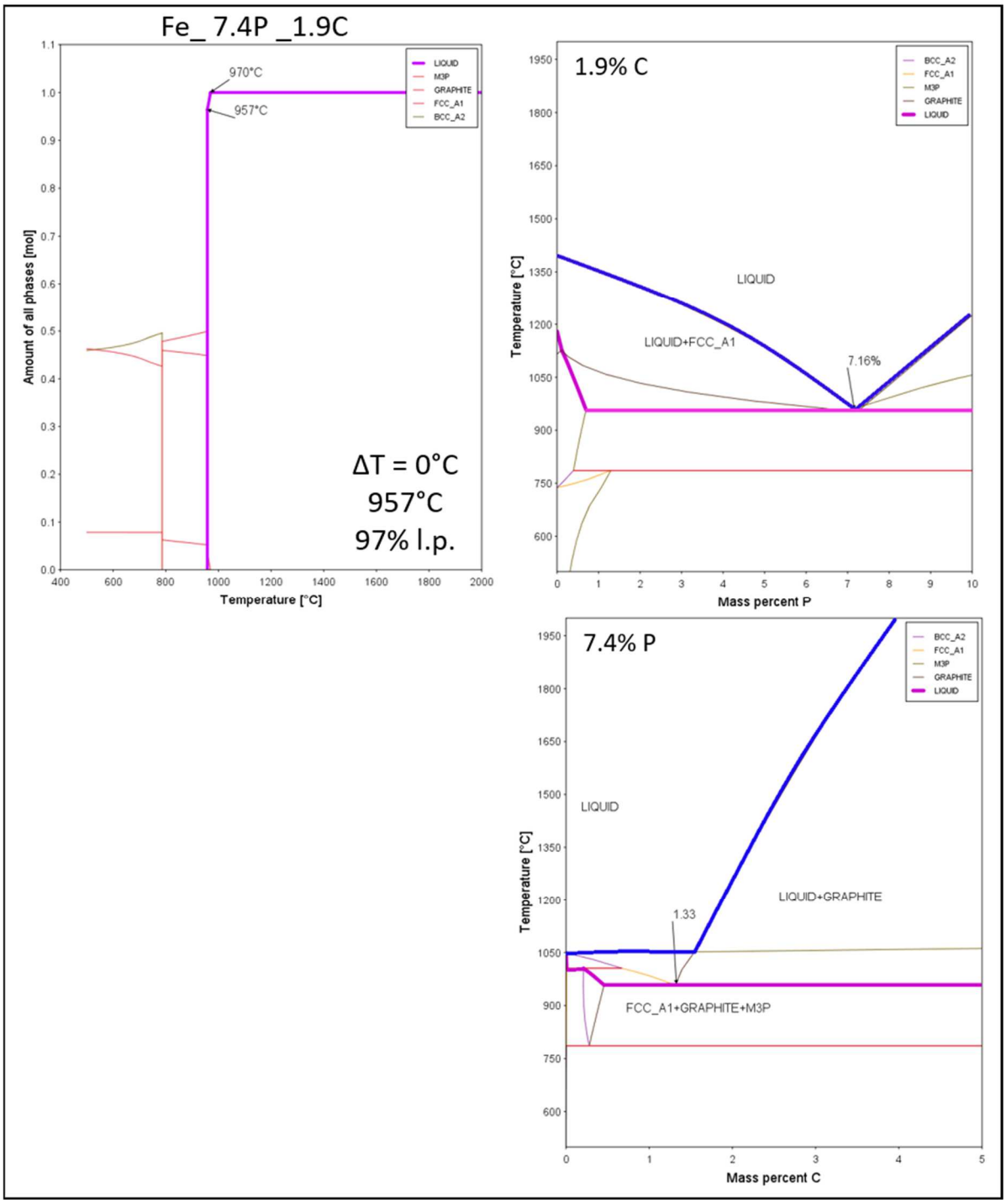

Figure 43 Evolution of phases and phase diagrams for P and C vs temperature for Fe_7.4P_1.9C

Figure 44 shows that with a small adjustment of the P content a system fully melting at 960°C can be obtained.

Die approbierte gedruckte Originalversion dieser Diplomarbeit ist an der TU Wien Bibliothek verfügbar.
The approved original version of this thesis is available in print at TU Wien Bibliothek.

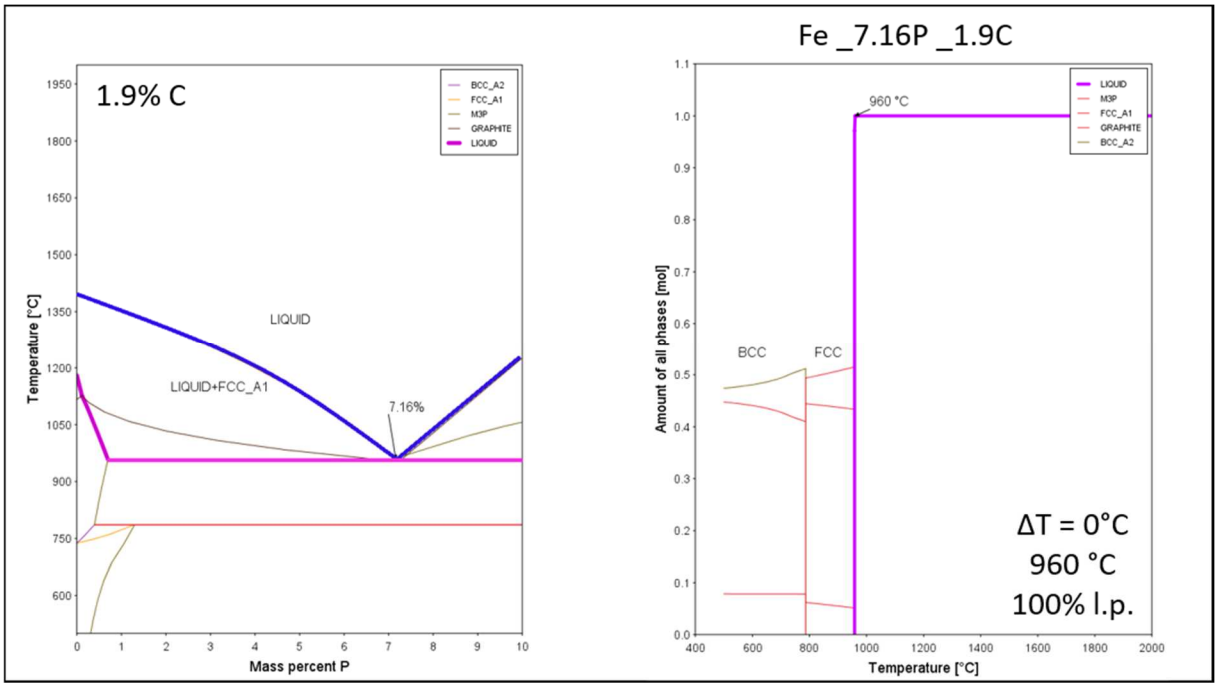

Figure 44 P vs temperature and evolution of phases for Fe_7.16P_1.9C

Summary: Starting from isothermal sections sometimes gives a good idea where a eutectic point could be. Especially for ternary systems it turned out to be a good approach.

3.1.4 Si and C containing systems

All systems in this chapter contain additional Si and C, because these elements help in the production process of the MA powders. There are no specific statements from the powder producer, but it can be assumed that it might have something to do with deoxidation, lowering of the melting point and achieving a more desired viscosity of the liquid. From previous studies [21] three different master alloy powder grades were available, so calculations and experiments were based on these existing powders. **Fe_32Cr_8Si_4C**, **Fe_42Mn_6Si_0.4C** and **Fe_28Mn_27Cr_6Si_3.7C**.

A difference between calculations in the previous chapters and calculations carried out in 3.1.4 Si and C containing systems is that powder processing limitations, according to the powder manufacturer, were considered as listed in Table 3.

Table 3 Limitations for the calculations in 3.1.4 Si and C containing systems

Alloying Element	Limitations
Cr	< 40%
Si	5 - 15 %
C	0.5 - 5 %

For Cr the limit was set because higher amounts of Cr would tendentially lead to higher melting temperatures. The Si minimum comes from the UHPWA powder production process, where at least 5% Si is beneficial according to the powder manufacturer. The maximum Si content of 15% was set for the same reason as Cr to avoid high melting systems due to a too high Si content. For C the minimum results from the powder production process. A limit of 5% C was set to avoid free graphite in the MA.

Die approbierte gedruckte Originalversion dieser Diplomarbeit ist an der TU Wien Bibliothek verfügbar.
The approved original version of this thesis is available in print at TU Wien Bibliothek.
TU Bibliothek Your knowledge hub WIEN

Even though it seems better to take another composition, sometimes different supposed behaviours of the liquid phase between the modifications, in terms of melting behaviour and liquid phase composition, had a higher priority to the initially declared “optimization criteria” like reducing the melting temperature, tighten the melting range and pushing the amount of alloying elements in the new powders.

- **Ternary diagrams**

Figure 45 shows the ternary phase diagrams for the system C-Cr-Fe both calculated and from the literature. [60] Comparing them with each other shows that the tendencies of the system seems to be rather accurate, but the effect of C seems to be not well predicted.

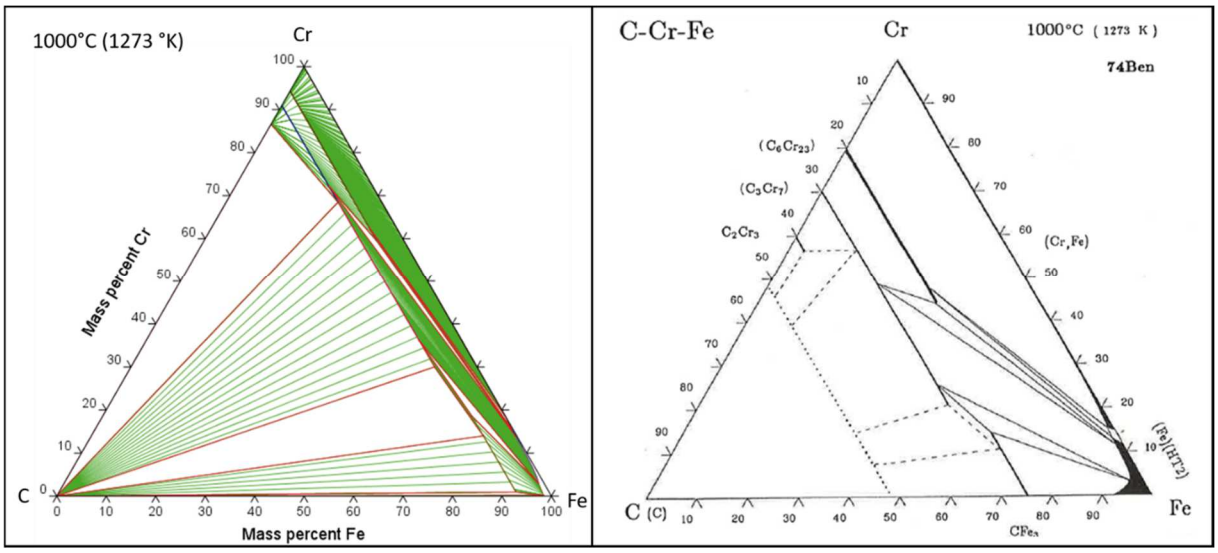

Figure 45 Ternary phase diagrams for C-Cr-Fe calculated (left) and from the literature [60](right). Isothermal section at 1000°C.

The calculated and experimentally determined phase diagrams [63] shown in Figure 46 describe the ternary system Cr-Fe-Si at 1050°C. For this system it is clear to see that prediction and literature fit together very accurately.

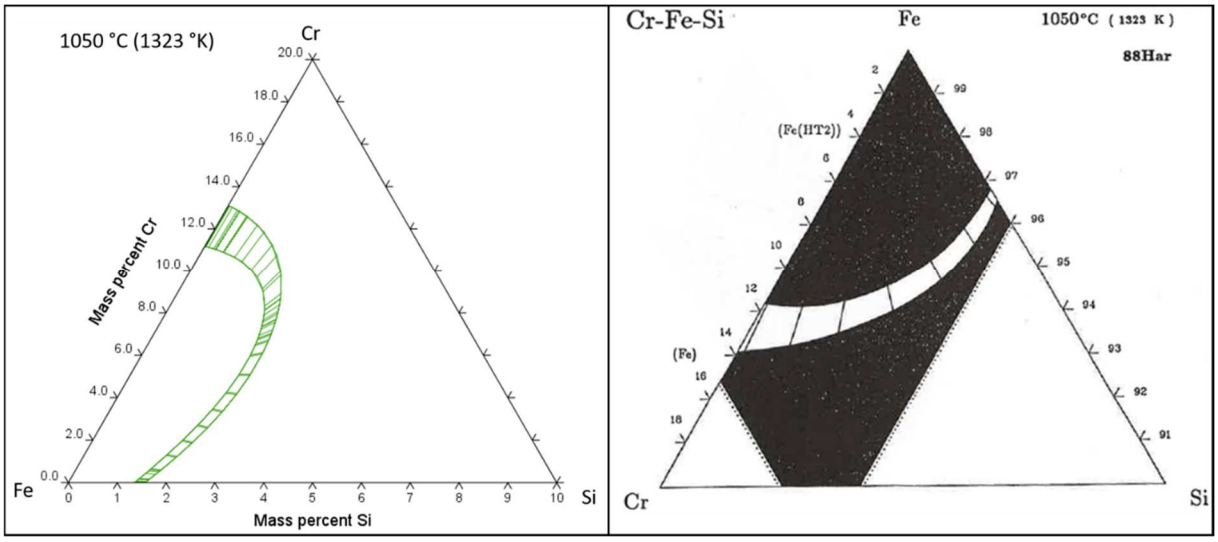

Figure 46 Ternary phase diagrams for Cr-Fe-Si calculated (left) and from the literature [63] (right). Isothermal section at 1050°C.

Die approbierte gedruckte Originalversion dieser Diplomarbeit ist an der TU Wien Bibliothek verfügbar.
The approved original version of this thesis is available in print at TU Wien Bibliothek.

Figure 47 shows phase diagrams for the ternary system C-Fe-Si, both calculated and the experimentally determined phase diagram from Raghavan. [64] Predictions and experiment seem to be somehow accurate at < 2% C and start to differ with higher C contents.

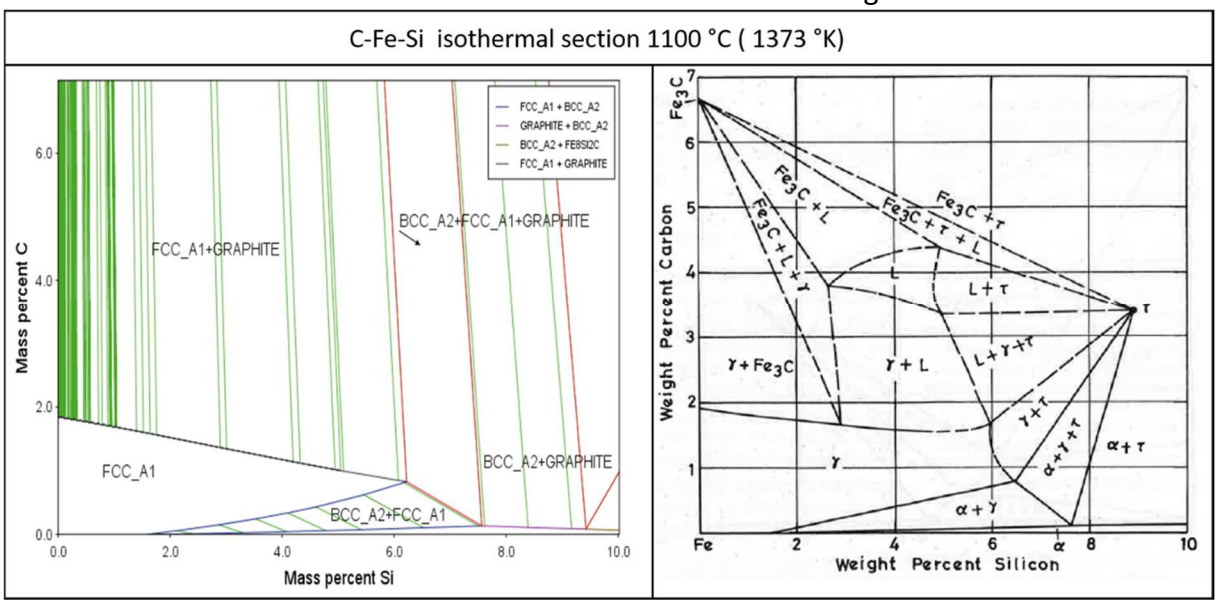

Figure 47 Ternary phase diagrams for C-Fe-Si calculated (left) and from the literature [64] (right). Isothermal section at 1100°C

Figure 48 shows phase diagrams for the ternary system C-Fe-Mn. Comparing the calculated phase diagram with the phase diagram from the literature [60] shows that the area between Fe and Mn up to 10% C seems to be predicted accurately. With higher C content the predictions are not accurate any more, showing just tendencies for the system.

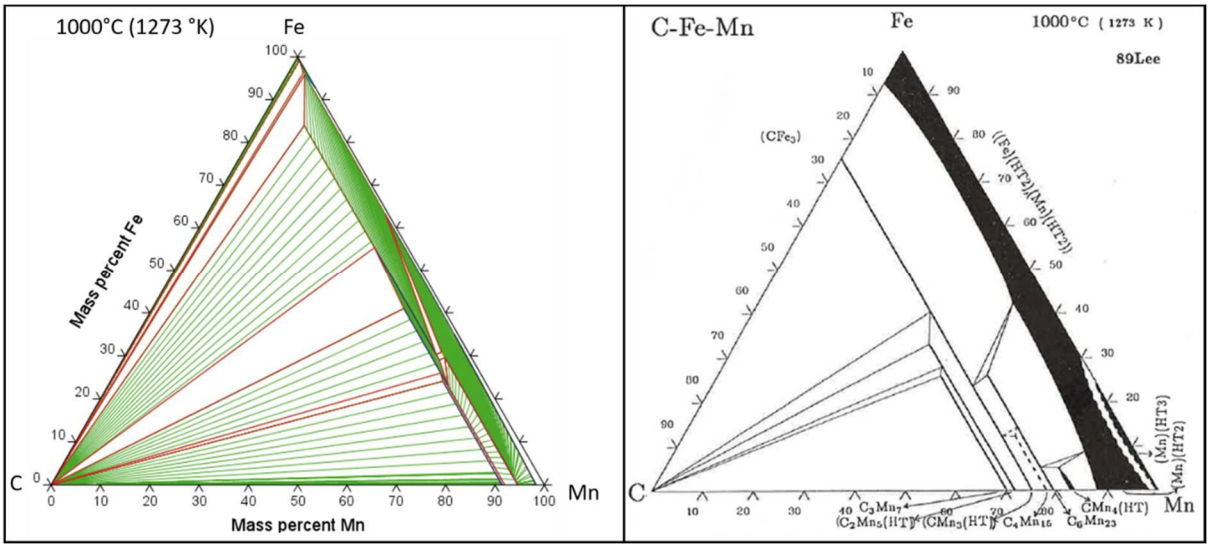

Figure 48 Ternary phase diagrams for C-Fe-Mn calculated (left) and from the literature [60] (right). Isothermal section at 1000°C

Figure 49 compares the experimentally determined phase diagram [58] of the ternary system Fe-Mn-Si with the calculated phase diagram. It is clear to see that the database from ThermoCalc does not have information about this system with Si contents 20%. Both phase diagrams seem to have some similarities but cannot be considered as accurate predictions.

Die approbierte gedruckte Originalversion dieser Diplomarbeit ist an der TU Wien Bibliothek verfügbar.
The approved original version of this thesis is available in print at TU Wien Bibliothek.

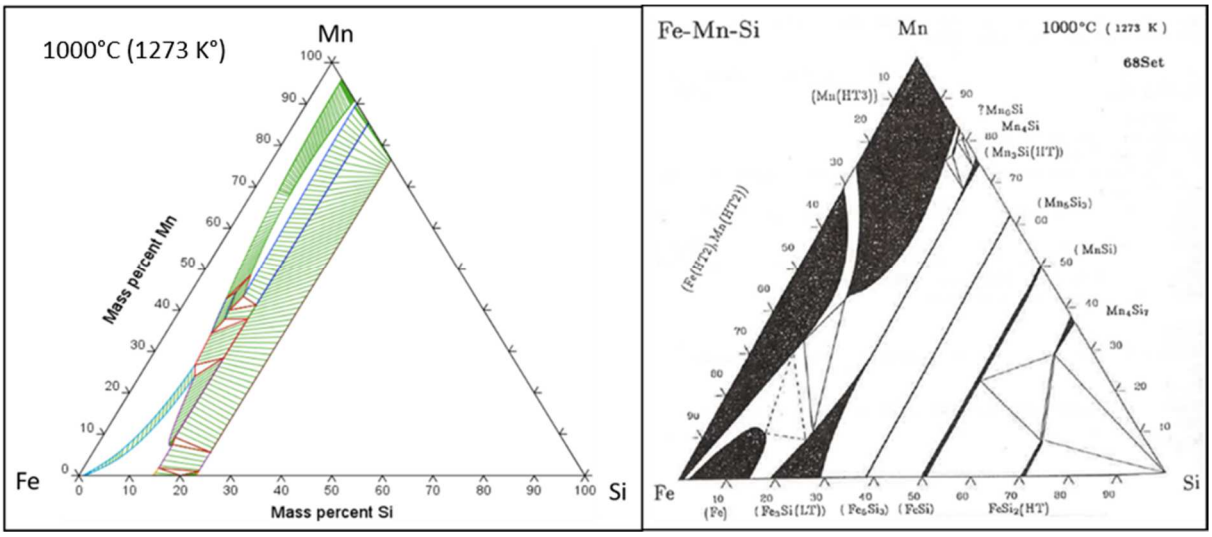

Figure 49 Ternary phase diagrams for Fe-Mn-Si calculated (left) and from the literature [58] (right). Isothermal section at 1000°C

Die approbierte gedruckte Originalversion dieser Diplomarbeit ist an der TU Wien Bibliothek verfügbar.
The approved original version of this thesis is available in print at TU Wien Bibliothek.

- **Cr-family Fe-Cr-Si-C**

The original composition of the Cr-family was **Fe_32Cr_8Si_4C**. Looking at Figure 50 several options show up to improve this system, but it seemed rather clear that it was not possible to achieve a fully molten system at 1120°C. The LT (blue line) is not below 1200°C, most of the time even higher than 1300°C. With this clear finding the aim to form as much liquid phase as possible at a certain ST (purple line) was declared.

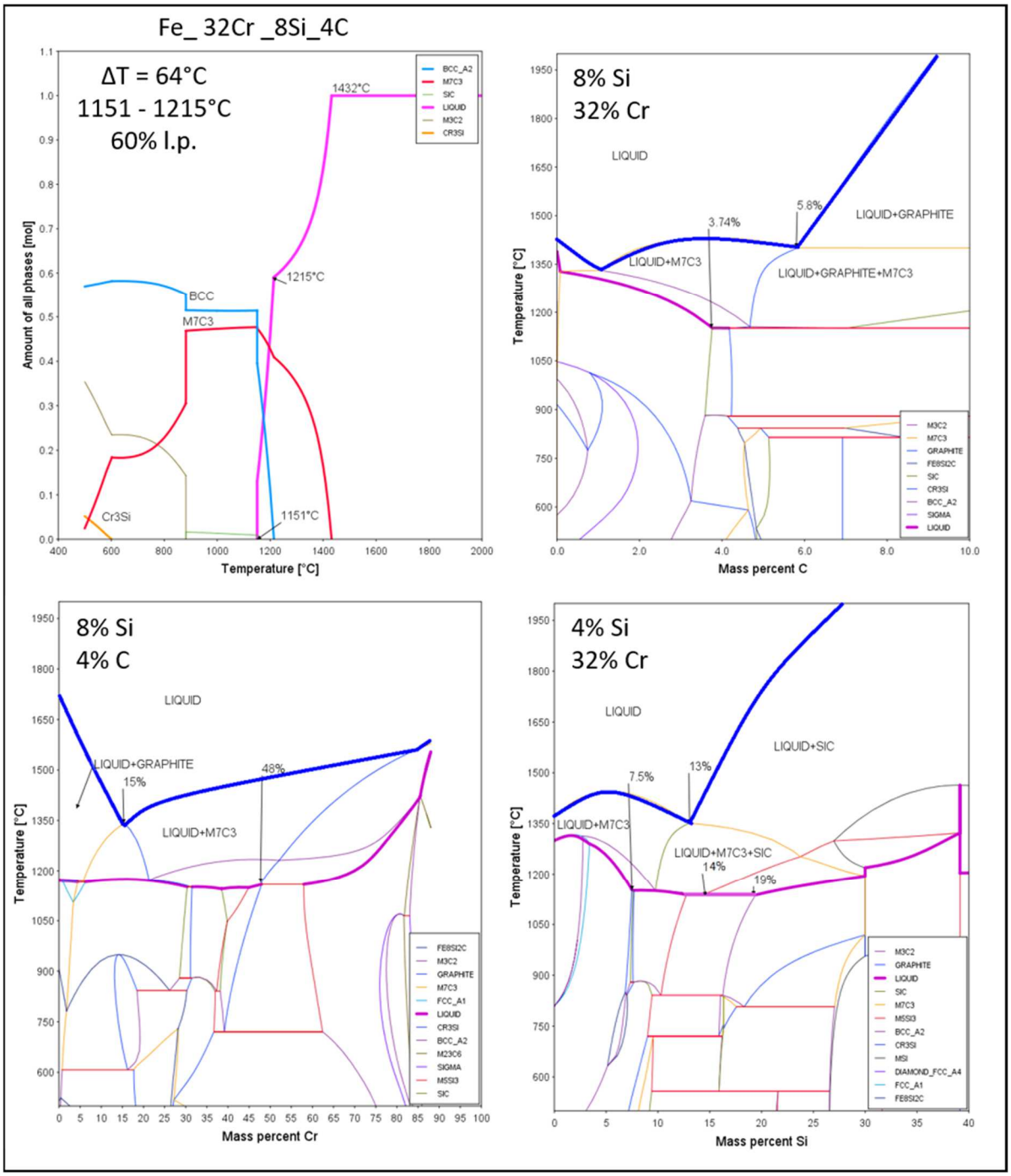

Figure 50 Evolution of phases and phase diagrams for Fe_32Cr_8Si_4C

Die approbierte gedruckte Originalversion dieser Diplomarbeit ist an der TU Wien Bibliothek verfügbar.
The approved original version of this thesis is available in print at TU Wien Bibliothek.

A.) Si group:

Looking closer at the Si vs T phase diagram shown in Figure 51 it is concluded that increasing the Si content is supposed to lead to lower solidus temperatures and narrower melting windows.

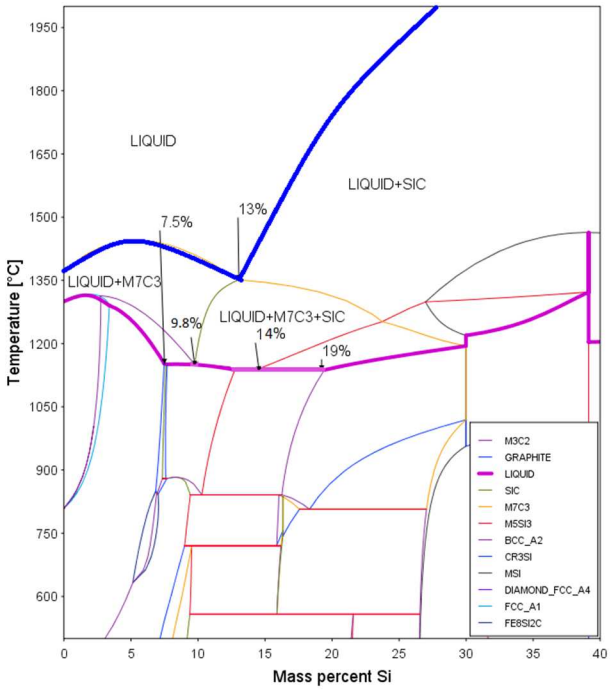

Figure 51 Si vs temperature for Fe_32Cr_8Si_4C

Figure 52 shows that a small increase of the Si content leads to a melting point for the first liquid formed, instead of a 64 K melting range.

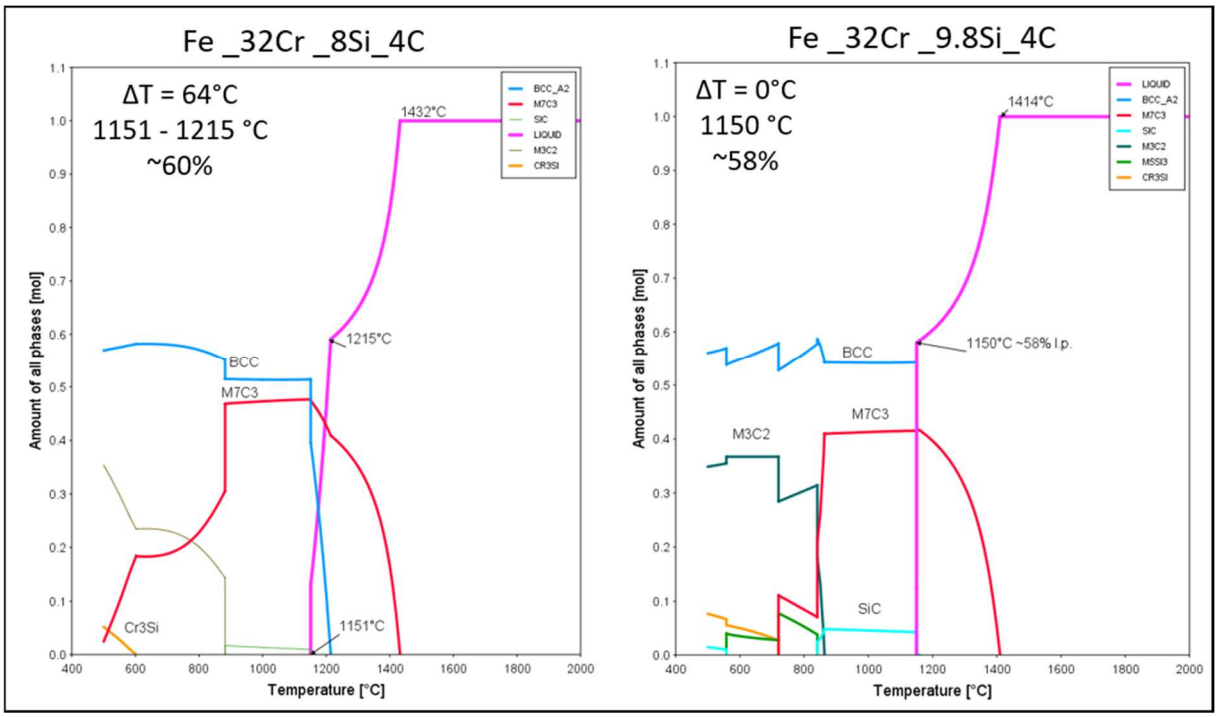

Figure 52 Evolution of phases for original composition and slightly higher Si content

Die approbierte gedruckte Originalversion dieser Diplomarbeit ist an der TU Wien Bibliothek verfügbar.
The approved original version of this thesis is available in print at TU Wien Bibliothek.
TU Bibliothek Your knowledge hub WIEN

B.) Cr group:

The phase diagram for Cr content vs T given in Figure 53 shows that the liquidus temperature does not change much by increasing the Cr content up to ~65% Cr, by constantly increasing the solidus temperature. So, two options showed up for the Cr content, either increasing it to 40%, accepting the fact that there is no fully molten system at a certain temperature but having as much alloying element in the system as possible, or decreasing the Cr content to 15% in first place achieving a lower solidus temperature and a tighter melting window.

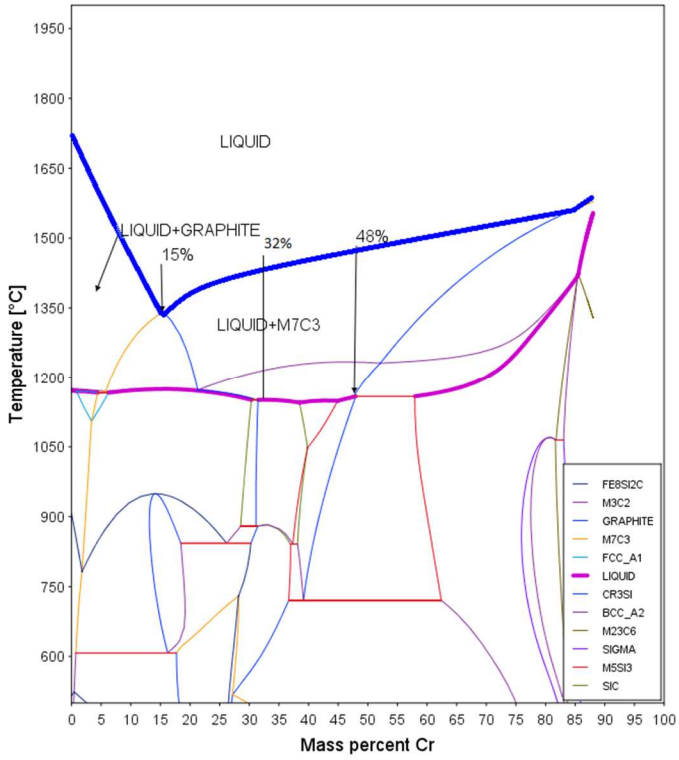

Figure 53 Cr vs temperature for Fe_32_8Si_4C

B – 1.) High Cr group:

Using the full range of the limitations shown in Table 3, 40% Cr was the maximum amount taken. Figure 54 shows that just increasing the Cr without other changes will broaden the melting range for the first liquid, so it was reasonable to combine the change of the Cr content with a change in the Si content.

Die approbierte gedruckte Originalversion dieser Diplomarbeit ist an der TU Wien Bibliothek verfügbar.
The approved original version of this thesis is available in print at TU Wien Bibliothek.

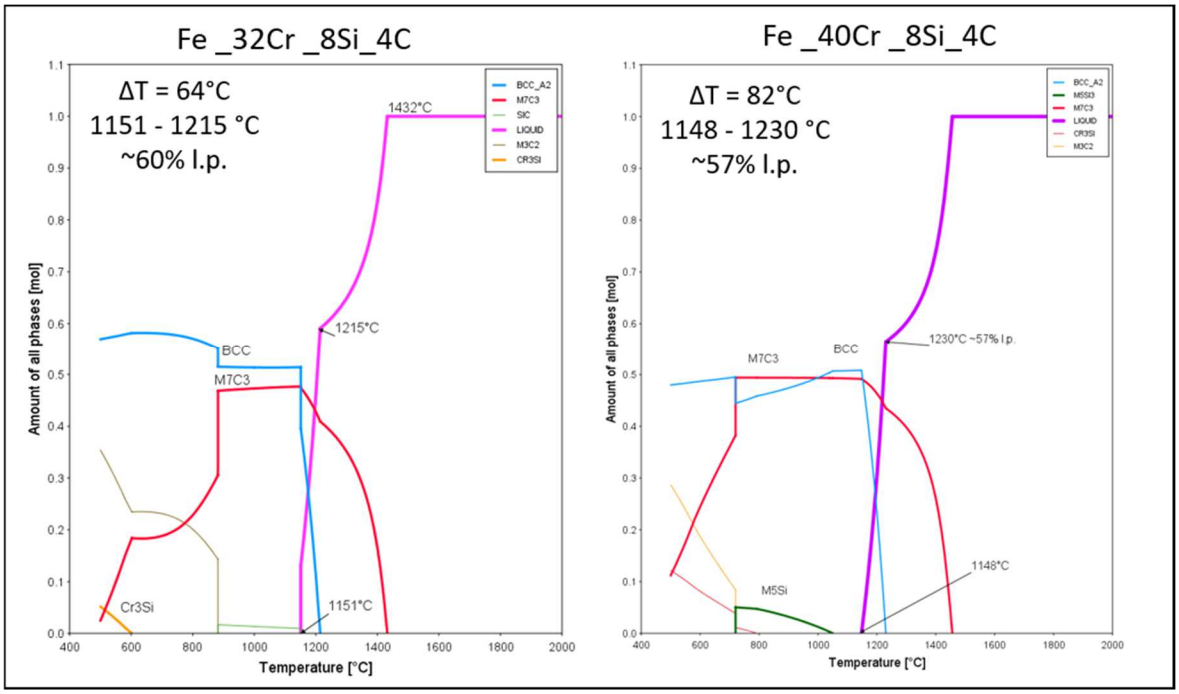

Figure 54 Evolution of phases for original composition and higher Cr content

Figure 55 is rather similar to Figure 51 showing an Si content vs T phase diagram for another Cr content. For a higher Cr content, it seems as well reasonable to increase the Si content to achieve a narrower melting window and a lower solidus temperature.

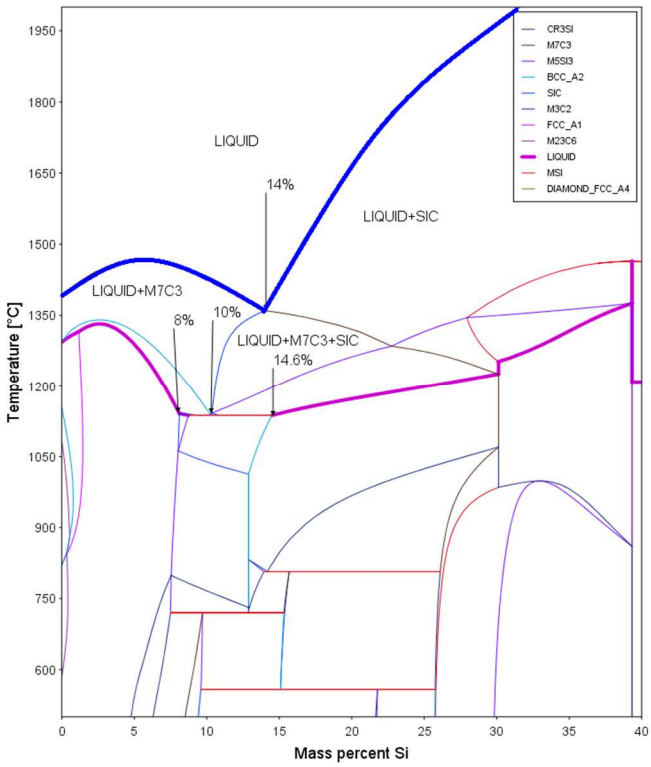

Figure 55 Si vs temperature for Fe_40Cr_8Si_4C

Figure 56 shows that the combined increasing of Si and Cr leads in the end to an improvement of the original composition in alloying element content and lower solidus temperature.

Die approbierte gedruckte Originalversion dieser Diplomarbeit ist an der TU Wien Bibliothek verfügbar.
The approved original version of this thesis is available in print at TU Wien Bibliothek.
TU Bibliothek Your knowledge hub WIEN

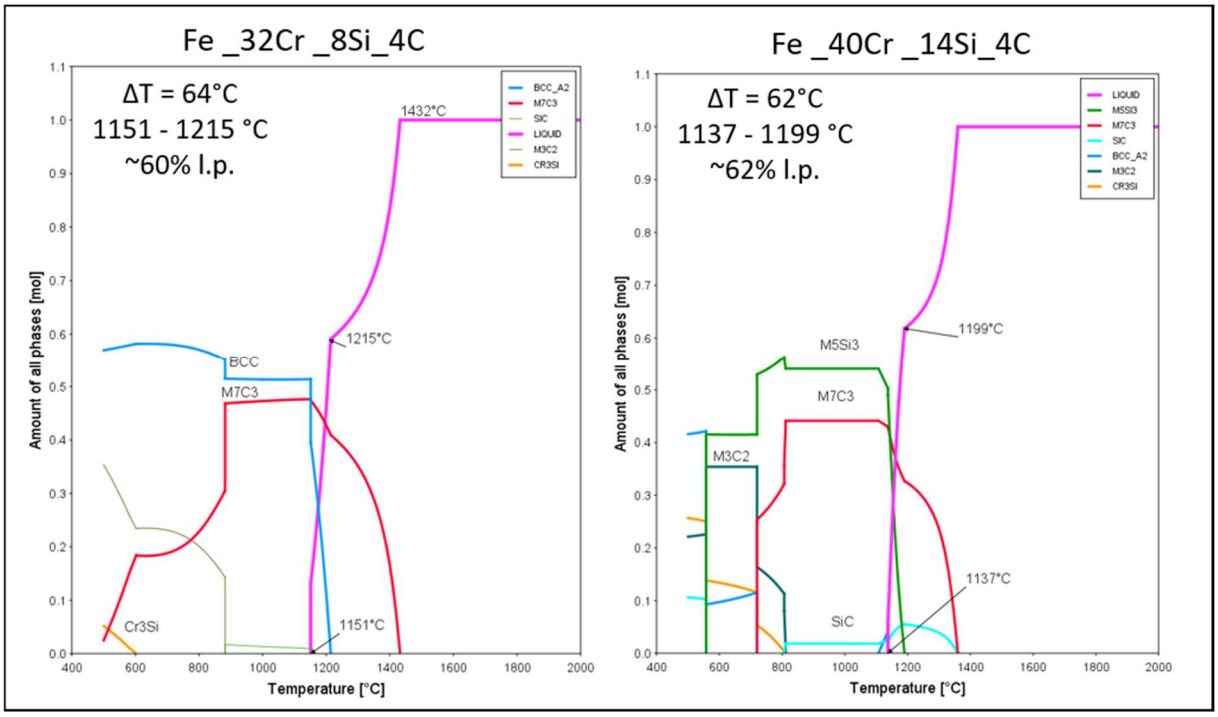

Figure 56 Evolution of phases for original composition and for increased Si and Cr content

B – 2.) Low Cr group:

Figure 57 shows the change in the melting behaviour by decreasing the Cr content from the original composition. More liquid phase at a certain temperature was achieved. Looking at the C vs T and Si vs T phase diagrams for the low Cr system was the next step.

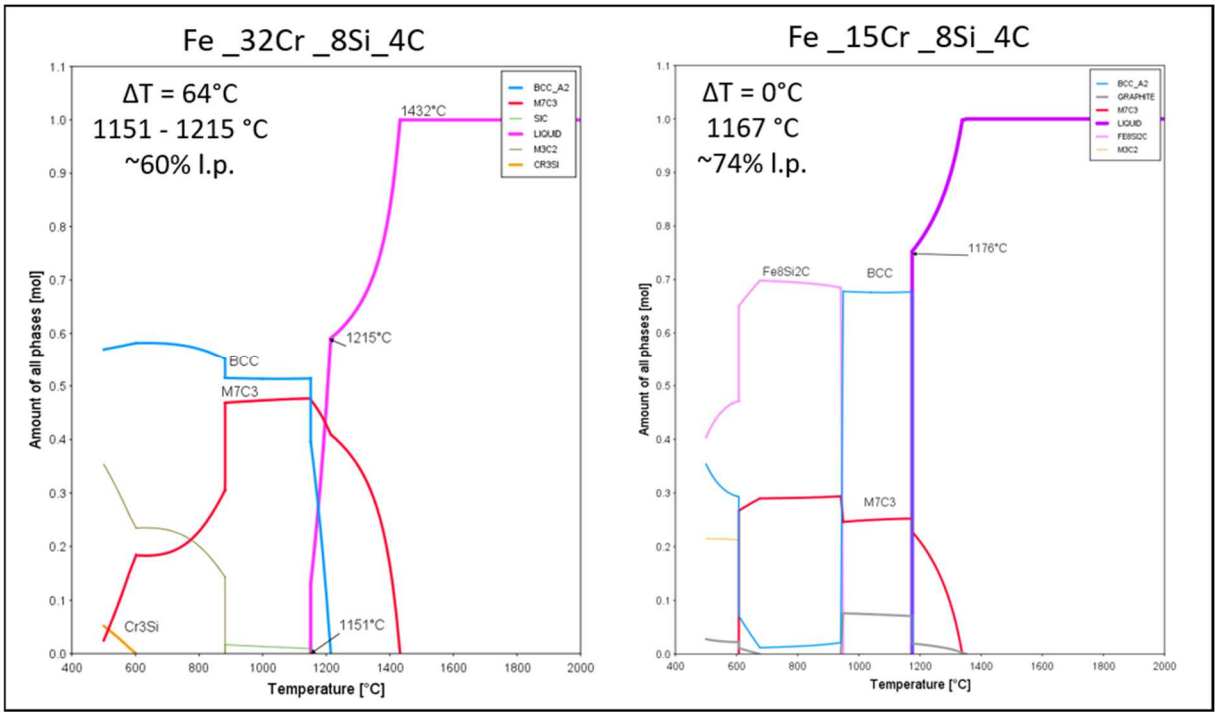

Figure 57 Evolution of phases for original composition and decreased Cr content

Figure 58 shows that for the low Cr system not a change in the Si content, but a reduction in the C content might achieve more liquid phase at a certain temperature.

Die approbierte gedruckte Originalversion dieser Diplomarbeit ist an der TU Wien Bibliothek verfügbar.
The approved original version of this thesis is available in print at TU Wien Bibliothek.
TU Bibliothek Your knowledge hub WIEN

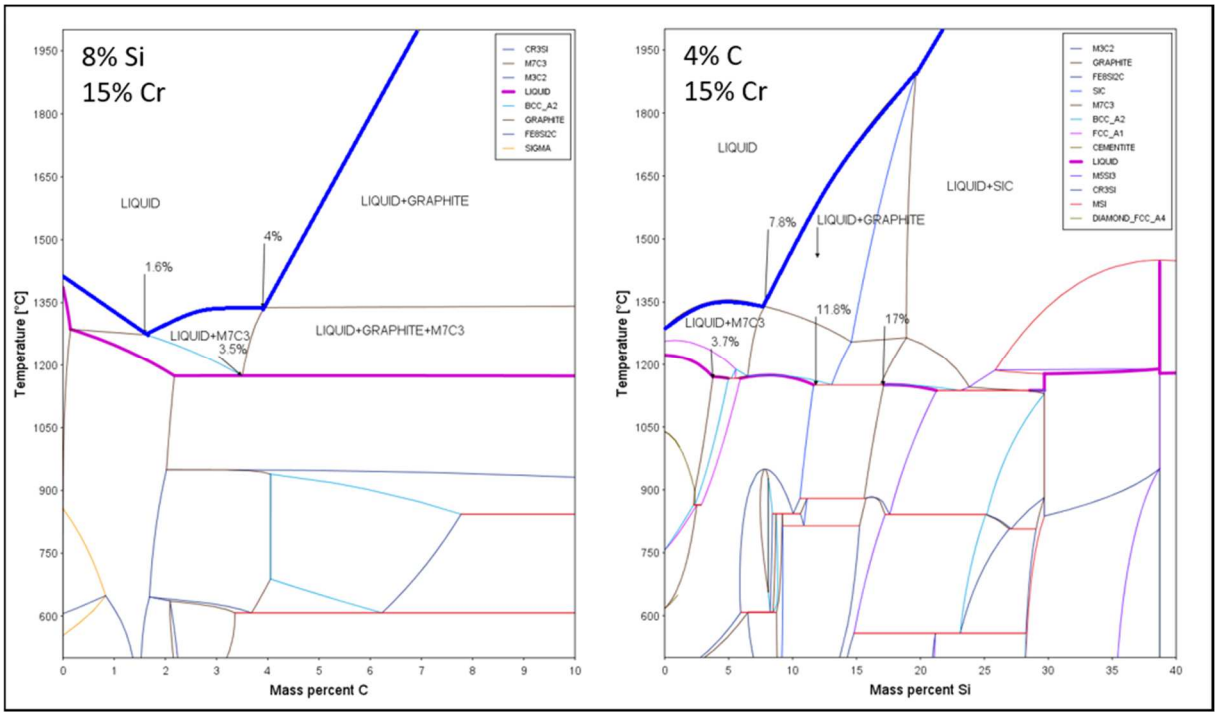

Figure 58 C and Si phase diagrams for low Cr system

Figure 59 shows that adjusting the C content to the lower Cr content leads on the one hand to a fully melting system, but on the other hand to increased melting temperatures and a broad melting range.

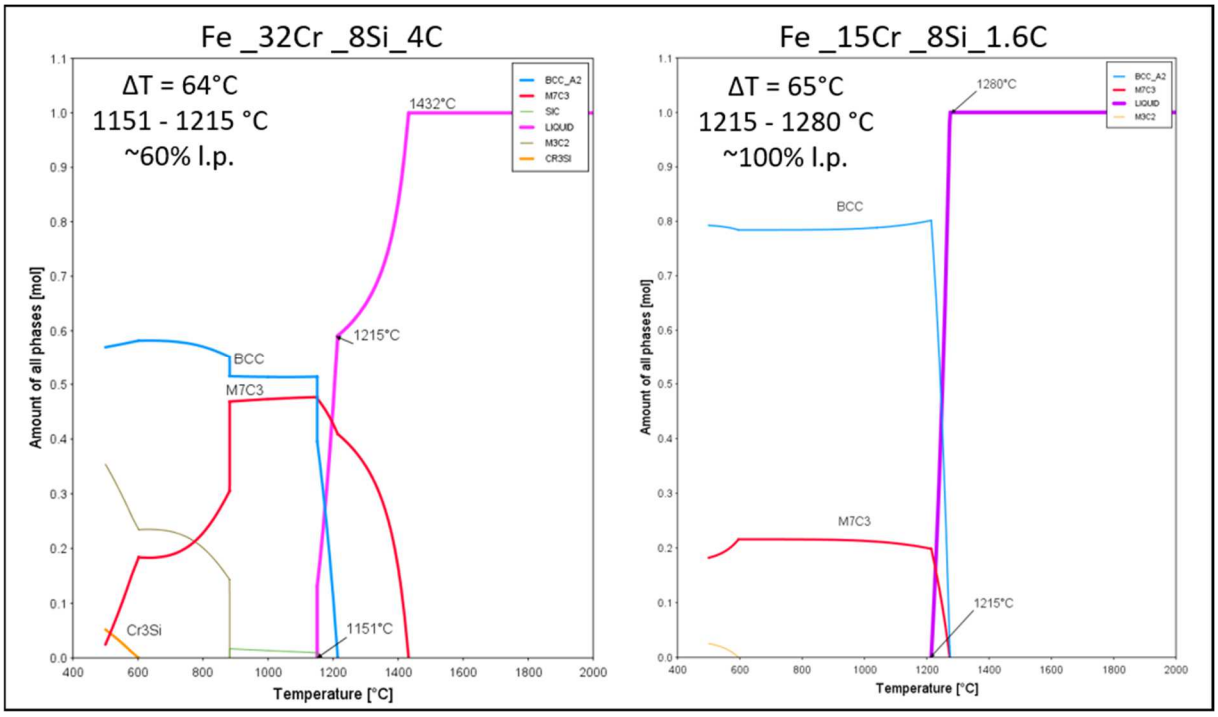

Figure 59 Evolution of phases for original composition and decreased C and Cr content

Figure 60 shows that with the adjusted C content, increasing the Si content again could lead to a much lower melting temperature and a tight melting for the first liquid appearing.

Die approbierte gedruckte Originalversion dieser Diplomarbeit ist an der TU Wien Bibliothek verfügbar.
The approved original version of this thesis is available in print at TU Wien Bibliothek.
TU Bibliothek Your knowledge hub WIEN

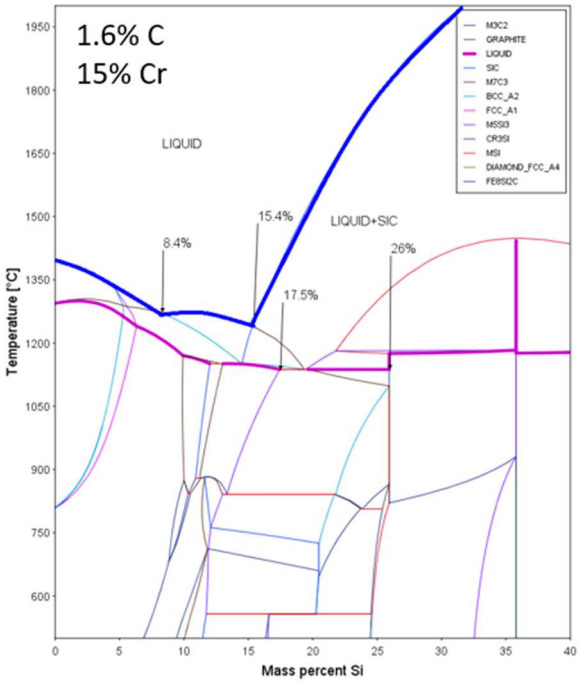

Figure 60 Si vs temperature for Fe_15Cr_8Si_1.6C

Figure 61 shows the effect of increasing the Si content for the system which measure reduces the melting temperature and tightens the first liquid appearing to a certain melting point. The effects of the alloying elements seem rather clear. The Cr content determines in which content range the Si and C can lower the solidus temperature. Cr content itself does not affect the solidus line much. Si seems to have a certain content range where a tight solid – liquid transition occurs. C helps lowering the melting temperature as well but seems to be more affected by the Cr content than the Si content.

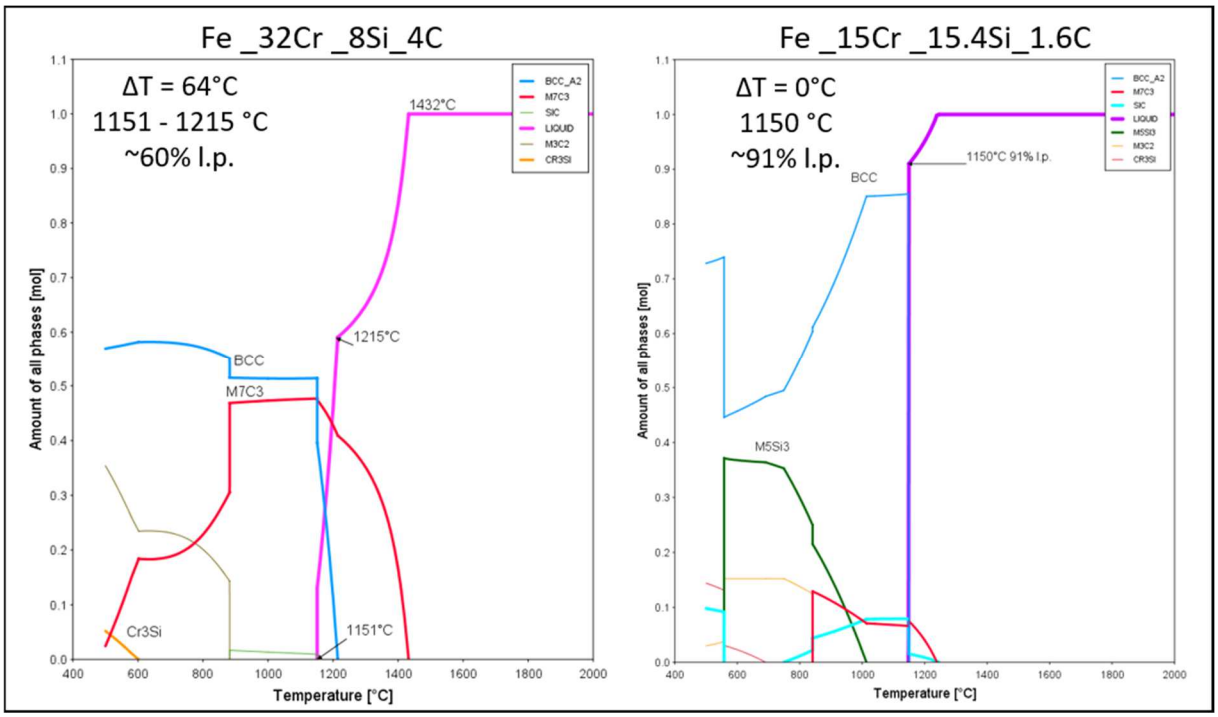

Figure 61 Evolution of phases for original composition and decreased C and Cr and increased Si content

Die approbierte gedruckte Originalversion dieser Diplomarbeit ist an der TU Wien Bibliothek verfügbar.
The approved original version of this thesis is available in print at TU Wien Bibliothek.
TU Bibliothek Your knowledge hub WIEN

- **Mn- family Fe-Mn-Si-C**

The original composition of the Mn-family was **Fe_42Mn_6Si_0.4C**. Figure 62 gives an overview of the Mn-family in its original composition. Adjusting the C content to 2% seemed to be a first general improvement of the system to gain a lower melting temperature and a narrower melting window.

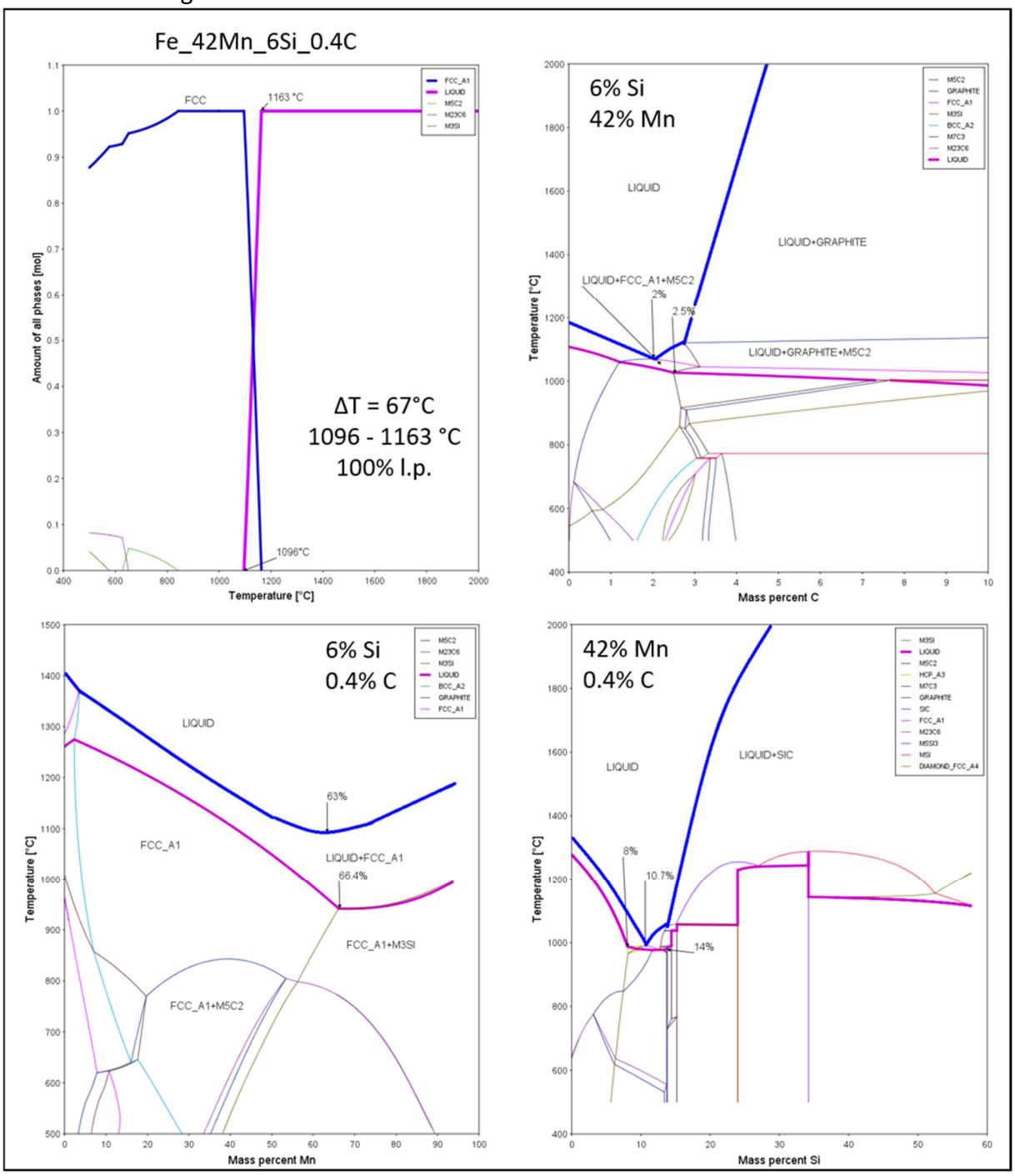

Figure 62 Evolution of phases and phase diagrams for Fe_42Mn_6Si_0.4C

Figure 63 shows the effect of increasing the C content to 2% which causes a lowering of the solidus temperature by approximately 50 K. This improvement was considered as very beneficial so that the calculations for all the other modifications started initially with an increased C content.

Die approbierte gedruckte Originalversion dieser Diplomarbeit ist an der TU Wien Bibliothek verfügbar.
The approved original version of this thesis is available in print at TU Wien Bibliothek.
TU Bibliothek Your knowledge hub WIEN

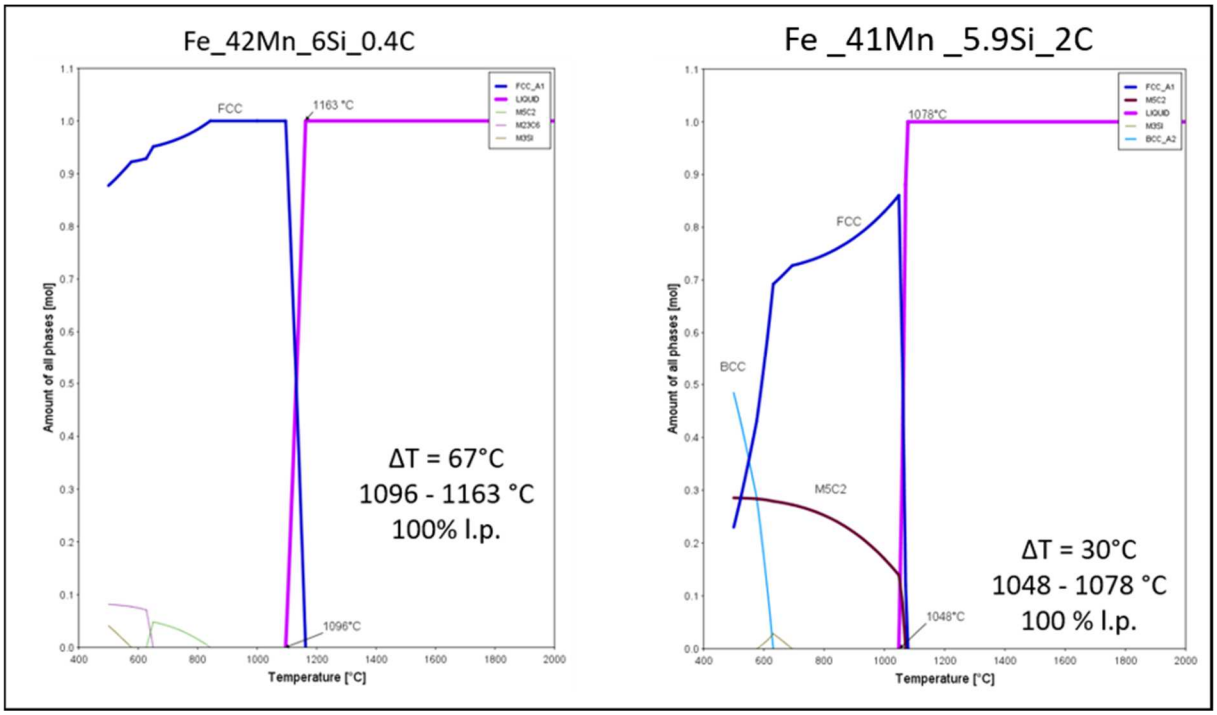

Figure 63 Evolution of phases for original composition and increased C content

Comparing Mn vs T and Si vs T phase diagrams in Figure 62 and Figure 64 shows that for Si the low solidus temperature between 8 and 14% Si did not change by changing the C content, but the Mn phase diagram did change massively, showing a much flatter solidus line at the higher C content.

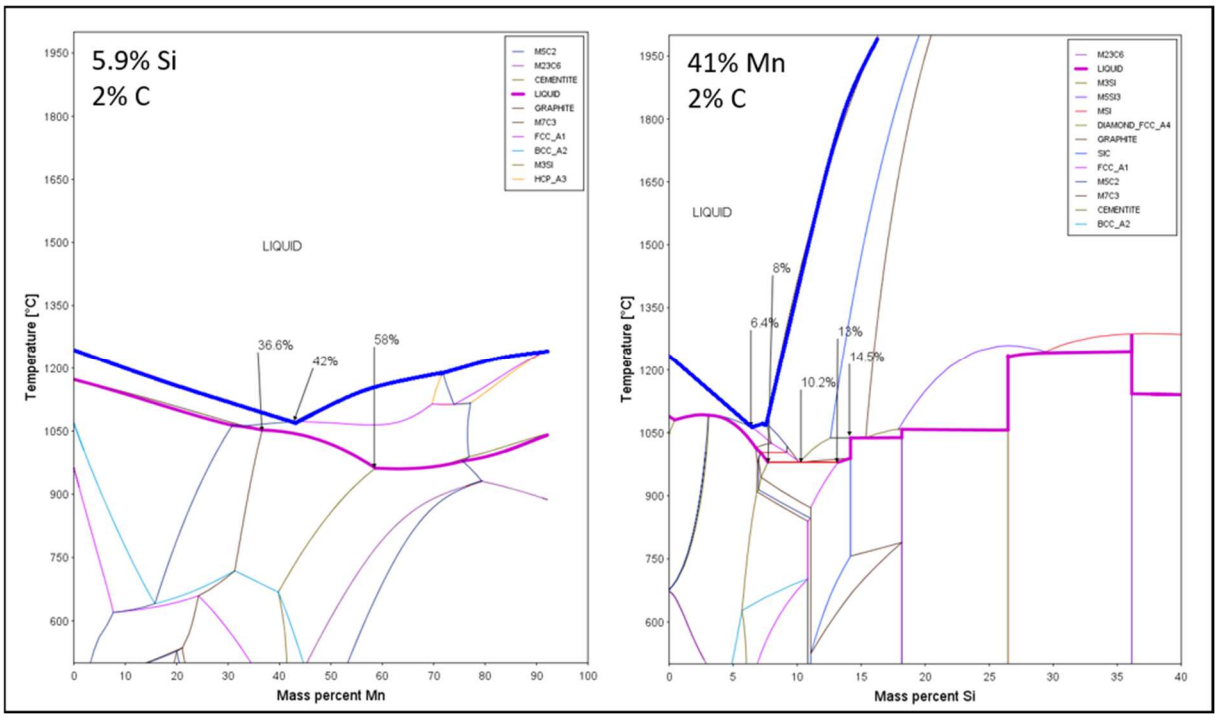

Figure 64 Mn and Si phase diagrams for Fe_41Mn_5.9Si_2C

Figure 65 shows the improvement of the original composition by increasing Si and C content in achieving a much lower melting temperature and narrowing the solid – liquid interval.

Die approbierte gedruckte Originalversion dieser Diplomarbeit ist an der TU Wien Bibliothek verfügbar.
The approved original version of this thesis is available in print at TU Wien Bibliothek.

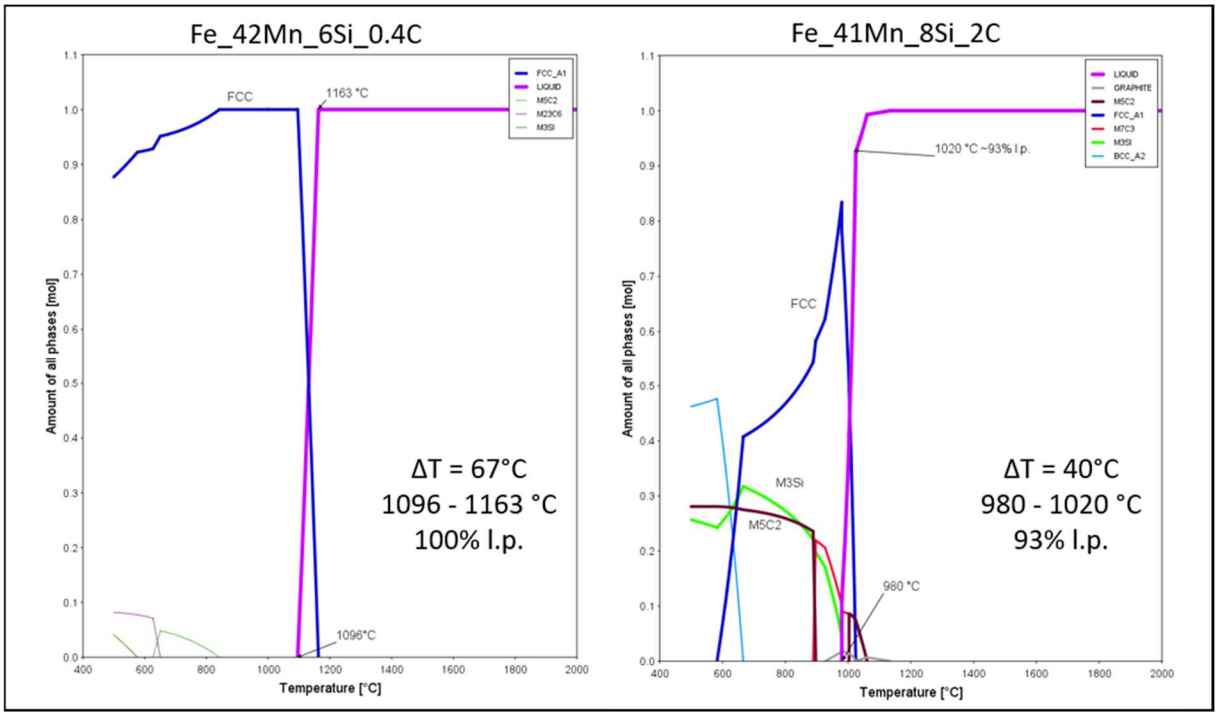

Figure 65 Evolution of phases for original composition and increased C and Si content

Figure 66 shows that there is the tendency of having a broader melting window with maximum Mn content or a narrower one with a lower Mn content in the range of the limits listed in Table 3. In comparison to the Cr-family the solidus temperature changes with the Mn content.

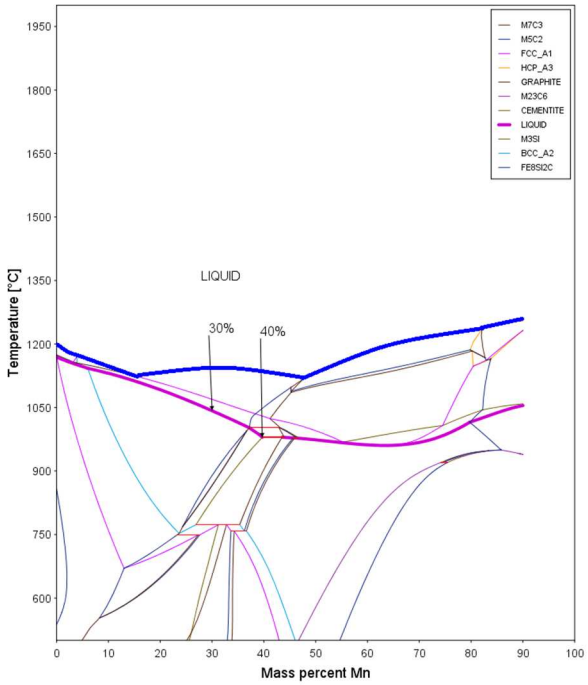

Figure 66 Mn vs temperature for Fe_41Mn_8Si_2C

Die approbierte gedruckte Originalversion dieser Diplomarbeit ist an der TU Wien Bibliothek verfügbar.
The approved original version of this thesis is available in print at TU Wien Bibliothek.

A.) High Mn group

The high Mn group with ~40% Mn tries to achieve a maximum of alloying elements on the one hand and getting a low solidus temperature while accepting a melting range on the other hand, by adjusting the C and Si contents.

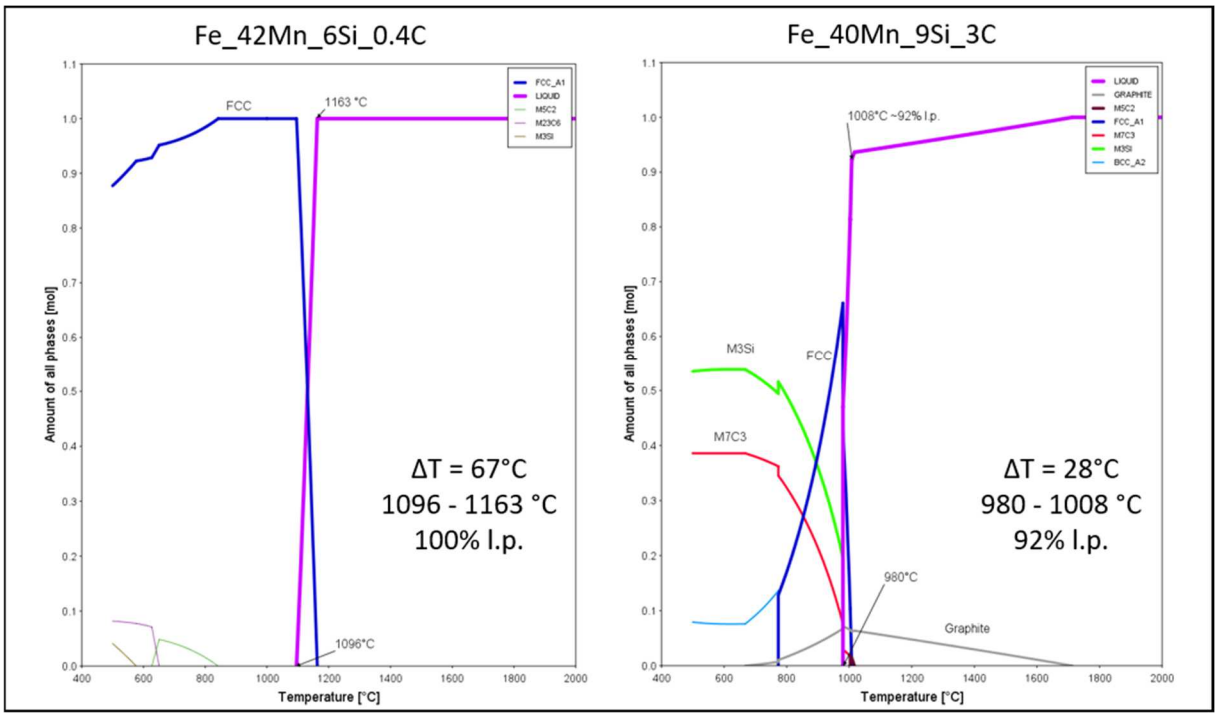

Figure 67 Evolution of phases for original composition and increased C and Si content

Figure 67 shows how adjusting C and Si with high Mn content can improve the system in terms of achieving low solidus temperatures.

Die approbierte gedruckte Originalversion dieser Diplomarbeit ist an der TU Wien Bibliothek verfügbar.
The approved original version of this thesis is available in print at TU Wien Bibliothek.

B.) Low Mn group

The low Mn group with ~30% Mn shows up with rather different supposed melting behaviour. Both compositions have ~3% C content, so the only difference between the compositions is related to the Si content. Figure 68 shows that the low Mn containing modifications of the original composition not necessarily show a narrow melting window. Si seems to have the same tendency as Mn in this system to decrease the solidus temperature by broadening the melting window.

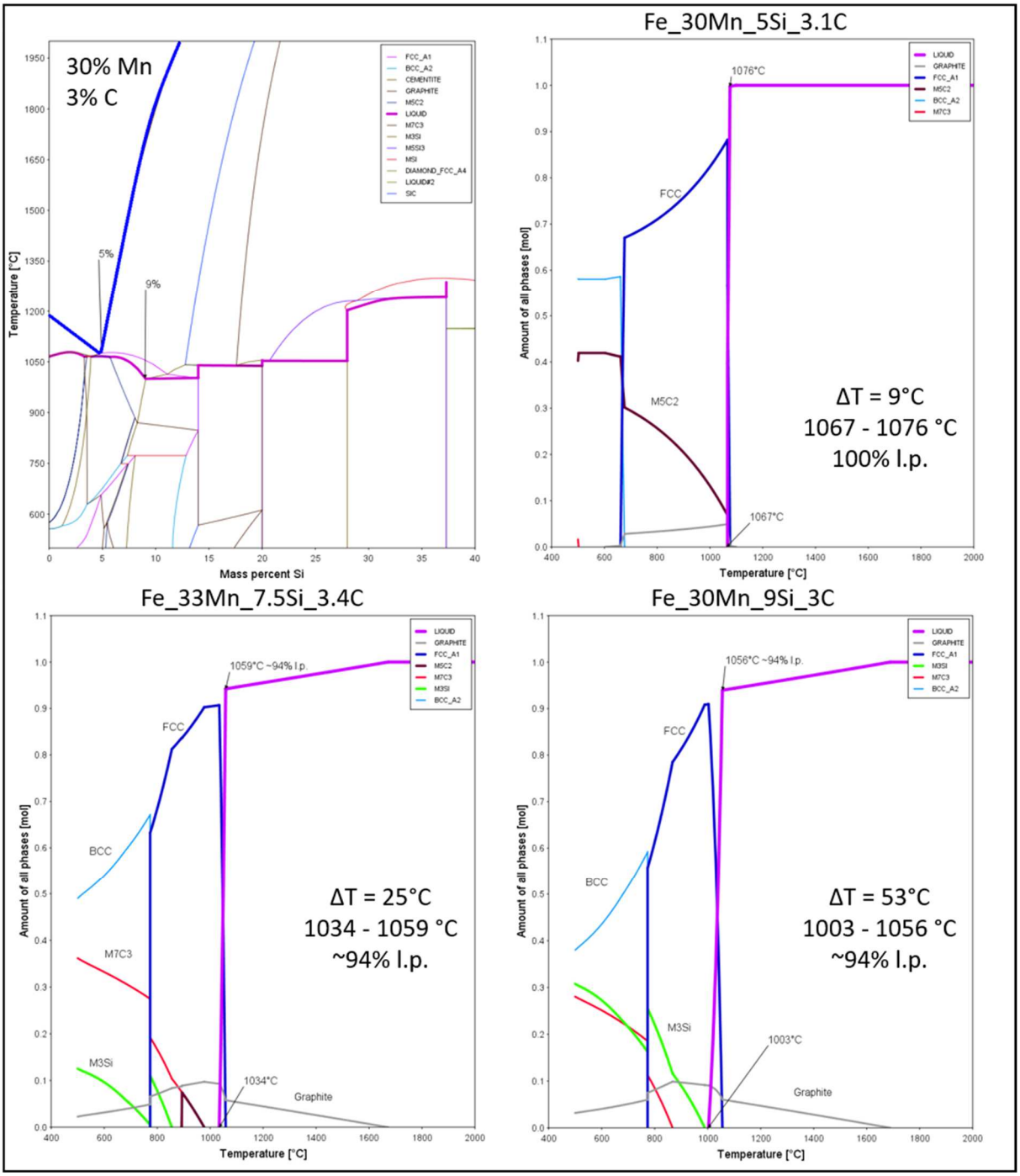

Figure 68 Si vs temperature for Fe_30Mn_8Si_3C and Evolution of phases for different low Mn compositions

Die approbierte gedruckte Originalversion dieser Diplomarbeit ist an der TU Wien Bibliothek verfügbar.
The approved original version of this thesis is available in print at TU Wien Bibliothek.

- **Cr-Mn-family Fe-Cr-Mn-Si-C**

The original composition of the Mn-family was **Fe_28Mn_27Cr_6Si_3.7C**. Figure 69 shows several possibilities to modify the Cr-Mn original composition Fe_28Mn_27Cr_6Si_3.7C. First a major improvement due to a lower solidus temperature could be attained by increasing the Mn content.

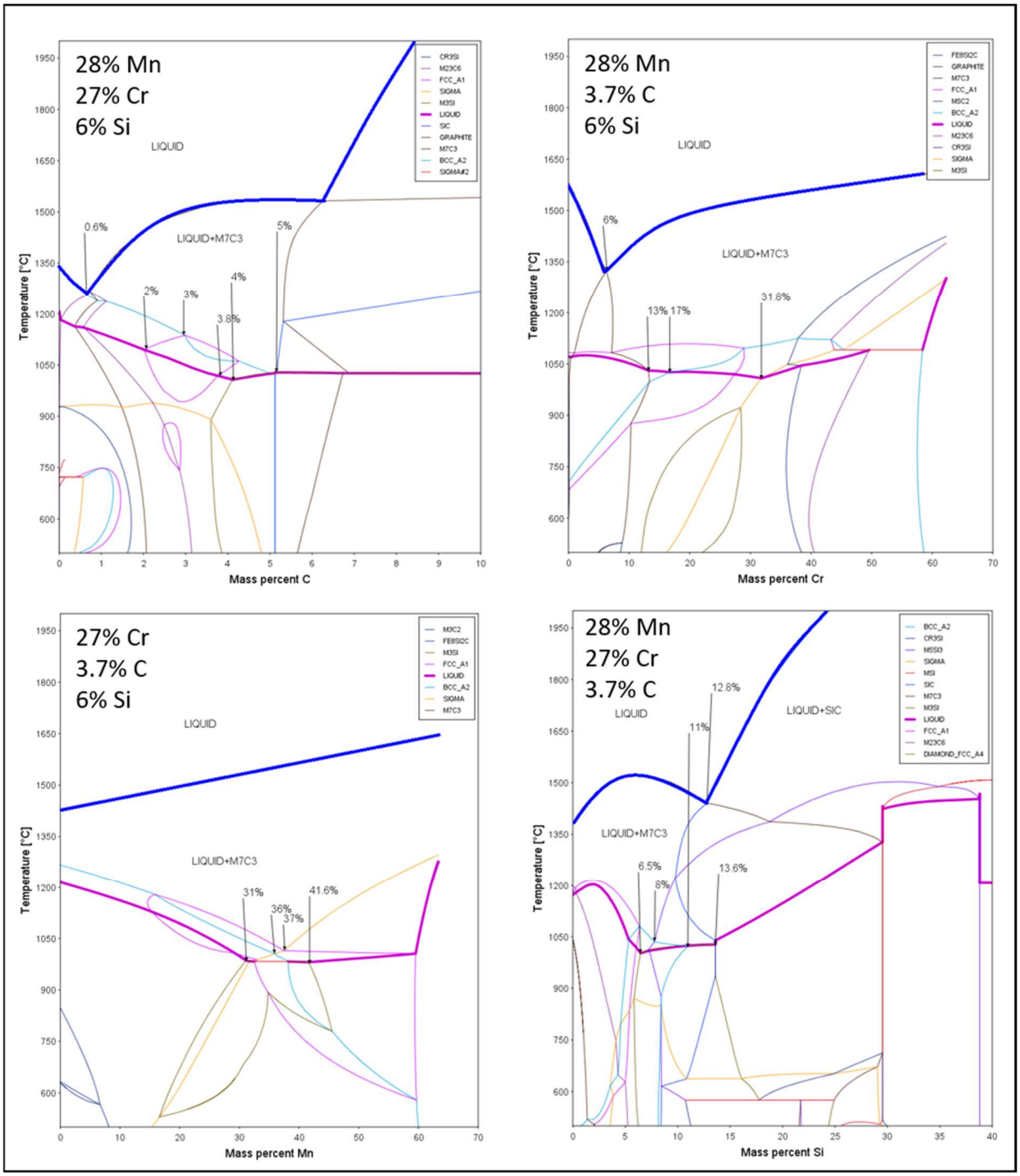

Figure 69 phase diagrams for Fe_28Mn_27Cr_6Si_3.7C

Figure 70 shows the effect of Mn to the system. Increasing the Mn content from 28 to 40% decreases the melting temperature of the first liquid formed from 1020°C to 983°C. This first liquid formed is supposed to melt in in a 30 K range instead of a 72 K range. The total amount of liquid phase formed in this first decreases from ~55% to 46%.

Die approbierte gedruckte Originalversion dieser Diplomarbeit ist an der TU Wien Bibliothek verfügbar.
The approved original version of this thesis is available in print at TU Wien Bibliothek.
TU Bibliothek Your knowledge hub WIEN

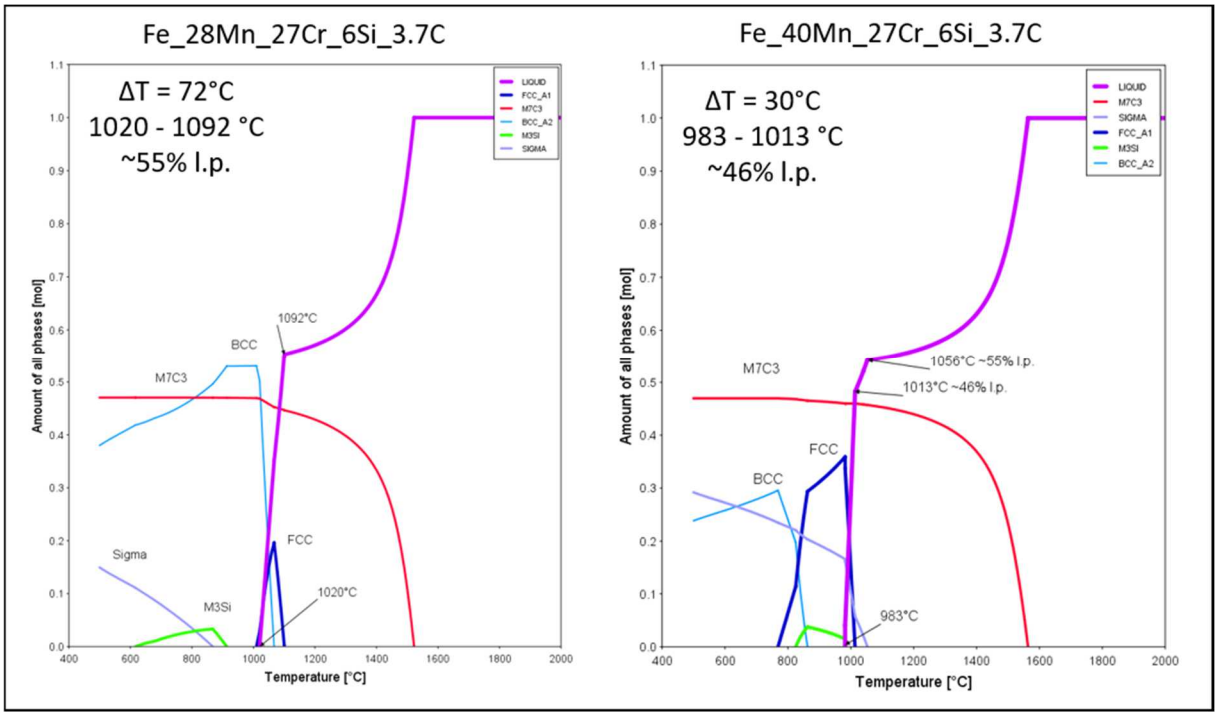

Figure 70 Evolution of phases for Cr-Mn-family Original composition Fe_28_27Cr_6Si_3.7C and with increased Mn

Figure 71 shows Si vs T phase diagrams for different Mn contents, finding out that 12% additional Mn does not affect the optimum Si content.

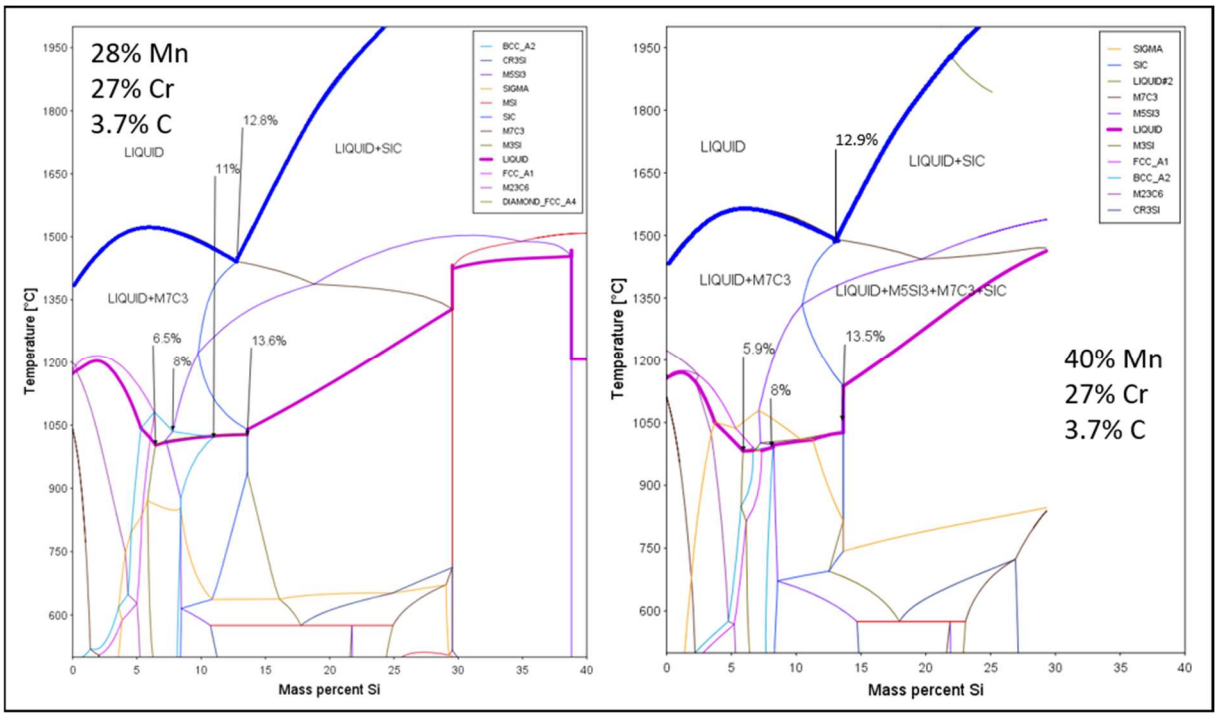

Figure 71 Si vs temperature for Cr-Mn-family original composition Fe_28_27Cr_6Si_3.7C and with increased Mn

Figure 72 shows the effect of additional 12% Mn for the Cr and C content. For the C content a plateau between 3.7 and 5% C appeared for the lowest solidus temperature. The solidus line in the Cr vs T phase diagram got flatter up to 28% Cr. The Mn content seems not to have much effect on the phase diagrams of the other elements, but it seems to be beneficial for the melting behaviour of the system to have a high Mn content.

Die approbierte gedruckte Originalversion dieser Diplomarbeit ist an der TU Wien Bibliothek verfügbar.
The approved original version of this thesis is available in print at TU Wien Bibliothek.
TU Bibliothek Your knowledge hub WIEN

Further calculations were carried out to understand how Cr, Si and C affect each other in terms of phase diagrams and the behaviour of the system. Si tends to have again its range where a low solidus temperature is possible, by broadening the melting range, like in the Mn-family. The range of this window seems to be heavily dependent on C. The C content has a big influence on the Cr vs T phase diagram as well.

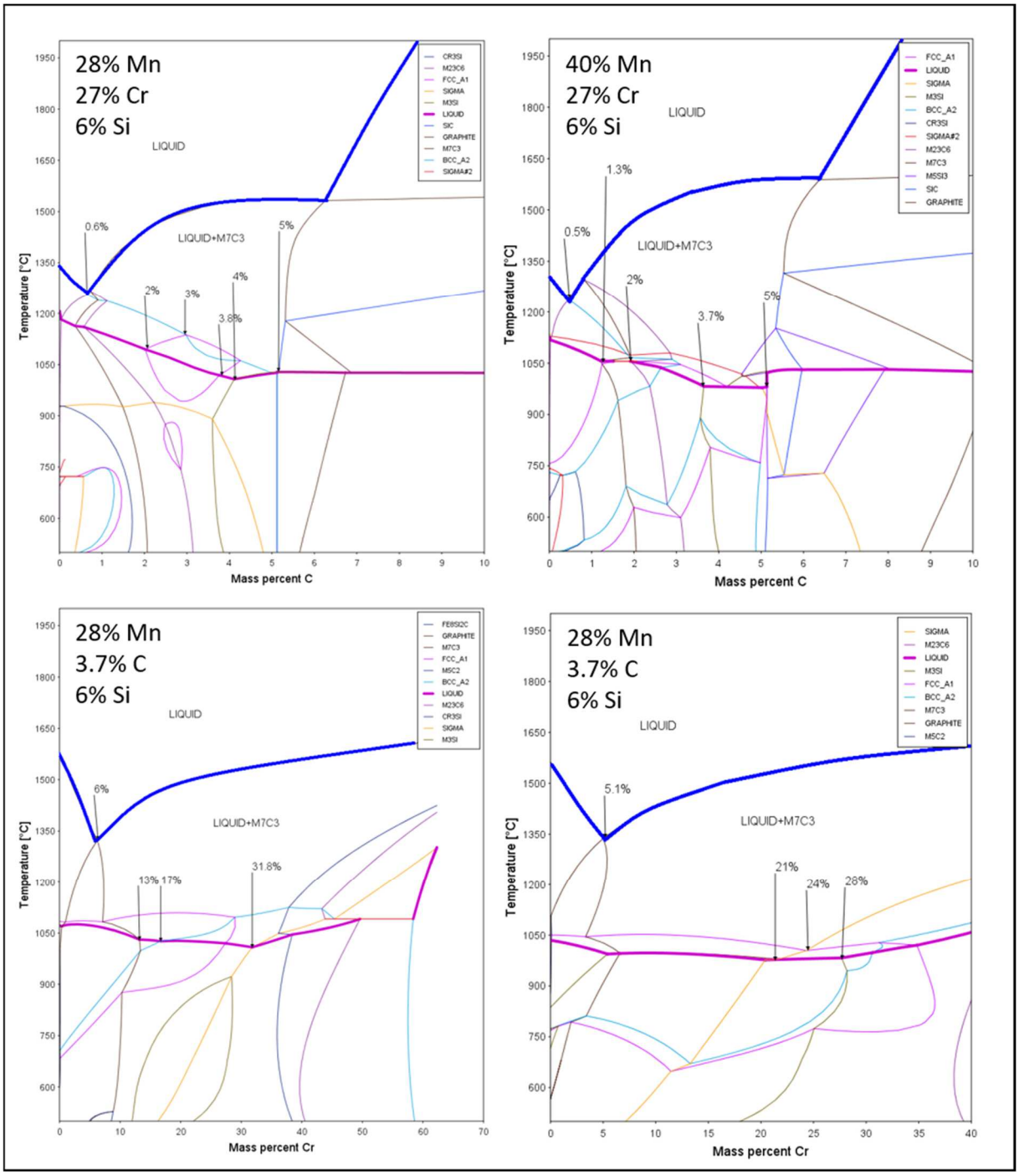

Figure 72 73 C and Cr vs temperature for Cr-Mn-family Original composition Fe_28_27Cr_6Si_3.7C and with increased Mn

Figure 74 shows the effect of C on Cr and Si phase diagrams in the Cr-Mn-family. It affects both elements in a reverse way. With lower C the Si window with the lowest solidus line shows up at much higher Si contents. For Cr it is the reverse way, with lower C the lowest solidus point is found at lower Cr contents.

Die approbierte gedruckte Originalversion dieser Diplomarbeit ist an der TU Wien Bibliothek verfügbar.
The approved original version of this thesis is available in print at TU Wien Bibliothek.
TU Bibliothek Your knowledge hub WIEN

Looking at the Cr phase diagram with 0.6% C it is good to see that the decreased C content is tightening the melting window.
Calculations were carried out for higher Si and lower Cr systems, meaning 11-12% Si and 10-14% Cr, and lower Si and higher Cr systems, meaning 6-8% Si and 21 -27% Cr.
With these tendencies, low solidus temperatures with a broader melting range, and systems with slightly higher melting temperatures with a first liquid formed at a certain temperature could be found for both groups.

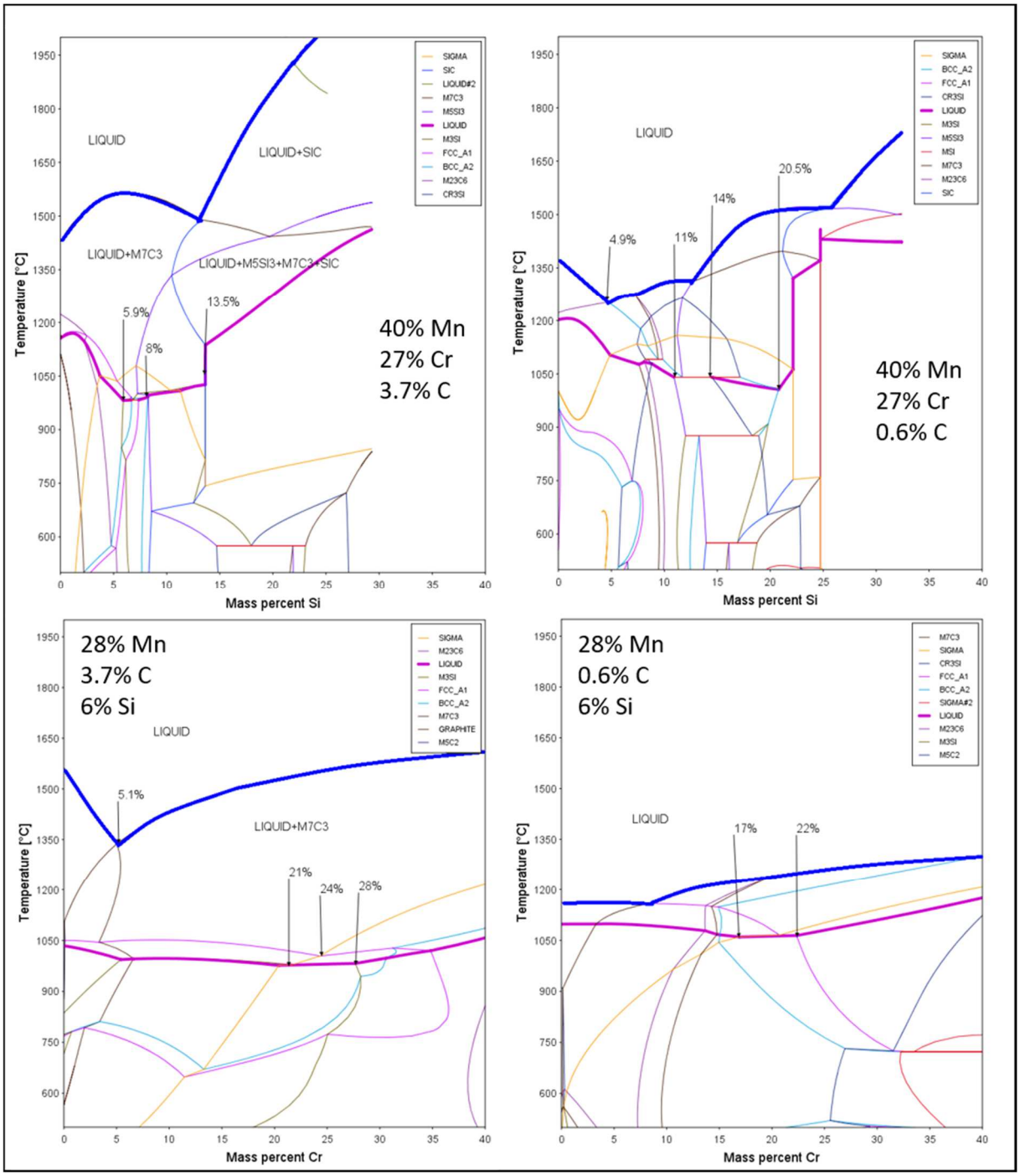

Figure 74 Cr and Si vs temperature for Fe_40Mn_27Cr_6Si_3.7C and Fe_40Mn_27Cr_6Si_0.6C

Die approbierte gedruckte Originalversion dieser Diplomarbeit ist an der TU Wien Bibliothek verfügbar.
The approved original version of this thesis is available in print at TU Wien Bibliothek.

3.2 Selection of the candidates

In the previous chapter, theoretical calculations were carried out for several systems, such as Cu-based MA and B, P and Si containing Fe-based MA from the literature. Further experiments in the experimental part were only carried out for Si and C containing Fe-based MA. The original Si and C containing Fe-based MA were already available. The new modifications were prepared from these original powders by admixing elemental powders to adjust the composition to those found through ThermoCalc calculations. The powders were mixed and afterwards melted at 1300°C for 1h in Ar/10% H_2. The produced ingots were used for the following experiments.

3.2.1 Cr-family

The candidates chosen for the Cr - family are listed in Table 4.

Table 4 Summary of Cr-family modifications

Group	Code	Fe [wt%]	Cr [wt%]	Si [wt%]	C [wt%]
Original composition	**H45**	56,0	32,0	8,0	4,0
High Cr group	**H45_E1**	45,5	40,0	11,0	3,5
	H45_E2	42,0	40,0	14,0	4,0
Si group	**H45_E3**	50,0	32,0	14,0	4,0
	H45_E4	54,3	32,0	9,8	4,0
Low Cr group	**H45_E5**	75,2	10,0	11,8	3,0
	H45_E6	72,5	11,7	13,6	2,2

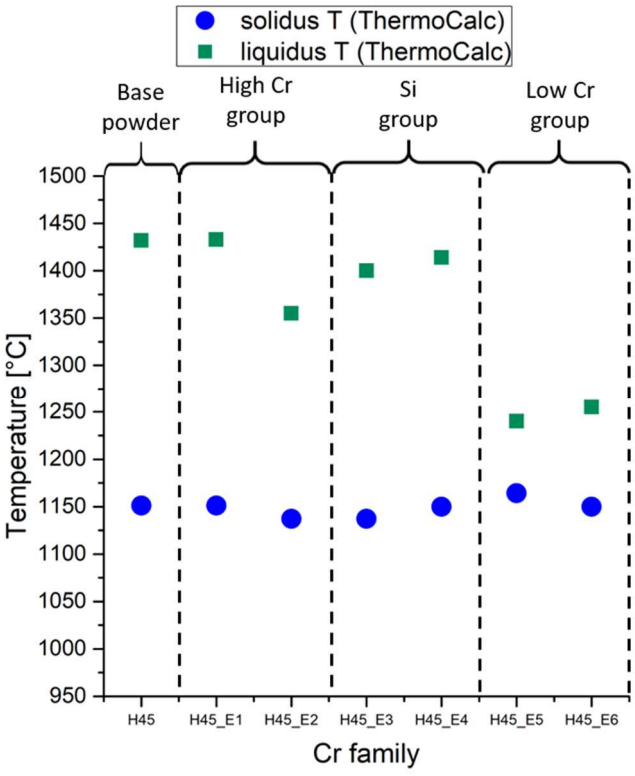

Figure 75 Solidus and liquidus temperatures for Cr-family original composition and modifications

Figure 75 shows that the solidus temperature was not much affected by the different compositions. It is clear to see that a system that melts completely below 1250°C is hard to achieve. Forming as much liquid phase as possible in a narrow range seemed to be a more reasonable approach to this family. The aim of the modifications was to cover different supposed behaviours in the melting in comparison to the original composition. The liquidus temperatures seem to be affected by the different compositions. Graphite phase was not taken into account for the liquidus temperature since it is considered as unlikely to be formed in these systems.

Die approbierte gedruckte Originalversion dieser Diplomarbeit ist an der TU Wien Bibliothek verfügbar.
The approved original version of this thesis is available in print at TU Wien Bibliothek.

If the MA contains a graphite phase or not might not be relevant for the planned application of the MA. Using 4% MA with Fe powder will lead to C diffusion and to dissipating of a graphite phase before the sintering temperatures are reached (similar to the admixed graphite common in ferrous PM).

High Cr group:

Figure 76 shows the two candidates from the High Cr family. Pushing the amount of the alloying elements was the major interest for this group.

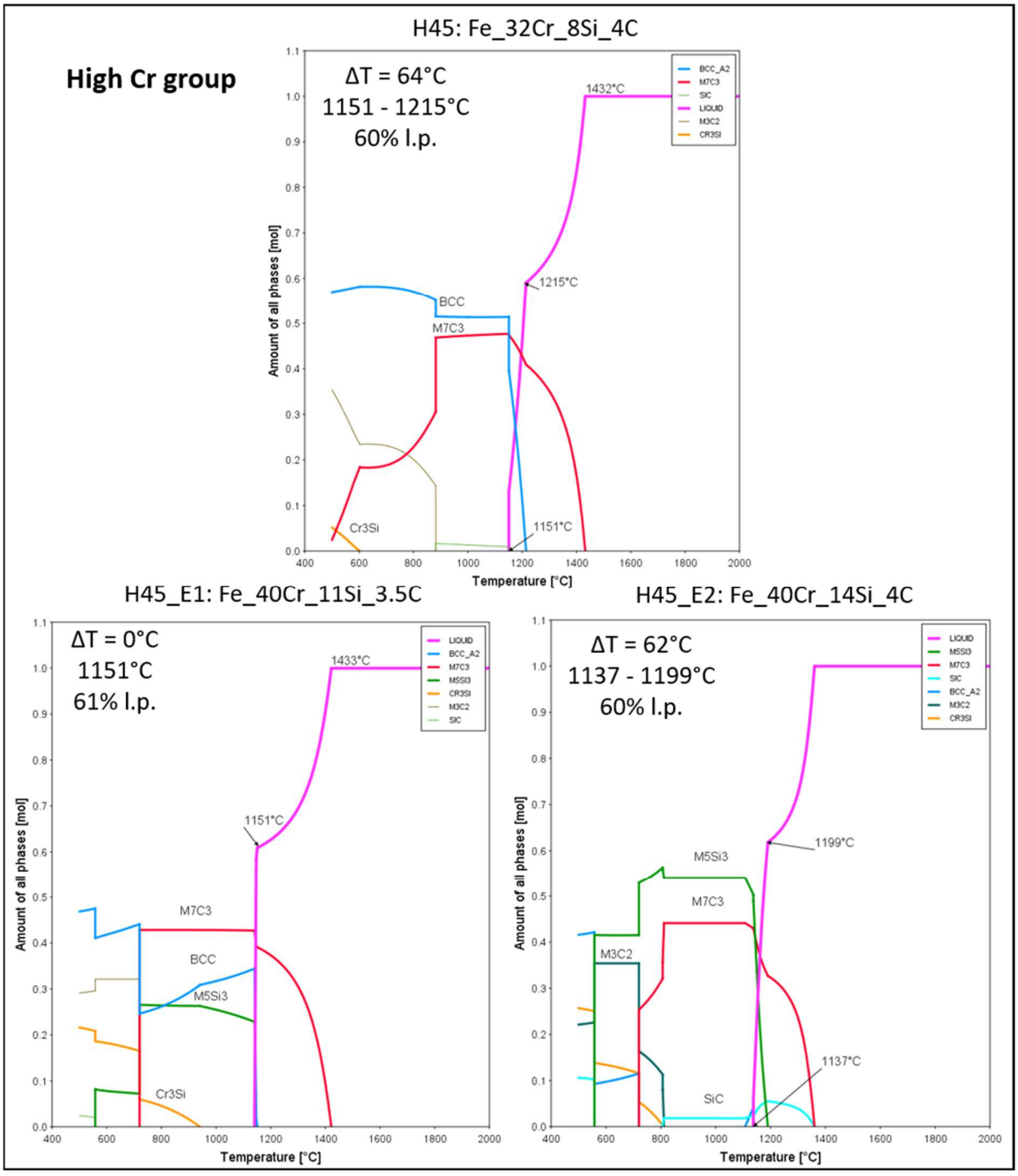

Figure 76 Evolution of phases from Cr-family original composition and the two candidates from high Cr group

Die approbierte gedruckte Originalversion dieser Diplomarbeit ist an der TU Wien Bibliothek verfügbar.
The approved original version of this thesis is available in print at TU Wien Bibliothek.

Si group:

When comparing the evolution of phases shown in Figure 77 a lower solidus temperature and a melting point for the first liquid was found as modification for the Si group.

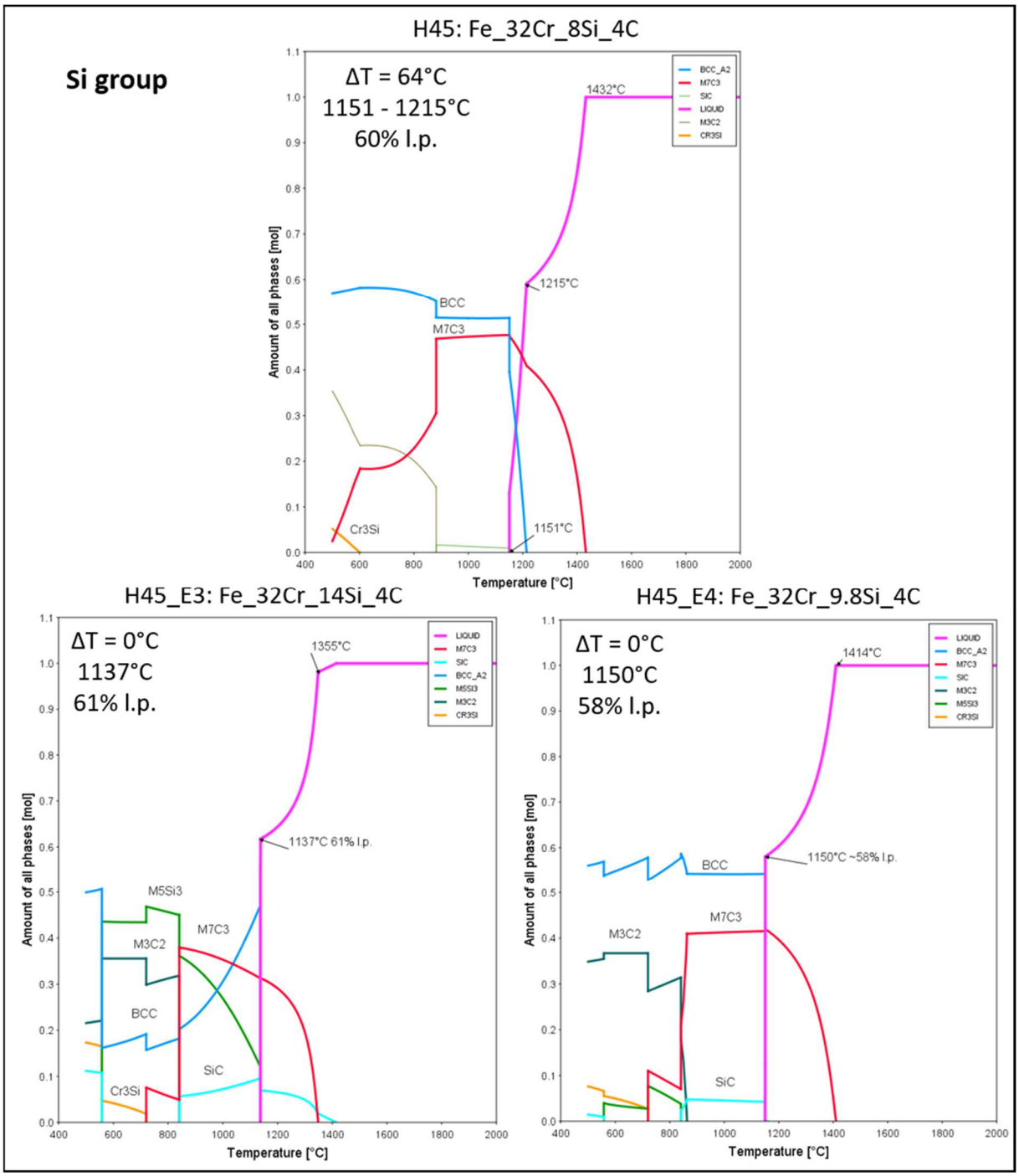

Figure 77 Evolution of phases from Cr-family original composition and the two candidates from Si group

Die approbierte gedruckte Originalversion dieser Diplomarbeit ist an der TU Wien Bibliothek verfügbar.
The approved original version of this thesis is available in print at TU Wien Bibliothek.

Low Cr group:

The low Cr group, shown in Figure 78, was chosen as systems forming as much liquid phase as possible at a certain melting point.

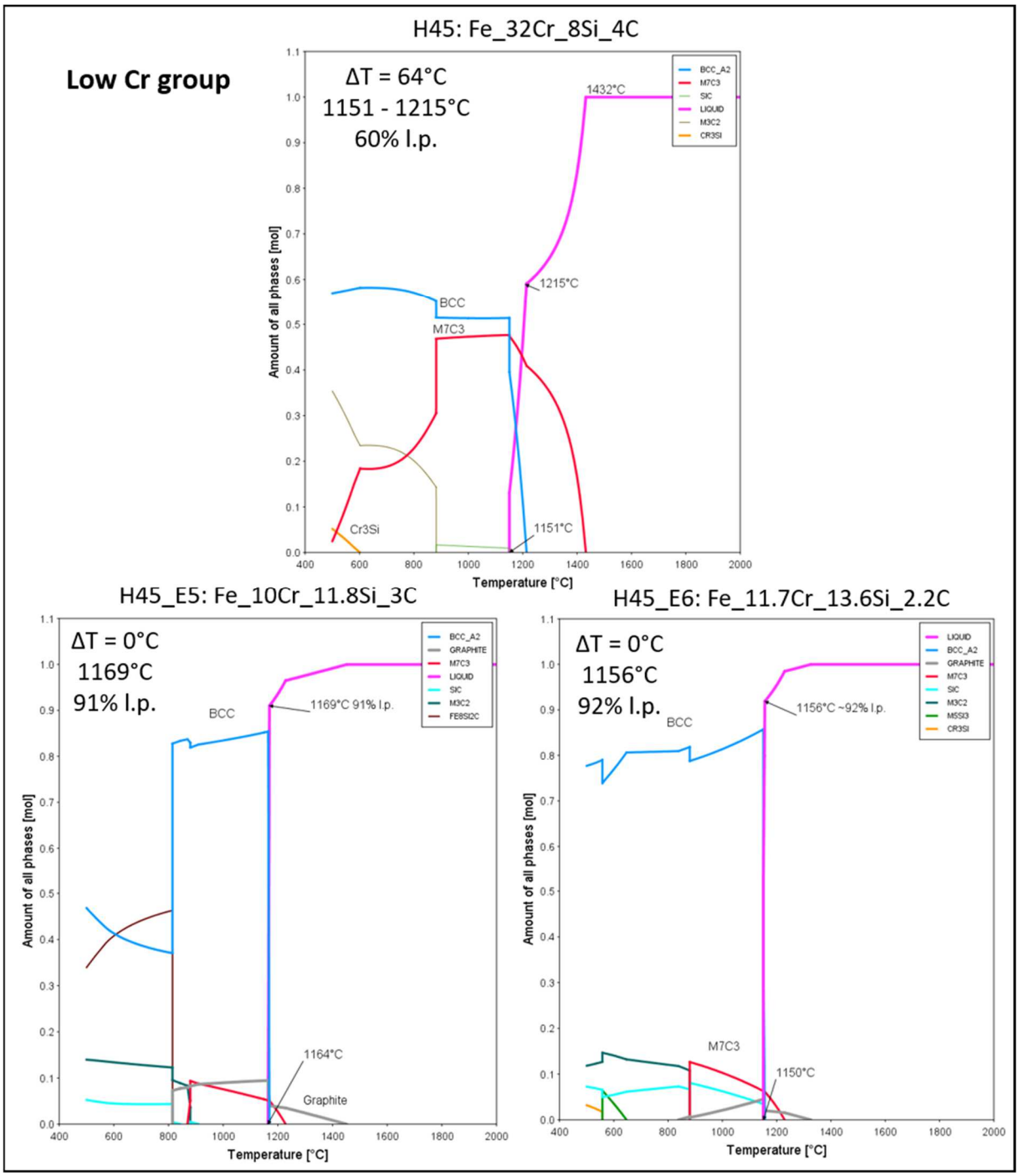

Figure 78 Evolution of phases from Cr-family original composition and the two candidates from low Cr group

Die approbierte gedruckte Originalversion dieser Diplomarbeit ist an der TU Wien Bibliothek verfügbar.
The approved original version of this thesis is available in print at TU Wien Bibliothek.

3.2.2 Mn-family

The candidates chosen for the Mn - family are listed in Table 5.

Table 5 Summary of Mn-family modifications

Group	Code	Fe [wt%]	Mn [wt%]	Si [wt%]	C [wt%]
Original composition	**H46**	51,6	42,0	6,0	0,4
High Mn group	**H46_E1**	51,1	41,0	5,9	2,0
	H46_E4	48,0	40,0	9,0	3,0
Low Mn group	**H46_E2**	56,1	33,0	7,5	3,4
	H46_E3	61,9	30,0	5,0	3,1
	H46_E5	58,0	30,0	9,0	3,0

Due to the adjusting of the C content for the Mn – family all candidates can be obtained as optimized systems compared to the original composition, gaining at least about 50 K lower melting temperatures. Different behaviours in the groups were searched and selected as the candidates for Mn – family.

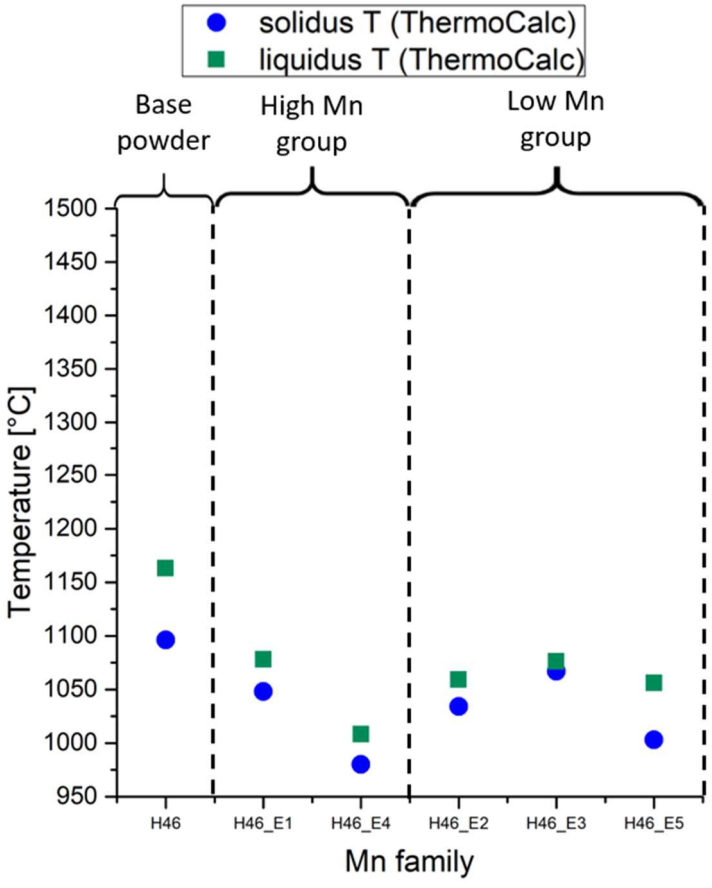

Figure 79 Solidus and liquidus temperatures for Mn-family original composition and modifications

Liquidus temperatures do not account for the graphite phase. If the MA contains a graphite phase or not might not be relevant for the planned application of the MA. Using 4% MA with Fe powder will lead to C diffusion and to dissipating of a graphite phase before sintering temperatures are reached.

Die approbierte gedruckte Originalversion dieser Diplomarbeit ist an der TU Wien Bibliothek verfügbar.
The approved original version of this thesis is available in print at TU Wien Bibliothek.

High Mn group:

Figure 80 shows the high Mn group, modifying the C and Si content to gain more desired melting properties with the high amount of alloying element. For this group the modification with the highest alloying element content H46_E4 shows the lowest solidus temperature and a narrower melting range.

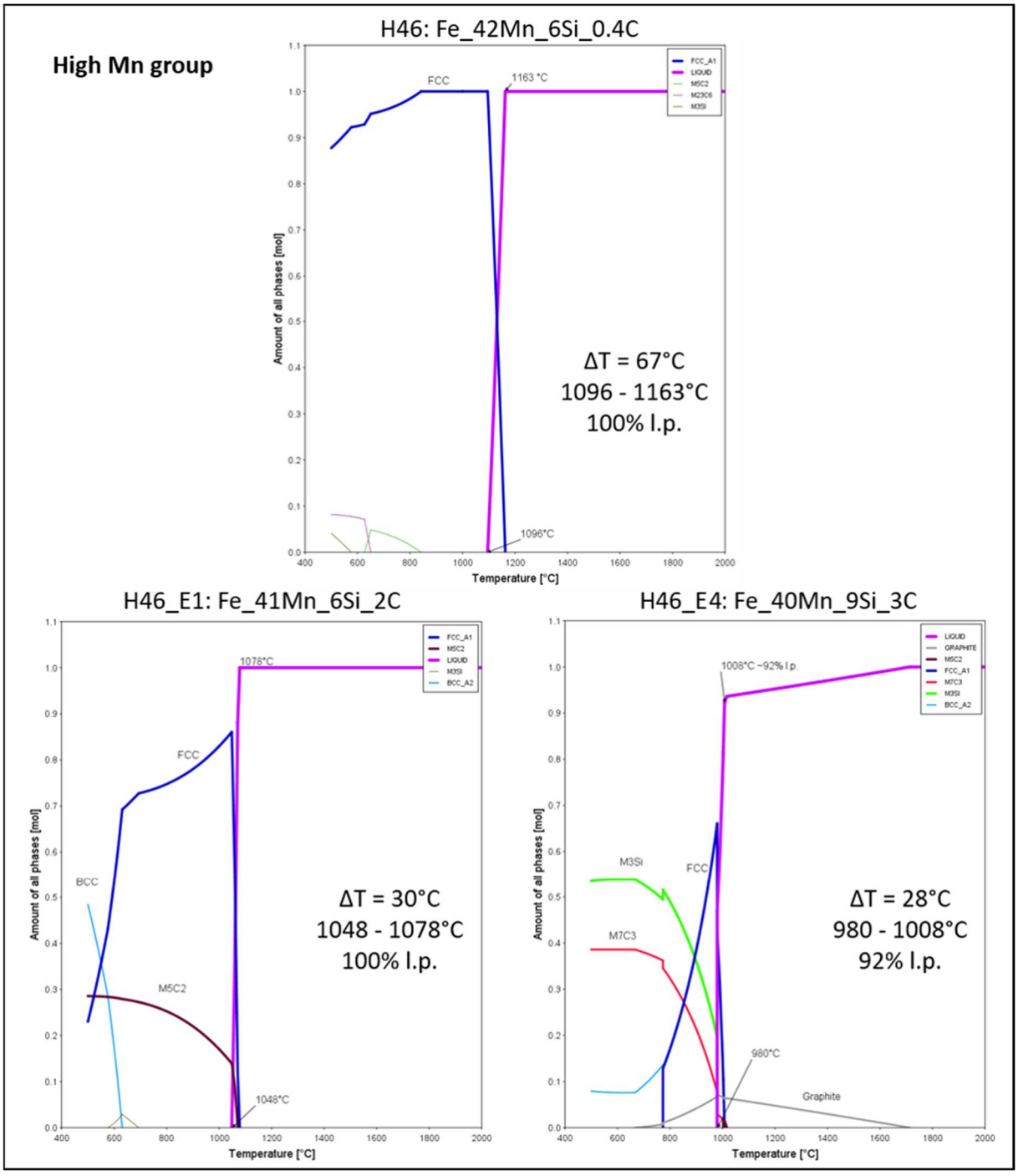

Figure 80 Evolution of phases from Mn-family original composition and the two candidates from high Mn group

Die approbierte gedruckte Originalversion dieser Diplomarbeit ist an der TU Wien Bibliothek verfügbar.
The approved original version of this thesis is available in print at TU Wien Bibliothek.

Low Mn group:

Figure 81 shows that for the lower Mn system either a narrow melting window or broad melting ranges with low solidus temperature can be achieved by modifying the Si content. Choosing three 2.5% Si steps covered this different behaviour.

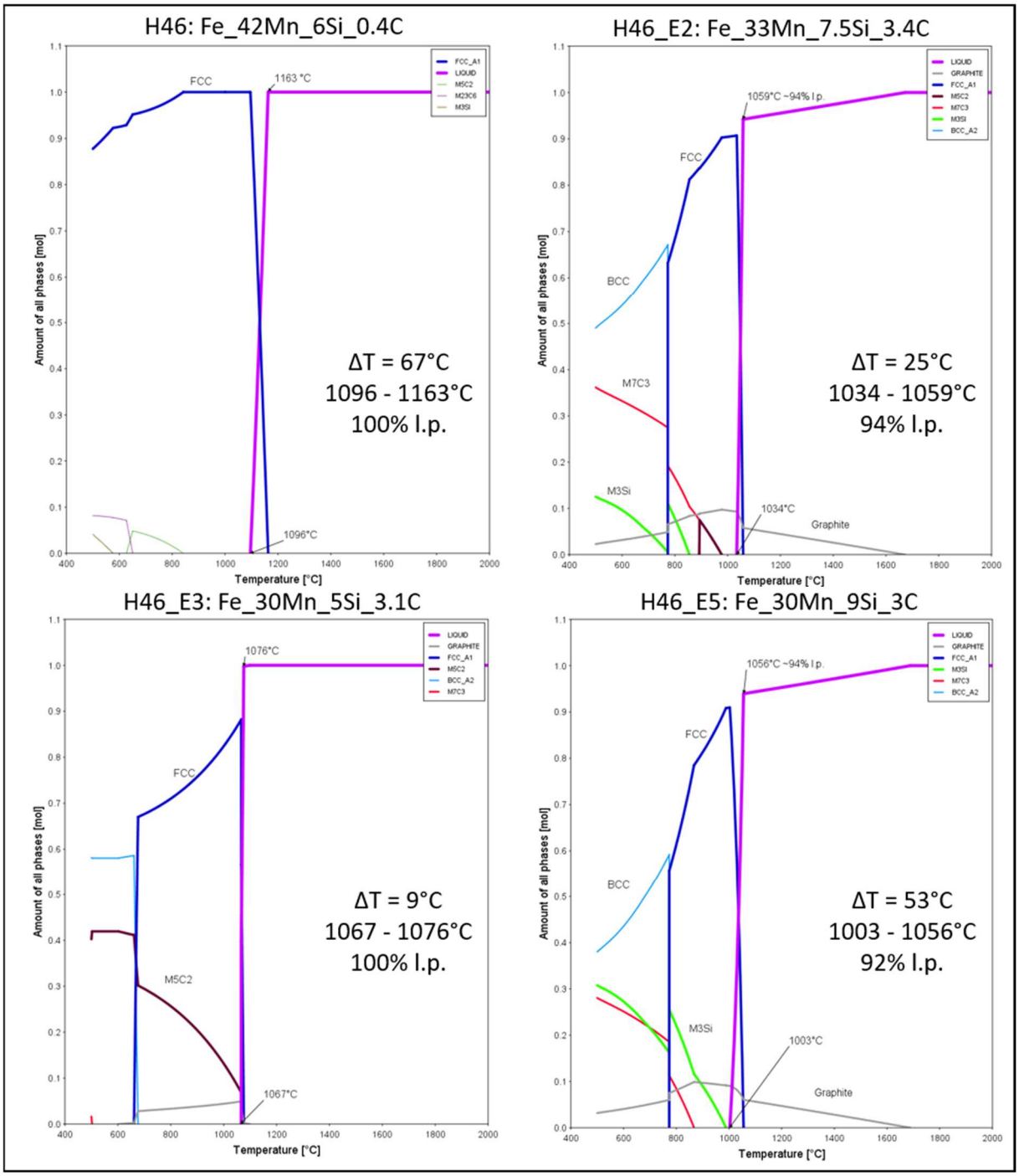

Figure 81 Evolution of phases from Mn-family original composition and the three candidates from low Mn group

Die approbierte gedruckte Originalversion dieser Diplomarbeit ist an der TU Wien Bibliothek verfügbar.
The approved original version of this thesis is available in print at TU Wien Bibliothek.

3.2.3 Cr-Mn family

The candidates chosen for the Cr- Mn - family are listed in Table 6.

Table 6 Summary of Cr-Mn-family modifications

Group	Code	Fe [wt%]	Mn [wt%]	Cr [wt%]	Si [wt%]	C [wt%]
Original composition	**H47**	35,3	28,0	27,0	6,0	3,7
High Cr low Si group	**H47_E2**	30,0	38,0	21,0	8,0	3,0
	H47_E4	34,0	28,0	27,0	6,0	5,0
Low Cr high Si group	**H47_E1**	36,2	35,0	14,0	11,0	3,8
	H47_E3	39,9	35,0	12,0	12,0	2,0
	H47_E5	58,0	40,0	10,0	12,0	0,5

For the Cr-Mn family modification, two different approaches were chosen in high Cr / low Si and low Cr / high Si systems. Both systems could achieve either a predicted melting point for the first liquid or relatively low solidus temperatures while accepting a melting range. Both groups were supposed to form different initial liquids so for both groups these behaviours were calculated and then candidates with different behaviours were chosen. Figure 82 shows that for the Cr-Mn family the solidus temperature cannot be changed much, as it is for the Cr family. Achieving a fully molten system in a narrow range seems not possible for this family, but the liquidus temperatures could be modified.

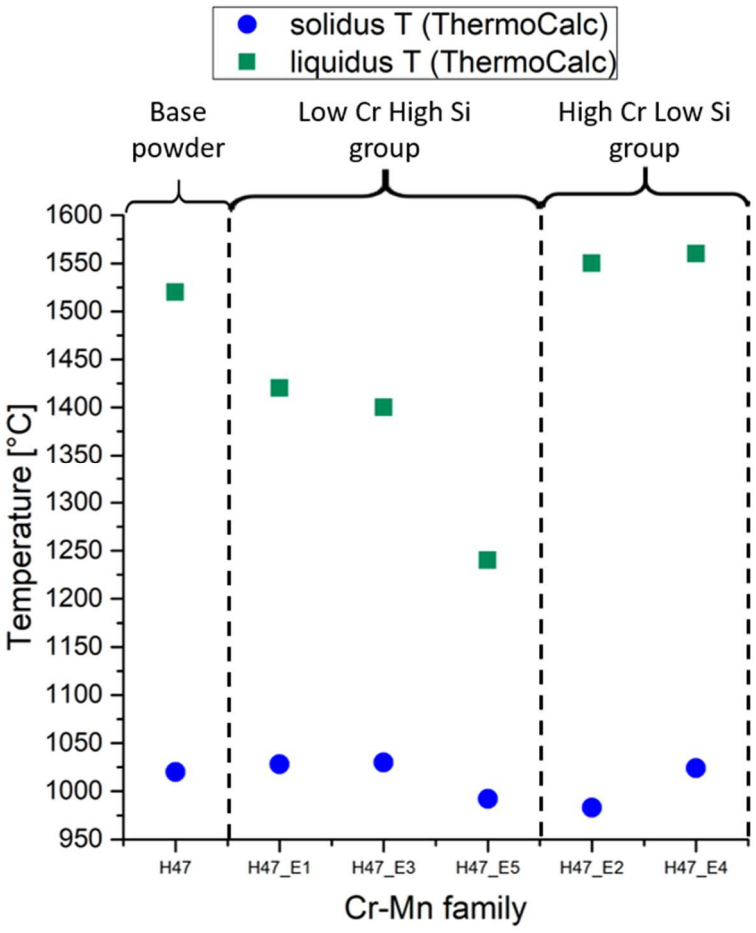

Figure 82 Solidus and liquidus temperatures for Cr-Mn family original composition and modifications

Liquidus temperatures do not account for the graphite phase. If the MA contains a graphite phase or not might not be relevant for the planned application of the MA. Using 4% MA with Fe powder will lead to C diffusion and to dissipating of a graphite phase before sintering temperatures are reached (see comment above).

Die approbierte gedruckte Originalversion dieser Diplomarbeit ist an der TU Wien Bibliothek verfügbar.
The approved original version of this thesis is available in print at TU Wien Bibliothek.

High Cr low Si group:

Figure 83 shows two different ideas for high Cr, meaning more than 20% Cr and low Si, meaning less than 10% Si. H47_E4 is only a C modification of the original composition, achieving a predicted melting point for a first formed liquid. H47_E2 shows that even with such a high amount of Cr relatively low liquidus temperatures seem to be achievable.

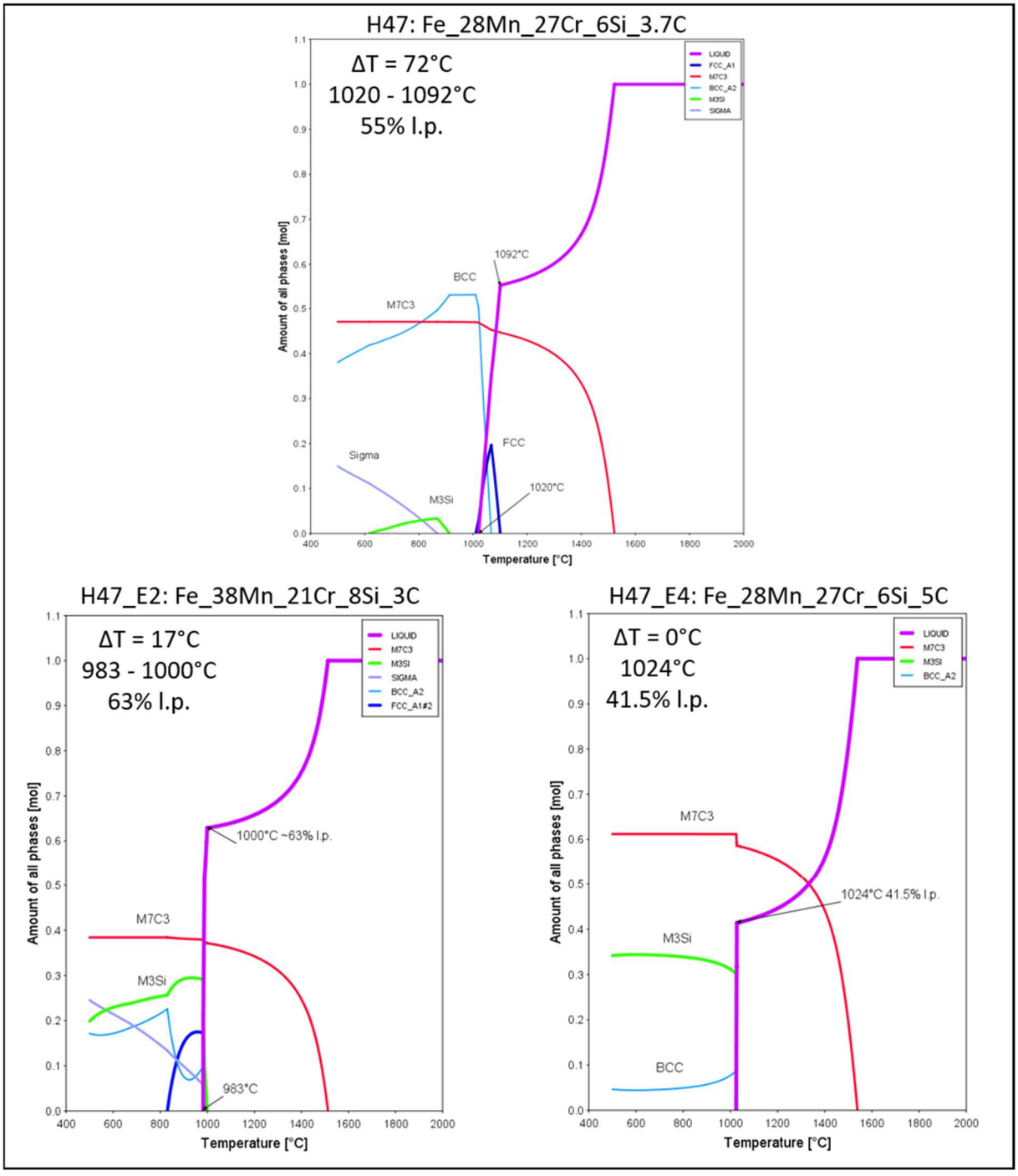

Figure 83 Evolution of phases from Cr-Mn-family original composition and the two candidates from high Cr low Si group

Die approbierte gedruckte Originalversion dieser Diplomarbeit ist an der TU Wien Bibliothek verfügbar.
The approved original version of this thesis is available in print at TU Wien Bibliothek.

Low Cr high Si group:

Figure 84 shows that with low Cr, meaning below 15%, and high Si, more than 10%, higher amounts of liquid phase are predicted to be achieved at a certain melting point.

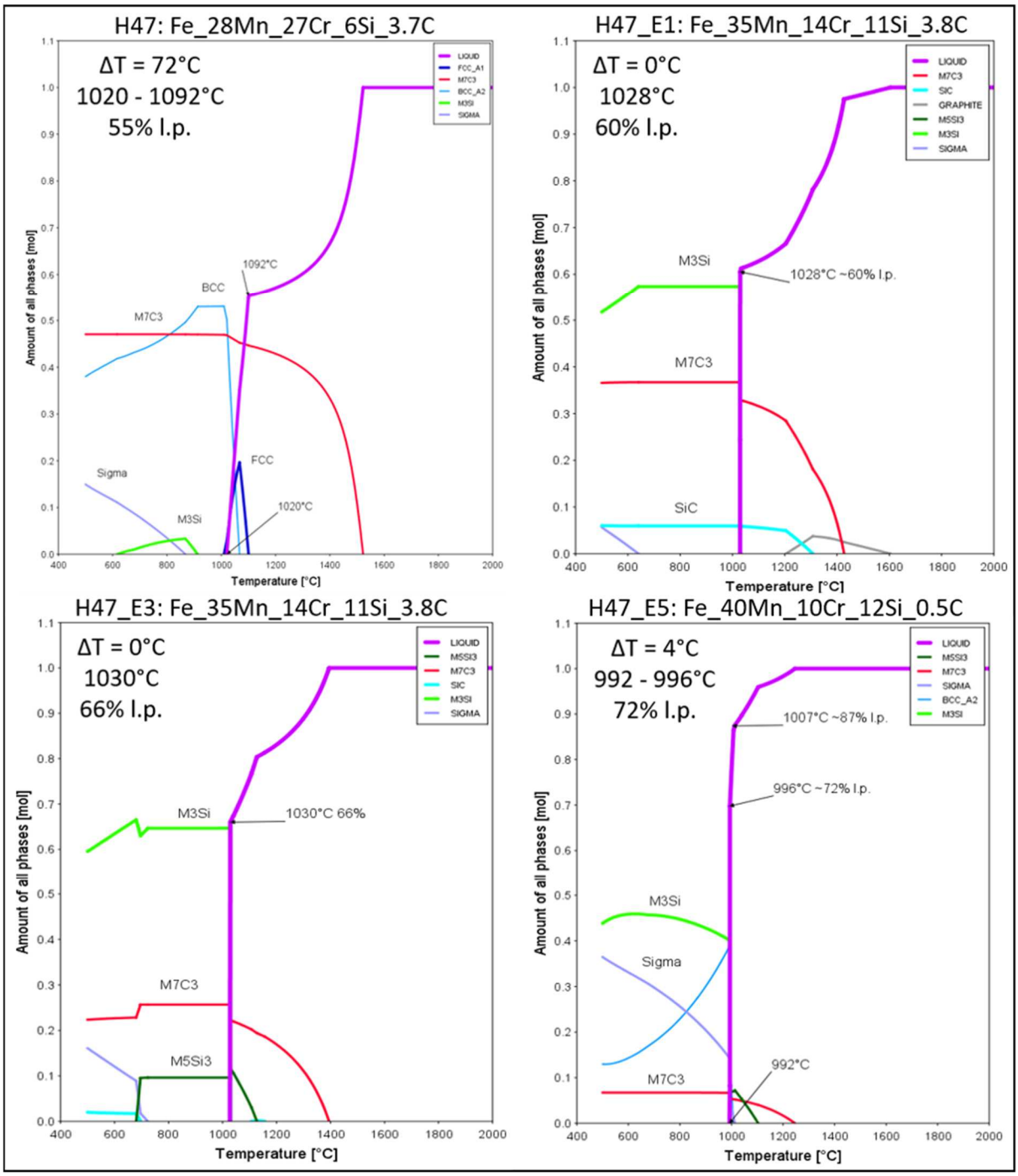

Figure 84 Evolution of phases from Cr-Mn-family original composition and the three candidates from low Cr high Si group.

Die approbierte gedruckte Originalversion dieser Diplomarbeit ist an der TU Wien Bibliothek verfügbar.
The approved original version of this thesis is available in print at TU Wien Bibliothek.

3.3 Characterization of the ingots

The ingots were characterized with DTA, XRD, XRF, Leco and SEM to get information about the melting behaviour and the phases formed. These experiments were compared with the theoretical calculations carried out before and described above. Table 7 shows the composition measured with XRF and SEM. The C content was determined with Leco measurements. EDX measurements show compositions close to the theoretical composition. XRF measurements show differences in the Cr content to the theoretical content. This loss is remarkably higher for H45_E1 and H45_E2 where ~8 g of elemental Cr was added to increase the Cr content from 32 wt% to 40 wt%. It seems that the Cr loss is higher with elemental Cr in these systems. The Cr might be lost due to evaporation either as Cr or as Cr-oxide. The evaporation is dependent on several factors as the formation of oxides, a possible diffusion of Cr into other elements of the powder mix or a dissolution in a formed melt. The sooner the Cr is dissolved the less Cr loss is suspected to occur.

Note: The Cr losses seem to be rather high in these MA's, if they are heated up without Fe substrate. Using the MA finely distributed in Fe substrate will probably not lead to any losses of elemental content.

Table 7 Composition of the Cr family ingots.

		Fe [wt%]	Cr [wt%]	Mn [wt%]	Si [wt%]	C [wt%]
	Theory	56,0	32,0	0,0	8,0	4,0
H45	EDX	55,9	32,0	0,0	9,0	3,1
	XRF	54,90	33,0	0,0	8,0	3,1
	Theory	45,5	40,0	0,0	11,0	3,5
H45_E1	EDX	45,0	40,0	0,0	11,0	3,36
	XRF	54,51	32,97	0,18	9,79	3,36
	Theory	42,0	40,0	0,0	14,0	4,0
H45_E2	EDX	42,1	40,0	0,0	14,0	3,87
	XRF	43,84	35,99	0,16	17,47	3,87
	Theory	50,0	32,0	0,0	14,0	4,0
H45_E3	EDX	49,4	33,0	0,0	14,0	3,60
	XRF	51,27	28,03	0,16	14,66	3,60
	Theory	54,3	32,0	0,0	9,8	4,0
H45_E4	EDX	55,9	29,0	0,0	11,0	4,09
	XRF	53,20	32,66	0,18	11,42	4,09
	Theory	75,2	10,0	0,0	11,8	3,0
H45_E5	EDX	75,5	11,0	0,0	11,0	2,48
	XRF	77,60	8,02	0,1	9,79	2,48
	Theory	72,5	11,7	0,0	13,6	2,2
H45_E6	EDX	72,1	13,0	0,0	13,0	1,94
	XRF	74,62	9,33	0,11	13,79	1,94

Die approbierte gedruckte Originalversion dieser Diplomarbeit ist an der TU Wien Bibliothek verfügbar.
The approved original version of this thesis is available in print at TU Wien Bibliothek.

Die approbierte gedruckte Originalversion dieser Diplomarbeit ist an der TU Wien Bibliothek verfügbar.
The approved original version of this thesis is available in print at TU Wien Bibliothek.

3.3.1 Cr family

- **Melting behaviour:**

Figure 85 compares ThermoCalc calculations (A) with DTA measurements (B). It is clear to see that for this family the predictions of the solidus temperature were rather good. Predictions of the liquidus temperatures were not so accurate but still in an acceptable range.

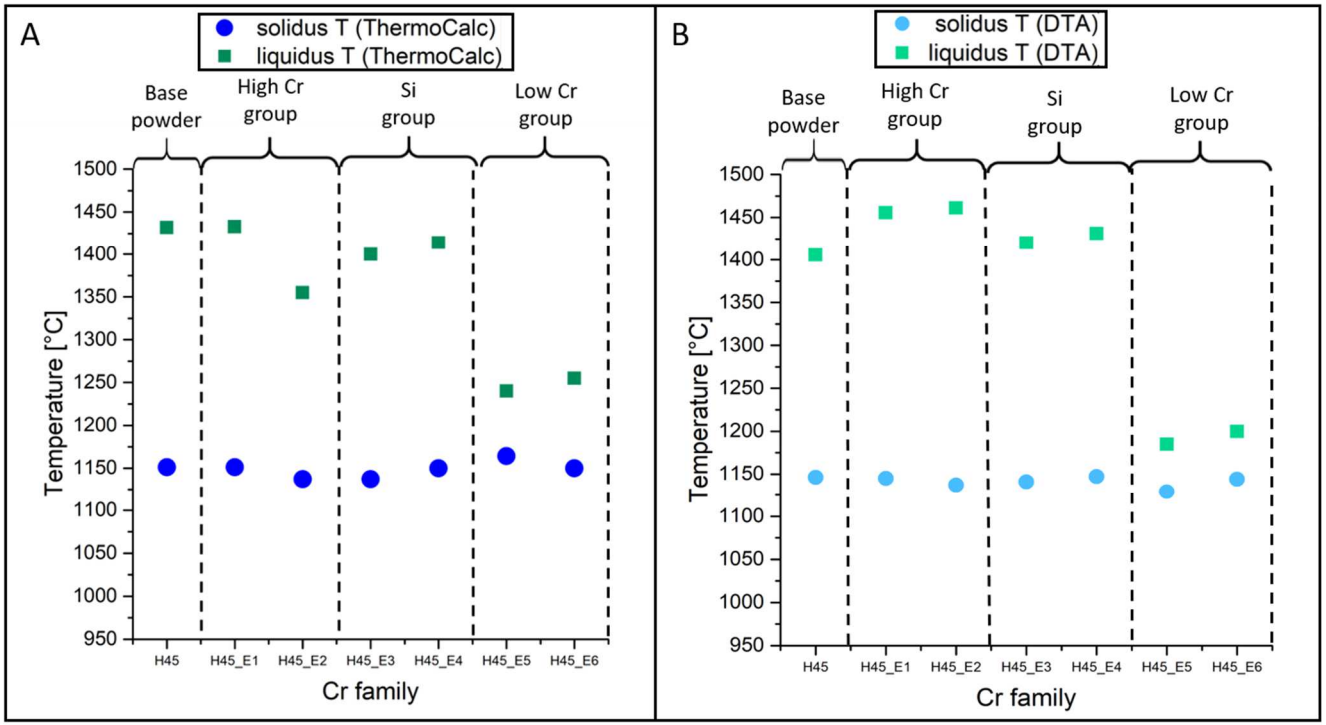

*Figure 85 Comparing solidus and liquidus temperatures predicted from ThermoCalc (**A**) and measured with DTA (**B**) for the Cr family*

Die approbierte gedruckte Originalversion dieser Diplomarbeit ist an der TU Wien Bibliothek verfügbar.
The approved original version of this thesis is available in print at TU Wien Bibliothek.

Figure 85 shows the DTA measurement for the Cr family ingots. The highlighted temperatures 1120°C and 1250°C are standard sintering temperatures for PM steels (belt and walking beam furnaces, respectively). The samples were produced by melting at 1300°C.

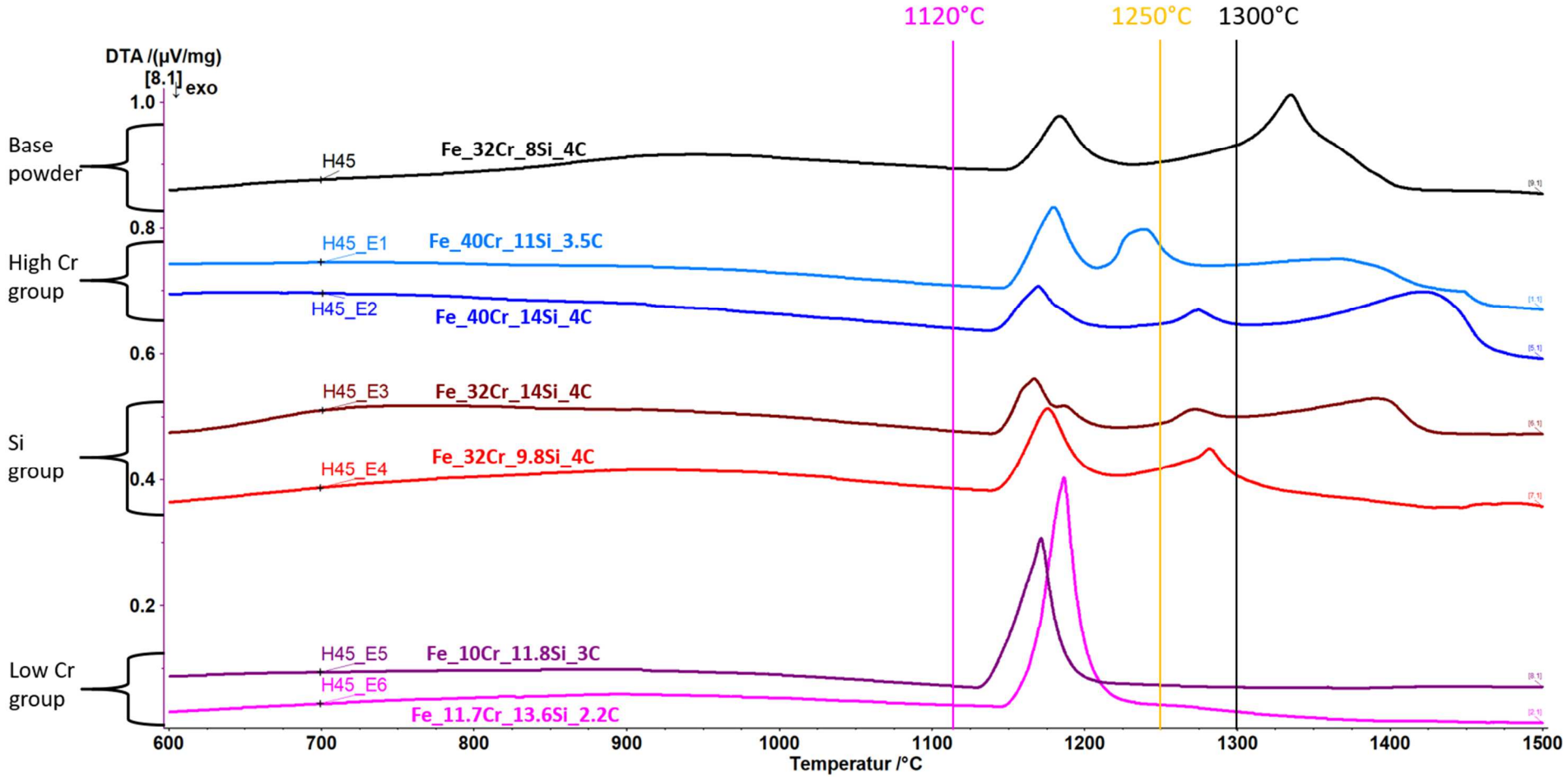

Figure 86 DTA for Cr family, heating phase

Die approbierte gedruckte Originalversion dieser Diplomarbeit ist an der TU Wien Bibliothek verfügbar.
The approved original version of this thesis is available in print at TU Wien Bibliothek.

Melting at 1300°C was not enough to fully melt the modifications except the members of the low Cr group. The low Cr group melts, as predicted, in a narrow range and most of the endothermal reactions are finished at 1200°C, showing only one peak in the DTA.
The original composition shows two peaks in the DTA. When increasing the Si content from the original composition, the temperature range where the endothermal reactions take place broadens up. Three different peaks can be observed for the Si and the high Cr group. The last peak gets more intense with the increasing Si content, while Cr does not seem to play such a big role in this case.

- **Stable phases:**

Figure 87 to Figure 90 show SEM measurements of the ingots, XRD measurements of milled ingots and the predicted evolution of phases (EoP) from ThermoCalc. Linking the phases from XRD to the SEM are suggestions based on several spot analysis and mappings. Differences of the composition of the phases in the different modifications might result in different brightness of these phases.

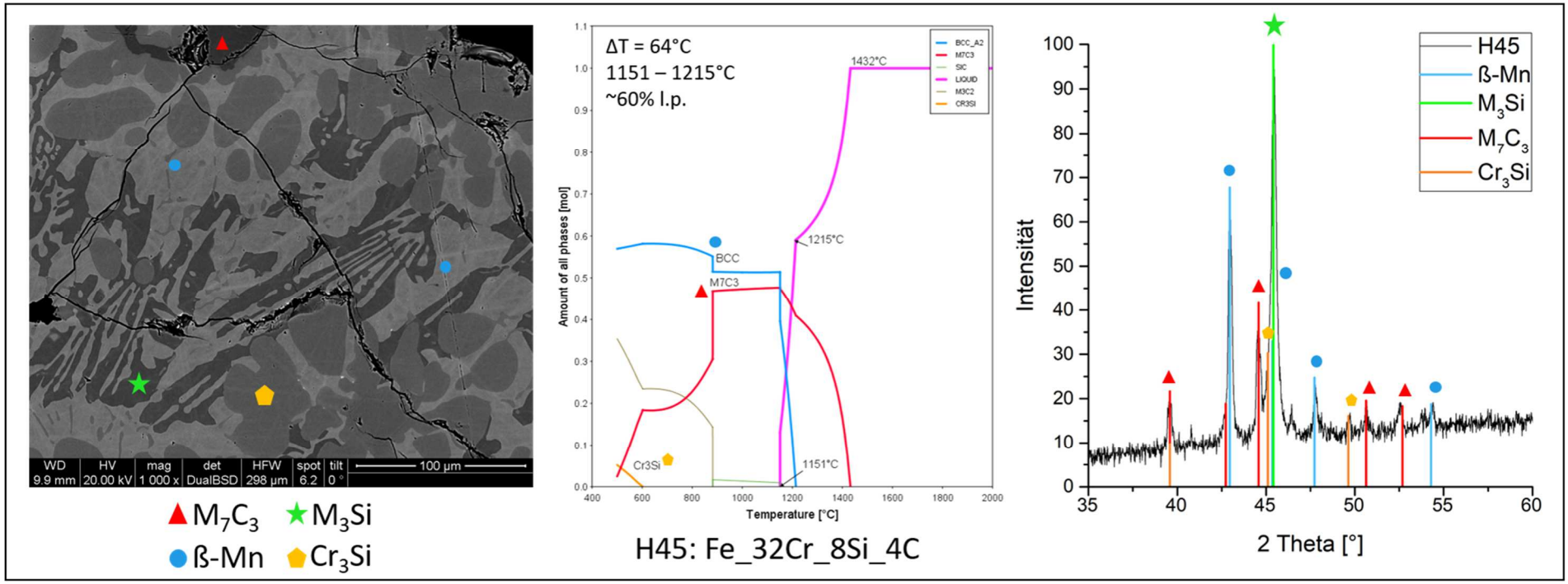

*Figure 87 SEM x1000, EoP and XRD analysis from H45 Ingot; **Phase References**: M_7C_3 (04-017-0806), M_3Si =(Fe_3Si (04-003-3871) and/or $Cr_{0.6}Fe_{2.6}Si$ (04-006-7480), Cr_3Si (04-001-2815), ß-Mn structured phase (04 007 2059)*

Die approbierte gedruckte Originalversion dieser Diplomarbeit ist an der TU Wien Bibliothek verfügbar.
The approved original version of this thesis is available in print at TU Wien Bibliothek.

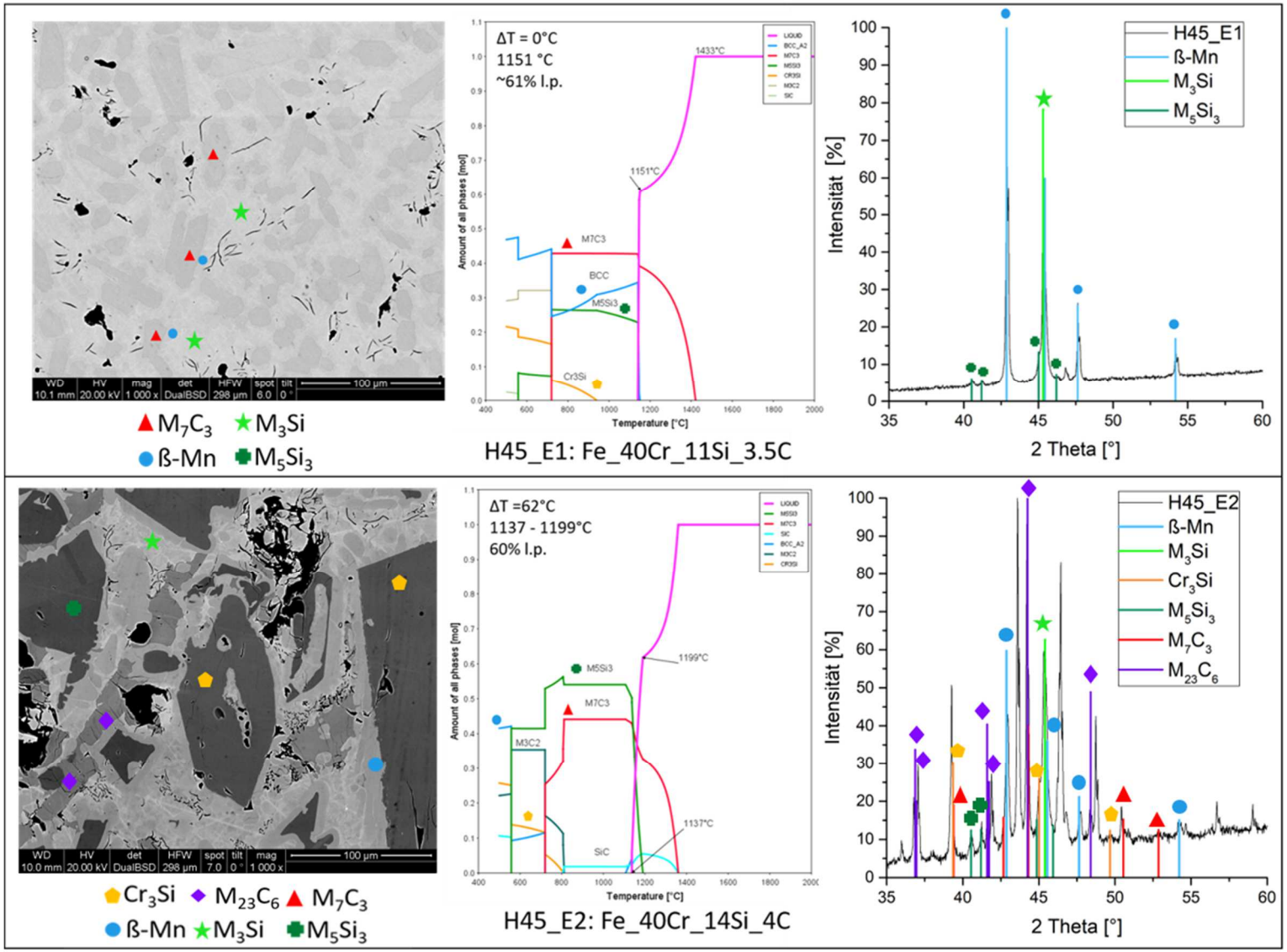

Figure 88 ***High Cr group****: SEM x1000, EoP and XRD analysis from H45_E1 Ingot (top) and H45_E2 (bottom)* ***Phase References****: M_7C_3 (04-017-0806), M_3Si =(Fe_3Si (04-003-3871) and/or $Cr_{0.6}Fe_{2.6}Si$ (04-006-7480), Cr_3Si (04-001-2815), ß-Mn structured phase (04 007 2059), M5Si3 (04-004-3035), $M_{23}C_6$ (04-003-6076)*

Die approbierte gedruckte Originalversion dieser Diplomarbeit ist an der TU Wien Bibliothek verfügbar.
The approved original version of this thesis is available in print at TU Wien Bibliothek.

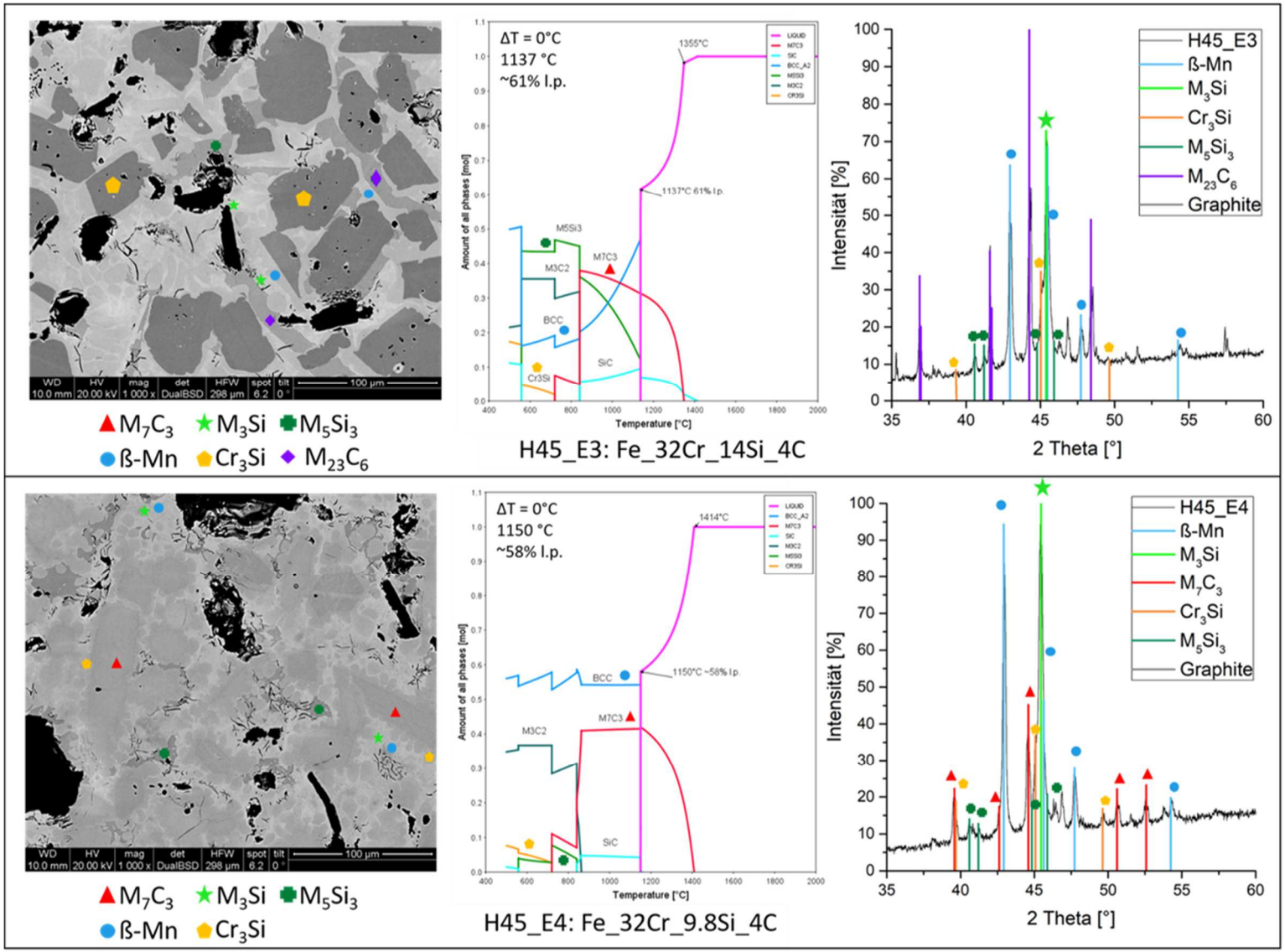

Figure 89 ***Si group****: SEM x1000, EoP and XRD analysis from H45_E3 Ingot (top) and H45_E4 (bottom)* ***Phase References****: M_7C_3 (04-017-0806), M_3Si =(Fe_3Si (04-003-3871) and/or $Cr_{0.6}Fe_{2.6}Si$ (04-006-7480), Cr_3Si (04-001-2815), ß-Mn structured phase (04 007 2059), $M_{23}C_6$ (04-003-6076), M_5Si_3 (04-004-3035)*

Die approbierte gedruckte Originalversion dieser Diplomarbeit ist an der TU Wien Bibliothek verfügbar.
The approved original version of this thesis is available in print at TU Wien Bibliothek.

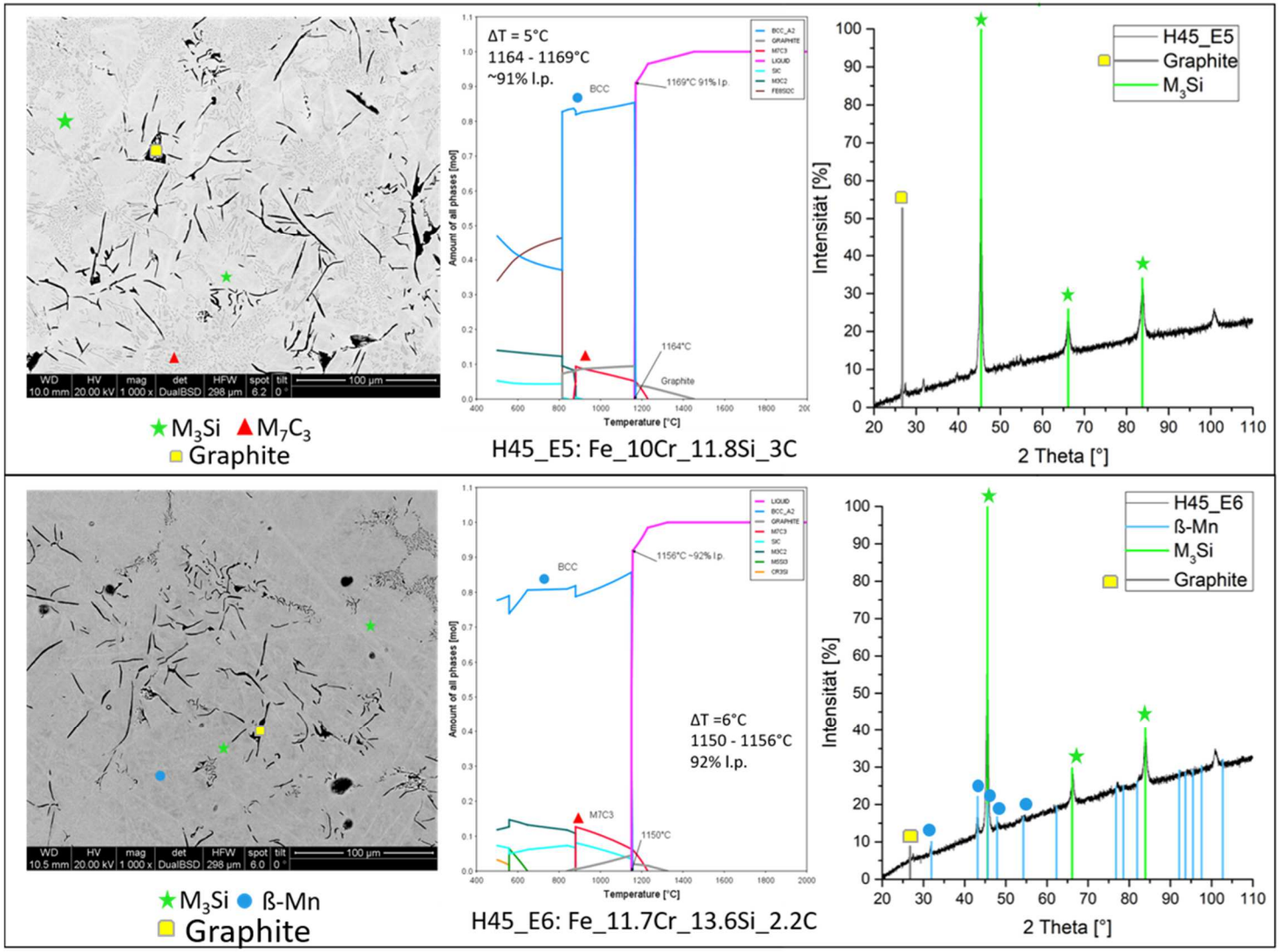

Figure 90 ***Low Cr group****: SEM x1000, EoP and XRD analysis from H45_E1 Ingot (top) and H45_E2 (bottom) M_3Si =(Fe_3Si (04-003-3871) and/or $Cr_{0.6}Fe_{2.6}Si$ (04-006-7480), ß-Mn structured phase (04-007-2059), Graphite*

Die approbierte gedruckte Originalversion dieser Diplomarbeit ist an der TU Wien Bibliothek verfügbar.
The approved original version of this thesis is available in print at TU Wien Bibliothek.

All members of the Cr family form an M_3Si, which is most likely Fe_3Si and/or $Cr_{0.6}Fe_{2.6}Si$, phase and, except H45_E5 a solid solution phase which is here described as a "ß-Mn structured phase" (which does not necessarily consist of Mn, see below!). This ß-Mn structured phase shows rather characteristic and unique peaks in the XRD which makes it rather sure to have this phase in these systems. The **low Cr group** does not show any carbides in the XRD measurements, this might explain the lack of high-temperature peaks in the DTA. According to the SEM pictures shown in Figure 90 the C forms a graphite phase. For the **Si group** an effect of Si could be obtained. While H45_E4 has the same phases as the original composition H45, the higher Si content in H45_E3 results in the formation of a different carbide. One big difference of the carbide M_7C_3 and $M_{23}C_6$ is that the M_7C_3 in H45_E4 contains no Si which can be observed with SEM mappings, while $M_{23}C_6$ in H45_E3 can contain Si.

Note: Fe_3Si is very unlikely to be a stable phase according to V.Raghavan. [64] The XRD patterns for Fe_3Si and $Cr_{0,6}Fe_{2,4}Si$ are the same. So, it is most likely to have $Cr_{0,6}Fe_{2,4}Si$ as M_3Si in the Cr family systems.

Note: ß-Mn structured phase describes a cubic phase crystallizing in ß-Mn structure. [65],[66],[67] This cubic structure type does not necessarily need Mn to be formed, [67] and it shows rather characteristic patterns in XRD diffractograms. [67] Different compositions in the ß-Mn structured phase might lead to shifts in the XRD diffractogram.

Die approbierte gedruckte Originalversion dieser Diplomarbeit ist an der TU Wien Bibliothek verfügbar.
The approved original version of this thesis is available in print at TU Wien Bibliothek.

Carbon studies for Cr family

These studies were carried out based on the observed influence of the Si content. The aim of this additional study was to clarify the effect of C on the system. Based on the findings of the chapter 3.4 Interaction with Fe this study was carried out with H45_E1 and its modifications in C content.

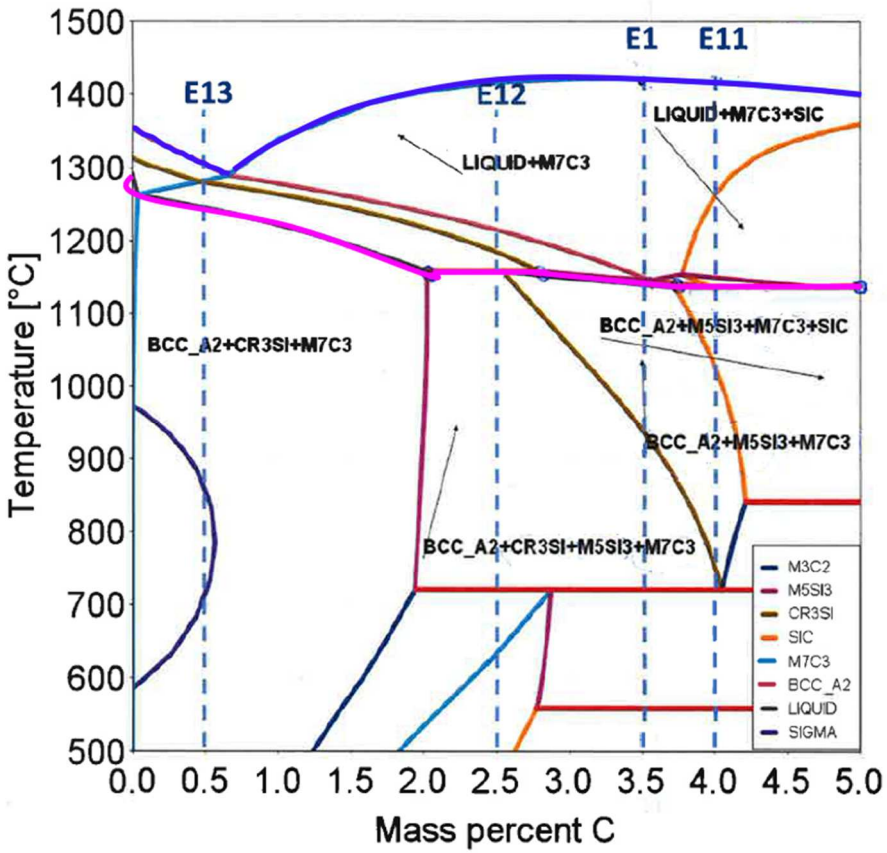

Figure 91 C content [wt%] vs temperature [°C] for H45_E1: Fe_40Cr_11Si_3.5C

H45_E11 has 0.5 %C in addition which leads to a lower solidus temperature (purple line). H45_E12 has 1.0 %C less than H45_E1 leading to another solidus line at slightly higher temperatures. H45_E13 is the lowest possible C content for the powder production process. These three modifications step through the C content by fixing all the other alloying elements. Based on these calculations these modifications were melted under different conditions to achieve full homogeneity.

The powder mixes were prepared from the original H45 MA with additional elemental powders. For this study the powders were molten at 1460°C in a vacuum furnace. Cr has a relatively high vapour pressure at these temperatures, so it was reasonable to control the composition of the molten ingots, finding 0.5 % C losses for H45_E11 and H45_E1 but in comparison no huge differences in the Cr composition.

Table 8 Ingot composition determined with combined SEM and LECO measurement

Code	Fe [wt%]	Cr [wt%]	Si [wt%]	C [wt%]
H45_E11	43,54	38,48	11,14	3,40
H45_E1	42,66	40,53	10,67	2,97
H45_E12	45,24	38,65	11,31	2,47
H45_E13	49,11	40,57	9,61	0,34

Die approbierte gedruckte Originalversion dieser Diplomarbeit ist an der TU Wien Bibliothek verfügbar.
The approved original version of this thesis is available in print at TU Wien Bibliothek.

Table 9 shows the composition measured with XRF and SEM. The C content was determined with Leco measurements. EDX measurements show compositions close to the theoretical composition, while XRF measurements show differences in the Cr content. These differences might be related to evaporation losses during the melting of the ingot. Added elemental Cr seems to lead to higher losses. Surprisingly there is no difference in the Cr content between the H45_E1 sample molten in the vacuum furnace at 1460°C and the H45_E1 sample molten at 1300°C under Ar/10 %H_2. The Si content differs which as well might be related as well to losses from elemental Si additions. The compositions are shown in Table 7.

Note: Losses of alloying elements during the heating stage might not occur if the MA used as provided for finely distributed in Fe powder.

Table 9 Composition of the Cr family ingots.

	Theory	45	40	0,0	11	4
H45_E11	EDX	43,54	38,5	0,0	11,1	3,4
	XRF	57,7	33,5	0,1	8,3	3,40
	Theory	45,5	40,0	0,0	11,0	3,5
H45_E1	EDX	42,66	40,5	0,0	10,7	3,0
	XRF	57,6	33,6	0,2	8,0	2,97
	Theory	46,5	40	0,0	11	2,5
H45_E12	EDX	45,24	38,65	0,0	11,3	2,47
	XRF	58,1	32,9	0,1	8,4	2,13
	Theory	48,5	40	0,0	11	0,5
H45_E13	EDX	49,11	40,6	0,0	9,6	0,34
	XRF	57,3	33,5	0,2	8,4	0,34

Die approbierte gedruckte Originalversion dieser Diplomarbeit ist an der TU Wien Bibliothek verfügbar.
The approved original version of this thesis is available in print at TU Wien Bibliothek.

- **Melting behaviour**

Looking at Figure 92 it is clear to see that from H45_E11 to H45_E12 the melting range tightens but the solidus temperature increases. The low C system H45_E13 shows a different behaviour overall. For this modification ThermoCalc predictions and DTA results do not fit together.

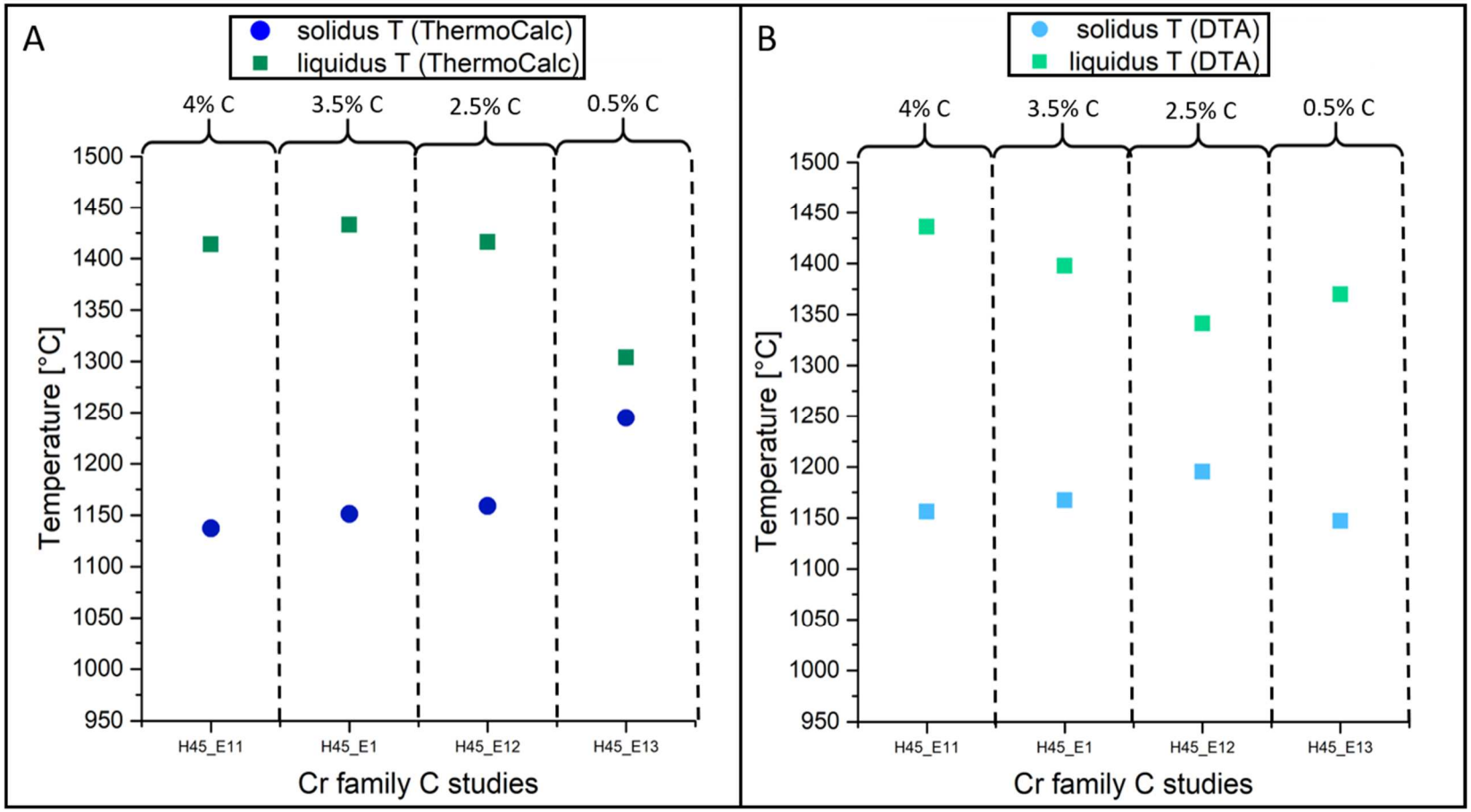

*Figure 92 Comparing solidus and liquidus temperatures predicted from ThermoCalc (**A**) and measured with DTA (**B**) for the Cr family H45_E1 studies*

Die approbierte gedruckte Originalversion dieser Diplomarbeit ist an der TU Wien Bibliothek verfügbar.
The approved original version of this thesis is available in print at TU Wien Bibliothek.

Figure 93 shows the DTA measurement of the C studies for the Cr family. The DTA measurement shows that with increasing C content the solidus temperature decreases by broadening up the melting range. The low C modification H45_E13 shows a completely different behaviour to the other systems. The infiltration and wetting experiments were still carried out at 1300°C under Ar/10 %H_2 where H45_E13 seems to be barely molten.

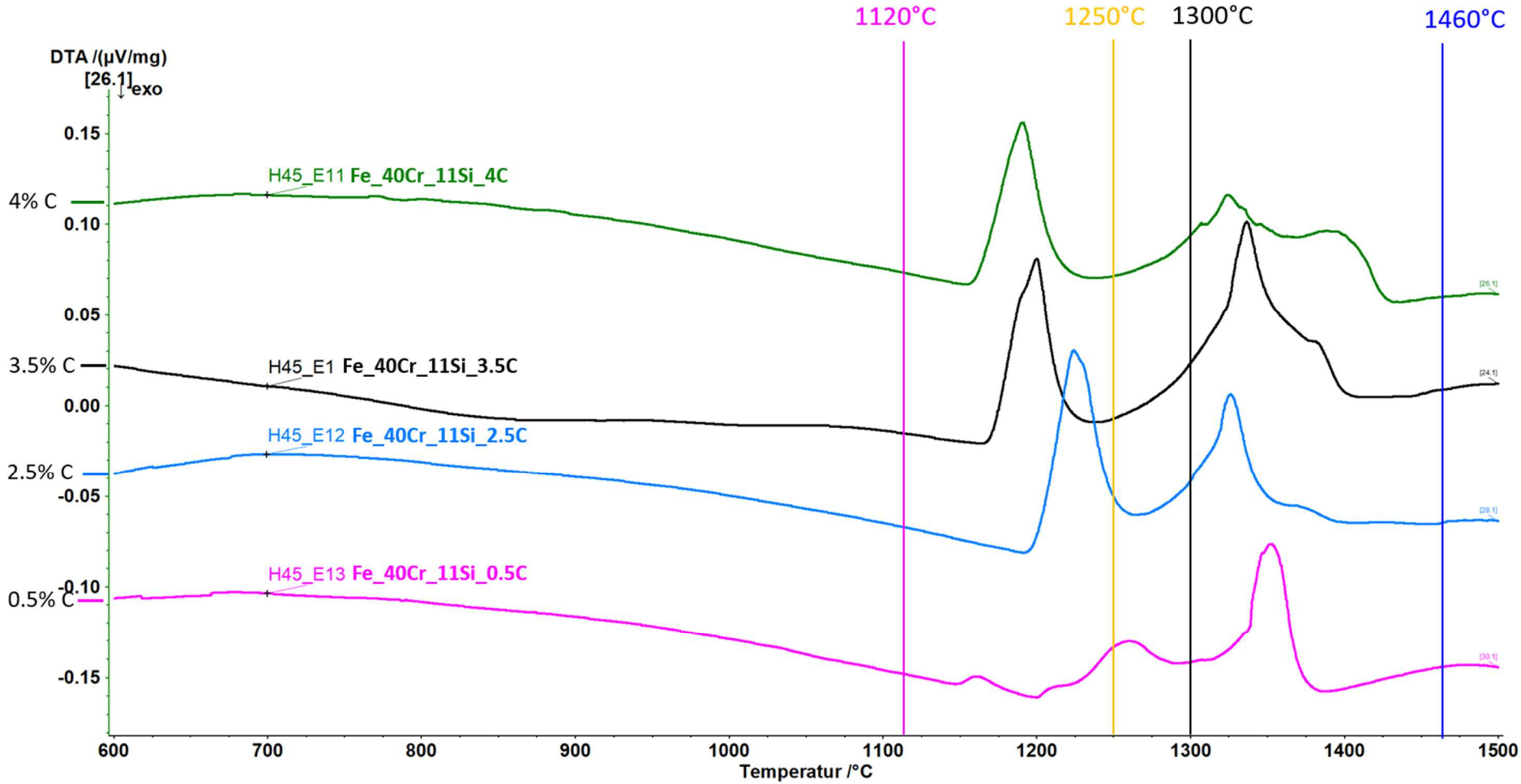

Figure 93 DTA for Cr family C studies with H45_E1 modifications, heating phase

Die approbierte gedruckte Originalversion dieser Diplomarbeit ist an der TU Wien Bibliothek verfügbar.
The approved original version of this thesis is available in print at TU Wien Bibliothek.

Stable phases

With lower C content, the amount of carbide decreases as well. All modifications form a ß-Mn structured phase[65], M_3Si, either Fe_3Si and/or $Cr_{0.6}Fe_{2.6}Si$ and Cr_3Si phases. H45_E13 does not form carbides or M5Si3 and shows up with a completely different microstructure which fits to its different behaviour in DTA.

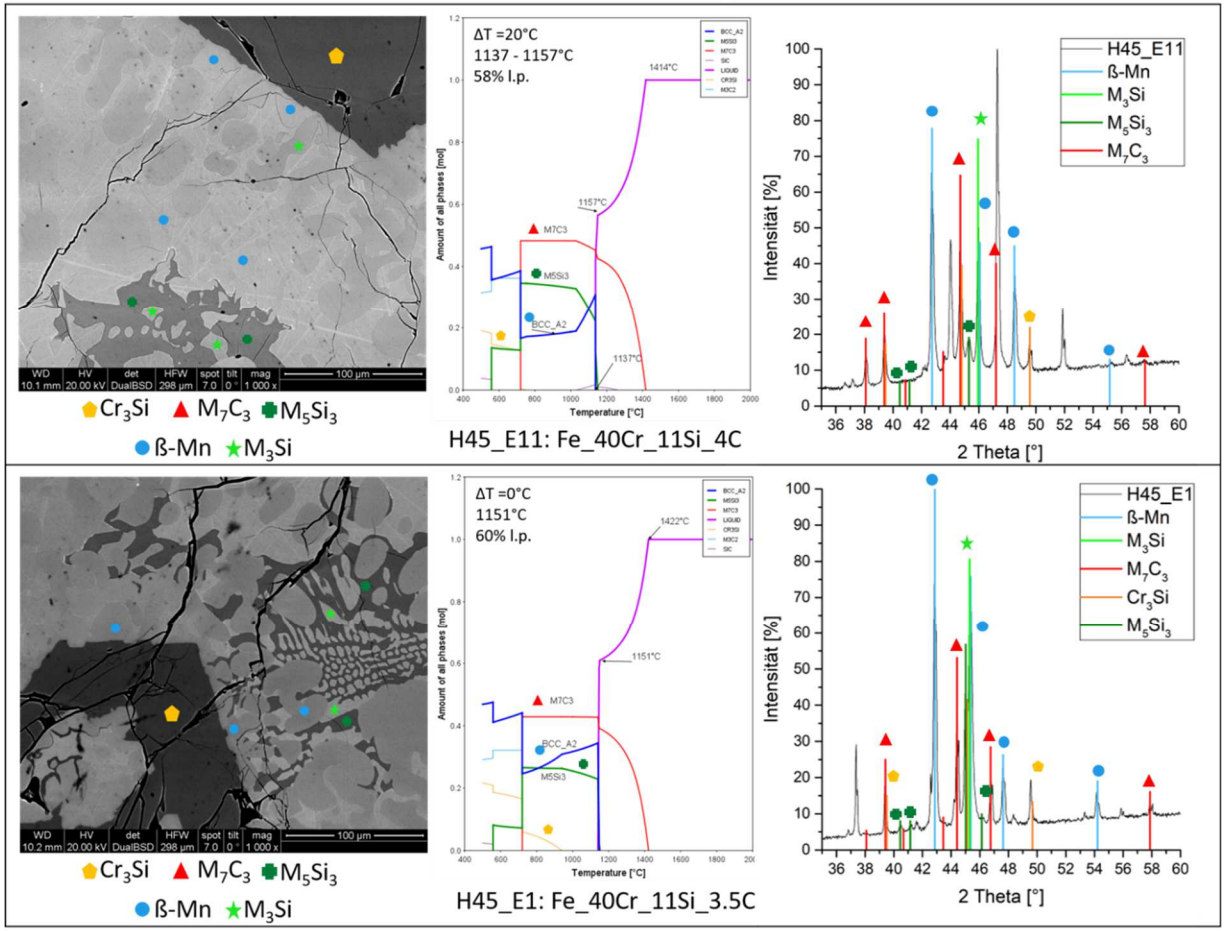

Figure 94 ***H45_E1 studies****: SEM x1000, EoP and XRD analysis from H45_E11 Ingot (4% C) (top) and H45_E1 (3.5% C) (bottom) Phase references: M7C3 (04-017-0806), M3Si =(Fe3Si (04-003-3871) and/or Cr0.6Fe2.6Si (04-006-7480), Cr3Si (04-001-2815), ß-Mn structured phase (04 007 2059), M5Si3 (04-004-3035)*

Die approbierte gedruckte Originalversion dieser Diplomarbeit ist an der TU Wien Bibliothek verfügbar.
The approved original version of this thesis is available in print at TU Wien Bibliothek.

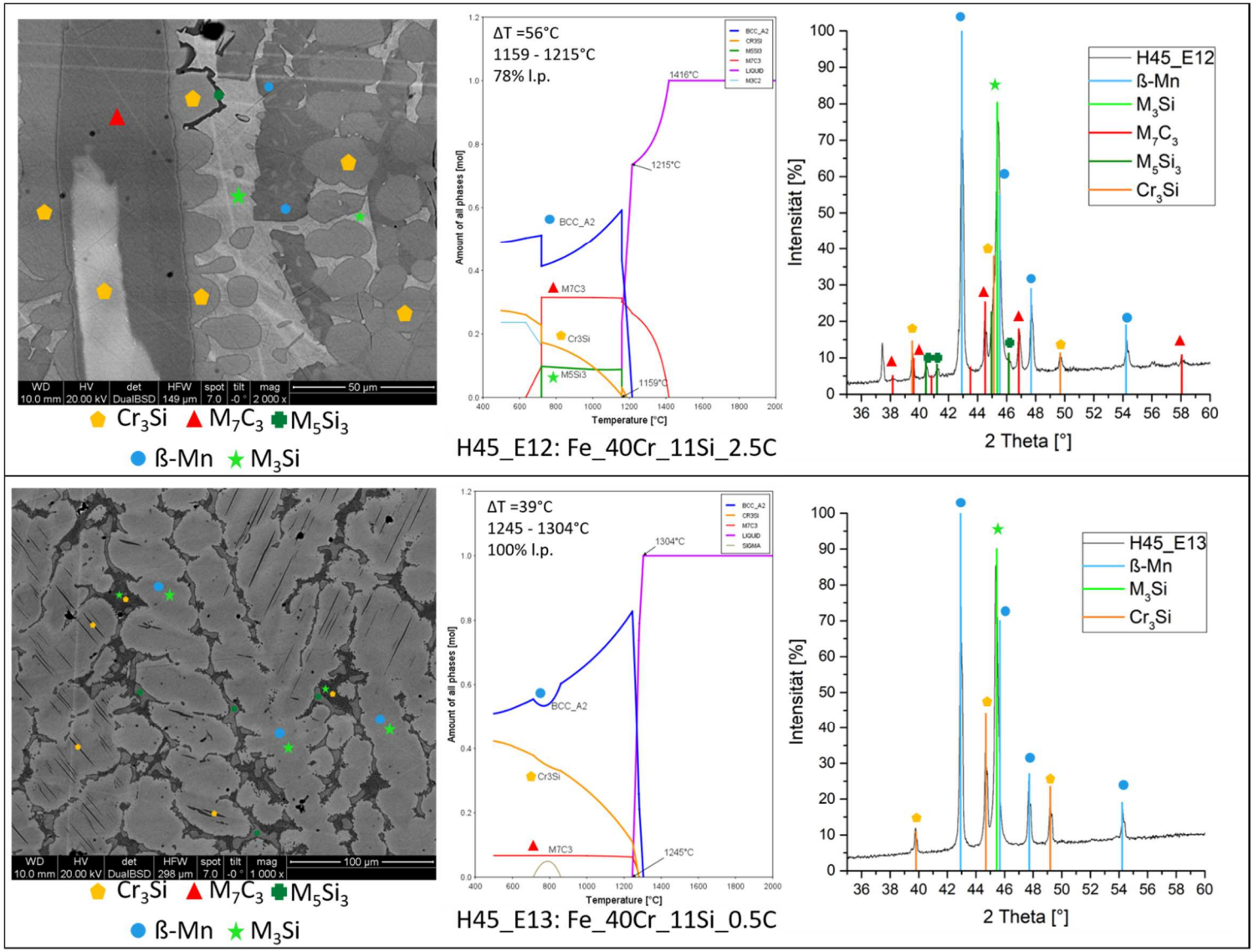

Figure 95 ***H45_E1 studies****: SEM x1000, EoP and XRD analysis from H45_E12 Ingot* ***(2.5% C)*** *(top) and H45_E3* ***(0.5% C)*** *(bottom)* ***Phase references:*** *M_7C_3 (04-017-0806), M_3Si =(Fe_3Si (04-003-3871) and/or $Cr_{0.6}Fe_{2.6}Si$ (04-006-7480), Cr_3Si (04-001-2815), ß-Mn structured phase (04 007 2059), M5Si3 (04-004-3035)*

3.3.2 Mn family

Table 10 shows the composition of the Mn family modifications determined with XRF and EDX. C content was determined via Leco measurements. It looks like the Mn family modifications contain a certain amount of Cr which comes from the powder production process. EDX measurements show compositions close to the theoretical composition. H46 shows a remarkable Mn loss in EDX measurements. XRF measurements shows a much bigger Mn loss for all Mn family modifications. Mn might be lost due to evaporation due to the same reason Cr is lost in Cr family. The evaporation is dependent on several factors as the formation of oxides, a possible diffusion of Mn into other elements of the powder mix or a dissolution in a formed melt. Mn evaporation takes place at a much earlier stage compared to Cr evaporation due to a much higher vapour pressure; This might be a reason for higher Mn losses.

Note: Losses of alloying elements during the heating stage might not occur if the MA used as provided for finely distributed in Fe powder.

Table 10 Composition of the Mn family ingots.

		Fe [wt%]	Cr [wt%]	Mn [wt%]	Si [wt%]	C [wt%]
	Theory	51,6	0	42	6	0,4
H46	EDX	58,6	4,0	29,0	8,0	0,4
	XRF	67,23	2,13	21,32	7,27	0,4
	Theory	51,1	0	41	5,9	2
H46_E1	EDX	49,6	5,0	37,0	6,0	2,43
	XRF	64,49	2,32	24,69	7,27	2,43
	Theory	56,1	0,0	33,0	7,5	3,4
H46_E2	EDX	59,2	3,0	29,0	6,0	2,82
	XRF	68,41	1,60	21,50	6,41	2,82
	Theory	61,9	0,0	30,0	5,0	3,1
H46_E3	EDX	63,7	3,0	25,0	5,0	3,30
	XRF	73,19	1,69	17,87	5,20	3,00
	Theory	48,0	0,0	40,0	9,0	3,00
H46_E4	EDX	49,9	3,0	36,0	8,0	3,05
	XRF	62,16	1,83	25,98	7,92	3,05
	Theory	58,0	0,0	30,0	9,0	3,00
H46_E5	EDX	56,0	3,0	27,0	11,0	3,00
	XRF	67,20	1,40	19,32	10,09	3,00

Die approbierte gedruckte Originalversion dieser Diplomarbeit ist an der TU Wien Bibliothek verfügbar.
The approved original version of this thesis is available in print at TU Wien Bibliothek.

Die approbierte gedruckte Originalversion dieser Diplomarbeit ist an der TU Wien Bibliothek verfügbar.
The approved original version of this thesis is available in print at TU Wien Bibliothek.

Melting behaviour

Figure 96 compares ThermoCalc calculations with DTA measurements, finding a good relation for ST for base powder and the high Mn group, while the differences for the low Mn group are higher. For the Mn family the LT is underestimated from ThermoCalc. It is remarkable that these modifications of H46 seem to be fully molten below 1150°C.

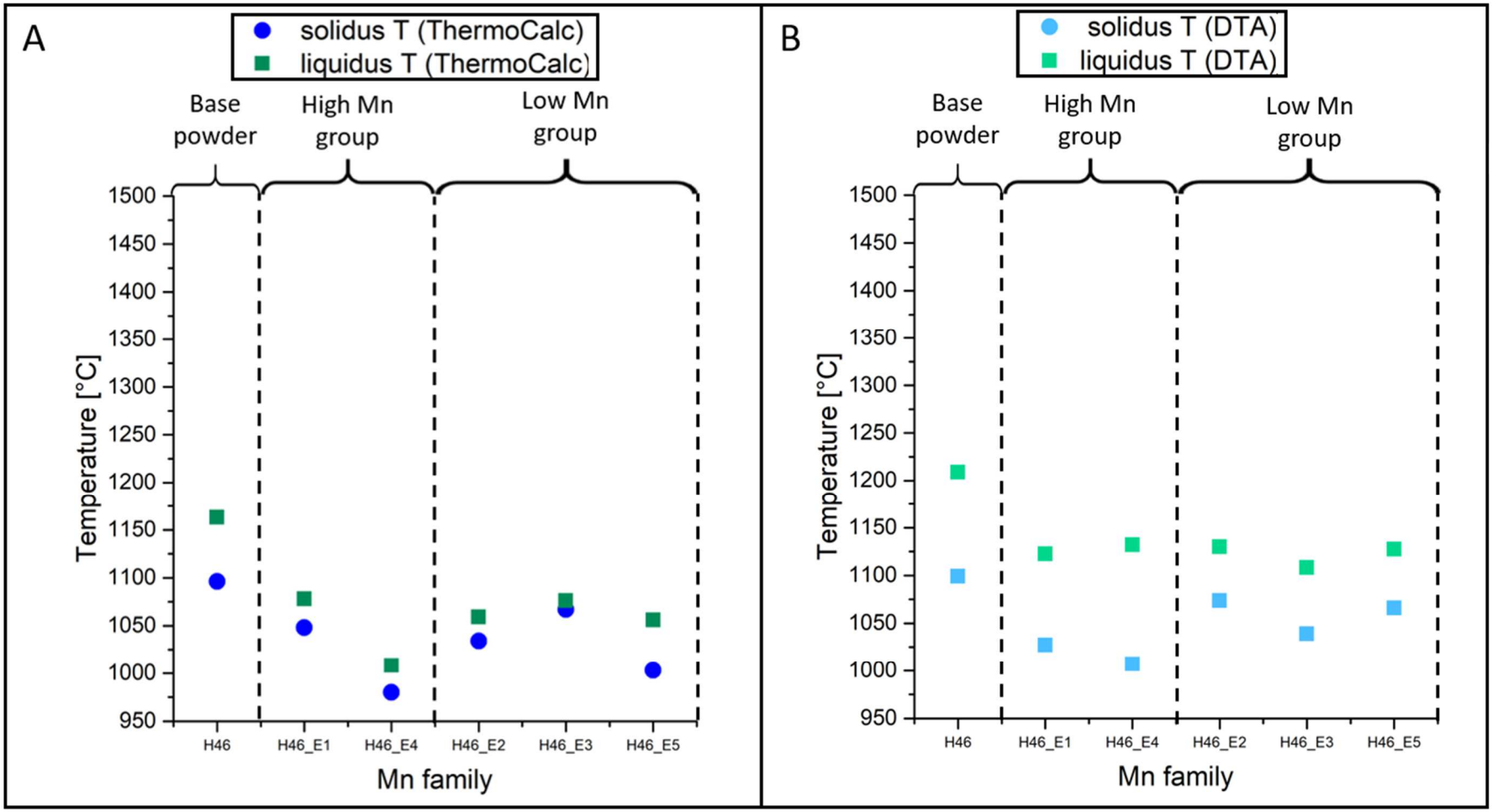

*Figure 96 Comparing solidus and liquidus temperatures predicted from ThermoCalc (**A**) and measured with DTA (**B**) for the Mn family*

Die approbierte gedruckte Originalversion dieser Diplomarbeit ist an der TU Wien Bibliothek verfügbar.
The approved original version of this thesis is available in print at TU Wien Bibliothek.

Figure 97 shows the DTA measurement of the Mn family. Increasing the C content leads to lower melting temperatures in this family. Varying the other alloying elements with higher C does not seem to have a big influence on the melting behaviour. The Mn family will be fully molten at 1300°C at which temperature the infiltration and wetting experiments are carried out.

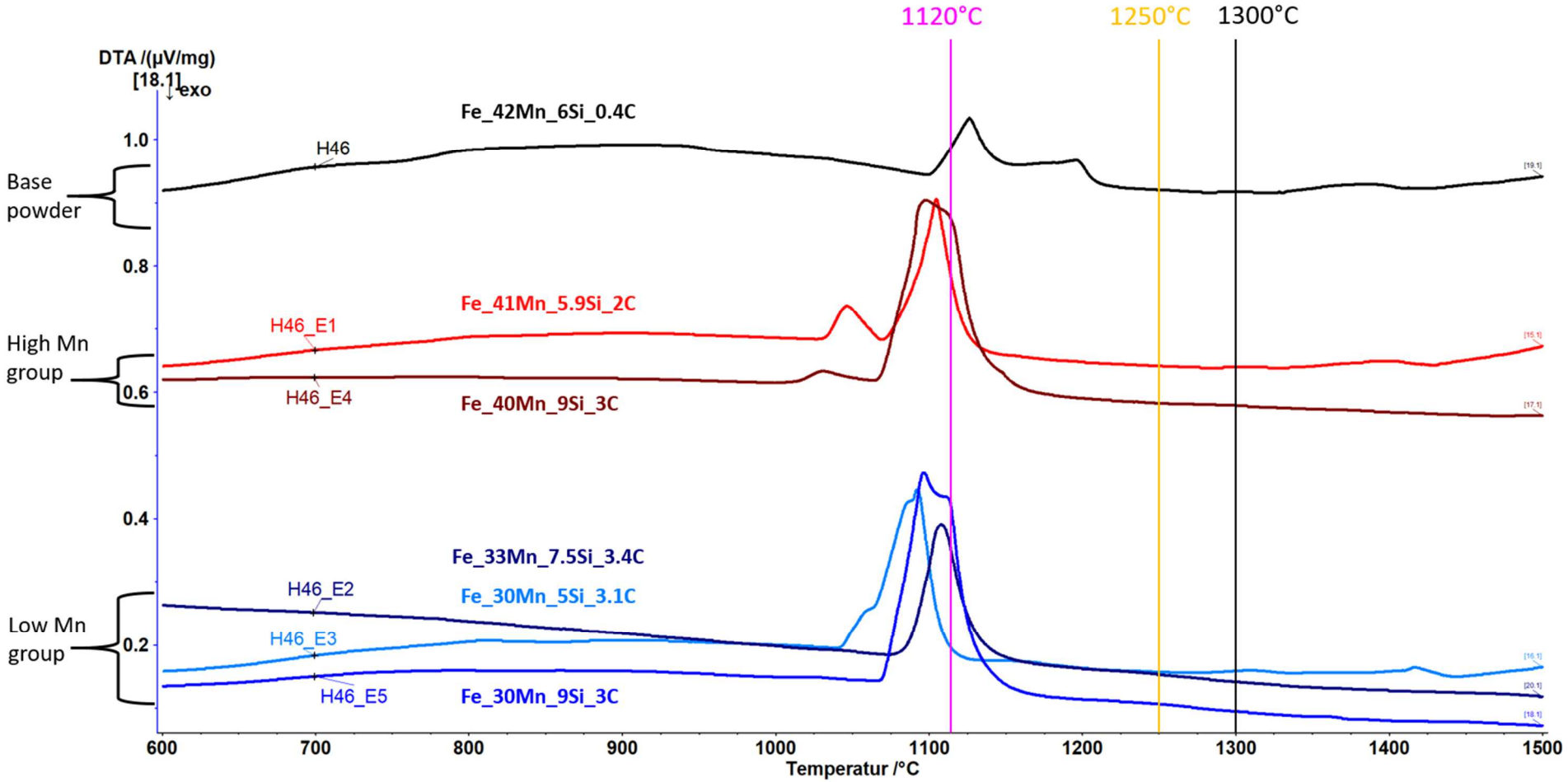

Figure 97 DTA for Mn family, heating phase

Die approbierte gedruckte Originalversion dieser Diplomarbeit ist an der TU Wien Bibliothek verfügbar.
The approved original version of this thesis is available in print at TU Wien Bibliothek.

- **Stable phases**

Figure 98 to Figure 101 show SEM measurements of the Mn family ingots, XRD measurements of milled ingots and the predicted evolution of phases (EoP) from ThermoCalc. Linking the phases measured in XRD to those found in SEM is supported by several spot analysis measurements and elemental mappings. All modifications form a M_3Si, Fe_3Si and/or Fe_2MnSi, and a ß-Mn structured phase [65] which is considered as a solid solution phase. All modifications besides the original H46 have a higher C content and form different types of carbides. The whole Mn family shows a very fine microstructure compared to the other families, which might be related to the lower melting temperatures of all modifications.

Note: Fe_3Si is very unlikely to be a stable phase according to V.Raghavan. [64] The XRD patterns for Fe_3Si and Fe_2MnSi are the same. So, it is most likely to have Fe_2MnSi as M_3Si in the Mn family systems.

Note: ß-Mn structured phase describes a cubic phase crystalizing in ß-Mn structure. [65],[66],[67] This cubic structure type does not necessarily need Mn to be formed, [67] and it shows rather characteristic patterns in XRD diffractograms. [67] Different compositions in the ß-Mn structured phase might lead to shifts in the XRD diffractogram.

Die approbierte gedruckte Originalversion dieser Diplomarbeit ist an der TU Wien Bibliothek verfügbar.
The approved original version of this thesis is available in print at TU Wien Bibliothek.

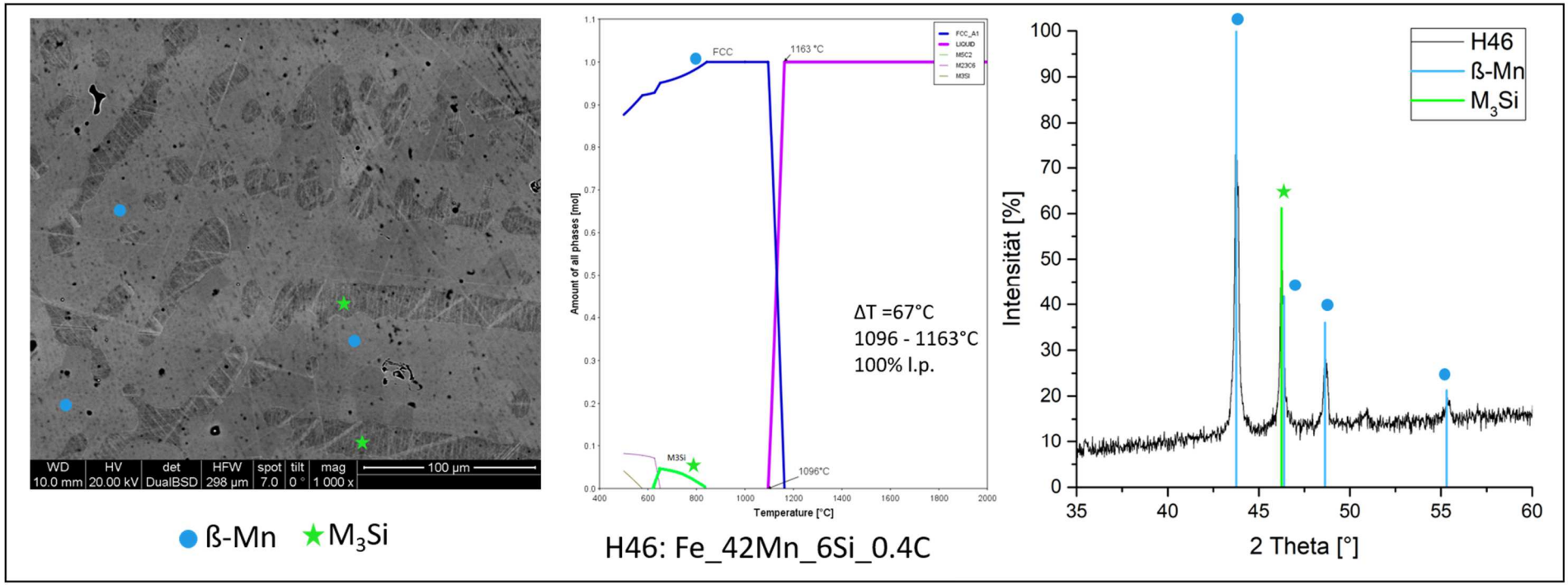

Figure 98 ***original composition*** *SEM x1000, EoP and XRD analysis from H46 Ingot* ***Phase references:*** *M_3Si = (Fe_3Si (04-003-3871) and/or Fe_2MnSi (01-077-7953)), ß-Mn structured phase (04 007 2059)*

Die approbierte gedruckte Originalversion dieser Diplomarbeit ist an der TU Wien Bibliothek verfügbar.
The approved original version of this thesis is available in print at TU Wien Bibliothek.

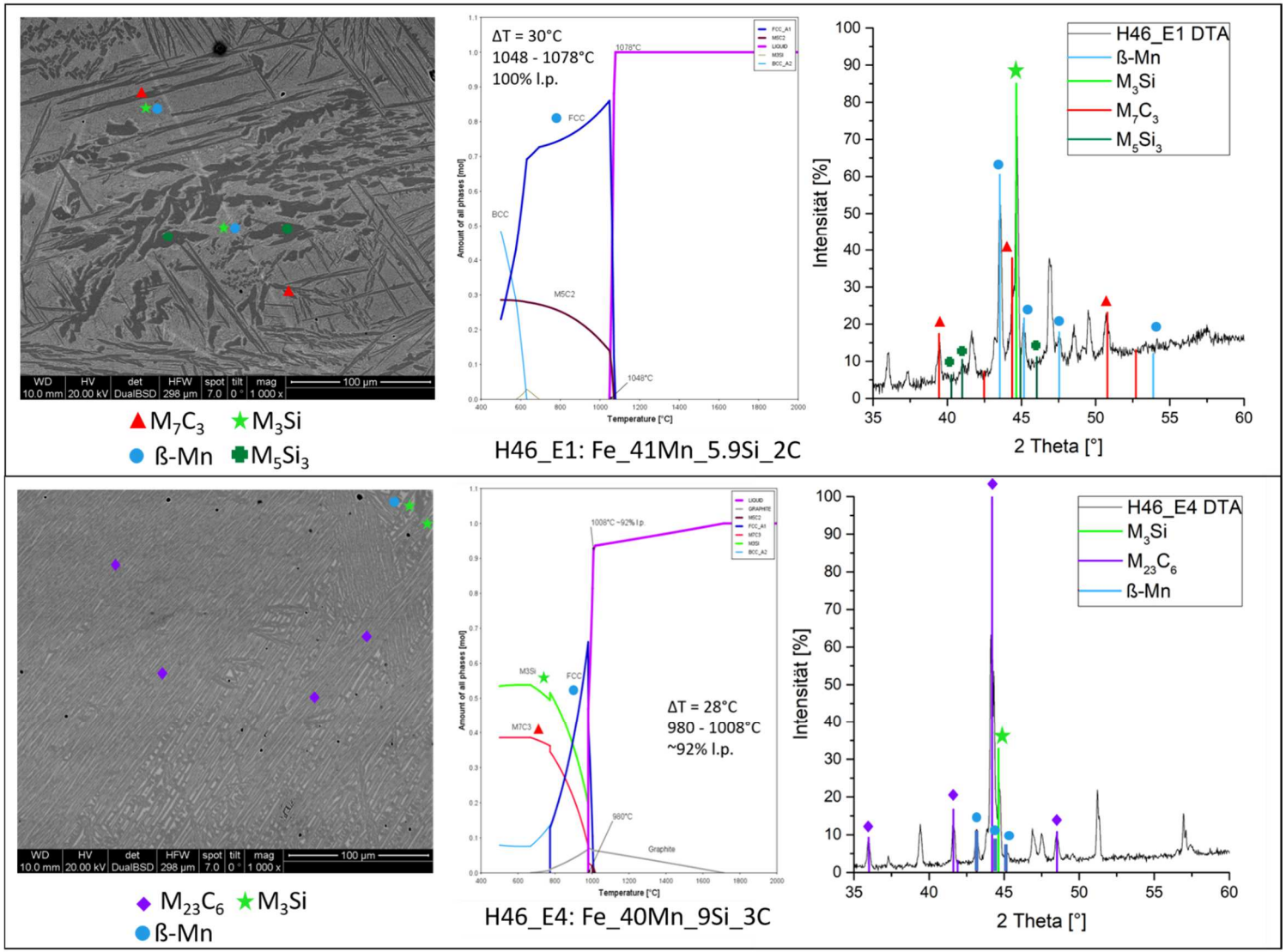

Figure 99 ***High Mn group****: SEM x1000, EoP and XRD analysis from H46_E1 Ingot (top) and H46_E4 (bottom)* ***Phase references: :*** *M_3Si = (Fe_3Si (04-003-3871) and/or Fe_2MnSi (01-077-7953)), ß-Mn structured phase (04 007 2059), M_7C_3 (04-017-0806), M5Si3 (04-004-3035), $M_{23}C_6$ (04-003-6076*

Die approbierte gedruckte Originalversion dieser Diplomarbeit ist an der TU Wien Bibliothek verfügbar.
The approved original version of this thesis is available in print at TU Wien Bibliothek.

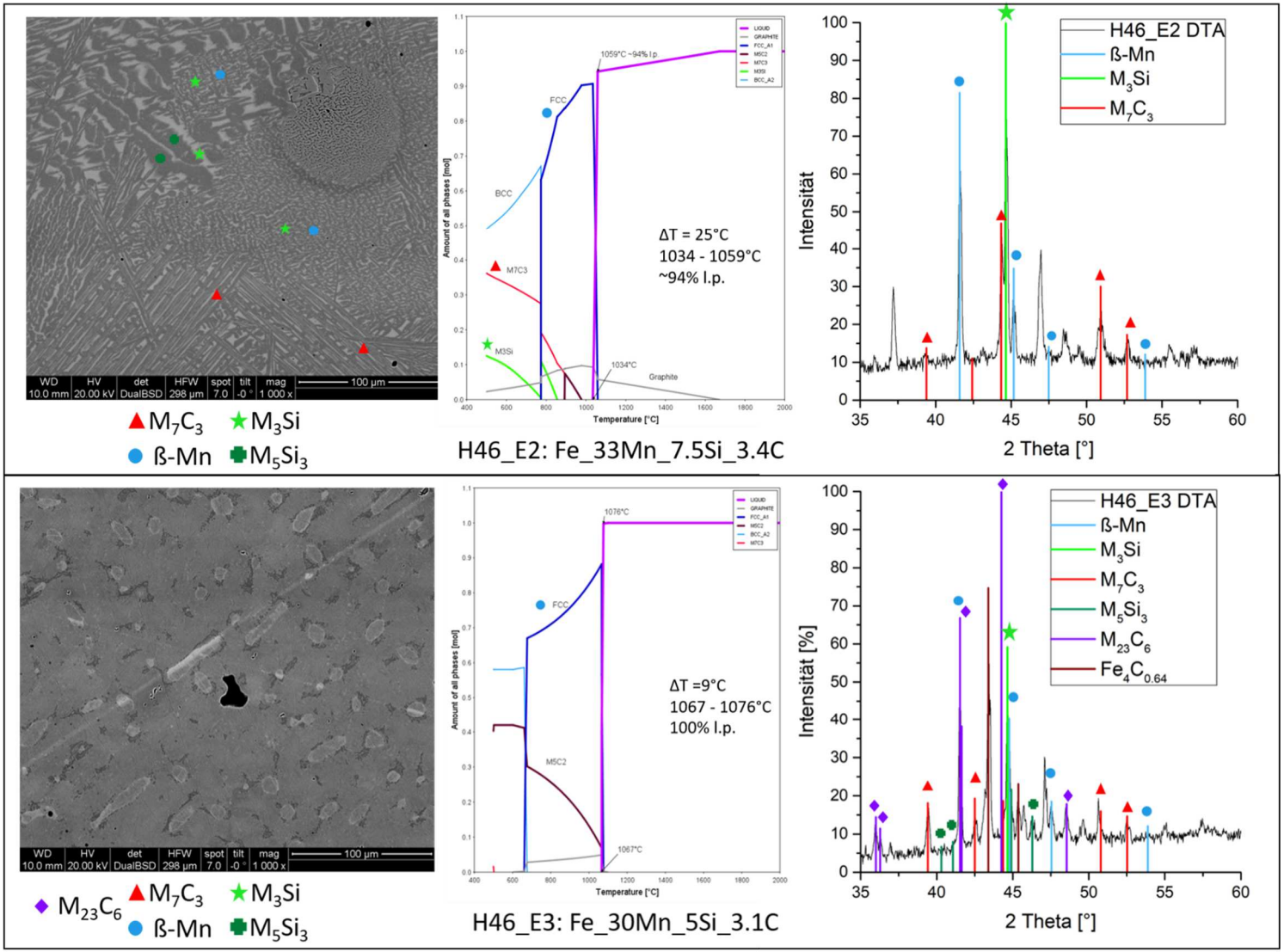

Figure 100 ***Low Mn group****: SEM x1000, EoP and XRD analysis from H46_E2 Ingot (top) and H46_E3 (bottom)* ***Phase references: :*** *M_3Si = (Fe_3Si (04-003-3871) and/or Fe_2MnSi (01-077-7953)), ß-Mn structured phase (04 007 2059), M_7C_3 (04-017-0806), M5Si3 (04-004-3035), $M_{23}C_6$ (04-003-6076, $Fe_4C_{0.64}$ (01-071-1174)*

Die approbierte gedruckte Originalversion dieser Diplomarbeit ist an der TU Wien Bibliothek verfügbar.
The approved original version of this thesis is available in print at TU Wien Bibliothek.

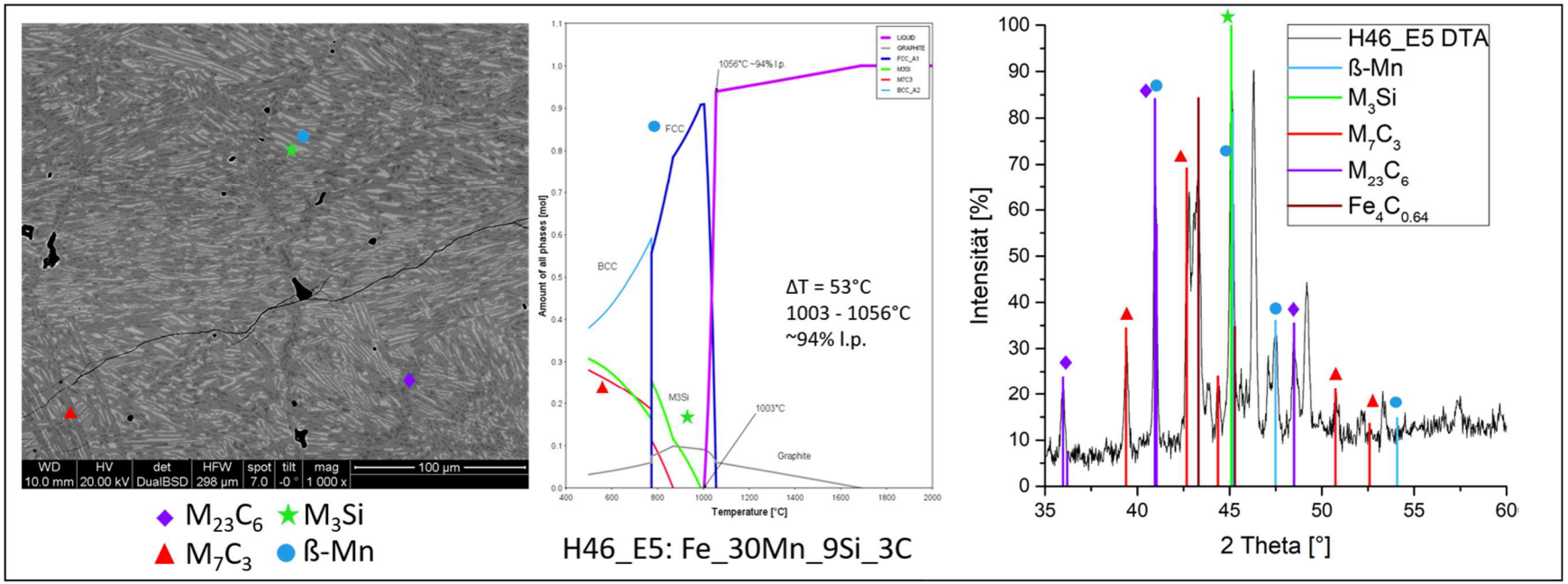

Figure 101 ***Low Mn group:*** *SEM x1000, EoP and XRD analysis from H46_E5 Ingot* ***Phase references: :*** *M_3Si = (Fe_3Si (04-003-3871) and/or Fe_2MnSi (01-077-7953)), ß-Mn structured phase (04 007 2059), M_7C_3 (04-017-0806), $M_{23}C_6$ (04-003-6076, $Fe_4C_{0.64}$ (01-071-1174)*

3.3.3 Cr-Mn family

Table 11 shows the composition of the Cr-Mn family modifications determined with XRF and EDX. C content was determined via Leco measurements. EDX measurements show compositions close to the theoretical composition. Differences in Mn content between 3-5 wt% might be related to evaporation losses during the ingot production. XRF measurements show a huge Mn loss as well and in addition bigger differences in Cr content as determined with EDX. These differences might be related to evaporation losses during the ingot production as described in the Cr family and the Mn family. Elemental additions seem to lead to higher losses than from the MA base powder.

Note: Losses of alloying elements during the heating stage might not occur if the MA used as provided for finely distributed in Fe powder.

Table 11 Composition of the Cr-Mn family ingots.

Code		Fe	Cr	Mn	Si	C
	Theory	35,3	27,0	28,0	6,0	3,7
H47	EDX	33,2	25,0	29,0	9,0	3,8
	XRF	41,09	23,40	22,61	10,44	3,80
	Theory	36,2	14,0	35,0	11,0	3,8
H47_E1	EDX	40,2	16,0	30,0	10,0	3,8
	XRF	48,81	10,76	25,51	12,70	2,67
	Theory	30,0	21,0	38,0	8,0	3,0
H47_E2	EDX	33,3	22,0	33,0	9,0	2,7
	XRF	41,71	16,87	28,39	10,46	2,72
	Theory	39,0	12,0	35,0	12,0	2,0
H47_E3	EDX	42,8	14,0	30,0	12,0	1,2
	XRF	51,44	9,64	24,46	12,21	1,21
	Theory	34,0	27,0	28,0	6,0	5,0
H47_E4	EDX	37,8	29,0	22,0	7,0	4,2
	XRF	38,82	18,97	24,43	14,66	4,16
	Theory	37,5	10,0	40,0	12,0	0,5
H47_E5	EDX	44,4	12,0	32,0	11,0	0,6
	XRF	51,16	7,98	26,30	12,56	0,63

Die approbierte gedruckte Originalversion dieser Diplomarbeit ist an der TU Wien Bibliothek verfügbar.
The approved original version of this thesis is available in print at TU Wien Bibliothek.

Die approbierte gedruckte Originalversion dieser Diplomarbeit ist an der TU Wien Bibliothek verfügbar.
The approved original version of this thesis is available in print at TU Wien Bibliothek.

- **Melting behaviour**

Figure 102 compares ThermoCalc predictions and DTA measurements of the ingots. For the Cr-Mn family the predictions were not very accurate.

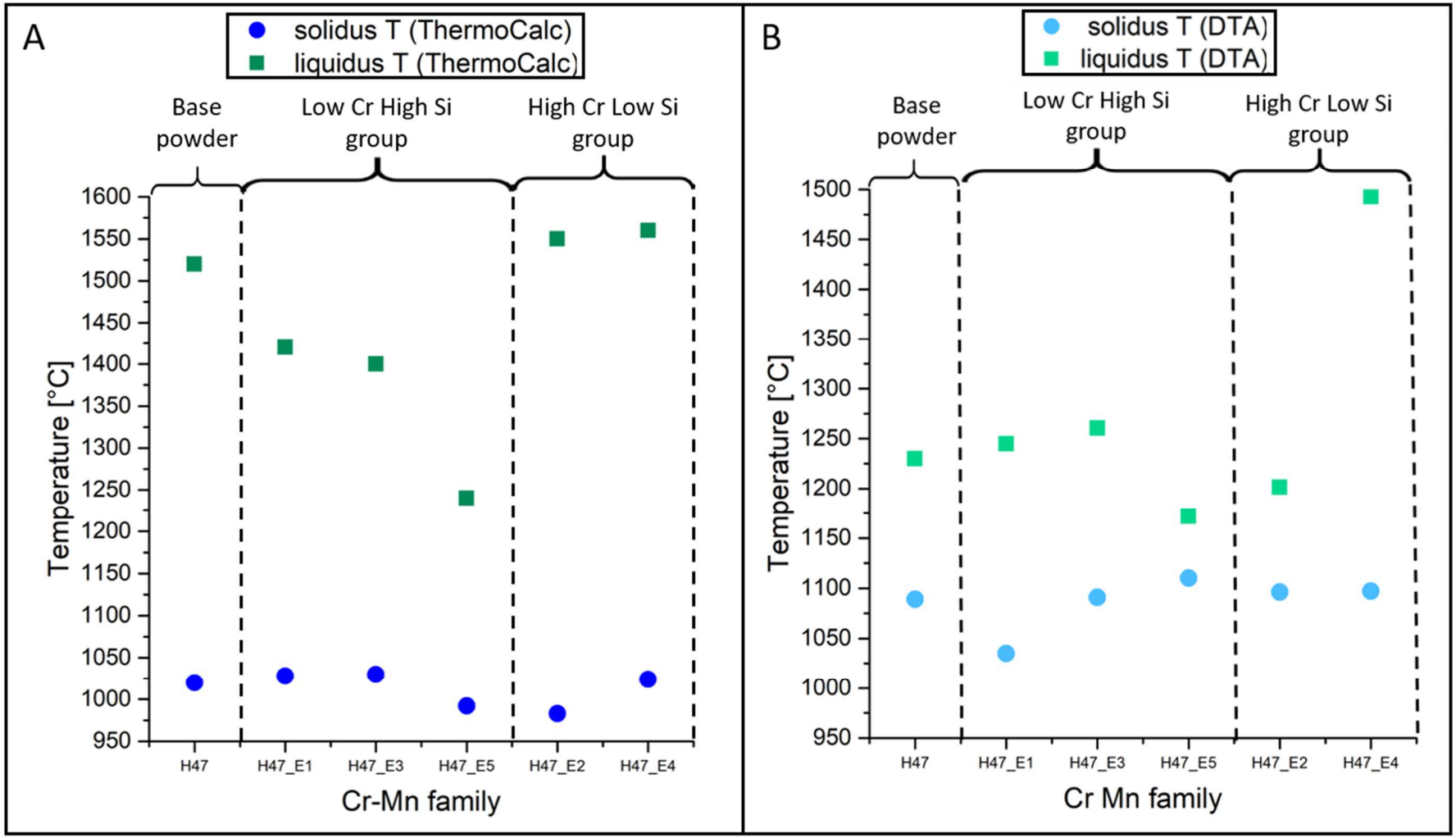

*Figure 102 Comparing solidus and liquidus temperatures predicted from ThermoCalc (**A**) and measured with DTA (**B**) for the Cr-Mn family*

Die approbierte gedruckte Originalversion dieser Diplomarbeit ist an der TU Wien Bibliothek verfügbar.
The approved original version of this thesis is available in print at TU Wien Bibliothek.

Figure 103 shows the DTA measurement of the Cr-Mn family. **The low Cr high Si group** shows a similar behaviour as obtained in the C studies of the Cr family. By increasing the C content the melting temperature is reduced but the melting range broadens. H47_E4 is just an increase of the C content from the original composition. This increase leads to an evident shift of the endothermal reactions to higher temperatures. H47_E2 shows a rather similar DTA to the original composition but slightly lower melting temperatures and a tigther melting window.

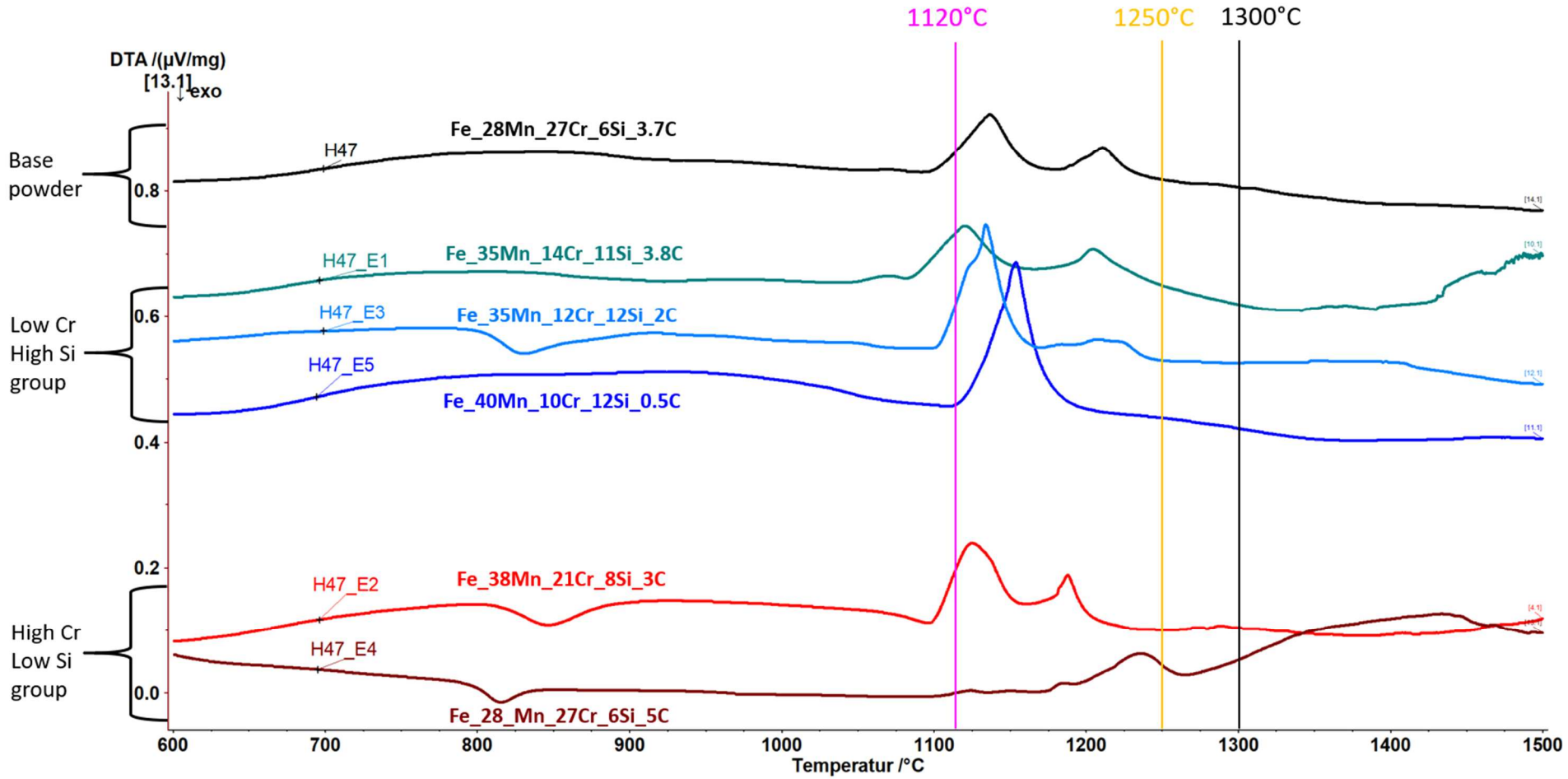

Figure 103 DTA for Cr - Mn family, heating phase

Die approbierte gedruckte Originalversion dieser Diplomarbeit ist an der TU Wien Bibliothek verfügbar.
The approved original version of this thesis is available in print at TU Wien Bibliothek.

- **Stable phases**

Figure 104 to Figure 107 show SEM measurements of the Cr-Mn family ingots, XRD measurements of milled ingots and the predicted evolution of phases (EoP) from ThermoCalc. Although the Cr-Mn family contains an additional element the formed phases get less complicated. All modifications of this family form M_3Si, either Fe_3Si and/or $Cr_{0.6}Fe_{2.4}Si$ and/or Fe_2MnSi, and a ß-Mn structured phase [65], which is considered as a solid solution phase. The modifications H47_E3 and H47_E5 do not form a carbide, while the other modifications form a M_7C_3 carbide, most likely $Fe_{3,5}Cr_{3,5}C_3$.

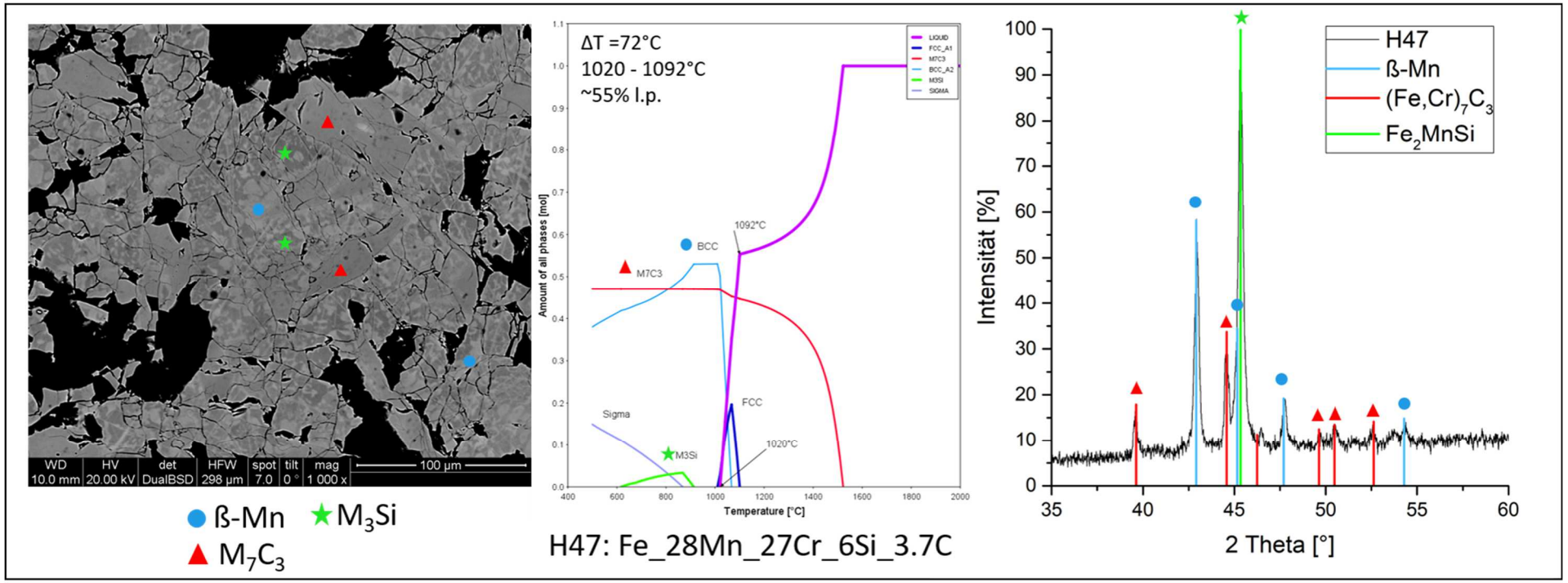

Figure 104 ***original composition*** *SEM x1000, EoP and XRD analysis from H47 Ingot* ***Phase references:*** *M_3Si = (Fe_3Si (04-003-3871) and/or Fe_2MnSi (01-077-7953) and/or $Cr_{0.6}Fe_{2.4}Si$ (04-006-7480)), ß-Mn structured phase (04 007 2059), M_7C_3 (04-017-0806)*

Die approbierte gedruckte Originalversion dieser Diplomarbeit ist an der TU Wien Bibliothek verfügbar.
The approved original version of this thesis is available in print at TU Wien Bibliothek.

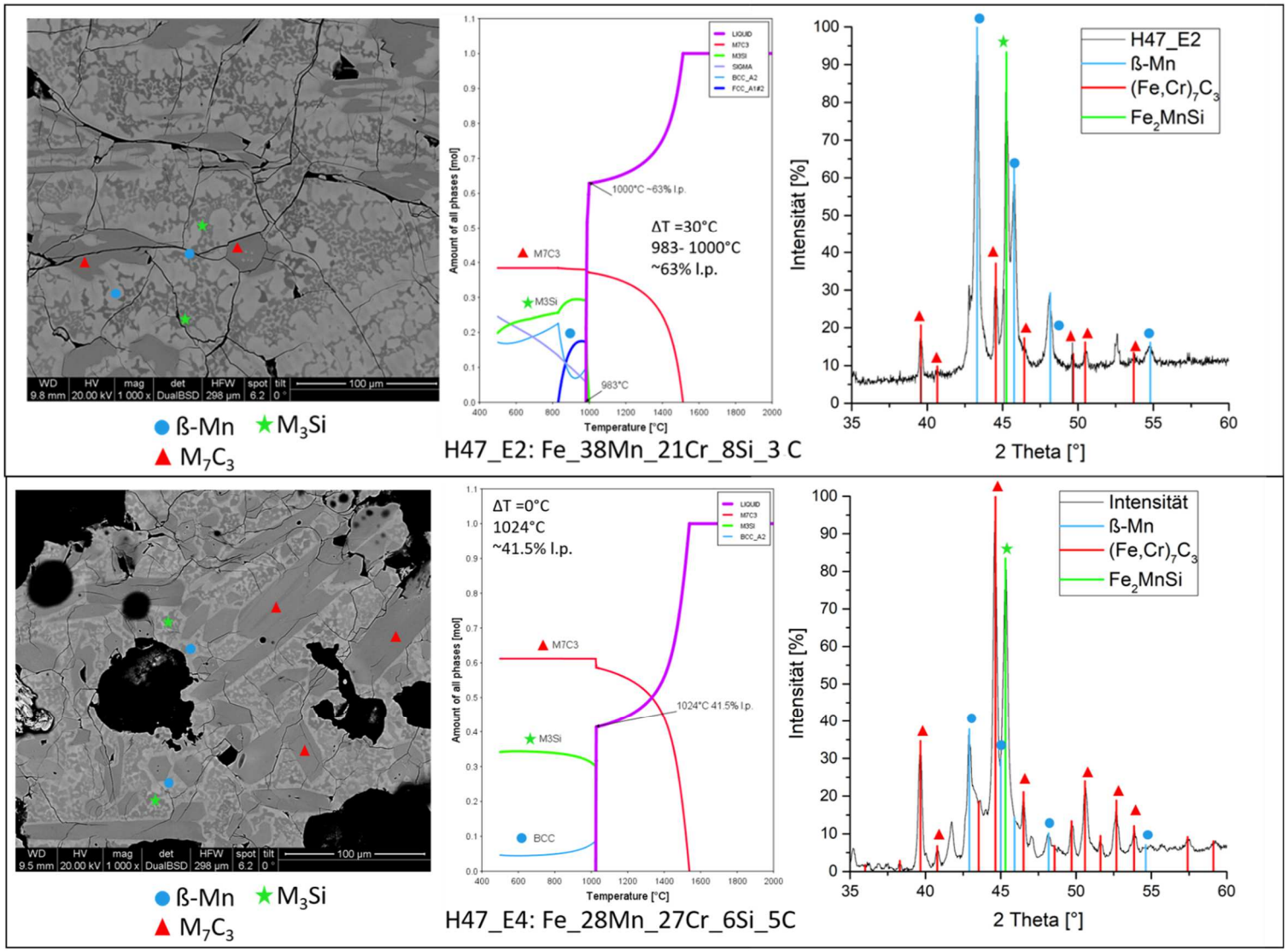

Figure 105 ***High Cr low Si group:*** *SEM x1000, EoP and XRD analysis from H47_E2 Ingot (top) and H47_E4 (bottom)* ***Phase references:*** *M_3Si = (Fe_3Si (04-003-3871) and/or Fe_2MnSi (01-077-7953) and/or $Cr_{0.6}Fe_{2.4}Si$ (04-006-7480)) , ß-Mn structured phase (04 007 2059), M_7C_3 (04-017-0806)*

Die approbierte gedruckte Originalversion dieser Diplomarbeit ist an der TU Wien Bibliothek verfügbar.
The approved original version of this thesis is available in print at TU Wien Bibliothek.

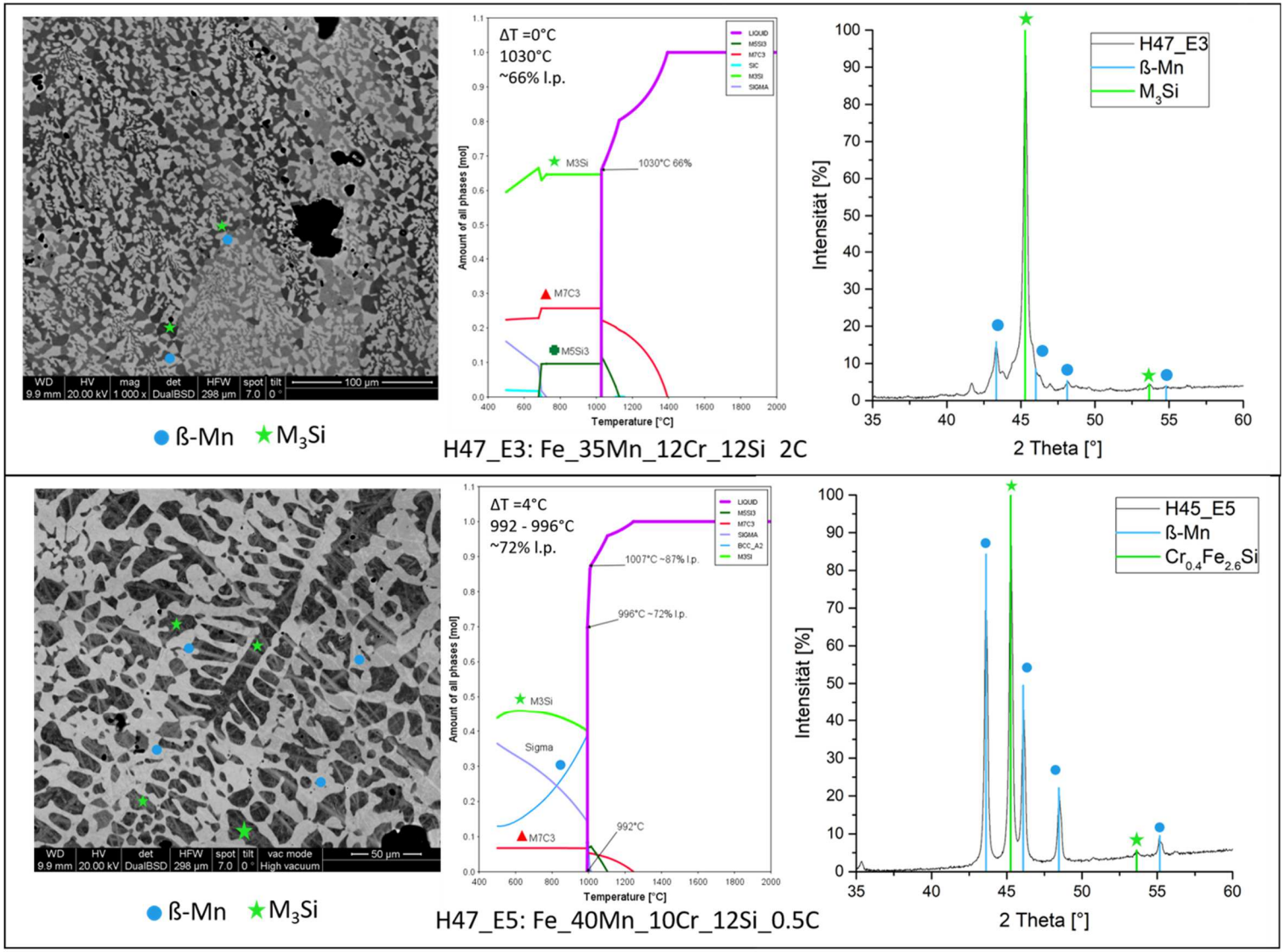

Figure 106 ***Low Cr high Si group:*** *SEM x1000, EoP and XRD analysis from H47_E3 Ingot (top) and H47_E5 (bottom)* ***Phase references:*** *M_3Si = (Fe_3Si (04-003-3871) and/or Fe_2MnSi (01-077-7953) and/or $Cr_{0.6}Fe_{2.4}Si$ (04-006-7480)) , ß-Mn structured phase (04 007 2059), M_7C_3 (04-017-0806)*

Die approbierte gedruckte Originalversion dieser Diplomarbeit ist an der TU Wien Bibliothek verfügbar.
The approved original version of this thesis is available in print at TU Wien Bibliothek.

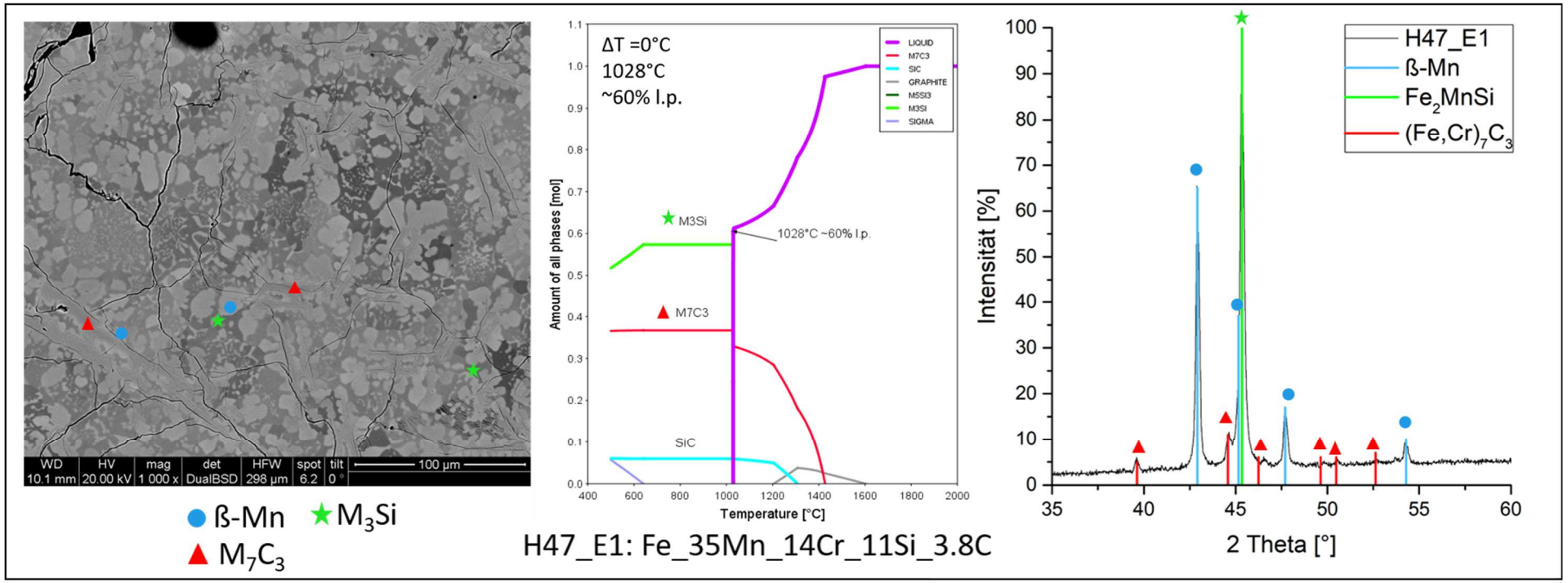

Figure 107 ***Low Cr high Si group:*** *SEM x1000, EoP and XRD analysis from H47_E1 Ingot* ***Phase references*** *M_3Si = (Fe_3Si (04-003-3871) and/or Fe_2MnSi (01-077-7953) and/or $Cr_{0.6}Fe_{2.4}Si$ (04-006-7480)) , ß-Mn structured phase (04 007 2059), M_7C_3 (04-017-0806)*

- **C and Si studies for the Cr-Mn family**

Table 12 shows the composition of the Cr-Mn family modifications, for the C and Si studies, determined with XRF and EDX. C content was determined via Leco measurements. EDX measurements show compositions close to the theoretical composition. Differences in Mn content between 3-5 wt% might be related to evaporation losses during the ingot production. XRF measurements show a huge Mn loss as well and in addition bigger differences in Cr content as determined with EDX. These differences might be related to evaporation losses during the ingot production as described in the Cr family and the Mn family. Elemental additions seem to lead to higher losses than from the MA base powder.

Note: Losses of alloying elements during the heating stage might not occur if the MA used as provided for finely distributed in Fe powder.

Table 12 Composition of the Cr-Mn family, C and Si studies, ingots.

		Fe	Cr	Mn	Si	C
	Theory	37,5	10,0	40,0	12,0	0,5
H47_E5	EDX	39,4	10,9	37,5	11,6	0,55
	XRF	46,77	6,20	30,91	13,94	0,55
	Theory	36,0	10,0	40,0	12,0	2,0
H47_E51	EDX	37,6	9,5	39,1	12,0	1,80
	XRF	48,09	6,99	30,23	12,60	1,80
	Theory	34,2	10	40	12	3,8
H47_E52	EDX	38,1	11,0	37,0	11,4	2,47
	XRF	45,88	6,15	31,56	14,21	2,47
	Theory	40,5	10,0	40,0	9,0	0,5
H47_E53	EDX	44,1	10,5	35,7	9,2	0,57
	XRF	48,70	6,69	31,74	10,74	0,57
	Theory	39,0	10,0	40,0	9,0	2,0
H47_E54	EDX	39,5	11,3	38,2	9,0	1,93
	XRF	49,99	6,66	30,72	10,51	1,93
	Theory	37,2	10,0	40,0	9,0	3,8
H47_E55	EDX	39,9	10,1	37,4	9,3	3,26
	XRF	51,40	7,14	29,30	13,94	3,26

Die approbierte gedruckte Originalversion dieser Diplomarbeit ist an der TU Wien Bibliothek verfügbar.
The approved original version of this thesis is available in print at TU Wien Bibliothek.

Die approbierte gedruckte Originalversion dieser Diplomarbeit ist an der TU Wien Bibliothek verfügbar.
The approved original version of this thesis is available in print at TU Wien Bibliothek.

- **Melting behaviour**

These studies were carried out with the aim to clarify the influence of Si and C on the Cr-Mn family. H47_E5 was chosen as starting material for this study considering the remarkable infiltration behaviour shown in chapter 3.4 Interaction with Fe. Figure 108 compares ThermoCalc predictions and DTA measurements of the liquidus and solidus temperatures for C and Si modifications of H47_E5. Huge differences between the calculated and the measured melting behaviour were obtained.

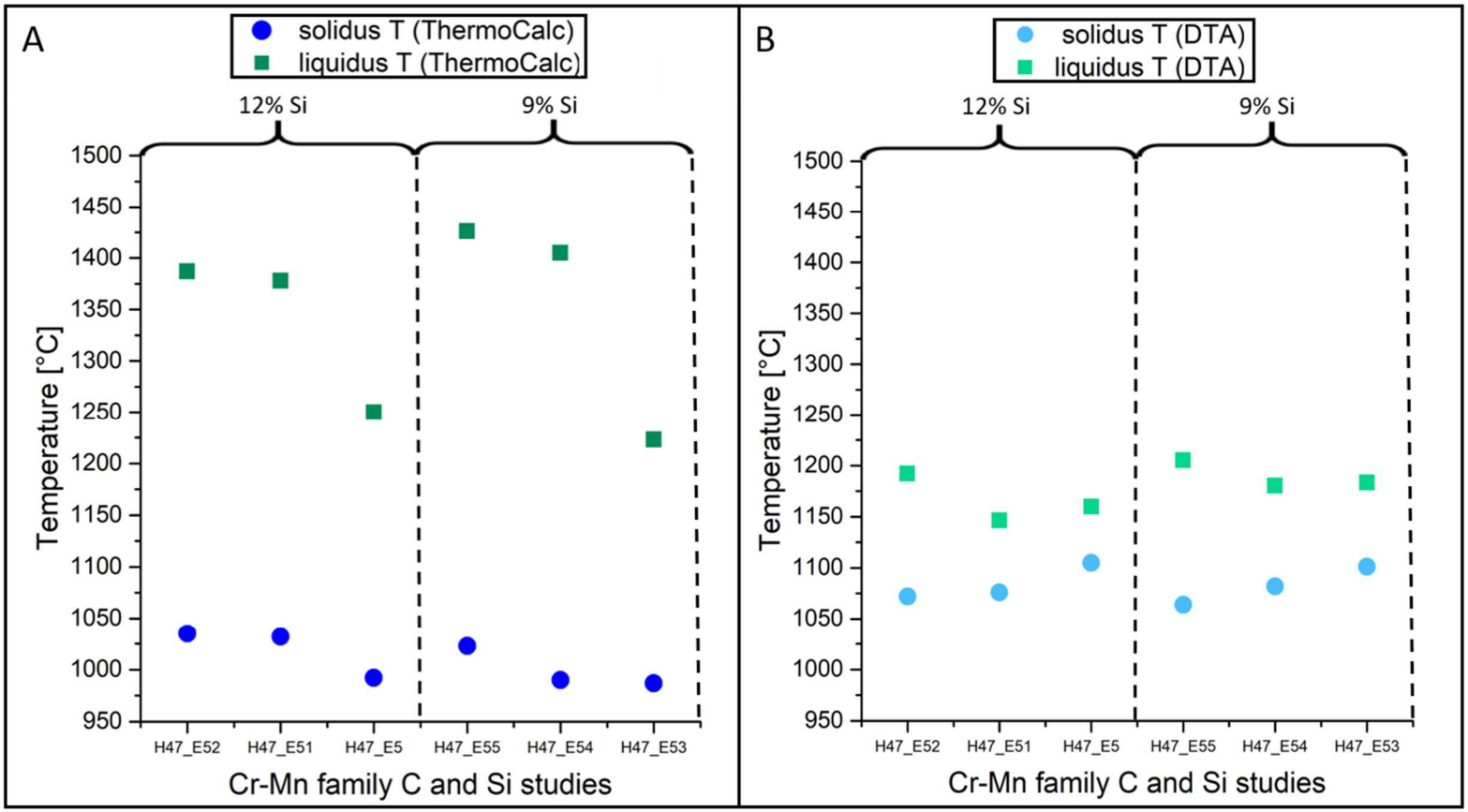

*Figure 108 Comparing solidus and liquidus temperatures predicted from ThermoCalc (**A**) and measured with DTA (**B**) for the Cr-Mn family*

Die approbierte gedruckte Originalversion dieser Diplomarbeit ist an der TU Wien Bibliothek verfügbar.
The approved original version of this thesis is available in print at TU Wien Bibliothek.

Figure 109 and Figure 110 show the same DTA measurements of the C and Si studies for the Cr-Mn family. Figure 109 clearly shows that with increasing C content for these systems the beginning of the melting process decreases in temperature but the melting range broadens.

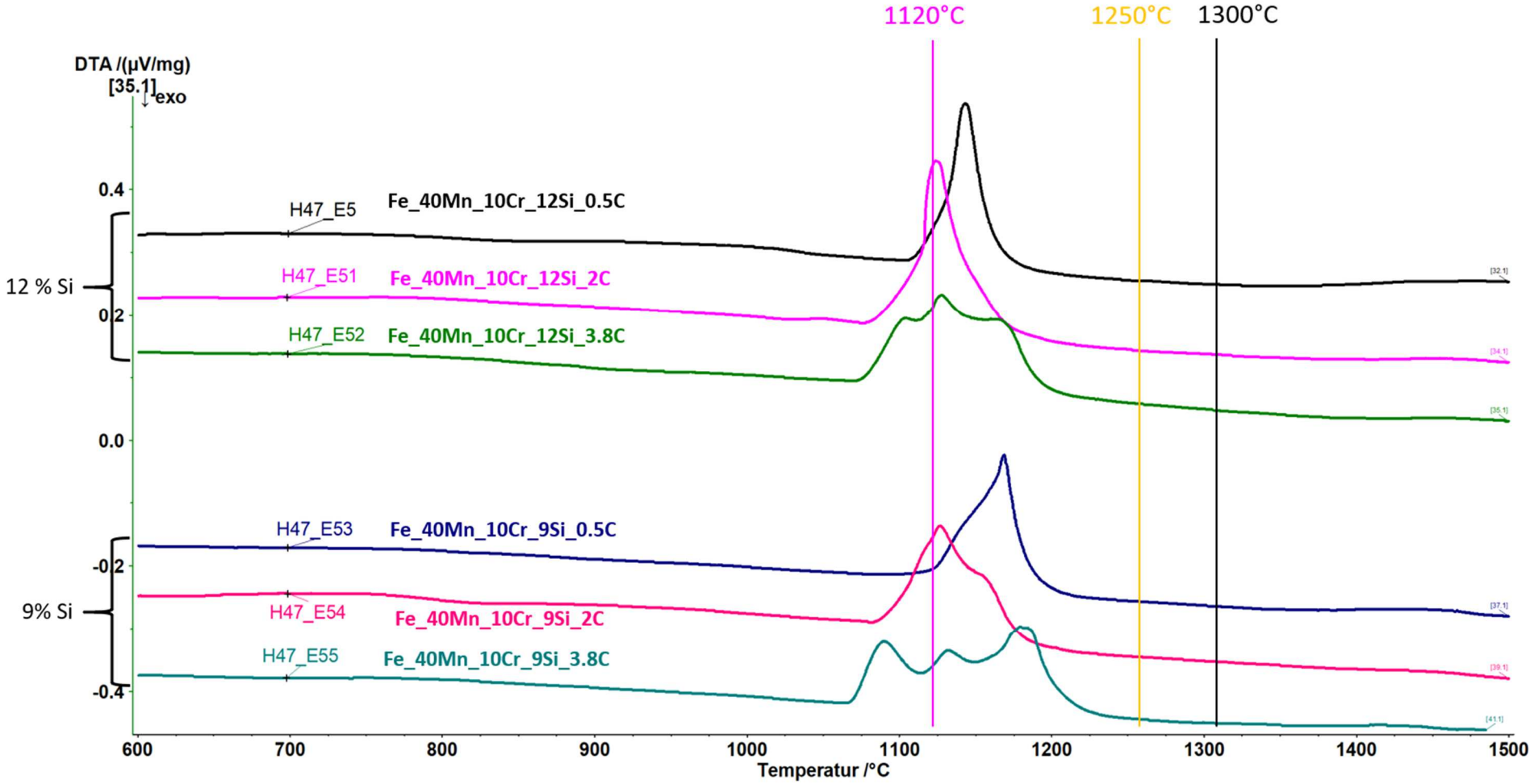

Figure 109 DTA for Cr - Mn family H47_E5 studies, heating phase, Si groups

Die approbierte gedruckte Originalversion dieser Diplomarbeit ist an der TU Wien Bibliothek verfügbar.
The approved original version of this thesis is available in print at TU Wien Bibliothek.

Figure 110 clearly shows the effect of Si in these modifications. It does not change the melting range but it clearly tightens the reaction peak. The two modifications with 3.8% show more differentiated endothermal reactions over their broadened melting range

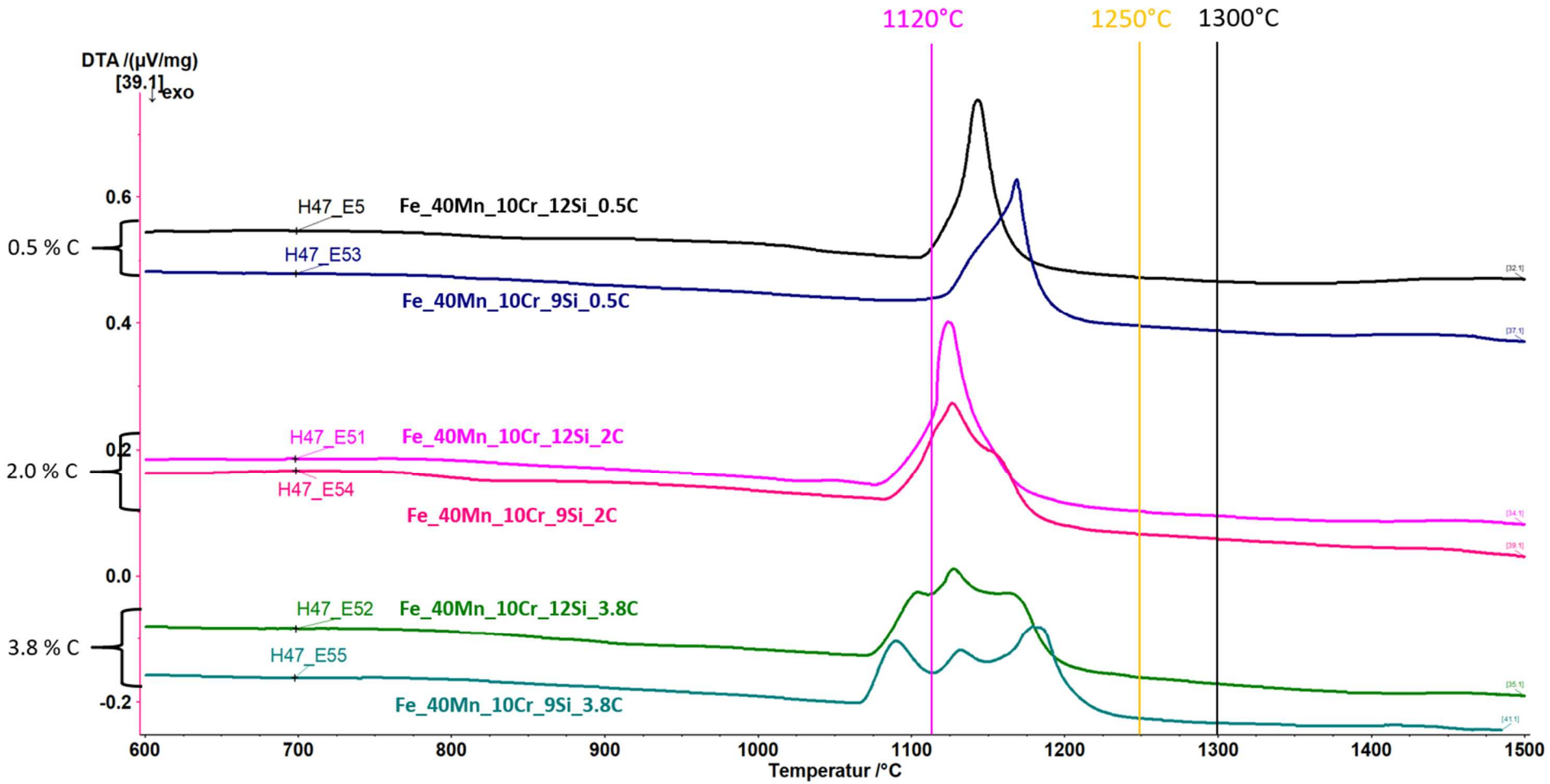

Figure 110 DTA for Cr - Mn family H47_E5 studies, heating phase, C groups

Die approbierte gedruckte Originalversion dieser Diplomarbeit ist an der TU Wien Bibliothek verfügbar.
The approved original version of this thesis is available in print at TU Wien Bibliothek.

- **Stable phases**

Figure 111 to Figure 113 show SEM measurements of the ingots, XRD measurements of milled ingots and the predicted evolution of phases (EoP) from ThermoCalc of the C and Si studies of the Cr-Mn family . All modifications form a ß-Mn structured phase which is considered as a solid solution. All modifications besides the system with the lowest amount of Si and C H47_E53 form a M_3Si phase. The modifications with higher amounts of C form $M_{23}C_6$ carbides and M_5Si_3 silicides. Please note that the SEM pictures for this study have a x2000 magnifications due to the very fine microstructures of these modifications.

Note: Fe_3Si is very unlikely to be a stable phase according to V.Raghavan. [64] The XRD patterns for Fe_3Si, Fe_2MnSi and $Cr_{0,6}Fe_{2,4}Si$ are the same. So, it is most likely to have $Cr_{0,6}Fe_{2,4}Si$ and Fe_2MnSi as M_3Si in the Cr-Mn family systems.

Note: ß-Mn structured phase describes a cubic phase crystalizing in ß-Mn structure. [65],[66],[67] This cubic structure type does not necessarily need Mn to be formed, [67] and it shows rather characteristic patterns in XRD diffractograms,. [67] Different compositions in the ß-Mn structured phase might lead to shifts in the XRD diffractogram.

Die approbierte gedruckte Originalversion dieser Diplomarbeit ist an der TU Wien Bibliothek verfügbar.
The approved original version of this thesis is available in print at TU Wien Bibliothek.

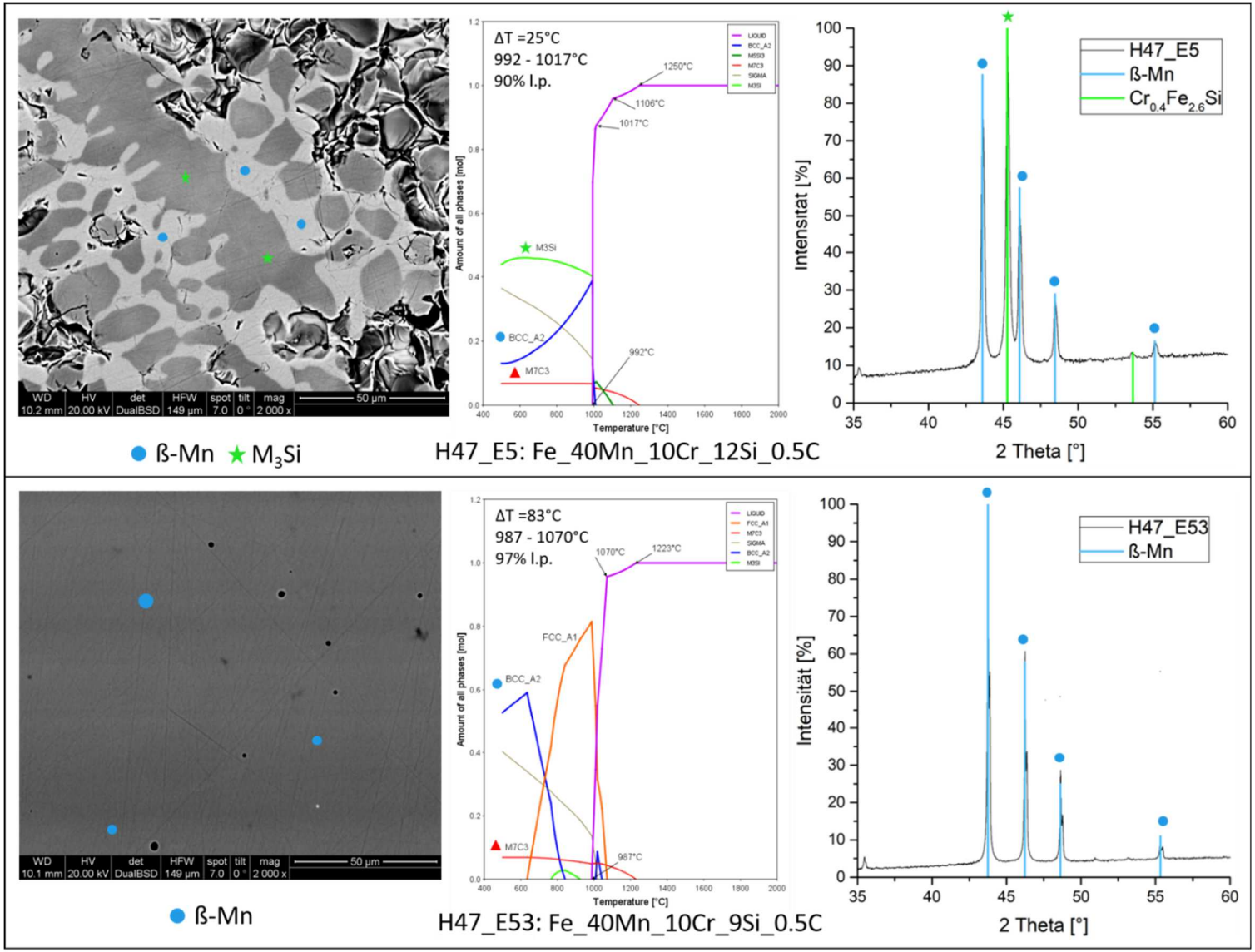

Figure 111 SEM x2000, EoP and XRD analysis from H47_E5 Ingot (top) and H47_E53 (bottom), ***0.5% C Phase references: references*** *M_3Si = (Fe_3Si (04-003-3871) and/or Fe_2MnSi (01-077-7953) and/or $Cr_{0.6}Fe_{2.4}Si$ (04-006-7480)), ß-Mn structured phase (04 007 2059),*

Die approbierte gedruckte Originalversion dieser Diplomarbeit ist an der TU Wien Bibliothek verfügbar.
The approved original version of this thesis is available in print at TU Wien Bibliothek.

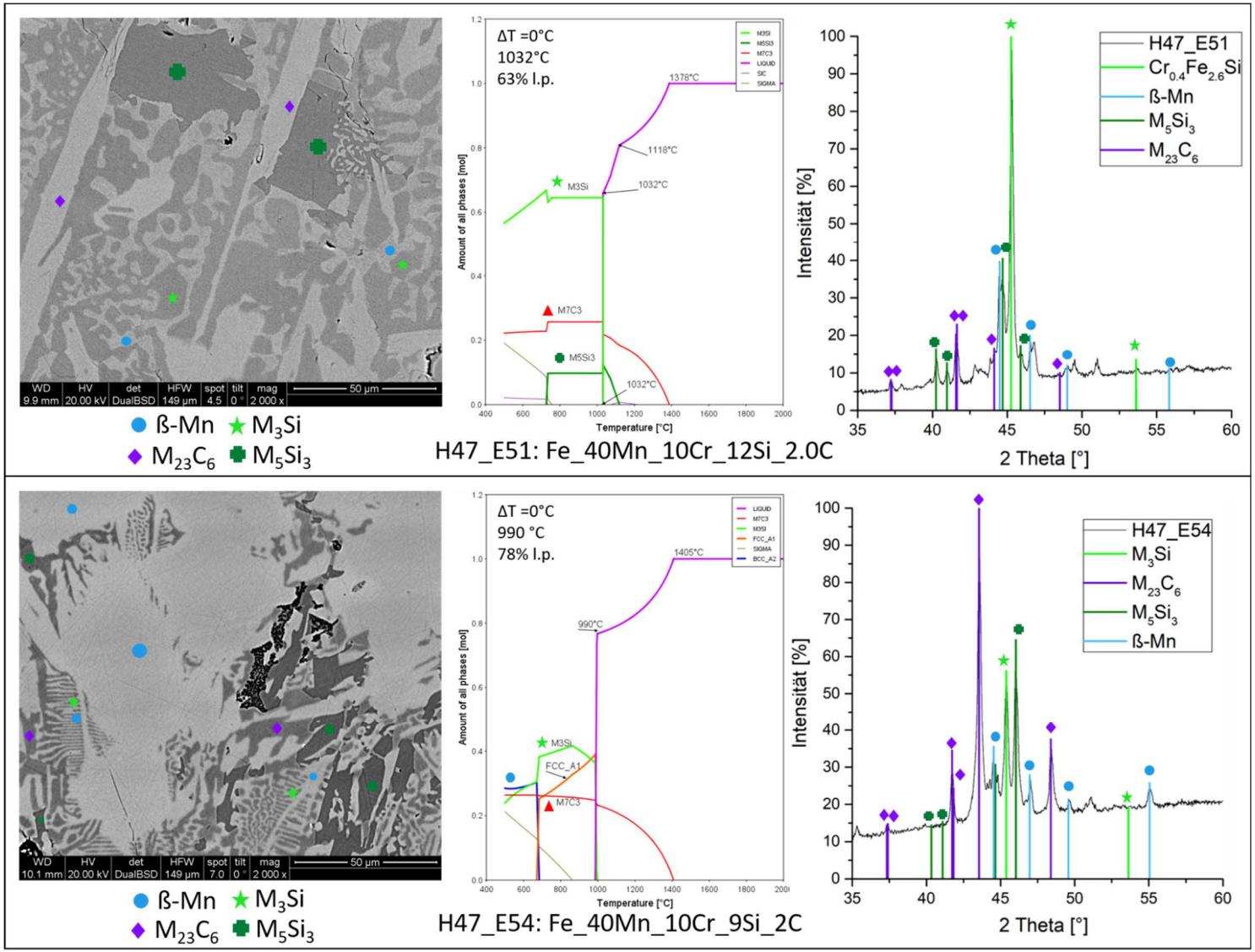

Figure 112 SEM x2000, EoP and XRD analysis from H47_E51 Ingot (top) and H47_E54 (bottom), ***2% C Phase references: references*** *M_3Si = (Fe_3Si (04-003-3871) and/or Fe_2MnSi (01-077-7953) and/or $Cr_{0.6}Fe_{2.4}Si$ (04-006-7480)), ß-Mn structured phase (04 007 2059), $M_{23}C_6$ (04-003-6076), M_5Si_3 (04-004-3035)*

Die approbierte gedruckte Originalversion dieser Diplomarbeit ist an der TU Wien Bibliothek verfügbar.
The approved original version of this thesis is available in print at TU Wien Bibliothek.

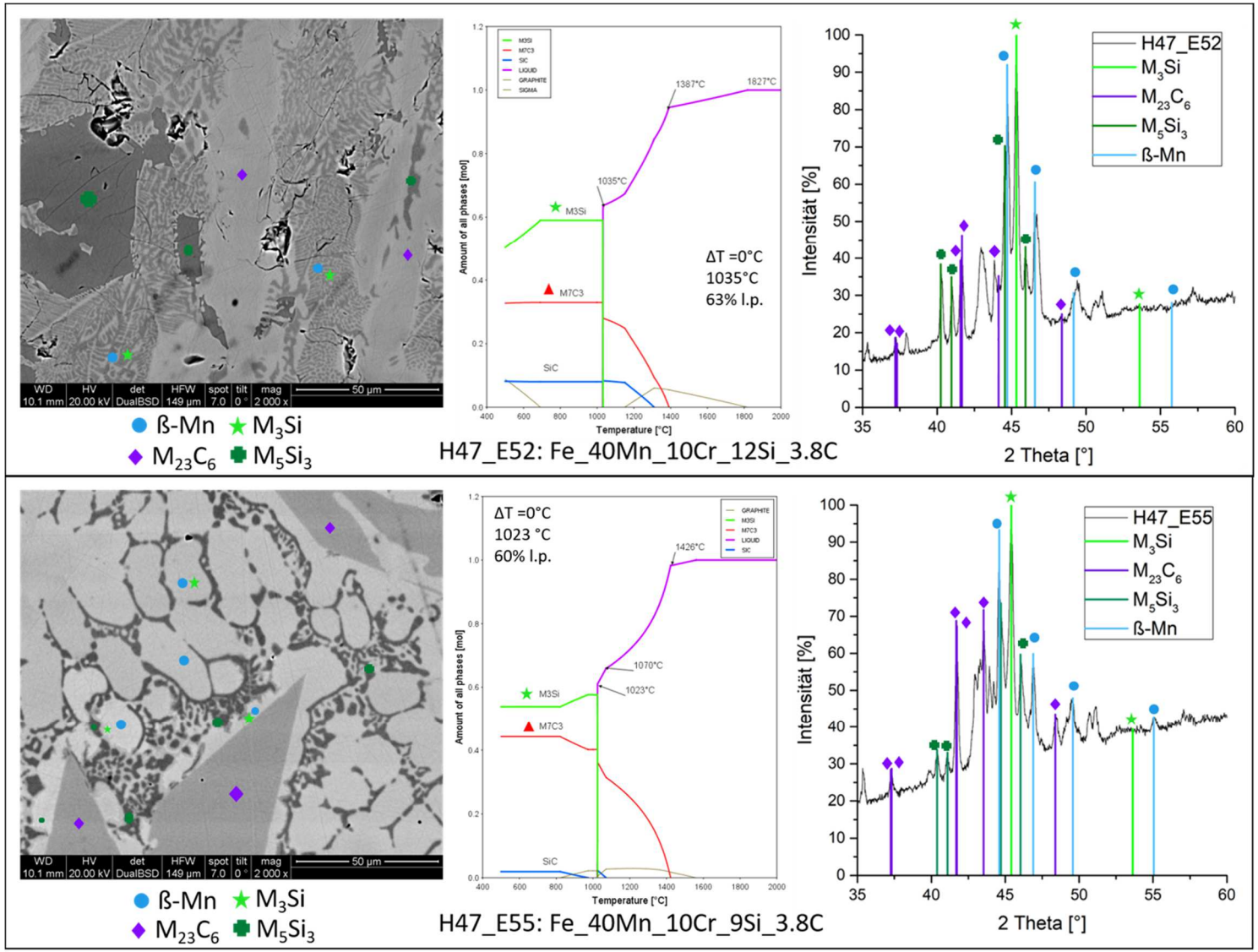

Figure 113 SEM x2000, EoP and XRD analysis from H47_E52 Ingot (top) and H47_E55 (bottom), ***3.8% C Phase references: references*** *M_3Si = (Fe_3Si (04-003-3871) and/or Fe_2MnSi (01-077-7953) and/or $Cr_{0.6}Fe_{2.4}Si$ (04-006-7480)), ß-Mn structured phase (04 007 2059), $M_{23}C_6$ (04-003-6076), M_5Si_3 (04-004-3035)*

3.4 Interaction with Fe

- Infiltration experiments

In this chapter the results of infiltration experiments under reducing conditions are presented. These experiments show the most noticeable differences between the different modifications of each family. Results of wetting experiments under reducing and inert conditions as well as infiltration experiments under inert conditions are less significant; they are therefore presented in the Attachment.

Infiltration experiments under reducing conditions were carried out on Charpy samples of Fe powders with 0.6C. The samples were prepared as for the inert conditions. The sintering was carried out for 1 h at 1300°C under Ar/10 %H_2.

3.4.1 Cr family

Figure 114 shows the cut and etched samples of the Cr family of the infiltration experiments under reducing conditions. Please **note** that the picture of H45_E2 shows a notch, this is the result of a last-minute change of the cutting direction. All modifications, except the remarkable difference of H45_E1, show a rather similar behaviour. The MA infiltrated the sample, and base material was dissolved; this led to an increase of the ST of the liquid phase resulting in a stopped infiltration process. This behaviour is similar to materials used as reactive sinter brazes mentioned by H.Danninger et.al. in [54]. These materials shall rapidly infiltrate the capillaries or pores and rapidly "freeze" there due to base material dissolution in the liquid phase and/or diffusion from C into the substrate to close the open porosity. [54]

It turned out that for these systems it seems not to be important to form as much liquid as possible at a certain temperature. **The low Cr group** melts over a comparable narrow melting window shown in Figure 86, but no big difference could be obtained to the other modifications.

H45_E1 shows a very unique behaviour for the Cr family and for all the other families. This modification fully infiltrates the sample, leaving barely residues on the surface. In addition, it shows a marked dissolution of the substrate ("erosion"), leaving behind craters in the substrate similar to the size of the initial MA piece placed on the surface. Such "erosive" effects can be obtained e.g. with pure Cu infiltrating porous Fe samples. Experiments with a Cu-wire in a porous iron compact showed that the Cu wire disappears completely during the sintering process even after a very short time of less than 5 min. [18] However this seems to be still a rather long time for a pure Cu system infiltrating a green iron body. R. Oro shows in [34] that the time between the Cu melting and the total infiltration of the specimen is ~10 s. In this work they could not obtain "erosion" through Cu. Comparing the behaviour of H45_E1 with the Cu liquid phase in both works it might be reasonable that the molten H45_E1 drop remained on top of the Charpy sample for a much longer time, dissolving base material in a dynamic process. Having most likely a diffusion of C out of the liquid phase and dissolution of Fe in the liquid phase, both phenomena would lead to an increase of the liquidus temperature of the liquid phase. In the case of H45_E1 the C "frontline" may reduce the melting point of the bulk material in a way that the liquid phase can just flow through the sample before it gets

Die approbierte gedruckte Originalversion dieser Diplomarbeit ist an der TU Wien Bibliothek verfügbar.
The approved original version of this thesis is available in print at TU Wien Bibliothek.
TU Bibliothek Your knowledge hub WIEN

saturated with Fe and solidifies. As the liquid flow is continuous there is always unsaturated liquid phase which can dissolve base material resulting in an erosive crater.

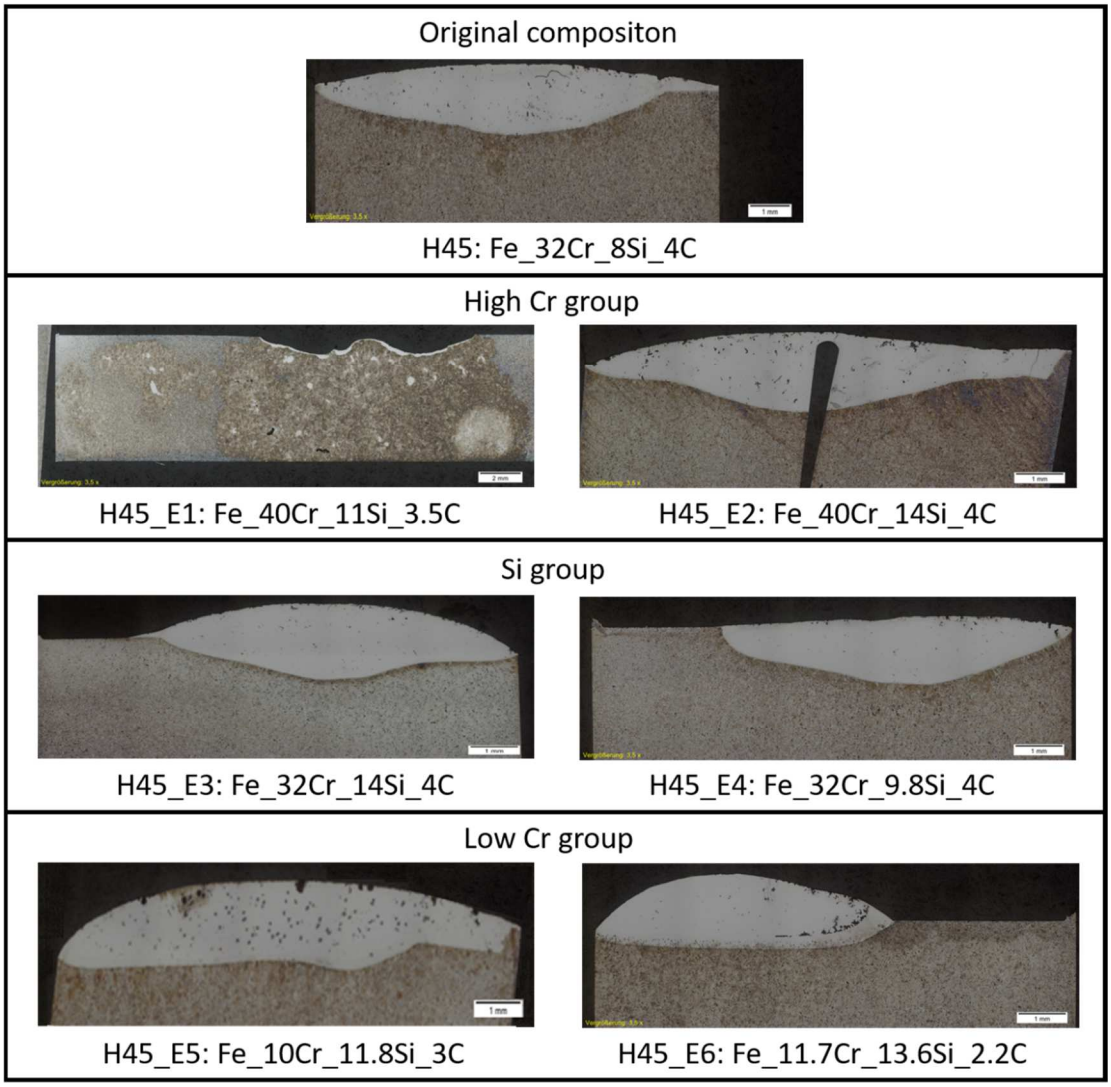

Figure 114 Infiltration of Cr-family on Fe + 0.6C Charpy samples at 1300°C under Ar / H_2

Die approbierte gedruckte Originalversion dieser Diplomarbeit ist an der TU Wien Bibliothek verfügbar.
The approved original version of this thesis is available in print at TU Wien Bibliothek.

- **C studies of the Cr family: Infiltration**

Figure 115 shows the results of the C studies for H45_E1.
H45_E11, with 4% C, shows a similar behaviour to the other modifications of the Cr family shown in Figure 114. It seems to infiltrate and dissolve. Infiltration seems to be stopped due to the dissolution of the substrate and resulting increase of the solidus temperatures of the melt. This results in the formation of an interface which is shown in Figure 116.
H45_E1, with 3.5% C, shows reproducibly the same behaviour. It infiltrates almost the whole sample dissolving a crater out of the substrate similar to the size of the ingot initially placed on the substrate.
H45_E2, with 2.5% C shows another behaviour. This MA infiltrates the Charpy sample as well all over but leaving a residue on the surface instead of a crater.
H45_E3, with 0.5% C slightly infiltrates and dissolves the substrate. According to DTA measurement this system seems to be barely molten at 1300°C so it is considered that there is not much liquid phase to interact with the substrate. The different C steps cover different MA behaviour pointing out the influence of the C on these MA systems in terms of liquid phase behaviour.

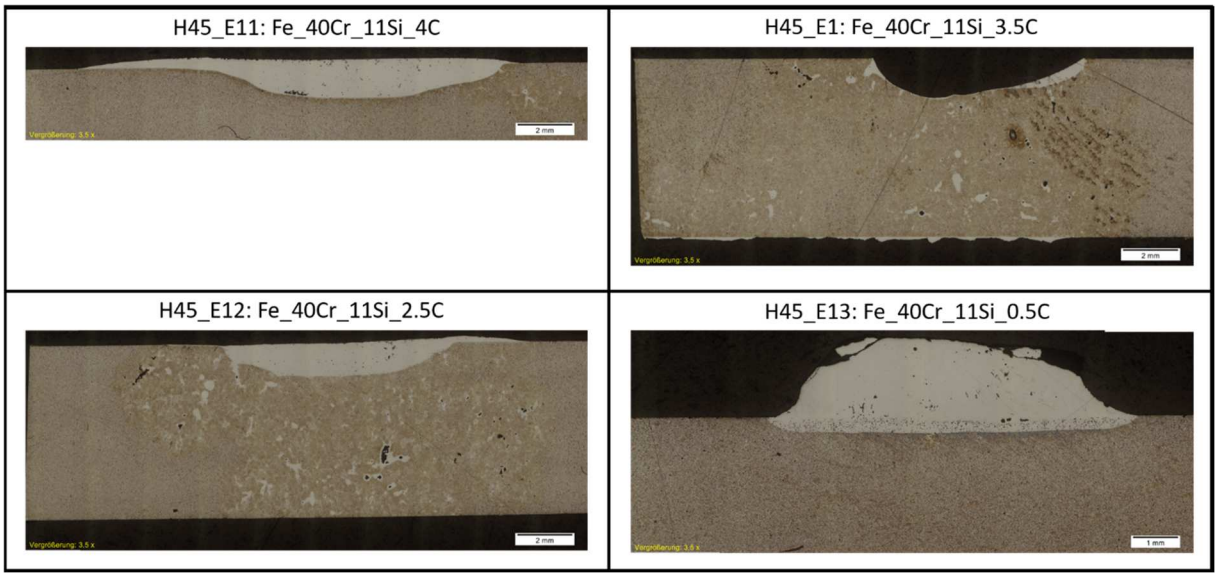

Figure 115 Infiltration of Cr-family H45_E1 studies on Fe + 0.6C Charpy samples at 1300°C under Ar / H_2

Die approbierte gedruckte Originalversion dieser Diplomarbeit ist an der TU Wien Bibliothek verfügbar.
The approved original version of this thesis is available in print at TU Wien Bibliothek.

- **C studies of the Cr family: Interfaces**

As a consequence of the significant differences in the infiltration behaviour of the H45_E1 modifications it seemed reasonable to take a closer look to the MA-Charpy interfaces.

H45_E11: Figure 116 shows an interface between the MA residue and the Charpy sample. This interface is supposed to inhibit infiltration of the MA and is considered to be formed in an early stage of the heating phase. On the bulk side a C rich zone, most likely formed through diffused C from the MA, can be obtained. The Interface itself does not seem to have much C, because the Nital etching could not etch the interface. This finding fits to the assumed processes of C diffusion out of the liquid phase and Fe dissolution in the liquid phase locally increasing the liquidus temperature and forming an interface shell which inhibits further infiltration.

Due to an unknown accidental reason there is one breakthrough in the interface. In this area infiltration could be obtained.

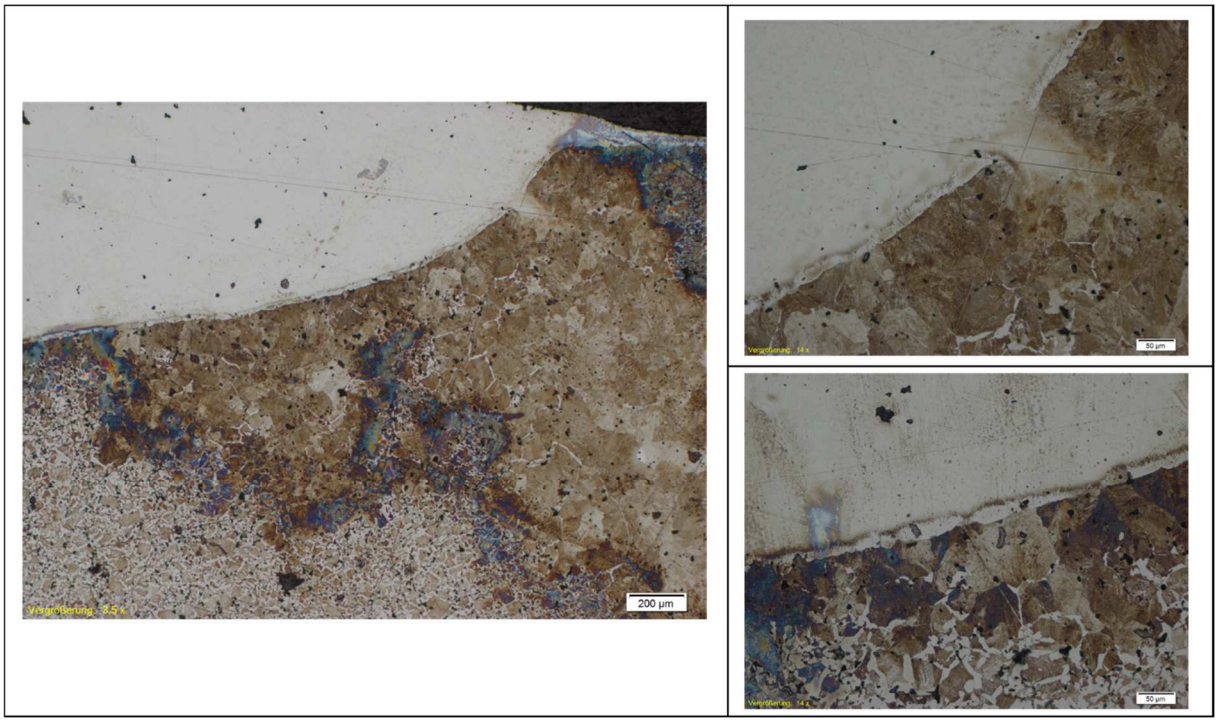

Figure 116 H45_E11 Interface between MA and substrate. Overview of the infiltration due to the breakthrough (left), detailed area of the breakthrough of the interface (right top), Interface between MA residue and Charpy sample (right bottom)

H45_E1: Figure 117 shows on the left side that there is no certain interface visible between MA residue and the substrate in H45_E1. This might be the reason why this modification can infiltrate so good, having no hindering shell.

H45_E12: In Figure 117 on the right side the interface of H45_E12 is shown. In this sample an interface could be obtained as well but it looks completely different to the interface obtained in H45_E11. This interface is supposed to be formed in a later stage of the sintering process after a first infiltration into the substrate has already happened. The infiltration of the early

Die approbierte gedruckte Originalversion dieser Diplomarbeit ist an der TU Wien Bibliothek verfügbar.
The approved original version of this thesis is available in print at TU Wien Bibliothek.
TU Bibliothek Your knowledge hub WIEN

liquid phase might change the composition and along with that most likely the liquidus temperature of the remaining MA.

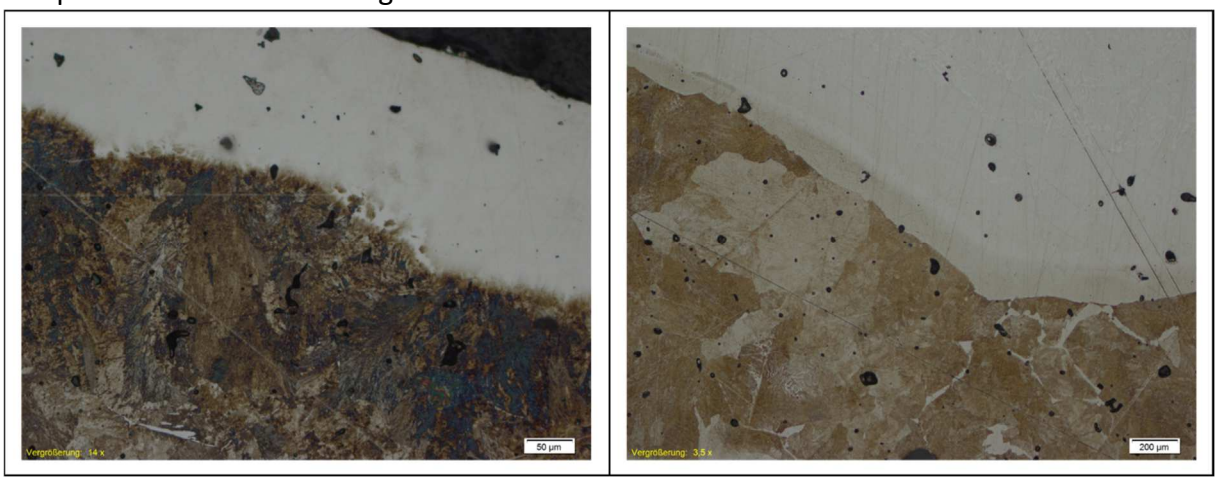

Figure 117 Interface between MA and substrate. H45_E1 (left) H45_E12 (right)

H45_E13: Even though H45_E13 is barely molten Figure 118 shows an interface formed between substrate and MA residue.

Figure 118 Interface between MA and substrate. H45_E13

Die approbierte gedruckte Originalversion dieser Diplomarbeit ist an der TU Wien Bibliothek verfügbar.
The approved original version of this thesis is available in print at TU Wien Bibliothek.

Die approbierte gedruckte Originalversion dieser Diplomarbeit ist an der TU Wien Bibliothek verfügbar.
The approved original version of this thesis is available in print at TU Wien Bibliothek.

- **H45_E1 Cr and Si distribution**

Figure 119 shows the **H45_E1: Fe_40Cr_11Si_3.5C** infiltration experiment under reducing conditions. The huge crater on the top of the sample is clearly visible. It is most likely that the MA did infiltrate in a dynamic process. The liquid phase was not hindered to infiltrate into the sample due to an inhibiting interface as shown in Figure 117. Finding a good distribution of all alloying elements from the MA through the whole sample makes sure that infiltration took place. The red lines show the area where EDX analysis was carried out to clarify Cr and Si distribution. The exact spots and the results are shown in Figure 120. The bright areas, like the residues on the top in the crater, but even those inside the samples are spots with a high concentration of Si and Cr.

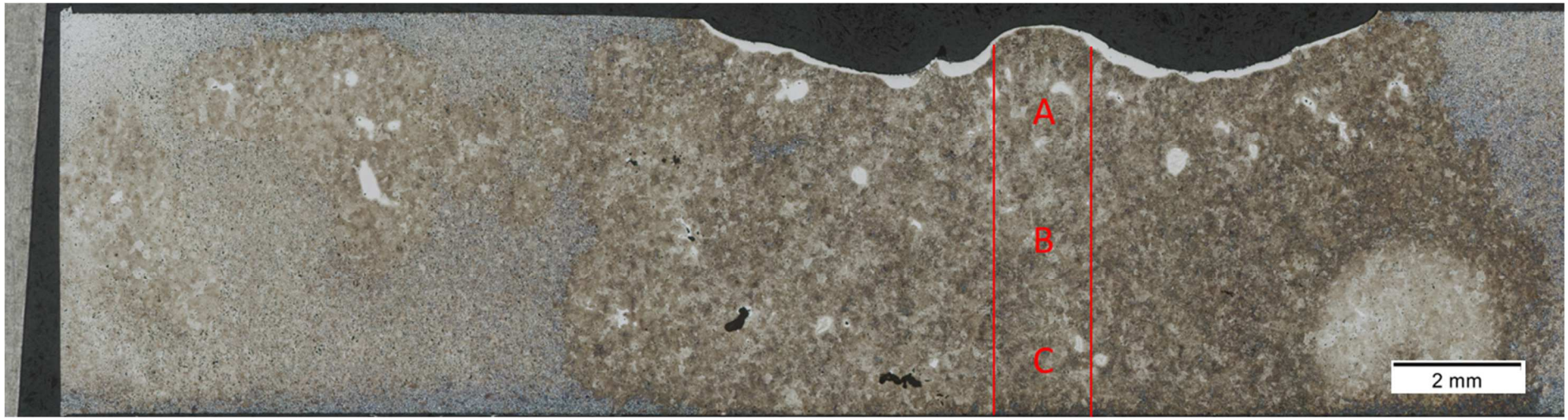

Figure 119 Infiltration experiment with H45_E1 under reducing conditions. Full infiltration through the whole sample.

Figure 120 shows the exact spots where EDX measurements were carried out. It was tried to keep the spots the same size 250 x 200 µm to have comparable results. Most spots show a Cr content of 2 ± 0.5wt%. Region B seems to have a little less Cr but is still in the range to consider homogeneous distribution of Cr with some exceptional areas as spot 6 or spot 9.

Table 13 Cr, Si and Fe content measured with EDX

Region A	Cr [wt%]	Si [wt%]	Fe [wt%]
Spot 1	1,55	0,28	98,17
Spot 2	1,89	0,34	97,76
Spot 3	2,24	0,49	97,27
Spot 4	2,02	0,34	97,64
Region B			
Spot 5	1,97	0,48	97,96
Spot 6	4,72	1,30	93,96
Spot 7	2,00	0,40	97,60
Spot 8	2,08	0,19	97,74
Spot 9	0,73	0,41	98,87
Spot 10	1,78	0,19	98,03
Region C			
Spot 11	2,35	0,42	97,23
Spot 12	2,15	0,19	97,66
Spot 13	1,61	0,22	98,17
Spot 14	2,35	0,23	97,41
Spot 15	2,74	0,34	96,92
Spot 16	1,87	0,23	97,89
Spot 17	2,16	0,17	97,35
Spot 18	1,95	0,20	97,85
Spot 19	2,96	0,65	96,36

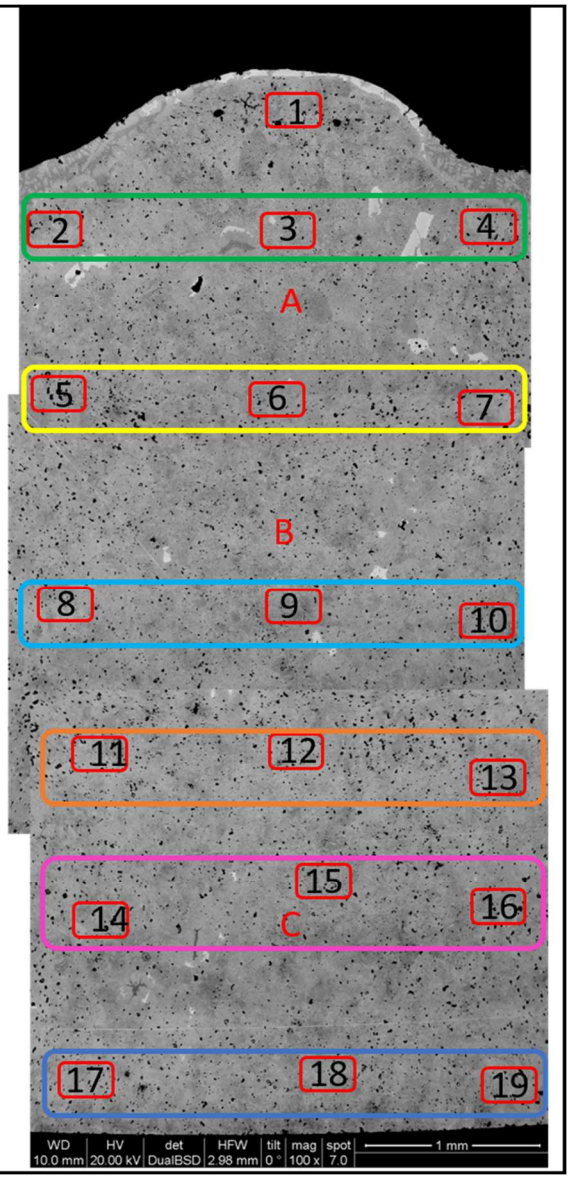

Figure 120 SEM pictures x100 of H45_E1 infiltration sample under reducing conditions

Die approbierte gedruckte Originalversion dieser Diplomarbeit ist an der TU Wien Bibliothek verfügbar.
The approved original version of this thesis is available in print at TU Wien Bibliothek.

3.4.2 Mn family

Figure 121 shows the cut and etched samples of the Mn family after infiltration experiments under reducing conditions. The original composition seems to barely interact with the substrate. H46_E1, H46_E2 and H46_E3 show a similar behaviour independently of their difference in alloying composition. It looks as if they infiltrate into the substrate and dissolve it until a point is reached where no further infiltration or dissolution takes place. For the Mn family modifications with the highest Si content H46_E4 and H46_E5, the infiltration does not seem to be interrupted by dissolution. This results in rather deep infiltration and some residues on the surface of the substrate.

These results show again that for these MA's forming as much liquid phase in an as narrow melting range as possible is not enough for a good infiltration behaviour. The composition of the liquid phase and the dependency of the ST of the liquid phase on dissolved base material and diffusion of alloying elements from the liquid phase into the matrix especially speaking of C in this case. In the case of C diffusion, again the sinter brazing effect mentioned from H.Danninger et.al. in [54] occurs.

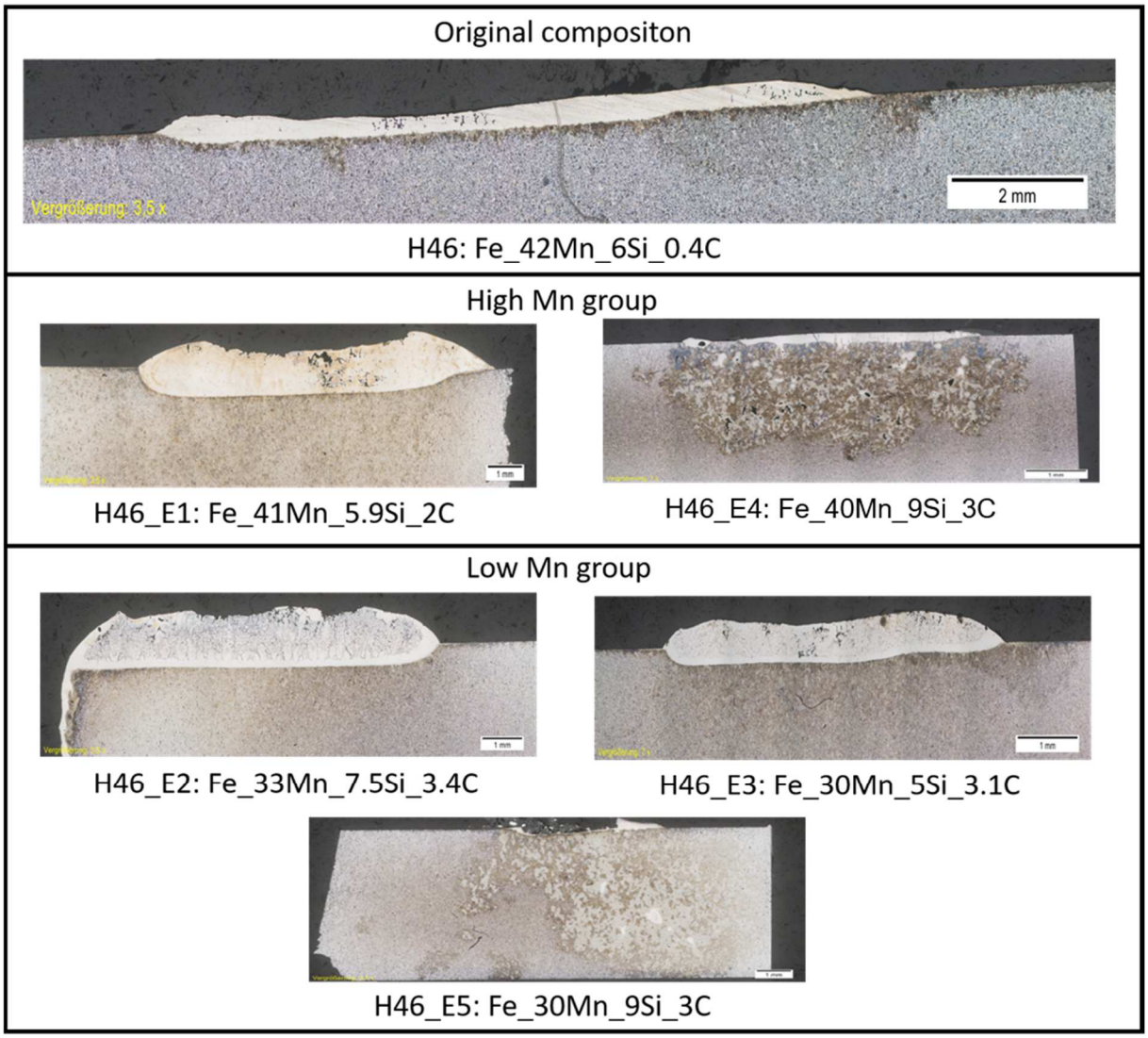

Figure 121 Infiltration of Mn-family on Fe + 0.6C Charpy samples at 1300°C under Ar / H_2

Die approbierte gedruckte Originalversion dieser Diplomarbeit ist an der TU Wien Bibliothek verfügbar.
The approved original version of this thesis is available in print at TU Wien Bibliothek.

- **Mn family: Interfaces**

Figure 122 shows the interface of MA and Charpy sample for some Mn family modifications.

H46: Shown in Figure 122 on the top left, shows a clear interface edge between MA residue and substrate material. A C enriched zone on the bulk side is clear to see. No infiltration took place for this MA.
H46_E3: Shown in Figure 122 on the top right, shows another clear interface between substrate and MA. It differs to the interface of H46 having a relatively broad interface which seems to be more or less fully dense. The bulk side of the interface shows a C enriched area most likely due to C diffusion out of the MA. This modification did not infiltrate the Charpy sample.
H46_E4: Shown in Figure 122 on the bottom left, shows no clear interface between MA and Charpy substrate. The border looks interlocked and a good infiltration took place for this modification.
H46_E5: Shown in Figure 122 on the bottom right, shows a C enriched interface area. This interface is not supposed to hinder infiltration as the sample shows a very good infiltration. It is remarkable that H46_E3 and H46_E5 only differ in 4 wt% Si. The higher Si content seems to either inhibit the formation of an interface or it helps the liquid phase to dissolve more iron and allows, due to that, infiltration before solidification takes place.

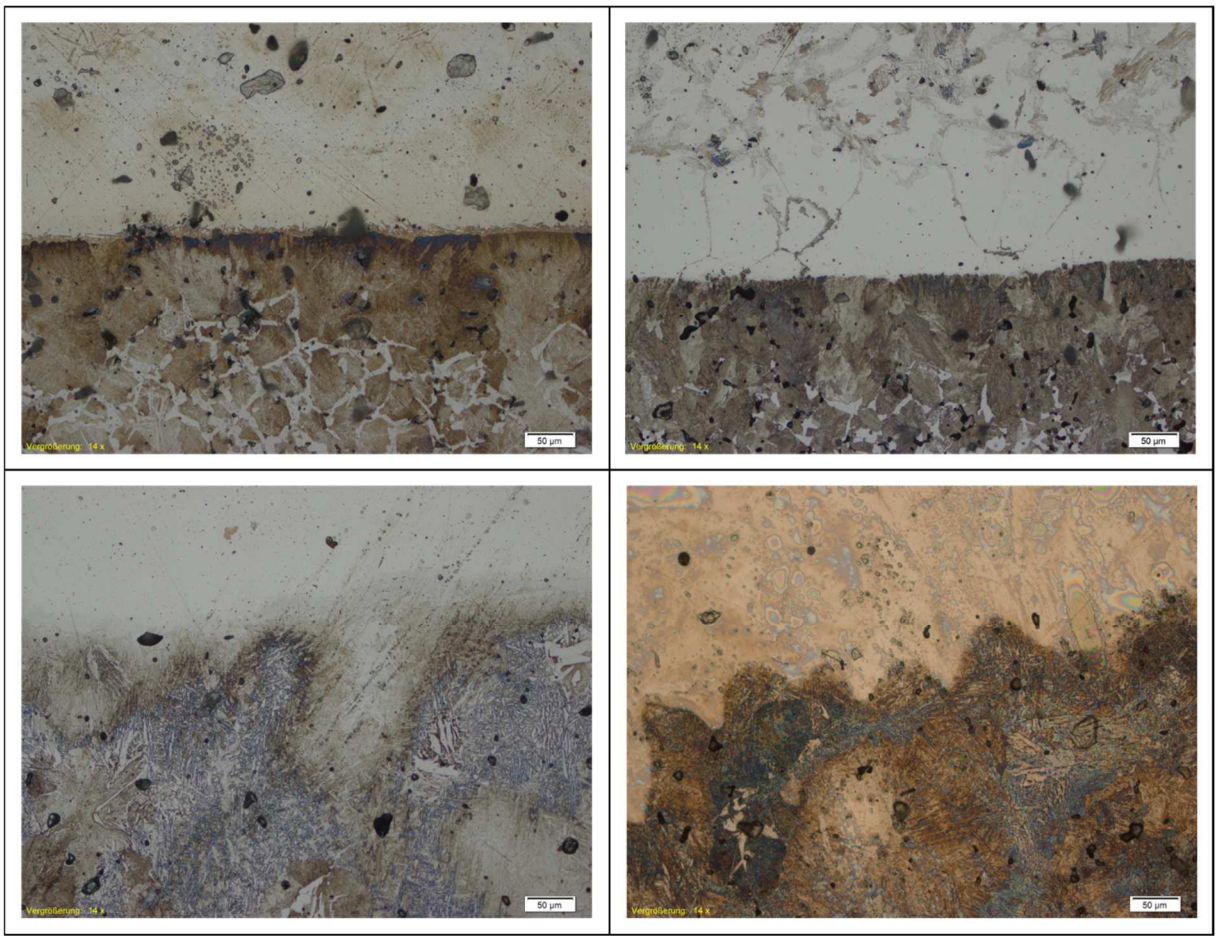

Figure 122 Interfaces of Mn family. H46 (left top), H46_E4 (left bottom), H46_E3 (right top), H46_E5 (right bottom)

Die approbierte gedruckte Originalversion dieser Diplomarbeit ist an der TU Wien Bibliothek verfügbar.
The approved original version of this thesis is available in print at TU Wien Bibliothek.
TU Bibliothek Your knowledge hub WIEN

3.4.3 Cr-Mn family

- **Infiltration under reducing conditions**

Figure 123 shows the cut and etched samples after the infiltration experiments with the Cr-Mn family under reducing conditions. Cr-Mn family master alloy **H47_E5** shows a unique behaviour under these conditions, fully infiltrating the substrate while showing no dissolution and leaving no residues of the MA on the surface. All the other modifications show a similar behaviour among them, infiltrating the sample and dissolving the substrate at least on the surface where the residues are "digged" into the matrix, which seems to not stop the infiltration. All these MA, except H47_E5, leave behind residues on the surface. The amount of residue left behind seems to be somehow linked to the amount of C in the MA.
For the modifications of the Cr-Mn family it seems that the "freezing" of the liquid happens due to C diffusion loss from the transient liquid phase, as mentioned in H.Danninger et.al. [54] as an effect observed for reactive sinter brazes.

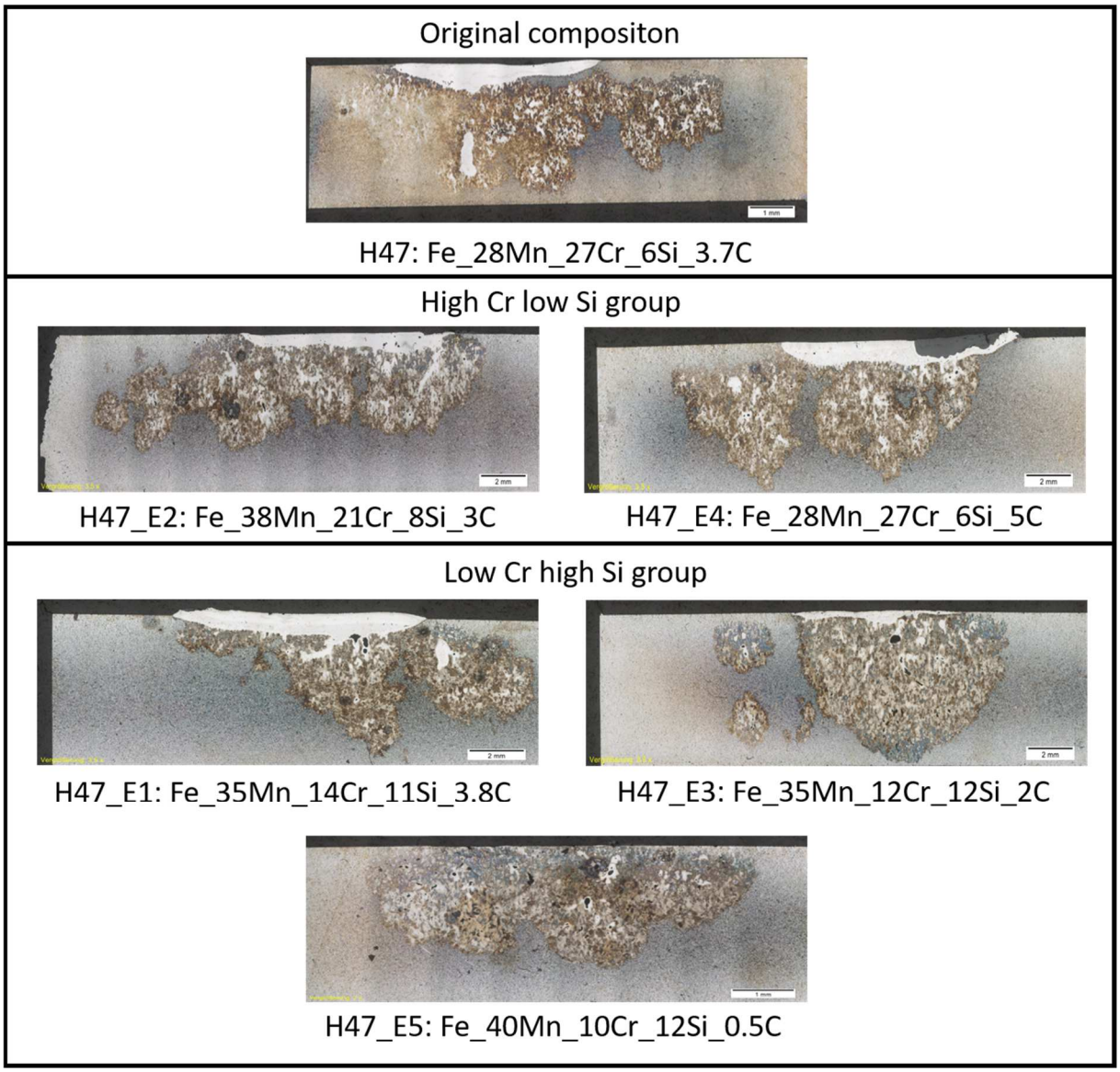

Figure 123 Infiltration of Mn-family on Fe + 0.6C Charpy samples at 1300°C under Ar / H_2

Die approbierte gedruckte Originalversion dieser Diplomarbeit ist an der TU Wien Bibliothek verfügbar.
The approved original version of this thesis is available in print at TU Wien Bibliothek.

- **Infiltration under inert conditions**

For infiltration experiments under inert conditions Charpy samples of Fe powders (without carbon) were pressed at 600 MPa. A piece of an ingot was placed on top of the Charpy sample, as shown in Figure 15, and the sample was sintered for 1 h at 1300°C under Ar.

Figure 124 shows some cut and etched samples of the Cr-Mn family after infiltration experiments under inert conditions (plain Fe substrate, Ar atmosphere). H47_E1 shows a unique behaviour compared to all other modifications of all families. It was the only MA composition of this study which showed some infiltration behaviour that was not fully interrupted by dissolution processes under inert conditions.

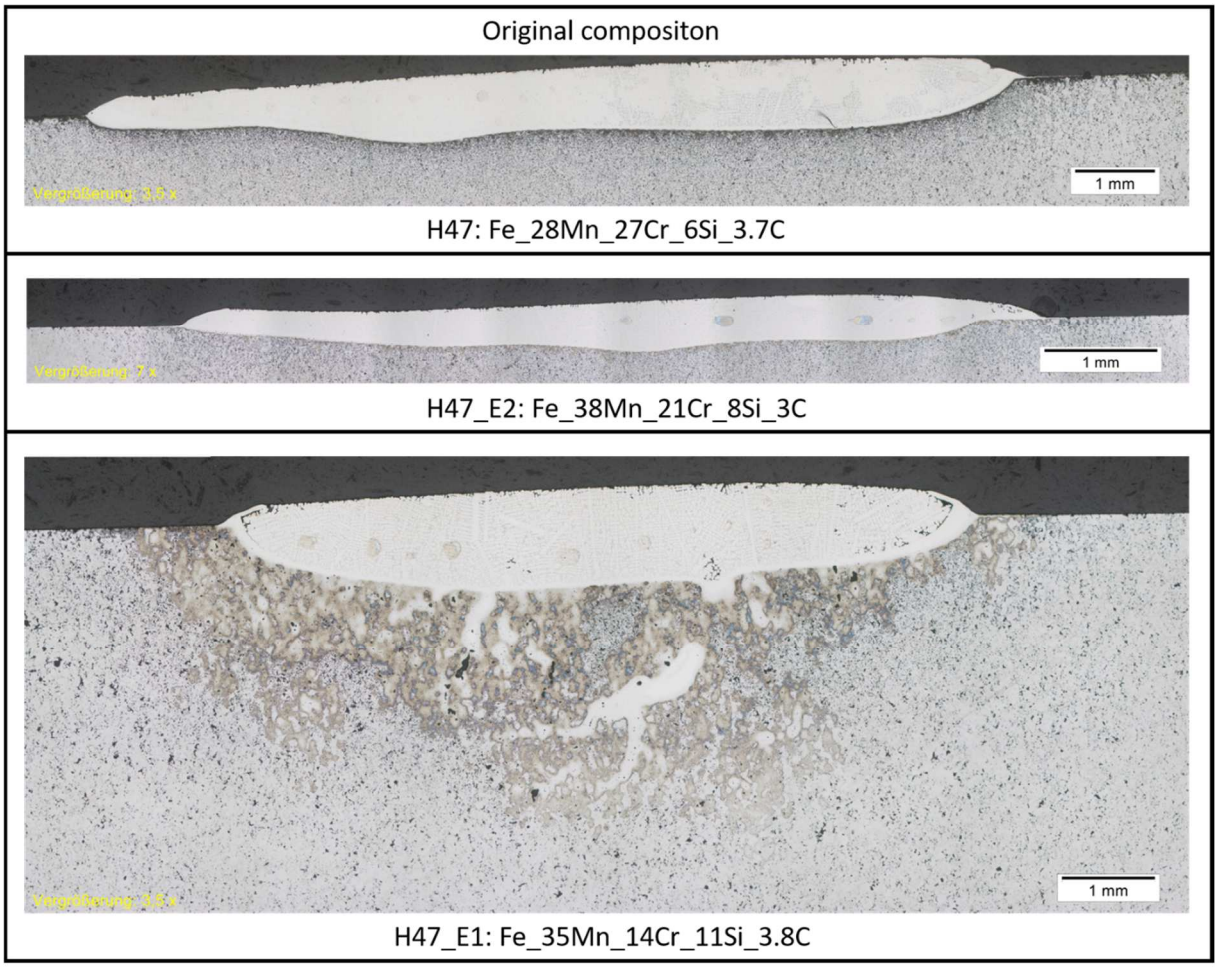

Figure 124 Infiltration of Mn-family on Fe Charpy samples at 1300°C under Ar

Die approbierte gedruckte Originalversion dieser Diplomarbeit ist an der TU Wien Bibliothek verfügbar.
The approved original version of this thesis is available in print at TU Wien Bibliothek.

- **C and Si studies of Cr-Mn family: Infiltration**

Figure 125 shows the cut and etched samples of the Cr-Mn family after the infiltration experiments under reducing conditions. This infiltration experiment shows the influence of C and Si on the infiltration and liquid phase behaviour of the MA. It is clear to see that the samples with higher Si content could infiltrate deeper into the sample under the process conditions. With increasing C content the amount of residue on the surface increases. The Si content seems to have an influence on this phenomenon as well.

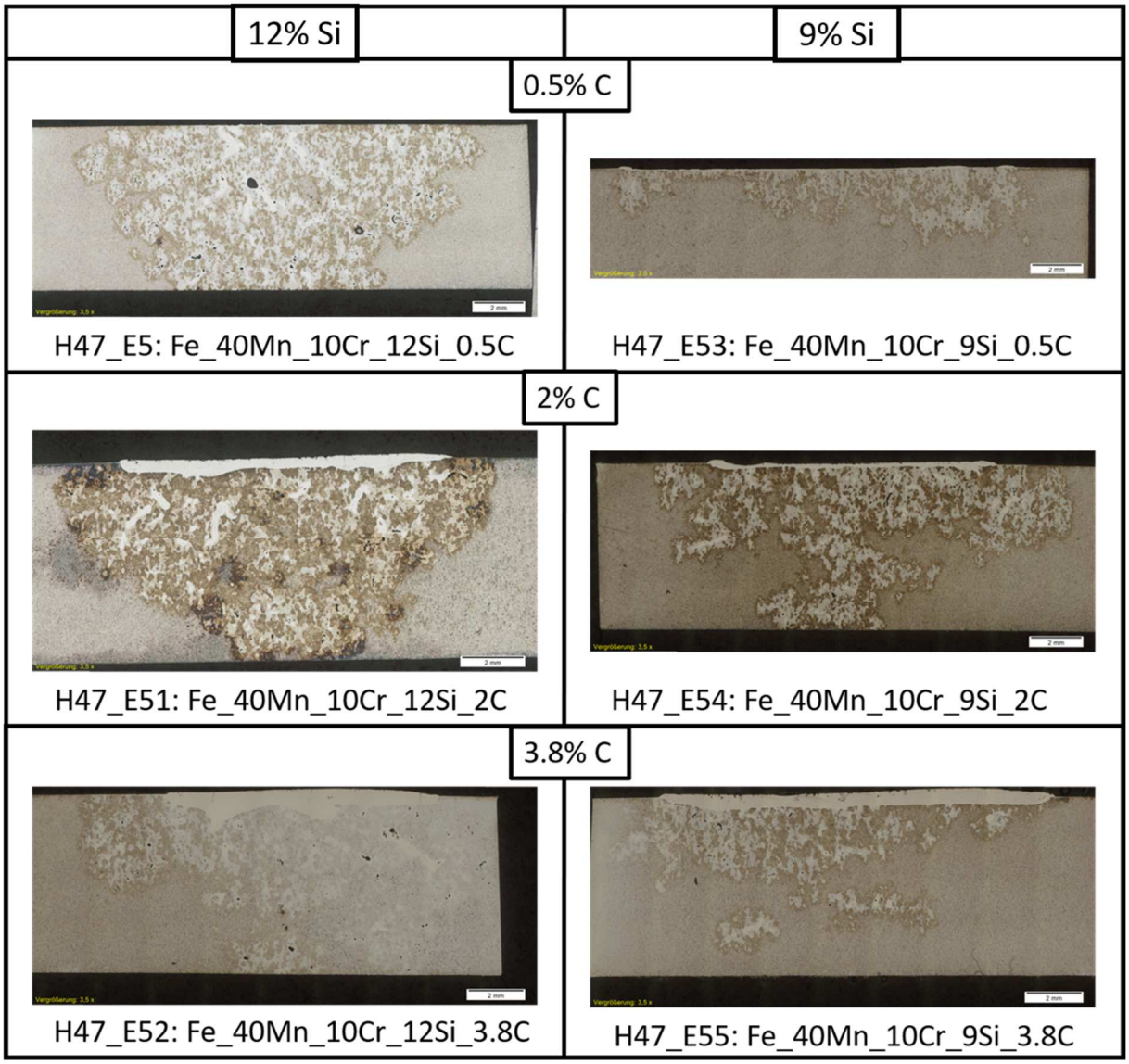

Figure 125 Infiltration of Cr-family H47_E51 studies on Fe + 0.6C Charpy samples at 1300°C under Ar / H_2

Die approbierte gedruckte Originalversion dieser Diplomarbeit ist an der TU Wien Bibliothek verfügbar.
The approved original version of this thesis is available in print at TU Wien Bibliothek.

- **C and Si studies of Cr-Mn family: Interfaces**

H47_E5 C and Si studies: Figure 126 shows the interfaces between MA and the Charpy substrate of the H47_E5 C and Si studies. All samples show an interlocked interface. With increasing C content from top (0.5% C), middle (2% C) to bottom (3.8% C) the interfaces seem to get more defined. H47_E51 on the middle left, H47_E52 on the bottom left and H47_E55 on the bottom right seem to form a more distinguishable interface at some point which might hinder further infiltration at a certain point. This would fit to the bigger residues left on the top of the samples shown in Figure 125.

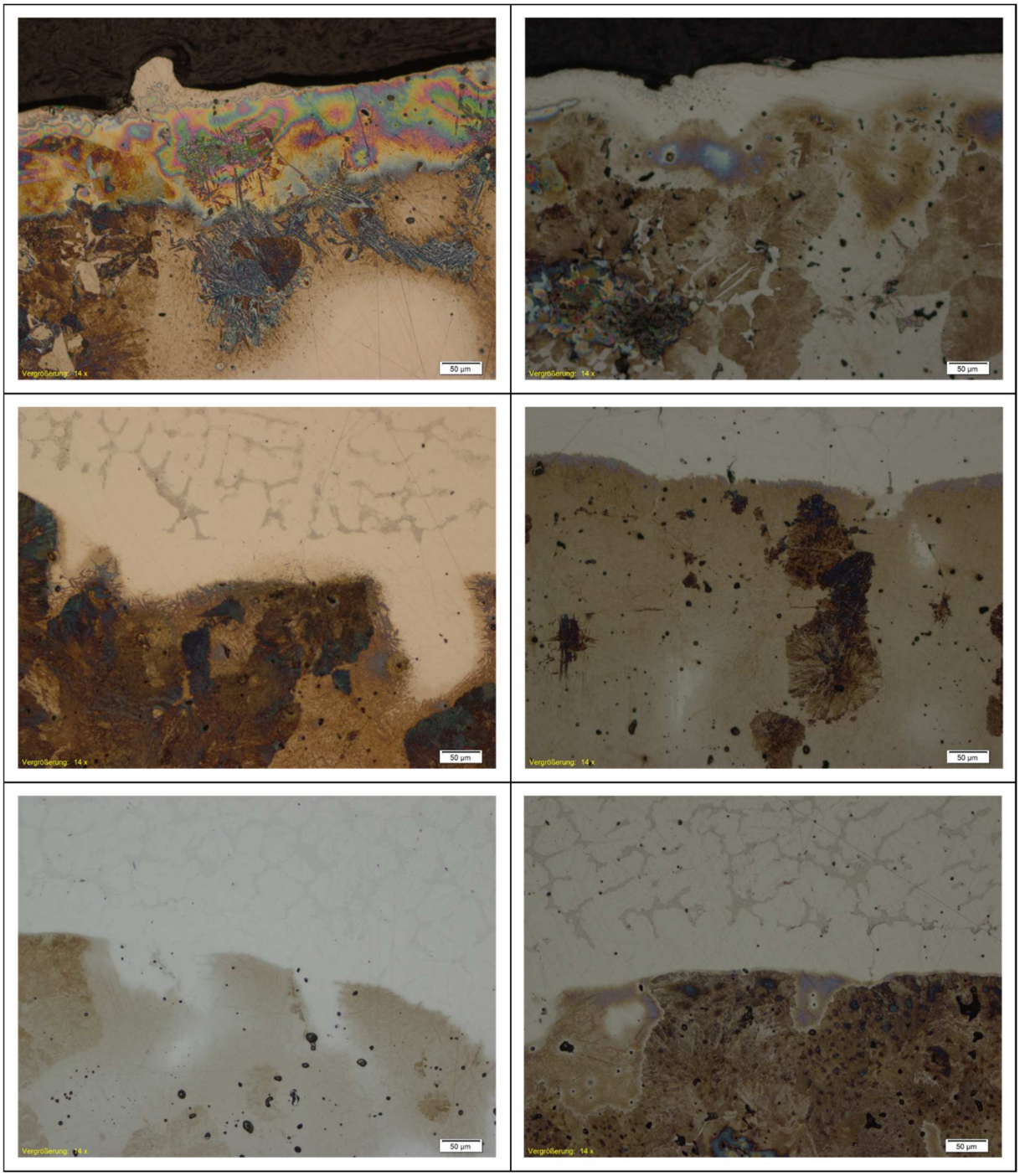

*Figure 126 Interfaces of Cr-Mn family H47_E5 C and Si studies: **12% Si (left)**: H47_E5 (left top), H47_E51 (left middle) H47_E52 (left bottom), **9% Si (right)**: H47_E53 (right top), H47_E54, H47_E54 (right middle), H47_E54, H47_E55 (right bottom)*

Die approbierte gedruckte Originalversion dieser Diplomarbeit ist an der TU Wien Bibliothek verfügbar.
The approved original version of this thesis is available in print at TU Wien Bibliothek.
TU Bibliothek Your knowledge hub WIEN

Die approbierte gedruckte Originalversion dieser Diplomarbeit ist an der TU Wien Bibliothek verfügbar.
The approved original version of this thesis is available in print at TU Wien Bibliothek.

- **DTA experiments with Fe**

These experiments were carried out only for the studies made with variations of C in H45_E1 (Cr family) and variations of Si and C in H47_E5 (Cr-Mn family).

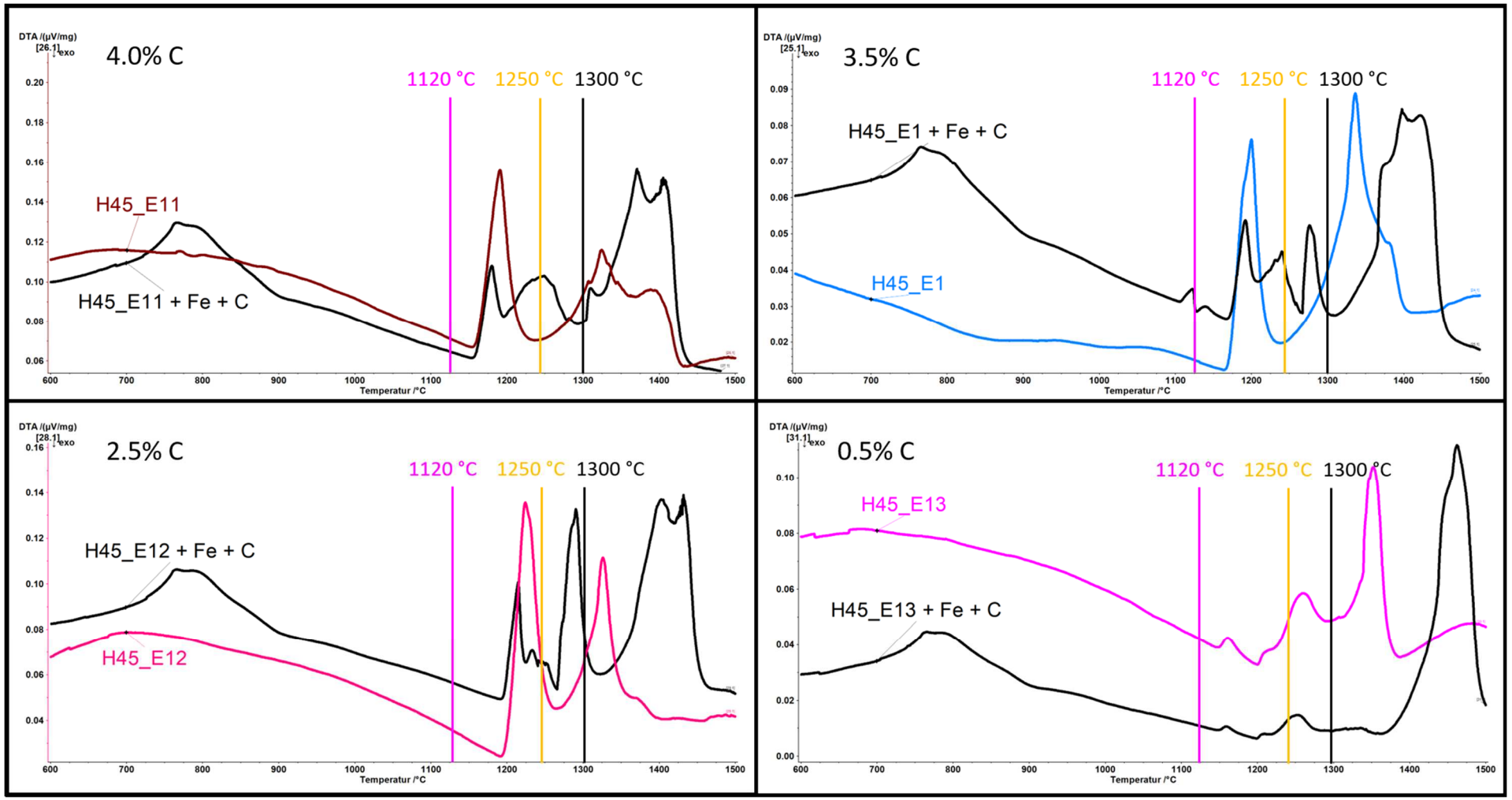

Figure 127 Cr family H45_E1 series DTA and DTA with Fe + C

Die approbierte gedruckte Originalversion dieser Diplomarbeit ist an der TU Wien Bibliothek verfügbar.
The approved original version of this thesis is available in print at TU Wien Bibliothek.

Cr family H45_E1 studies: These DTA experiments were carried out in mixes containing powder from the selected ingot and a powder mix Fe + 0.6 %C powder. The mass ratio between ingot and Fe+0.6 %C mix was 80 : 20 (Fe+C : MA). Figure 127 shows the difference between DTA and DTA + Fe + C for the different modifications. Several additional reactions show up, starting at lower temperatures and showing a major peak around 1400°C. This means that this reaction did not take place during the infiltration experiments – since these were done at lower temperature - and might be an explanation for the residues on top of the infiltration samples. Of course, it should also be considered that the ratio substrate-infiltrant was quite different in case of the infiltration experiments, the substrate acting as a large sink for the infiltrant.

H45_E11: This shows one big additional peak at ~ 1250°C, probably the reaction between the liquid and the Fe + C powder.

H45_E1: This composition shows additional reactions around 1123°C which are unique for the Cr family. Two additional reactions show up around 1240°C and 1276°C which might represent the interaction between liquid and the Fe + C powder but better differentiated due to the fact that the peaks here are sharp and clear to separate from each other.

H45_E12: The DTA graph is like that for H45_E1 besides the first reactions before 1195°C which do not show up in this system. The reaction at 1290°C is much more dominant than in any other of the systems.

H45_E13: This system seems not to interact with the Fe + C powder at all, since the same peaks are found in both DTA measurements. The major peak shifted to higher temperatures shows the melting of the Fe.

Die approbierte gedruckte Originalversion dieser Diplomarbeit ist an der TU Wien Bibliothek verfügbar.
The approved original version of this thesis is available in print at TU Wien Bibliothek.

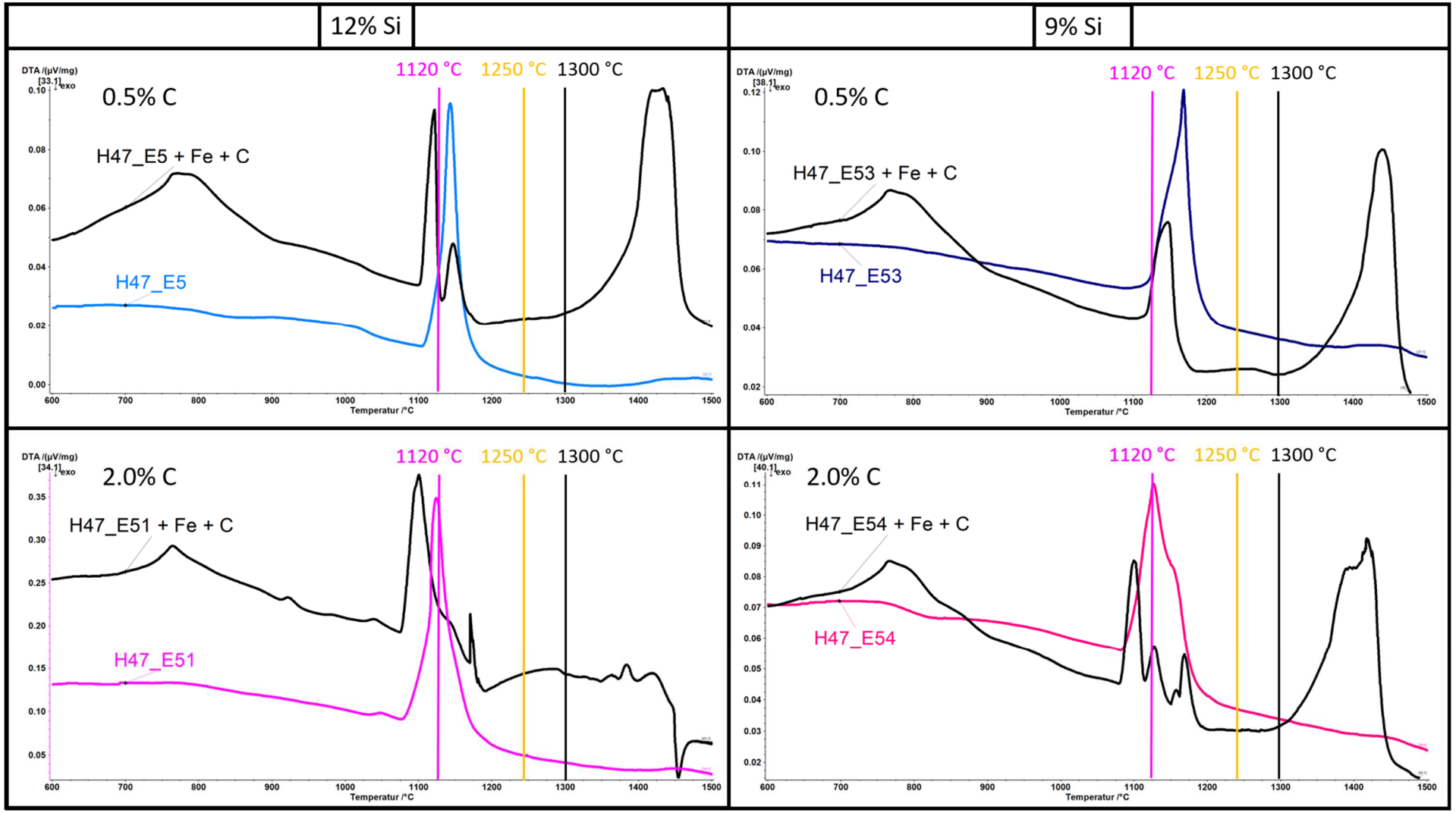

Figure 128 Cr-Mn family H47_E5 series (0.5% and 2% C) DTA and DTA with Fe + C

Die approbierte gedruckte Originalversion dieser Diplomarbeit ist an der TU Wien Bibliothek verfügbar.
The approved original version of this thesis is available in print at TU Wien Bibliothek.

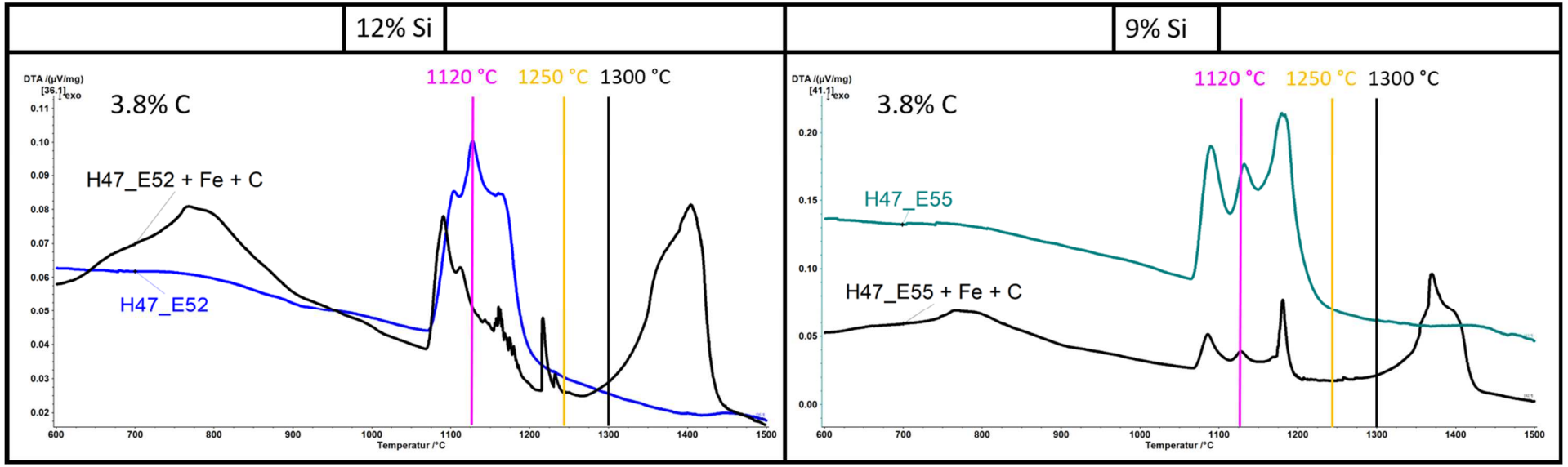

Figure 129 Cr-Mn family H47_E5 series (0.5% and 2% C) DTA and DTA with Fe + C

Cr-Mn family H47_E5 studies: These DTA experiments were carried out in mixes containing powder from the selected ingot and a powder mix Fe + 0.6% C. Once more the mass ratio between ingot and Fe+0.6C mix was 50/50. Figure 128 and Figure 129 show the difference between DTA and DTA + Fe + C for the different modifications. The huge peak shown in most experiments at high temperatures is most likely the melting of the Fe.

0.5% C: H47_E5 with Fe shows three reactions with additional Fe + C. The major peak of the H47_E5 is divided in two different reactions and another reaction shows up at high temperatures. The first two peaks are considered as the forming of the first liquid and the interaction between the liquid and the Fe + C. With less Si only two reactions show up. It can be assumed that the first peak shows reaction and melting at the same time for H47_E3.

2.0% C: DTA measurement for H47_E51 + Fe + C shows only a less dominant peak compared to the master alloy without Fe + C. Some reactions seem to happen at higher temperatures. It could not be clarified if there are endothermal and exothermal reactions happening at the same time or no reactions take place. H47_E54 does not show big residues in infiltration experiments. H47_E54 shows a DTA more similar to high C modifications having three instead of one peak. This is possibly due to the 0.6% C which is enough to change the reaction path from one reaction at more or less the same time to three reactions which can be separated in the DTA.

Die approbierte gedruckte Originalversion dieser Diplomarbeit ist an der TU Wien Bibliothek verfügbar.
The approved original version of this thesis is available in print at TU Wien Bibliothek.

3.8% C: For these modifications in principle no big changes show up besides the huge peak at high temperatures which is assumed to be the melting of the residues. See H47_E52 + Fe + C at 1217°C which could be an additional reaction or just a shift of the three reactions which take place in the pure master alloy.

4. Conclusions

4.1 ThermoCalc

- Theoretical calculations with ThermoCalc turned out to be very useful in predicting tendencies in multi-element systems. They are not always fully accurate but giving a first idea of temperature ranges and tendencies of the influence of different elements

- ThermoCalc seems to have especially difficulties with higher C contents. These problems could be observe with the ternary phase diagrams, comparing them with those from the literature as well as with the predicted behaviour of phases including C.

- A correlation between ThermoCalc calculations and the melting behaviour of the modifications could be observed, showing that C and Si are the key elements to achieve beneficial melting conditions while Cr and Mn determine the “windows” of the optimum C and Si content.

- **Cr family**: ThermoCalc gave a good prediction of the solidus temperature for this system as well as the tendency of the MA to have a broad or a narrow melting window, having some misfits in the liquidus temperature, but still in range.

- **Mn family**: ThermoCalc predictions in terms of melting behaviour and temperatures are in range but not as good as for the Cr-family. Maybe the Cr impurities (~2%) in the H46 base powder play a role in these misfits as well.

- **Cr_Mn family**: ThermoCalc predictions for this family are comparatively bad, which could be expected with an additional alloying element.

- A correlation between ThermoCalc calculations and the infiltration behaviour of the modifications could not be observed. The elemental composition of the liquid phases which remain, and which infiltrate the green bodies could not be determined during this study. Due to the fact that the remaining liquid phase will differ to the MA composition for sure in C and, if present, in Mn content. Due to dissolving, diffusion and in the case of Mn in addition evaporation phenomena it is not possible to proof if the composition of the remaining liquid fits to the ThermoCalc calculation or not.

4.2 Master alloy families

- **General**: Having as much liquid phase formed from the MA at a certain temperature turned out to be not enough for a well infiltrating system. It seems to be more beneficial to have a continuous formation of liquid phase over a certain range.

Die approbierte gedruckte Originalversion dieser Diplomarbeit ist an der TU Wien Bibliothek verfügbar.
The approved original version of this thesis is available in print at TU Wien Bibliothek.
TU Bibliothek Your knowledge hub WIEN

- **General**: Using elemental powder to adjust the desired modifications lead to higher elemental losses than they could be obtained from MA.

- **Cr family**: The C studies with H45_E1 showed that increasing the C content goes along with a broadening of the melting window and a reduction of the ST. However, it seems that the C content influences the formation of an interface**. H45_E11** (4% C) forms an interface most likely at an early stage of the sinter process which completely inhibited the infiltration into the substrate, besides the area where this interface has a breakthrough. With less C in **H45_E1** (3.5% C) no interface could be obtained and a dynamic infiltration could take place. **H45_E2** (2.5% C) forms an interface different to the interface obtained in H45_E11 after a certain amount of liquid phase did infiltrate the sample. The formation of this interface might be related to a change of composition due to the missing elements of the first infiltrating liquid. **H45_E13** (0.5% C) did not melt and along with that no infiltration was possible, but it seems that this MA formed as well an interface between MA and substrate.

- **Cr family**: For this family H45_E1: Fe_40Cr_11Si_3.5C turned out to be infiltrating and having a good solubility under reducing conditions. This system showed a first liquid phase formation below 1250°C.

- **Cr family**: Varying the C content for H45_E1 pointed out that there is a C content range for the system in which the infiltration into a Fe + C green body is enhanced.

- **Mn family**: This family seems very promising due to the possibility to obtain liquidus temperatures below 1120°C. Mn loss was less than expected for Mn rich systems.

- **Mn family**: For this family two systems H46_E4: Fe_40Mn_9Si_3C and H46_E5: Fe_30Mn_9Si_3C presented infiltrating properties under reducing conditions. The Si content seems to play a big role in these systems. Only the systems with the highest Si content (9 wt%) presented a good infiltration behaviour. Significant differences in the formation of MA-substrate interfaces could be obtained, for the samples with 9% Si and those with less Si content. Comparing H46_E3 and H46_5 which differ in 4% Si content show that the higher Si content either inhibits the formation of an inhibiting interface and /or allows more Fe to be dissolved in the liquid phase before it starts to solidify.

- **Cr_Mn family** All systems in this family presented a good infiltration behaviour under reducing conditions. Liquidus temperatures are above 1250°C.

- **Cr_Mn family**: One system H47_E1: Fe_35Mn_14Cr_11Si_3.8C showed reproducible infiltrating behaviour even under inert conditions (Ar atmosphere and Fe substrates). H47_E5: Fe_30Mn_10Cr_12Si_0.5C was fully infiltrating leaving no residues behind. No crater was observed in the upper part of the infiltrated samples which indicates

Die approbierte gedruckte Originalversion dieser Diplomarbeit ist an der TU Wien Bibliothek verfügbar.
The approved original version of this thesis is available in print at TU Wien Bibliothek.
TU Bibliothek Your knowledge hub WIEN

that either dissolution of the substrate was negligible or that infiltration occurred well before the dissolution was significant.

- **Cr_Mn family**: C and Si variations on H47_E5: Fe_30Mn_10Cr_12_0.5C pointed out the significant influence of these elements on the infiltration behaviour of the alloy. From the variations in C and Si it was concluded that H47_E5 presented the optimal contents of Si and C. Lower Si contents decrease the infiltration distance. With a similar Si content but increasing amounts of C the melting range is broadened, more ingot residues are found on top of the infiltrated samples and the infiltration process seems to be worsen. The broadening of the melting range leads to a smaller amount of liquid phase at lower temperatures, which might lead to an infiltration of the first liquid changing the melting behaviour of the residue, which probably never melts due to the compositional change or leads to a formation of an interface between the remaining MA and the substrate which inhibits further infiltration.

- **General:** Wetting experiments turned out as expected better wetting behaviour being observed for all MA systems under reducing conditions.

- **DTA experiments of ingot powder mixed with Fe** showed that for H45_E1 modifications, additional reactions take place. This might be an indication of the presence of dissolutive processes. However, in H47_E5 the DTA signals in the ingot and ingot + Fe mixes did not show such significant differences. This might be an indication that dissolutive phenomena between liquid phase and solid Fe are less intense for this alloy. This latter hypothesis would be in agreement with the findings described in the infiltration experiments. Ingots with H47_E5 composition present no crater on top of the sample after the infiltration experiment

Summary: The initial aims of the work could be achieved. It was possible to find at least one variation for each master alloy family which could be optimized in terms of alloying element content, melting and infiltration behaviour**. The Si and C content seem to play a major** role in determining these different properties, while Cr, Fe and Mn have an influence on the content of Si and C needed to achieve a certain property of the liquid phase. Si and C seem to have an influence on the formation of interfaces between MA and the Charpy substrates as well.

Die approbierte gedruckte Originalversion dieser Diplomarbeit ist an der TU Wien Bibliothek verfügbar.
The approved original version of this thesis is available in print at TU Wien Bibliothek.
TU Bibliothek Your knowledge hub WIEN

5. References

1. Gierl, C., *Vorsintern von PM-Eisenbasiswerkstoffen*, Diplomarbeit, TU Wien, Wien, (1996).
2. Wolfsgruber, E., *Sintern von PM-Stählen im Bereich der Ferrit-Austenit Umwandlung*, Dissertation, Technisch-Naturwissenschaftliche Fakultät, TU Wien, Wien, (1996).
3. Khraisat, W., *Liquid phase sintering of coarse steel powder*, Departement of Materials Science and Engineering, Chalmers university of technology, Göteborg, Sweden, (2003).
4. Sundaram, M.V., *Novel approaches for achieving full density powder metallurgy steels*, Doctor of Philosophy, Department of Industrial and Materials Science, Chalmers University of Technology, Göteborg, (2019).
5. Castro Pinto, F.S., M.; Baumgaertner, F.; Dougan, M.; Mitchell, S.; Lipp, K.; Bender, H.; Coffin, C.; Dunkley, J. *Alloying and sintering behaviour of selected iron-graphite-master alloy powder mixtures*. in Proc. EuroPM 2005 Prague, new opportunities in a new Europe, **Prague**. (2005): **Vol.3**: p. 7.
6. Zhang, Z.Y. and Sandstrom, R., *Fe-Mn-Si master alloy steel by powder metallurgy processing.* Journal of Alloys and Compounds, (2004). **363**(1-2): p. 194-202. DOI: 10.1016/s0925-8388(03)00462-6.
7. Klein, A.N., Oberacker, R. and Thummler, F., *High-Strength Si-Mn-Alloyed Sintered Steels - Microstructure and Mechanical-Properties.* Powder Metallurgy International, (1985). **17**(1): p. 13-16.
8. Danninger, H. and Gierl, C., *Processes in PM steel compacts during the initial stages of sintering.* Materials Chemistry and Physics, (2001). **67**(1-3): p. 49-55. DOI: 10.1016/s0254-0584(00)00419-3.
9. Cias, A., *Chemical reactions during sintering of Fe-Cr-Mn-Si-Ni-Mo-C-steels with special reference to processing in semi-closed containers.* Science of Sintering, (2015). **47**(1): p. 61-69. DOI: 10.2298/sos1501061c.
10. Danninger, H., *Homogenization and Pore Formation during Sintering with Transient Liquid-Phase.* Powder Metallurgy International, (1988). **20**(1): p. 21-25.
11. Youseffi, M. and Chong, K.Y., *Enhanced sintering and mechanical properties of 316L stainless steel with silicon additions as sintering aid.* Powder Metallurgy, (2003). **46**(1): p. 30-38. DOI: Doi 10.1179/003258903225010460.
12. Gierl, C., *Herstellung von Pm-Formteilen durch optimiertes Sintern*, Dissertation, E161 Institut für chemische Technologie anorganischer Stoffe, TU Wien, Vienna, (2000).
13. Voorhees, P.W., *Ostwald ripening of two-phase mixtures.* Annual Review of Materials Science, (1992). **22**(1): p. 197-215.
14. Kingery, W., *Densification during sintering in the presence of a liquid phase. I. Theory.* Journal of Applied Physics, (1959). **30**(3): p. 301-306.
15. de Oro Calderon, R., Campos, M., Torralba, J.M. and Capdevila, C., *Lean alloys in PM: from design to sintering performance.* Powder Metallurgy, (2012). **55**(4): p. 294-301. DOI: 10.1179/1743290112y.0000000016.
16. Üregen, B., Gierl-Mayer, C. and Danninger, H., *Phosphorus in Sintered Steels: Effect of Phosphorus Content and P Carrier in Sintered Steel Fe-C-P.* Powder Metallurgy Progress, (2016). **16**(1): p. 1-13.

Die approbierte gedruckte Originalversion dieser Diplomarbeit ist an der TU Wien Bibliothek verfügbar.
The approved original version of this thesis is available in print at TU Wien Bibliothek.
TU Bibliothek Your knowledge hub WIEN

17. Klocke, F., *Fertigungsverfahren 5: Gießen, Pulvermetallurgie, Additive Manufacturing*. 4 ed. VDI-Buch. Springer Vieweg, Berlin Heidelberg (2015): p. 172.
18. Danninger, H., *Pore formation during sintering of Fe-Cu and its effects on mechanical properties.* Powder Metall. Int., (1987). **19**(No.1): p. 5.
19. Azadbeh, M. and Ahmadi, N.P., *Effect of alloying contents and processing factors on the microstructure and homogenization of Si alloyed Cr–Mo sintered steels.* Current Applied Physics, (2009). **9**(4): p. 777-782. DOI: 10.1016/j.cap.2008.
20. Kieback, B. and Schatt, W., *Anwendung eines kurzzeitigen Flüssigphasensinterns für die Herstellung von Fe-Ti-Sinterlegierungen.* Planseeberichte für Pulvermetallurgie, (1980). **Band 28**: p. 204 - 215.
21. de Oro Calderon, R., Dunkley, J., Gierl, C. and Danninger, H., *New opportunities for master alloys: Ultra-high pressure water atomised powders.* Powder Metallurgy Review, Inovar Communications Ltd, (2019). **8**: p. 55 - 66.
22. Youseffi, M., Wright, C. and Jeyacheya, F., *Effects of silicon addition and process conditions upon α-phase sintering, sinter hardening, and mechanical properties of Fe-1.5 Mo powder.* Powder Metallurgy, (2002). **45**(1): p. 53-62.
23. Klein, A.N., Oberacker, R. and Thümmler, F., *High-Strength Si-Mn-Alloyed Sintered Steels - Sinterability and Homogenization.* Powder Metallurgy International, (1985). **17**(2): p. 71-74.
24. A.N.Klein, R.Oberacker and Thümmler, F., *Development of new high strength Si-Mn-alloyed sintered steels.* Modern Developments in Powder Metallurgy, (1983): p. 141 - 152.
25. Wu, M.W. and Cai, W.Z., *The Promotion of Liquid Phase Sintering of Boron-Containing Powder Metallurgy Steels by Adding Nickel*, in *2015 4th International Conference on Engineering and Innovative Materials*, C. Guojian and Y. Muhammad, Editors. (2015).
26. Narasimhan, K.S., Lindsley, B., Sokolowski, P. and Nishida, T., *Lower Cost Solutions For Higher Performance Powder Metallurgical Parts.* Journal of the Japan Society of Powder and Powder Metallurgy, (2010). **57**(2): p. 96-105. DOI: 10.2497/jjspm.57.96.
27. Zhang, Z., Frisk, K., Salwen, A. and Sandstrom, R., *Mechanical properties of Fe-Mo-Mn-Si-C sintered steels.* Powder Metallurgy, (2004). **47**(3): p. 239-246. DOI: 10.1179/003258904225015572.
28. Zapf, G. and Dalal, K., *Introduction of high oxygen affinity elements manganese, chromium, and vanadium in the powder metallurgy of P/M parts.* Modern Developments in Powder Metallurgy, (1977). **10**: p. 129-152.
29. Dai, H., Wang, L.M., Zhang, J.G., Liu, Y.B., Wang, Y.F., Wang, L. and Wan, X.L., *Iron based partially pre-alloyed powders as matrix materials for diamond tools.* Powder Metallurgy, (2015). **58**(2): p. 83-86. DOI: 10.1179/0032589915z.000000000220.
30. *Master Alloys and Alloying Additives Information*. 2019 [cited 2019 11.04.2019]; Available from: https://www.globalspec.com/learnmore/materials_chemicals_adhesives/metals_alloys/master_alloys_alloying_additives
31. Sundaram, M.V., Surreddi, K.B., Hryha, E., Veiga, A., Berg, S., Castro, F. and Nyborg, L., *Enhanced Densification of PM Steels by Liquid Phase Sintering with Boron-Containing Master Alloy*. Metallurgical and Materials Transactions a-Physical Metallurgy and Materials Science, (2018). **49A**(1): p. 255-263. DOI: 10.1007/s11661-017-4383-4.
32. Vassileva, V., Danninger, H., Strobl, S., Gierl-Mayer, C., de Oro Calderon, R. and Hutter, H., *The Role of the Atmosphere on Boron-Activated Sintering of Ferrous Powder*

Die approbierte gedruckte Originalversion dieser Diplomarbeit ist an der TU Wien Bibliothek verfügbar.
The approved original version of this thesis is available in print at TU Wien Bibliothek.
TU Bibliothek Your knowledge hub WIEN

Compacts. Powder Metallurgy Progress, (2018). **18**(1): p. 6-20. DOI: 10.1515/pmp-2018-0002.
33. Gierl, C., Zbiral, J. and Danninger, H. *Enhanced Sintering of PM Steels by Addition of Fe-Ni-B Masteralloy*. in Proc.Euro PM2014, **Salzburg, Österreich**. (2014): Low Alloy Steels: p. 6(on CD).
34. de Oro Calderon, R., Bernardo, E., Campos, M. and Torralba, J.M. *Liquid phase sintering: Spreading, wetting and infiltration behavior in a successful reference system, Fe-C-Cu*. in Proceedings of the Euro International Powder Metallurgy Congress and Exhibition, Euro PM 2011, **Barcelona, Spain**. (2011): Sintering: Fundamentals: p. 6.
35. Bernardo, E., de Oro Calderon, R., Campos, M. and Torralba, J.M., *Wetting phenomena for liquid Cu and Cu alloys on Fe-base substrate.* Advanced Powder Technology, (2016). **27**(3): p. 1027-1035. DOI: 10.1016/j.apt.2016.05.004.
36. Chen, M.-H., *Liquid phase sintering of iron with copper base alloy powders*, M.E. thesis, Materials and Molecular research Division Lawrence Berkeley Laboratory and Department of Mechanical Engineering, University of California, Berkeley, California 94720, (1976 (Publication Date: 02.09.2010)).
37. Berner, D., Exner, H.E. and Petzow, G., *Swelling of Iron-Copper Mixtures During Sintering and Infiltration.* Modern Developments in Powder Metallurgy, (1974). **6**: p. 237 -250.
38. Huppmann, W.J., Kaysser, W. and Esper, F.J., *Sintern von Eisen–Mangan mit Zinnzusätzen.* Materialwissenschaft und Werkstofftechnik, (1976). **7**(5): p. 190-192. DOI: 10.1002/mawe.19760070507.
39. Danninger, H., Frauendienst, G., Streb, K.-D. and Ratzi, R., *Dissolution of different graphite grades during sintering of PM steels.* Materials Chemistry and Physics, (2001). **67**(1-3): p. 72-77.
40. Salak, A., *Sintered Manganese Steels. I.-- Effect of Structure of Initial Iron Powders Upon Mechanical Properties.* Powder Metall. Int., (1980). **12**(1): p. 28-31.
41. Salak, A., *Sintered Manganese Steels. II.--Manganese Evaporation During Sintering.* Powder Metall. Int., (1980). **12**(2): p. 72-75.
42. Danninger, H. and Gierl, C., *New Alloying Systems for Ferrous Powder Metallurgy Precision Parts.* Science of Sintering, (2008). **40**(1): p. 33-46. DOI: 10.2298/SOS0801031D.
43. Vassileva, V., Krecar, D., Tomastik, C., Gierl-Mayer, C., Hutter, H. and Danninger, H., *Phosphorus in sintered steels: impact fracture behaviour of sintered Fe-P with varying P content.* Powder Metallurgy Progress, (2015). **15**(1): p. 36 - 49.
44. Danninger, H., Jaliliziyaeian, M., Gierl, C., Hryha, E. and Bengtsson, S., *Sintered steels prealloyed with manganese - chances and risks.* World Powder Metallurgy Congress and Exhibition, World PM 2010; Florence; Italy; 10 October 2010 through 14 October 2010, (2010). **3**: p. 3 - 10.
45. Salak, A., *Manganese vapor-protection of premixed manganese steels against oxidation during sintering.* Powder Metall. Int., (1986). **18**(4): p. 266.
46. E. Rat, *Verordnung (EG) Nr. 428/2009 des Rates vom 5. Mai 2009 über eine Gemeinschaftsregelung für die Kontrolle der Ausfuhr, der Verbringung, der Vermittlung und der Durchfuhr von Gütern mit doppeltem Verwendungszweck (Neufassung)*, (428/2009), **1C240**, EUR-Lex, (2009).
47. Tahir, A.M., Amberg, G., Hedstrom, P., Bergman, O., Chasoglou, D. and Frisk, K., *Behaviour of master alloy during sintering of PM steels: redistribution and dimensional*

Die approbierte gedruckte Originalversion dieser Diplomarbeit ist an der TU Wien Bibliothek verfügbar.
The approved original version of this thesis is available in print at TU Wien Bibliothek.
TU Bibliothek Your knowledge hub WIEN

variations. Powder Metallurgy, (2015). **58**(2): p. 133-141. DOI: 10.1179/1743290114y.0000000117.
48. Xiu, Z., Salwen, A., Qin, X., He, F. and Sun, X., *Sintering behaviour of iron-molybdenum steels withtheadditionof Fe-B-C master alloy powders.* Powder metallurgy, (2003). **46**(2): p. 171-174.
49. Bernardo, E., de Oro Calderon, R., Campos, M. and Torralba, J.M., *New Findings on the Wettability and Spreading of Copper on Iron-Base Substrates.* International Journal of Powder Metallurgy, (2015). **51**(4): p. 29-36.
50. Khraisat, W. and Nyborg, L., *Liquid phase sintering of ferrous powder by carbon and phosphorus control.* Powder Metallurgy, (2003). **46**(3): p. 265-270. DOI: 10.1179/003258903225008535.
51. de Oro Calderon, R., Bernardo, E., Campos, M., Gierl-Mayer, C., Danninger, H. and Torralba, M.J., *Liquid Phases Tailored for Introducing Oxidation-Sensitive Elements through the Master Alloy Route.* Journal of the Japan Society of Powder and Powder Metallurgy, (2016). **63**(4): p. 172-184. DOI: 10.2497/jjspm.63.172.
52. Kariyawasam, N.C., *Advances in Sintering of Powder Metallurgy Steels*, McMasters University, (2017).
53. Banerjee, S., Gemenetzis, V. and Thümmler, F., *Liquid Phase Formation During Sintering of Low-Alloy Steels with Carbide-Base Master Alloy Additions.* Powder Metallurgy, (1980). **23**(3): p. 126-129. DOI: 10.1179/pom.1980.23.3.126.
54. Danninger, H., Garmendia Gutierrez, J.M., Ratzi, R. and Seyrkammer, J., *Reactive sinter brazing of ferrous PM parts using iron-carbon fillers.* Powder Metallurgy Progress, (2010). **10**: p. 12.
55. Flegler, S.L., Heckman, J.W. and K.L., K., *Elektronenmikroskopie : Grundlagen - Methoden - Anwendungen*. Spektrum Akademischer Verlag, Heidelberg (1995): p. 279.
56. Harris, K.D.M. and Tremayne, M., *Crystal Structure Determination from Powder Diffraction Data.* Chemistry of Materials, (1996). **8**(11): p. 2554-2570. DOI: 10.1021/cm960218d.
57. Brouwer, P., *Theory of XRF: Getting acquainted with the principles*. 3rd Edition ed., Panalytical, The Netherlands, Almelo (2010). 62.
58. Villars, P., Prince, A. and Okamoto, H., *Handbook of ternary alloy phase diagrams*. Cu-Mg-Si - Ga-Hg-Te. ASM International, Materials Park, Ohio Vol. 8. (1995): p. 9690 - 9691, 9812 - 9817, 10430 - 10431. 7.
59. H.Baker, S.D.Henry and Okamoto, H., *ASM handbook*. Alloy phase diagrams. Materials Park, Ohio : ASM International, Materials Park, Ohio (1992): p. 79-625. 546.
60. Villars, P., Prince, A. and Okamoto, H., *Handbook of ternary alloy phase diagrams*. B-Ba-Ir - C-Ga-V. ASM International, Materials Park, Ohio Vol. 5. (1995): p. 5332 - 5335, 6616 - 6627, 6730 - 6731. 15.
61. Straffelini, G., Fontanari, V., Molinari, A. and Tesi, B., *Tensile and Fatigue Behaviour of Phosphorus Alloyed Sintered Steels.* Powder Metallurgy, (1993). **36**(2): p. 135-141. DOI: 10.1179/pom.1993.36.2.135.
62. Raghavan, V., *Phase diagrams of ternary iron alloys Part 3*. Monograph series on alloy phase diagrams. Indian Institute of Metals, Delhi (1988): p. 11. 33 - 44.
63. Villars, P., Prince, A. and Okamoto, H., *Handbook of ternary alloy phase diagrams*. Co-Fe-Ni - Cu-Mg-Sb. ASM International, Materials Park, Ohio Vol. 7. (1995): p. 8894 - 8895. 1.
64. Raghavan, V., *Phase diagrams of ternary iron alloys Part 6A*. Monograph series on alloy phase diagrams. Indian Institute of Metals, Delhi (1992): p. 11. 523 - 534.

Die approbierte gedruckte Originalversion dieser Diplomarbeit ist an der TU Wien Bibliothek verfügbar.
The approved original version of this thesis is available in print at TU Wien Bibliothek.
TU Bibliothek Your knowledge hub WIEN

65. Shoemaker, C.B., Shoemaker, D.P., Hopkins, T.E. and Yindepit, S., *Refinement of the structure of ß-manganese and of a related phase in the Mn–Ni–Si system.* Acta Crystallographica Section B Structural Crystallography and Crystal Chemistry, (1978). **34**(12): p. 3573-3576. DOI: 10.1107/s0567740878011620.
66. Liu, T.F. and Wu, C.C., *ß-Mn structure in an Fe-Al-Mn-Cr alloy.* Scripta Metallurgica, (1989). **23**(7): p. 1087-1092. DOI: 10.1016/0036-9748(89)90305-0.
67. Prior, T.J. and Battle, P.D., *Facile synthesis of interstitial metal nitrides with the filled ß-manganese structure.* Journal of Solid State Chemistry, (2003). **172**(1): p. 138-147. DOI: 10.1016/s0022-4596(02)00171-8.
68. Raynor, G.V. and Rivilin, V.G., *Phase equilibria in iron ternary alloys. A critical assessment of the experimental literature*. Institute of Metal books. Institute of Metals, London (1988): p. 143-156. 13.

Die approbierte gedruckte Originalversion dieser Diplomarbeit ist an der TU Wien Bibliothek verfügbar.
The approved original version of this thesis is available in print at TU Wien Bibliothek.
TU Bibliothek Your knowledge hub WIEN

Die approbierte gedruckte Originalversion dieser Diplomarbeit ist an der TU Wien Bibliothek verfügbar.
The approved original version of this thesis is available in print at TU Wien Bibliothek.

6. Attachment

6.1 Infiltration experiments

- **Cr family**

Figure 130 shows the results of the infiltration experiments under inert and under reducing conditions for the Cr family.

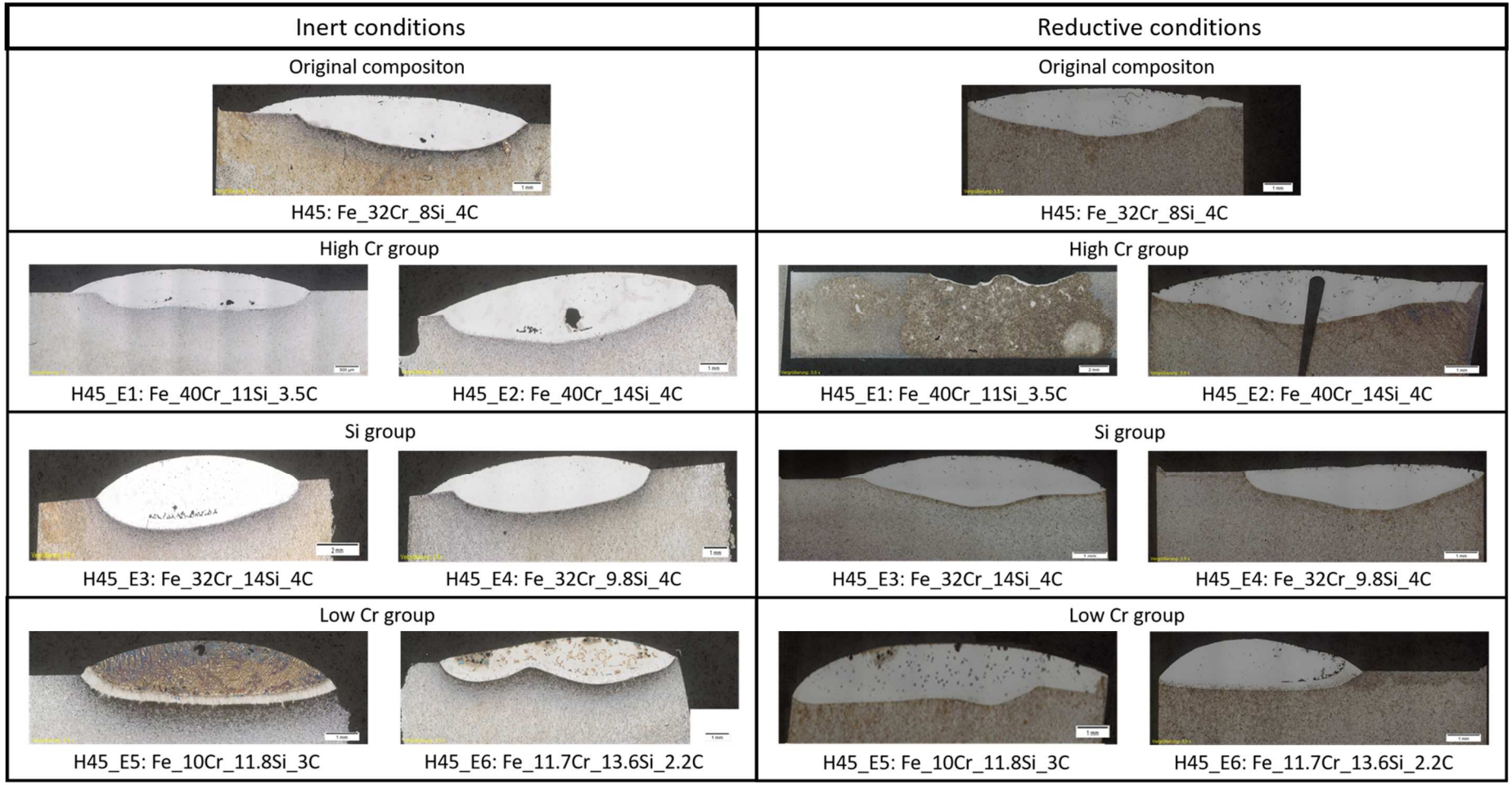

Figure 130 Infiltration of Cr-family on Fe Charpy samples at 1300°C under Ar (left), Infiltration of Cr-family on Fe +0.6C Charpy samples at 1300°C under Ar /H_2 (right)

Die approbierte gedruckte Originalversion dieser Diplomarbeit ist an der TU Wien Bibliothek verfügbar.
The approved original version of this thesis is available in print at TU Wien Bibliothek.

- **Mn family**

Figure 131 shows the results of the infiltration experiments under inert and under reductive conditions for the Mn family.

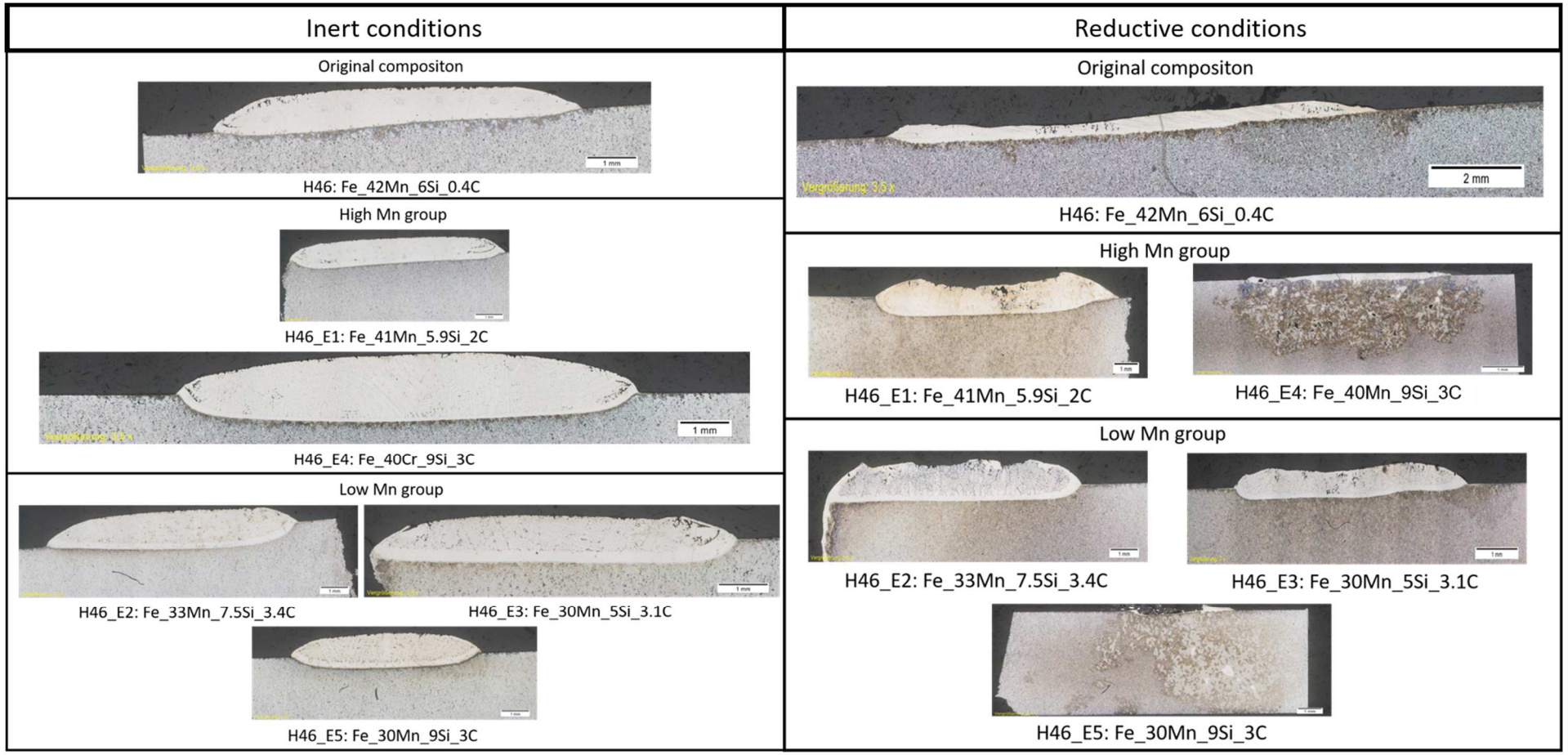

Figure 131 Infiltration of Mn-family on Fe Charpy samples at 1300°C under Ar (left), Infiltration of Mn-family on Fe +0.6C Charpy samples at 1300°C under Ar /H_2 (right)

Die approbierte gedruckte Originalversion dieser Diplomarbeit ist an der TU Wien Bibliothek verfügbar.
The approved original version of this thesis is available in print at TU Wien Bibliothek.

- **Cr-Mn family**

Figure 132 shows the results of the infiltration experiments under inert and under reductive conditions for the Mn family.

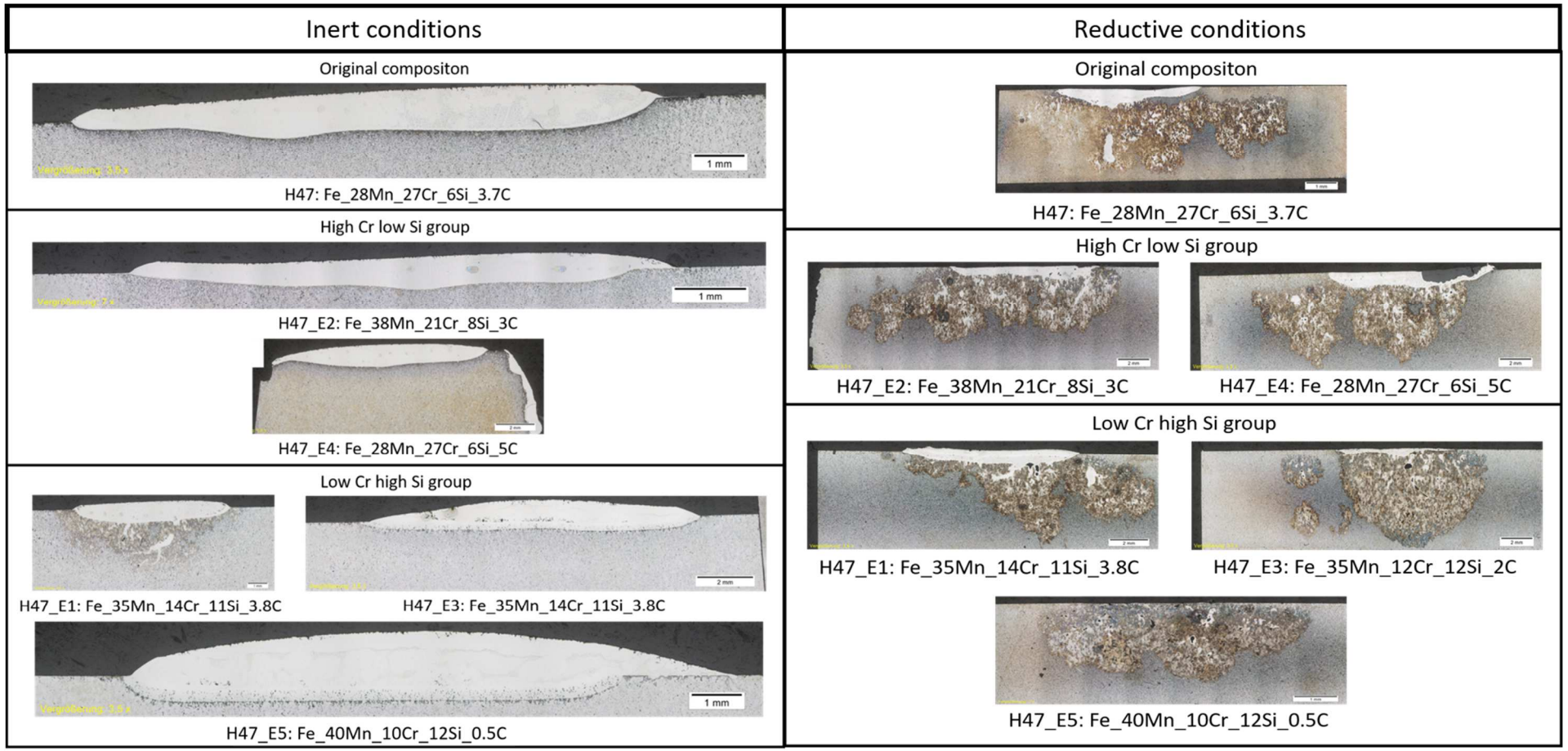

Figure 132 Infiltration of Cr-Mn family on Fe Charpy samples at 1300°C under Ar (left), Infiltration of Cr-Mn family on Fe +0.6C Charpy samples at 1300°C under Ar /H_2 (right)

Die approbierte gedruckte Originalversion dieser Diplomarbeit ist an der TU Wien Bibliothek verfügbar.
The approved original version of this thesis is available in print at TU Wien Bibliothek.

6.2 Wetting experiments

- **Cr family**

Figure 133 shows the results of the wetting experiments under inert and under reductive conditions for the Cr family.

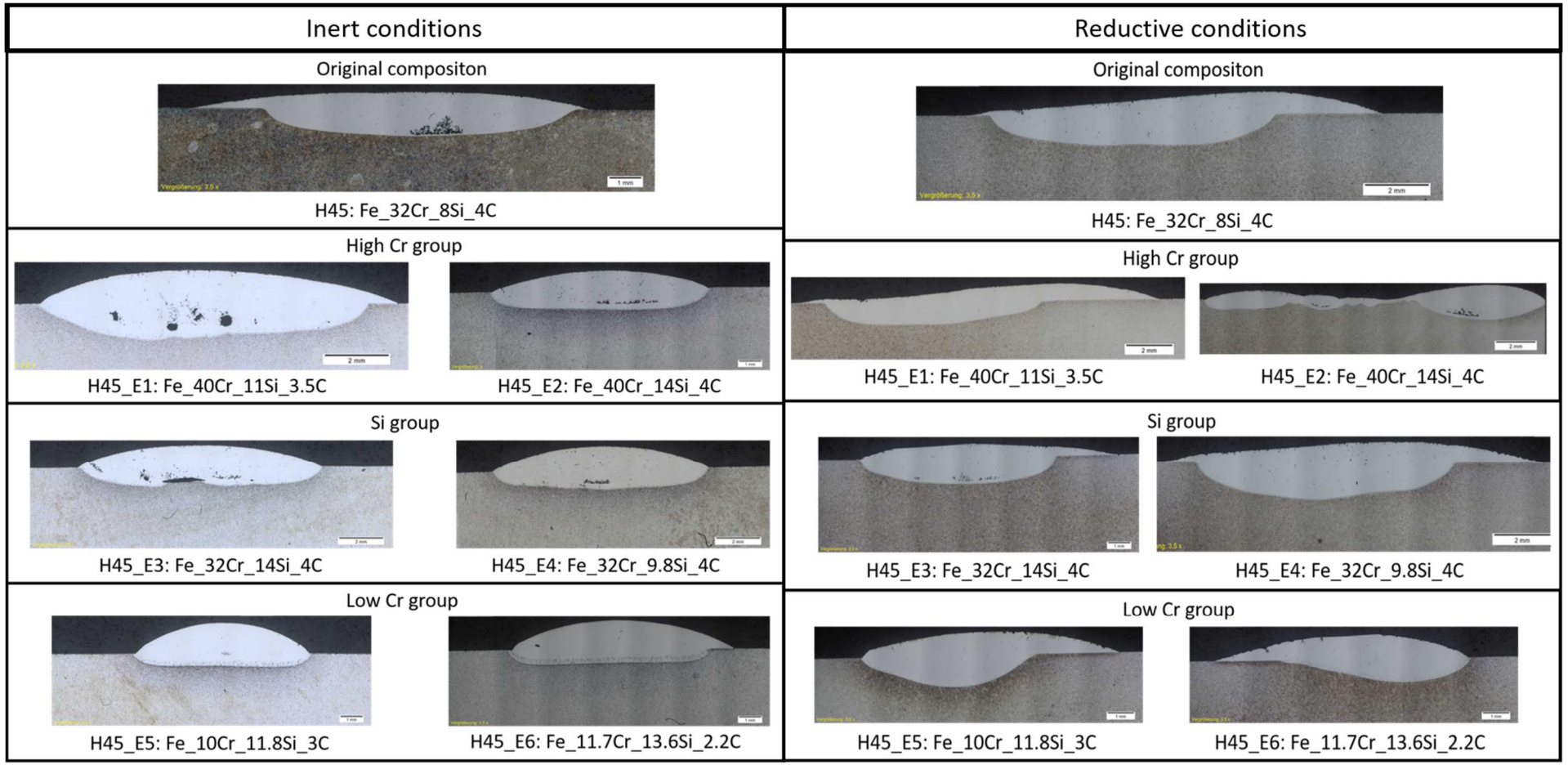

Figure 133 Wetting of Cr family on Fe Charpy samples at 1300°C under Ar, (left), Wetting of Cr family on Fe + 0.8C Charpy samples at 1300°C under Ar /H_2 (right)

Die approbierte gedruckte Originalversion dieser Diplomarbeit ist an der TU Wien Bibliothek verfügbar.
The approved original version of this thesis is available in print at TU Wien Bibliothek.

- **Mn family**

Figure 134 shows the results of the wetting experiments under inert and under reductive conditions for the Mn family.

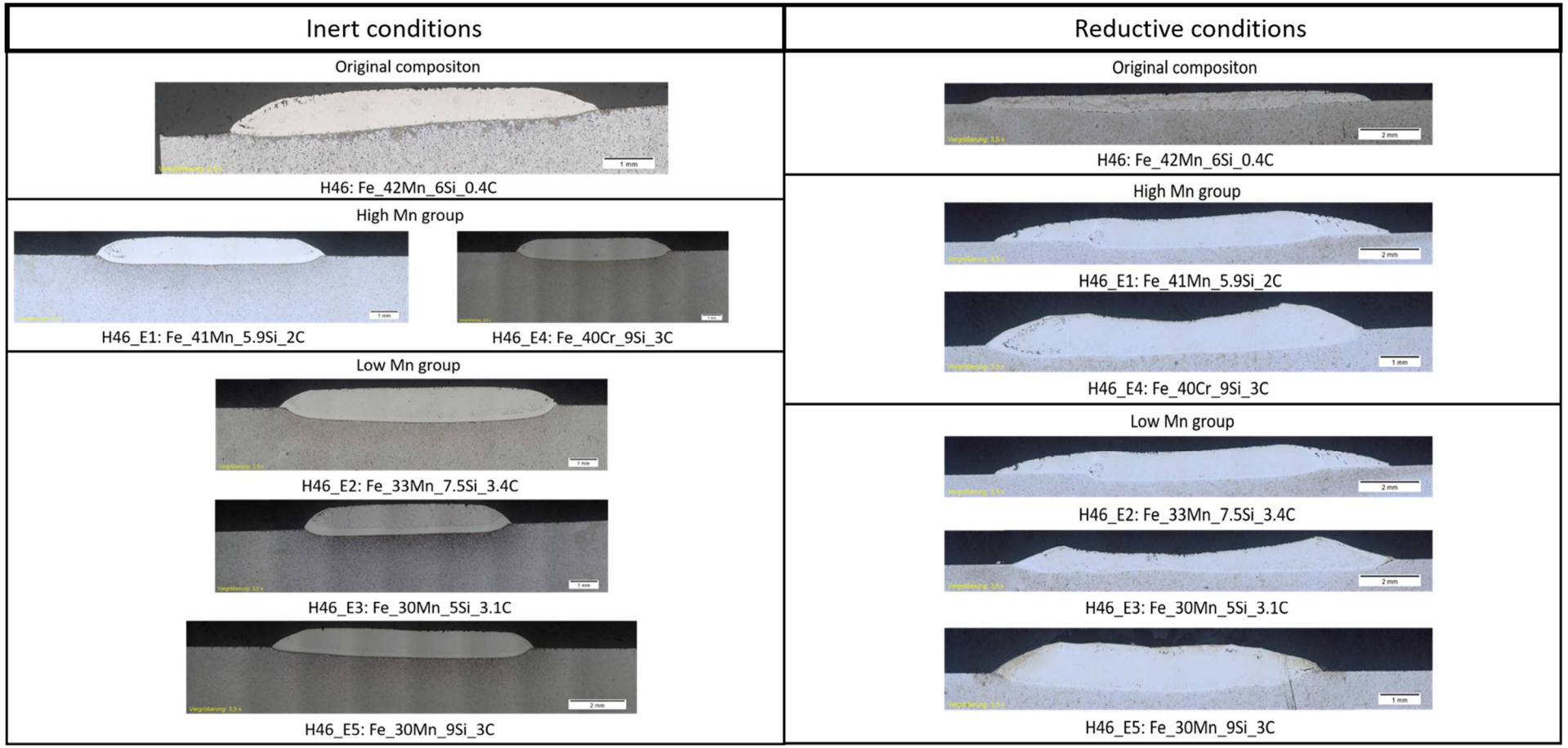

Figure 134 Wetting of Mn family on Fe Charpy samples at 1300°C under Ar, (left), Wetting of Mn family on Fe + 0.8C Charpy samples at 1300°C under Ar /H_2 (right)

Die approbierte gedruckte Originalversion dieser Diplomarbeit ist an der TU Wien Bibliothek verfügbar.
The approved original version of this thesis is available in print at TU Wien Bibliothek.

- **Cr-Mn family**

Figure 135 shows the results of the wetting experiments under inert and under reductive conditions for the Cr-Mn family.

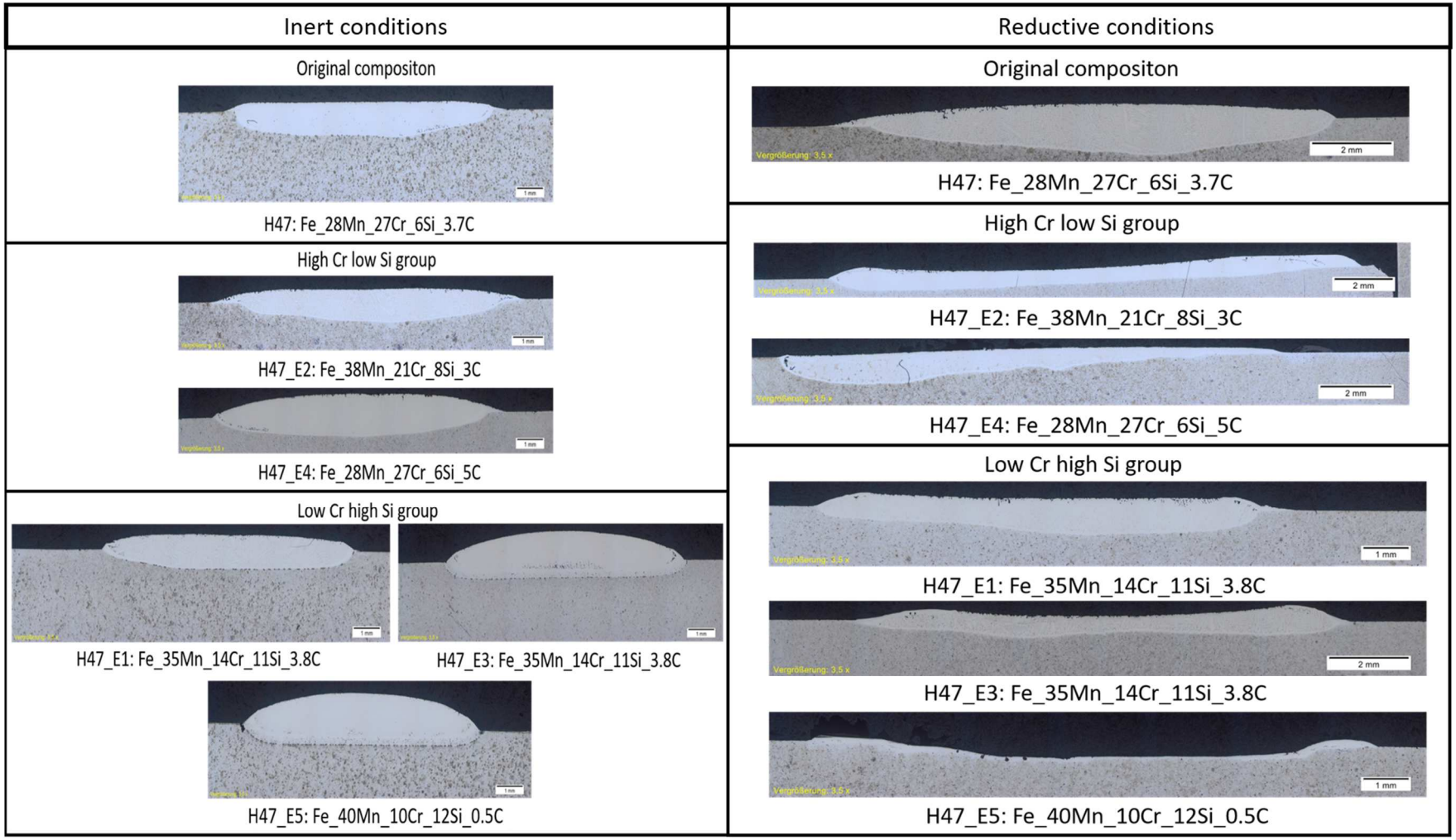

Figure 135 Wetting of Cr-Mn family on Fe Charpy samples at 1300°C under Ar, (left), Wetting of Cr-Mn family on Fe + 0.8C Charpy samples at 1300°C under Ar /H_2 (right)

Die approbierte gedruckte Originalversion dieser Diplomarbeit ist an der TU Wien Bibliothek verfügbar.
The approved original version of this thesis is available in print at TU Wien Bibliothek.

6.3 Detailed overview of the MA ingots

The ingots were molten at 1300°C under Ar/10%H_2 for 1h and characterized with DTA, XRD, LECO and REM in terms of melting behaviour, composition and phases. Linking the phases between ThermoCalc calculations, XRD and SEM results was attempted

H45: Fe_32Cr_8Si_4C

Figure 136 shows the DTA measurement of H45. Under the conditions used for melting the ingots (1200°C), this composition might not melt completely as the DTA graph shows the last endothermic peak at 1335°C.

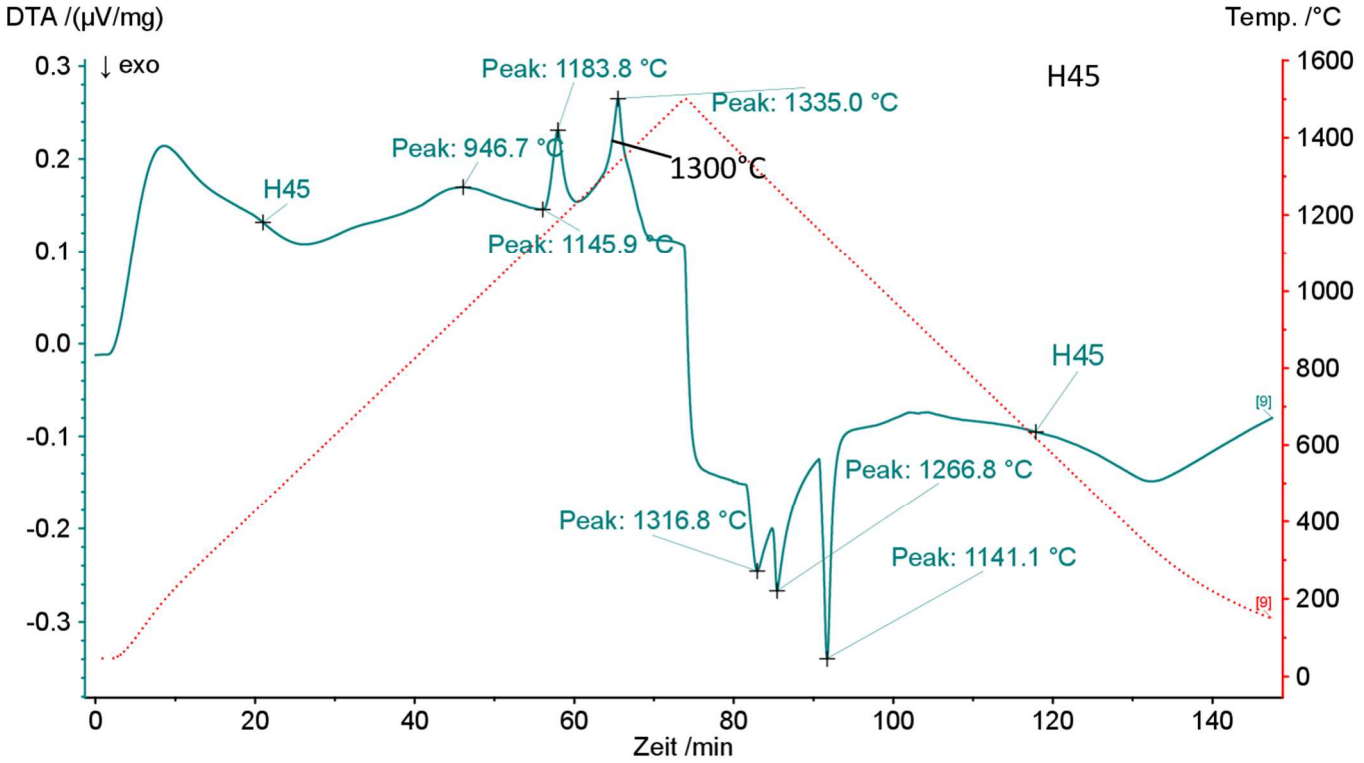

Figure 136 DTA analysis of H45 Ingot

Die approbierte gedruckte Originalversion dieser Diplomarbeit ist an der TU Wien Bibliothek verfügbar.
The approved original version of this thesis is available in print at TU Wien Bibliothek.

Phases: Figure 137 shows that with XRD and SEM for H45 four phases could be identified. Two different silicides, Cr_3Si and M_3Si, mostly Fe_3Si and/or $Cr_{0.6}Fe_{2.4}Si$. A ß-Mn structured phase is considered as a solid solution phase. The ß-Mn structured phase shows a rather characteristic peak "fingerprint" which shows up in this and most of the other modifications of all families. M_7C_3, ($Fe_{3,5}Cr_{3,5}C_3$) is a carbide, with no Si content. ThermoCalc predicts a silicide, a carbide and a Fe-BCC phase.

Composition: H45 should have 56Fe_32Cr_8Si_4C. Combined EDX analysis and LECO measurement result in a composition **Fe56_32Cr_9Si_3C**, which is rather close to the initial composition. The problem of inhomogeneity during the melting resulted in a relatively huge error of the LECO measurement ± 0.89% C.

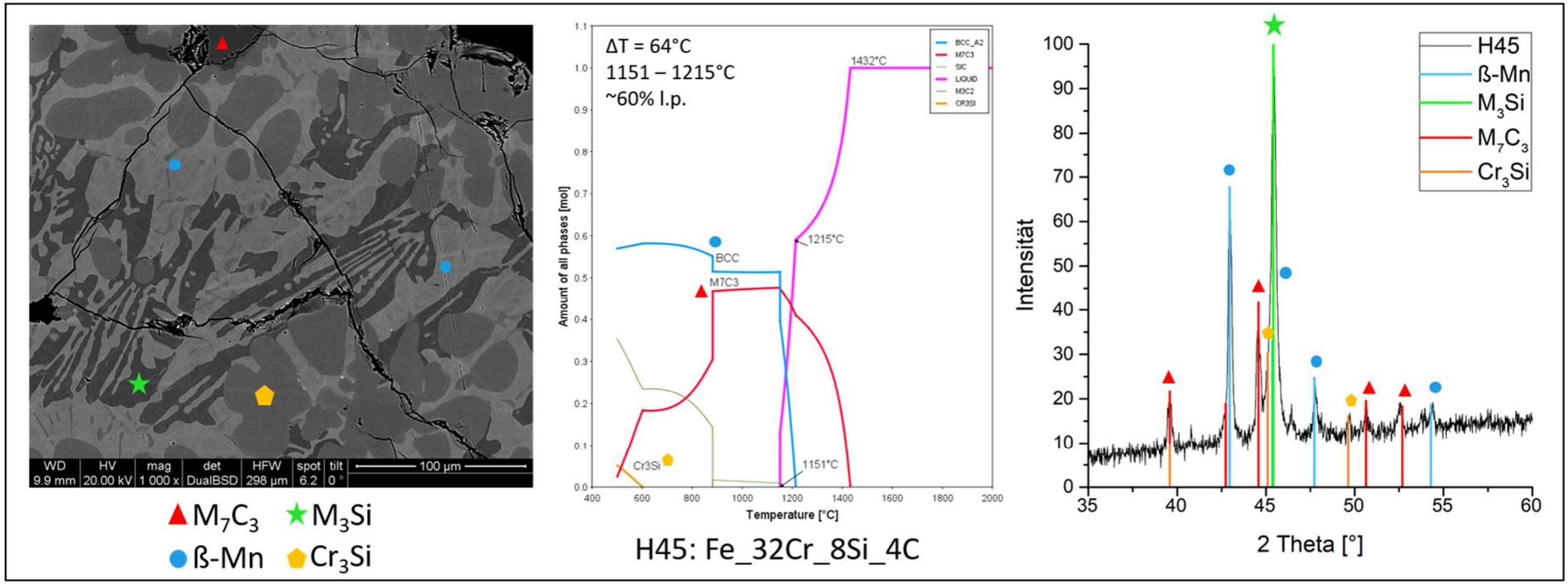

Figure 137 SEM x1000, EoP and XRD analysis from H45 Ingot; ***Phase references*** *M_7C_3 (04-017-0806), M_3Si =(Fe_3Si (04-003-3871) and/or $Cr_{0.6}Fe_{2.6}Si$ (04-006-7480), Cr_3Si (04-001-2815), ß-Mn structured phase (04 007 2059)*

Die approbierte gedruckte Originalversion dieser Diplomarbeit ist an der TU Wien Bibliothek verfügbar.
The approved original version of this thesis is available in print at TU Wien Bibliothek.

H45_E1: Fe_40Cr_11Si_3.5C

Figure 138 shows the DTA measurement of H45_E1. This system was not fully molten at 1300°C. The heating stage shows 3 endothermal peaks. The cooling stage shows three exothermal peaks.

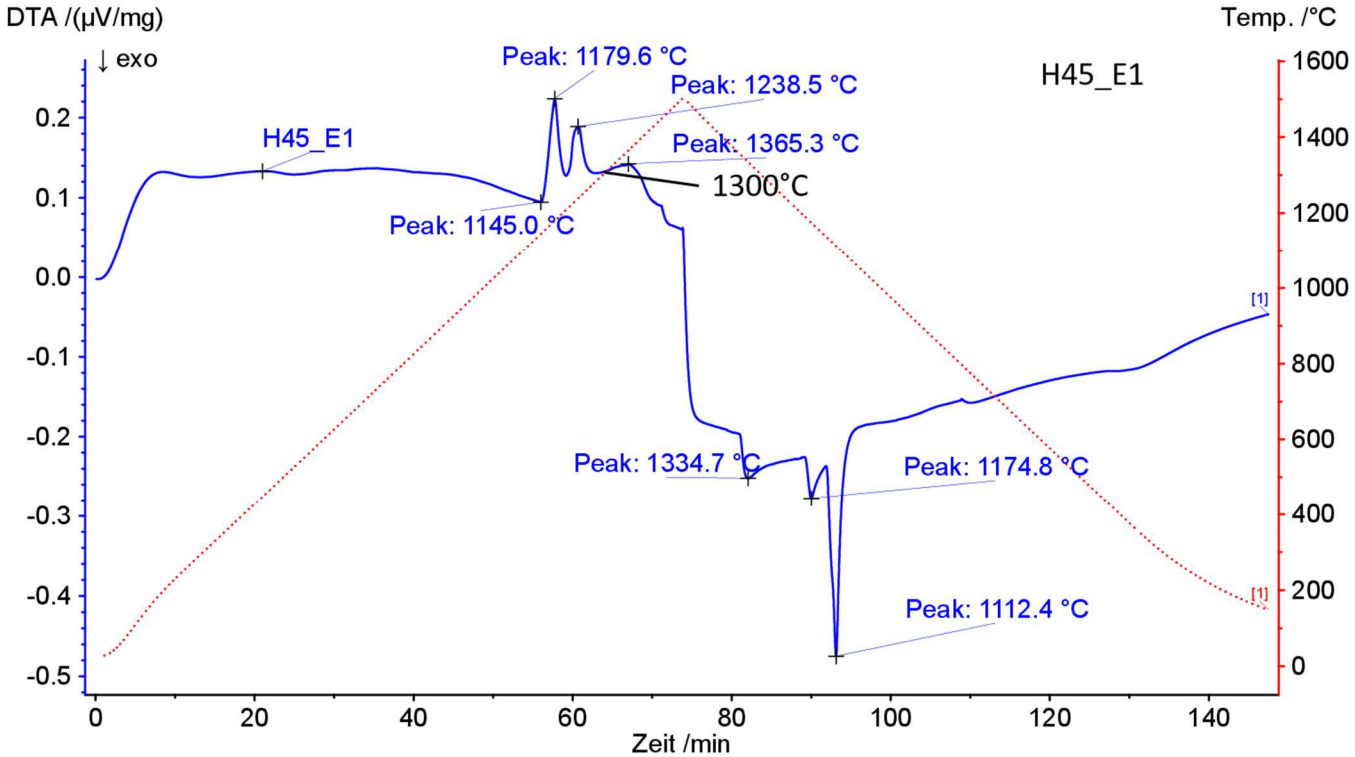

Figure 138 DTA analysis of H45_E1

Die approbierte gedruckte Originalversion dieser Diplomarbeit ist an der TU Wien Bibliothek verfügbar.
The approved original version of this thesis is available in print at TU Wien Bibliothek.

Phases: Figure 139 shows that with XRD and REM for H45_E1 three phases could be obtained. M_3Si, mostly Fe_3Si and/or $Cr_{0.6}Fe_{2.4}Si$, and a ß-Mn structured phase, considered as a solid solution. M_7C_3 was still found in the REM but could not be detected in XRD. The XRD pattern showed M_5Si_3, which could not be observed in the SEM.

Composition: H45_E1 should have 45Fe_40Cr_11Si_3.5C. Combined EDX analysis and LECO measurement result in a composition **Fe45_40Cr_11Si_3.4C**, which is almost the desired composition.

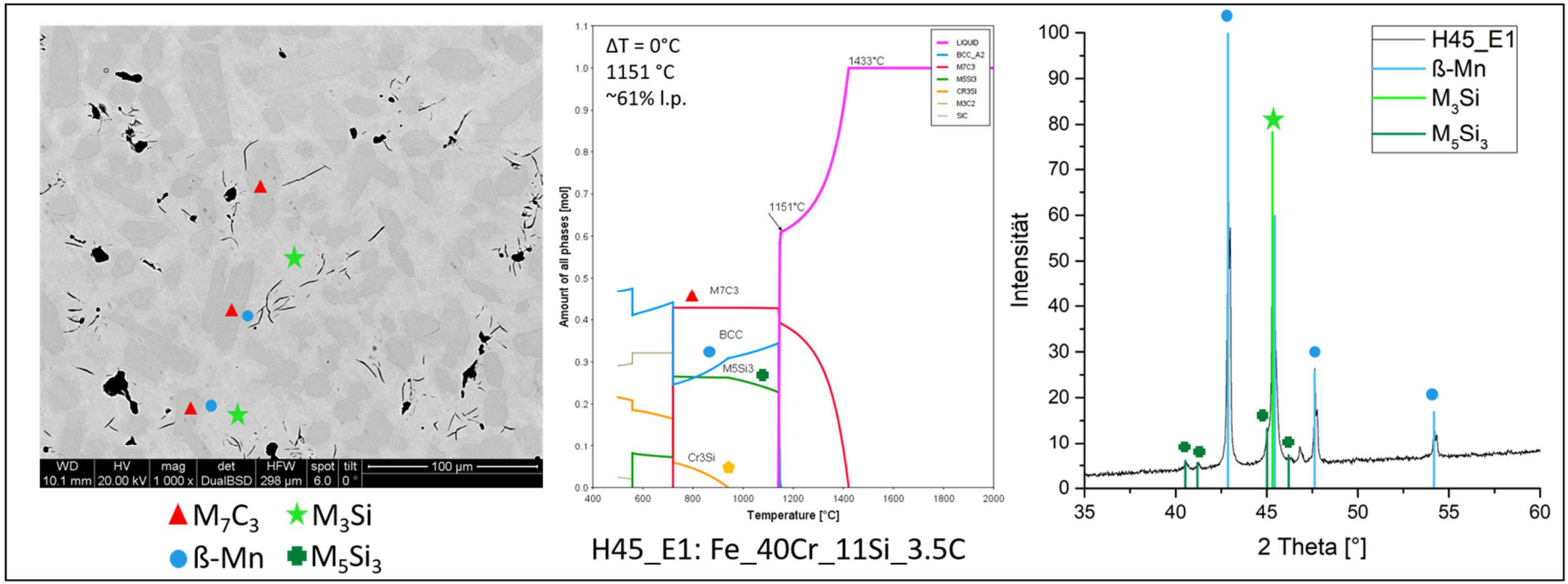

Figure 139 SEM x1000, EoP and XRD analysis from H45_E1 Ingot; ***Phase references*** *M_7C_3 (04-017-0806), M_3Si =(Fe_3Si (04-003-3871) and/or $Cr_{0.6}Fe_{2.6}Si$ (04-006-7480), ß-Mn structured phase (04 007 2059), M_5Si_3 (04-004-3035)*

Die approbierte gedruckte Originalversion dieser Diplomarbeit ist an der TU Wien Bibliothek verfügbar.
The approved original version of this thesis is available in print at TU Wien Bibliothek.

H45_E2: Fe_40Cr_14Si_4C

Figure 140 shows the DTA measurement of H45_E2. It is clearly visible that this composition was not fully molten at 1300°C. This composition shows three endothermal peaks during the heating stage. During the cooling stage three exothermal peaks could be obtained.

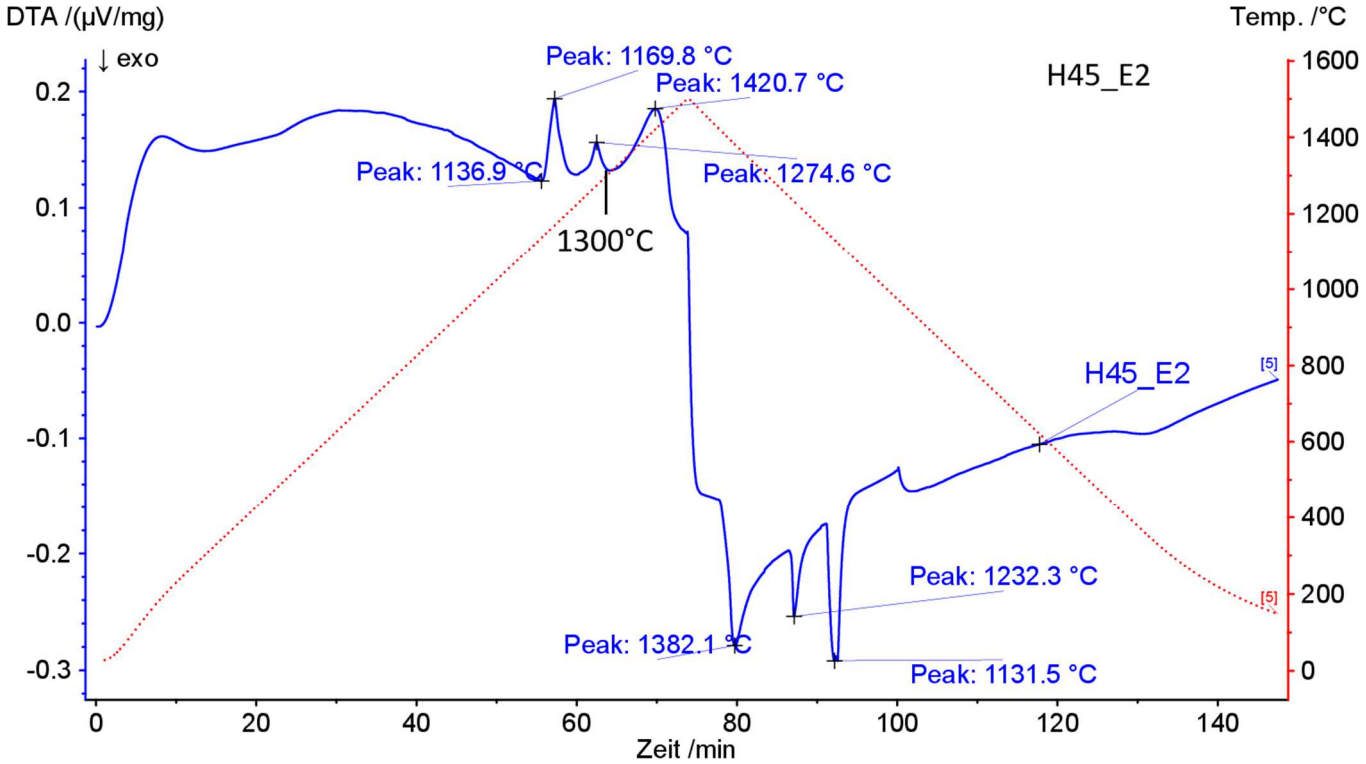

Figure 140 DTA analysis of H45_E2

Die approbierte gedruckte Originalversion dieser Diplomarbeit ist an der TU Wien Bibliothek verfügbar.
The approved original version of this thesis is available in print at TU Wien Bibliothek.

Phases: Figure 141 shows that with XRD and REM for H45_E2 several phases could be obtained. It was not possible to identify every peak of the XRD measurement. A ß-Mn structured phase and M_3Si, most likely Fe_3Si and/or $Cr_{0.6}Fe_{2.4}Si$ phase could be identified for this system. M_5Si_3 shows up as well in XRD, SEM and in the ThermoCalc prediction. M_7C_3 could not be found in SEM analysis, considering M_7C_3 as a Si free carbide. It is very likely that this composition shows an equilibrium of M_7C_3 and $M_{23}C_6$ as described from G.V. Raynor and V.G. Rivlin in [68].

Composition: H45_E2 should have 42Fe_40Cr_14Si_4C. Combined EDX analysis and LECO measurement result in a composition **Fe42_40Cr_14Si_3.9C**, which is almost the desired composition.

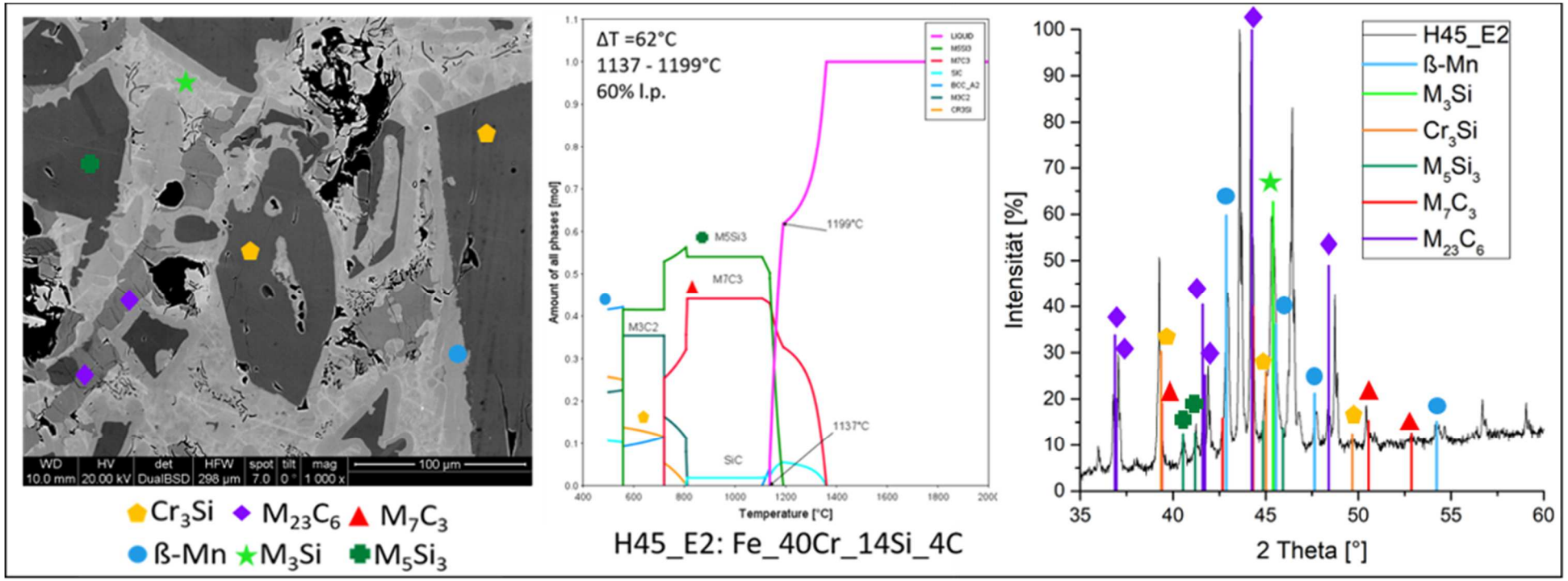

Figure 141 SEM x1000, EoP and XRD analysis from H45_E2 Ingot; ***Phase references*** *M_7C_3 (04-017-0806), M_3Si =(Fe_3Si (04-003-3871) and/or $Cr_{0.6}Fe_{2.6}Si$ (04-006-7480), Cr_3Si (04-001-2815), ß-Mn structured phase (04 007 2059), $M_{23}C_6$ (04-003-6076), M_5Si_3 (04-004-3035)*

Die approbierte gedruckte Originalversion dieser Diplomarbeit ist an der TU Wien Bibliothek verfügbar.
The approved original version of this thesis is available in print at TU Wien Bibliothek.

H45_E3: Fe_32Cr_13Si_4C

Figure 142 shows the DTA measurement of H45_E3. This MA modification does not fully melt during under the selected melting conditions. H45_E3 shows three endothermal peaks during the heating stage. The first peak shows a shoulder. During the cooling stage three different exothermal peaks could be obtained.

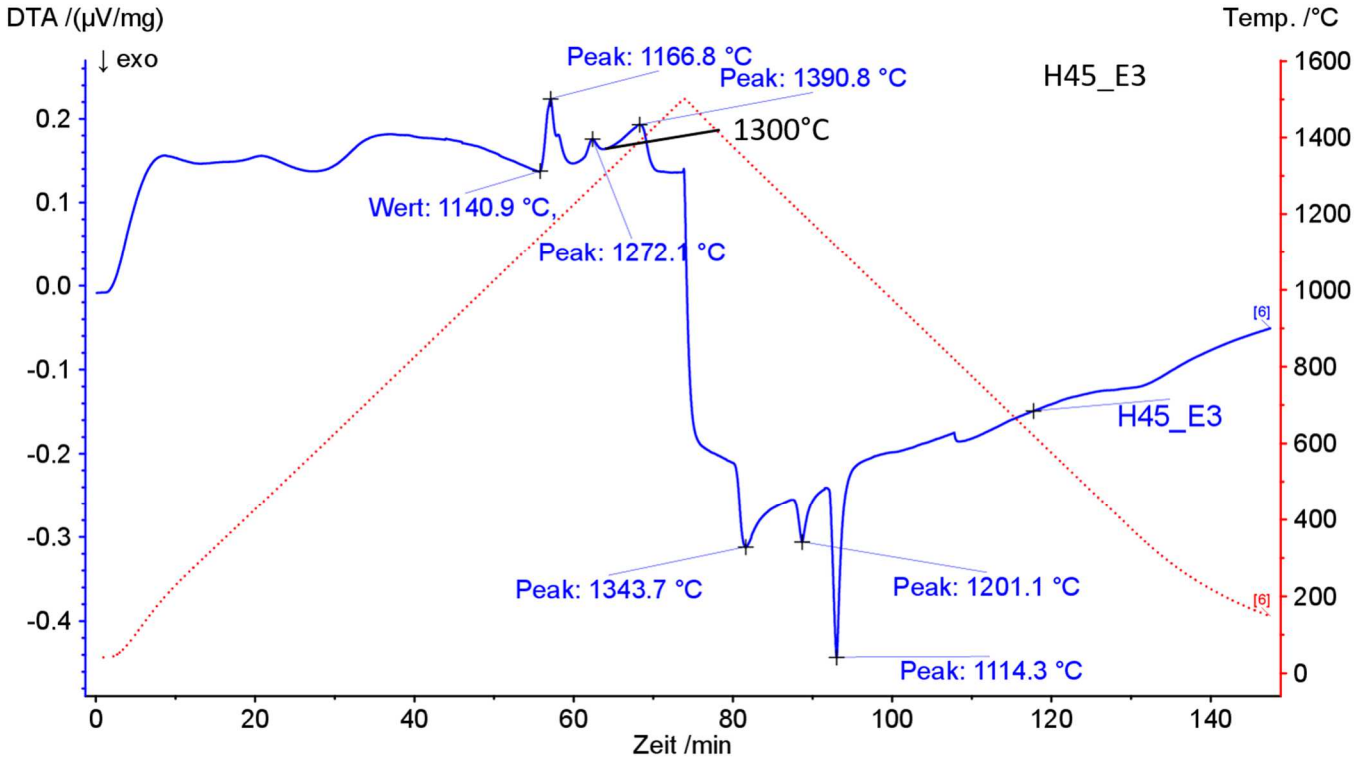

Figure 142 DTA analysis of H45_E3

Die approbierte gedruckte Originalversion dieser Diplomarbeit ist an der TU Wien Bibliothek verfügbar.
The approved original version of this thesis is available in print at TU Wien Bibliothek.

Phases: Figure 143 shows that with XRD and REM for H45_E3 five phases could be obtained. A ß-Mn structured phase considered as a solid solution and M_3Si could be found again. M_5Si_3 shows up as well in XRD, SEM and in the ThermoCalc prediction. Another C containing carbide, $M_{23}C_6$, did fit to the XRD measurement. It seems reasonable that different compositions form different types of carbides. In general, again a carbide, several silicides and a ß-Mn structured phase could be found.

Composition: H45_E3 should have 50Fe_32Cr_14Si_4C. Combined EDX analysis and LECO measurement result in a composition **Fe49_33Cr_14Si_3.6C**, which is almost the desired composition.

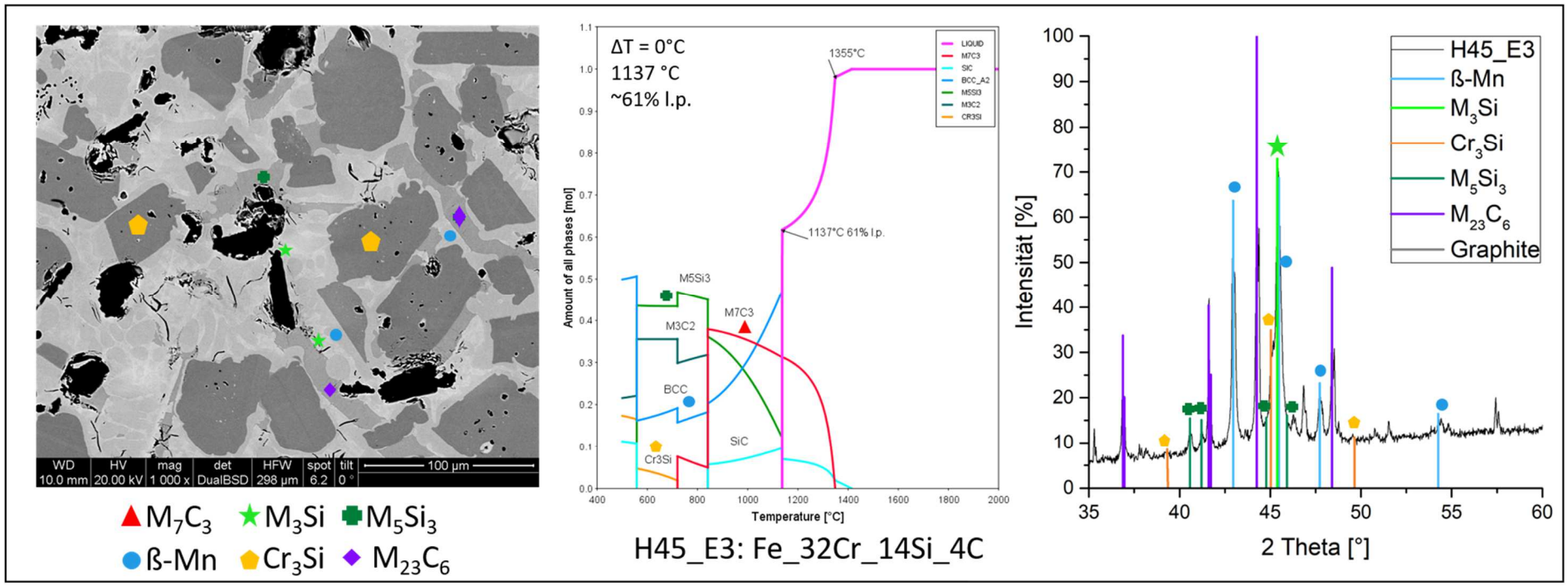

*Figure 143 SEM x1000, EoP and XRD analysis from H45_E3 Ingot; **Phase references** M_3Si =(Fe_3Si (04-003-3871) and/or $Cr_{0.6}Fe_{2.6}Si$ (04-006-7480), Cr_3Si (04-001-2815), ß-Mn structured phase (04 007 2059), $M_{23}C_6$ (04-003-6076), M_5Si_3 (04-004-3035)*

Die approbierte gedruckte Originalversion dieser Diplomarbeit ist an der TU Wien Bibliothek verfügbar.
The approved original version of this thesis is available in print at TU Wien Bibliothek.

H45_E4: Fe_32Cr_9.8Si_4C

Figure 144 shows the DTA measurement of H45_E4. This composition seems to be almost molten at 1300°C. The heating stage shows two different endothermal peaks, while the cooling stage shows three different exothermal peaks for this MA.

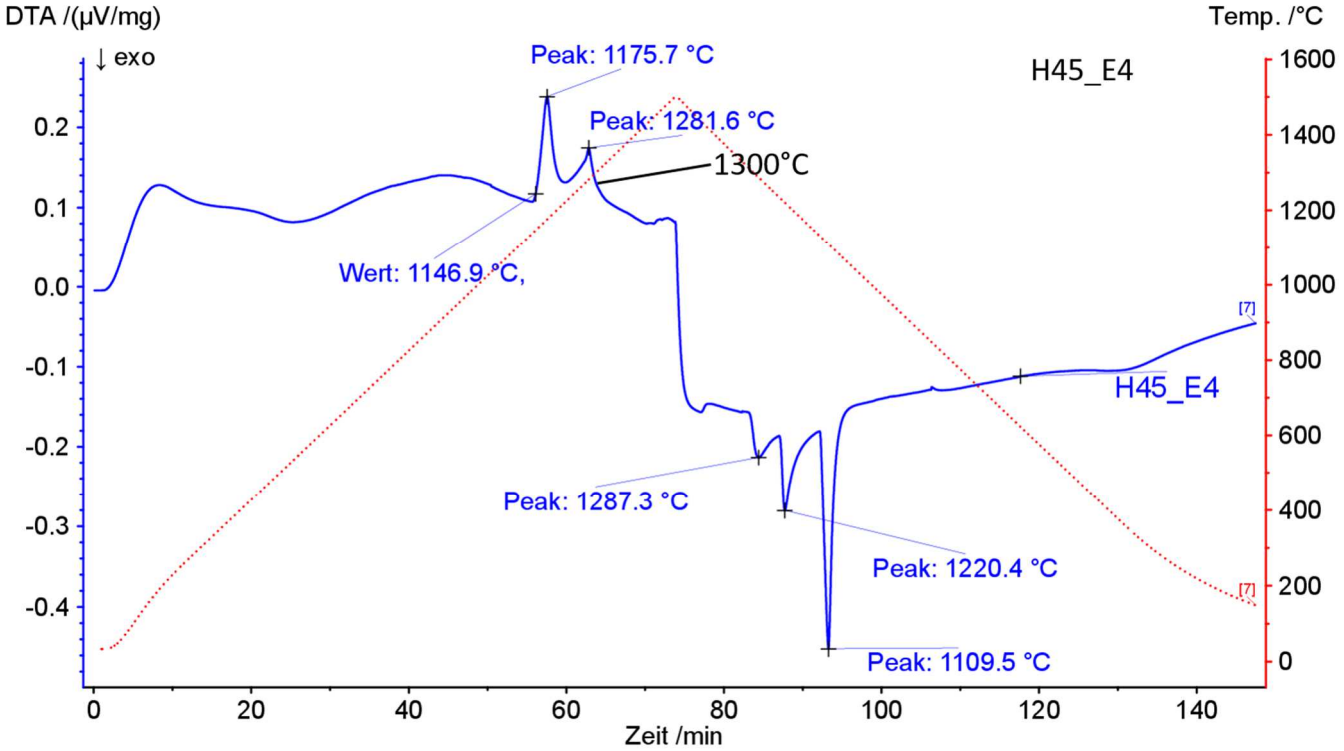

Figure 144 DTA analysis of H45_E4

Die approbierte gedruckte Originalversion dieser Diplomarbeit ist an der TU Wien Bibliothek verfügbar.
The approved original version of this thesis is available in print at TU Wien Bibliothek.

Phases: Figure 145 shows that with XRD and SEM for H45_E4 five phases could be obtained: A ß-Mn structured phase, considered as a solid solution, and M_3Si. M_7C_3 show up as well in XRD, REM and in the ThermoCalc prediction. Cr_3Si and M_5Si_3 could be obtained as well in XRD and SEM.
Composition: H45_E4 should have 44Fe_32Cr_9.8Si_4C. Combined EDX analysis and LECO measurement result in a composition **Fe56_29Cr_11Si_4.1C**, which differs from the initial composition in 2% Si and 3%Cr.

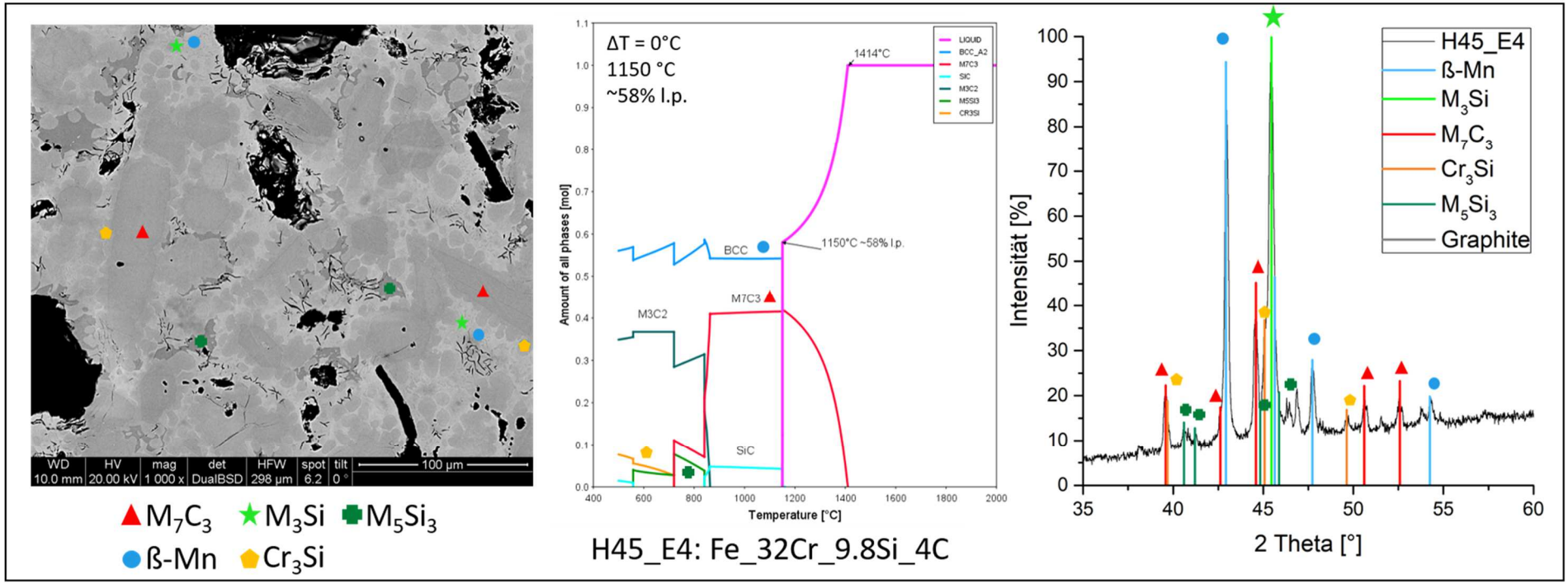

*Figure 145 SEM x1000, EoP and XRD analysis from H45_E4 Ingot; **Phase references** M_7C_3 (04-017-0806), M_3Si =(Fe_3Si (04-003-3871) and/or $Cr_{0.6}Fe_{2.6}Si$ (04-006-7480), Cr_3Si (04-001-2815), ß-Mn structured phase (04 007 2059), M_5Si_3 (04-004-3035)*

Die approbierte gedruckte Originalversion dieser Diplomarbeit ist an der TU Wien Bibliothek verfügbar.
The approved original version of this thesis is available in print at TU Wien Bibliothek.

H45_E5: 10Cr_11.8Si_3C

Figure 146 shows the DTA measurement of H45_E5. This composition is fully molten under these conditions. The DTA curve shows one peak during the heating and one peak during the cooling stage. This system seems to fully melt in a relatively narrow melting range.

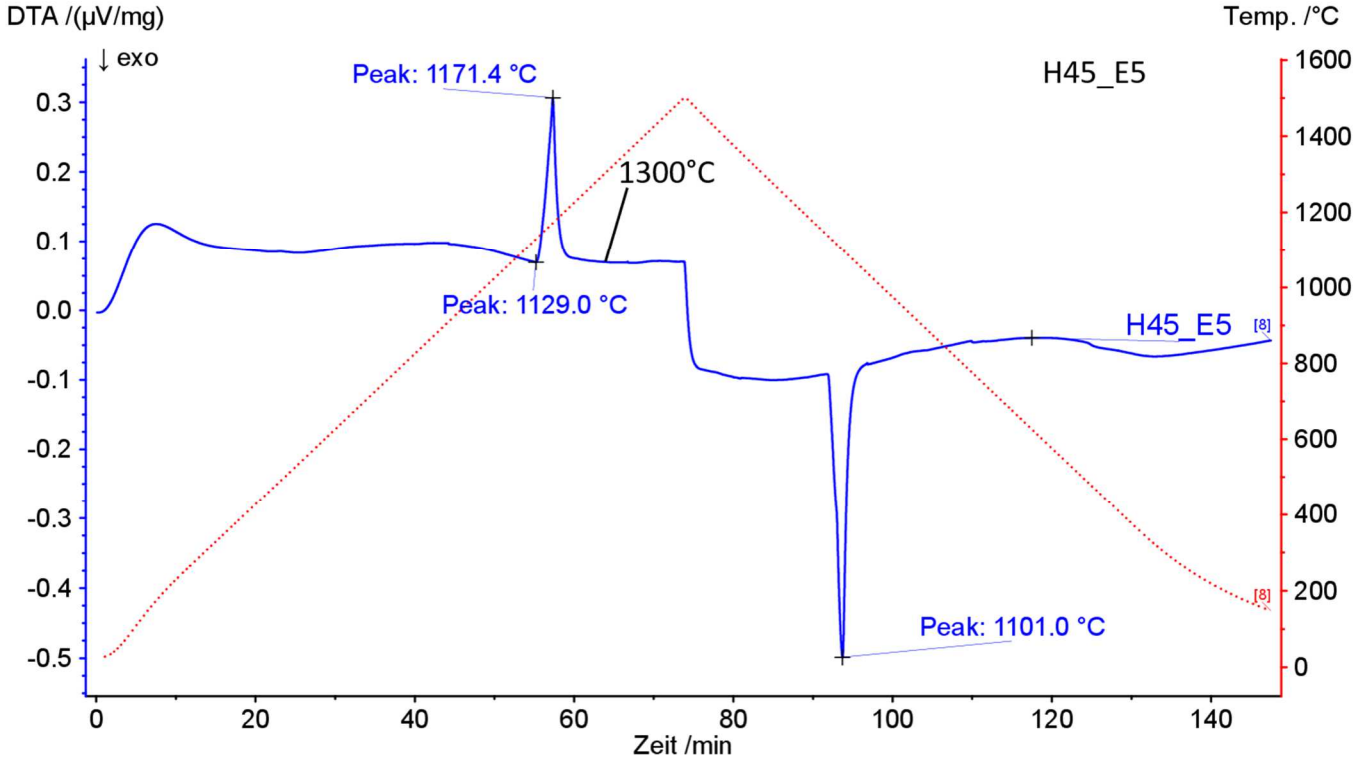

Figure 146 DTA analysis of H45_E5

Die approbierte gedruckte Originalversion dieser Diplomarbeit ist an der TU Wien Bibliothek verfügbar.
The approved original version of this thesis is available in print at TU Wien Bibliothek.

Phases: Figure 147 shows that with XRD for H45_E5 two phases could be obtained. M_3Si and Graphite

Composition: H45_E5 should have 44Fe_10Cr_11.8Si_3C. Combined EDX analysis and LECO measurement result in a composition **Fe75_11Cr_11Si_2.5C**.

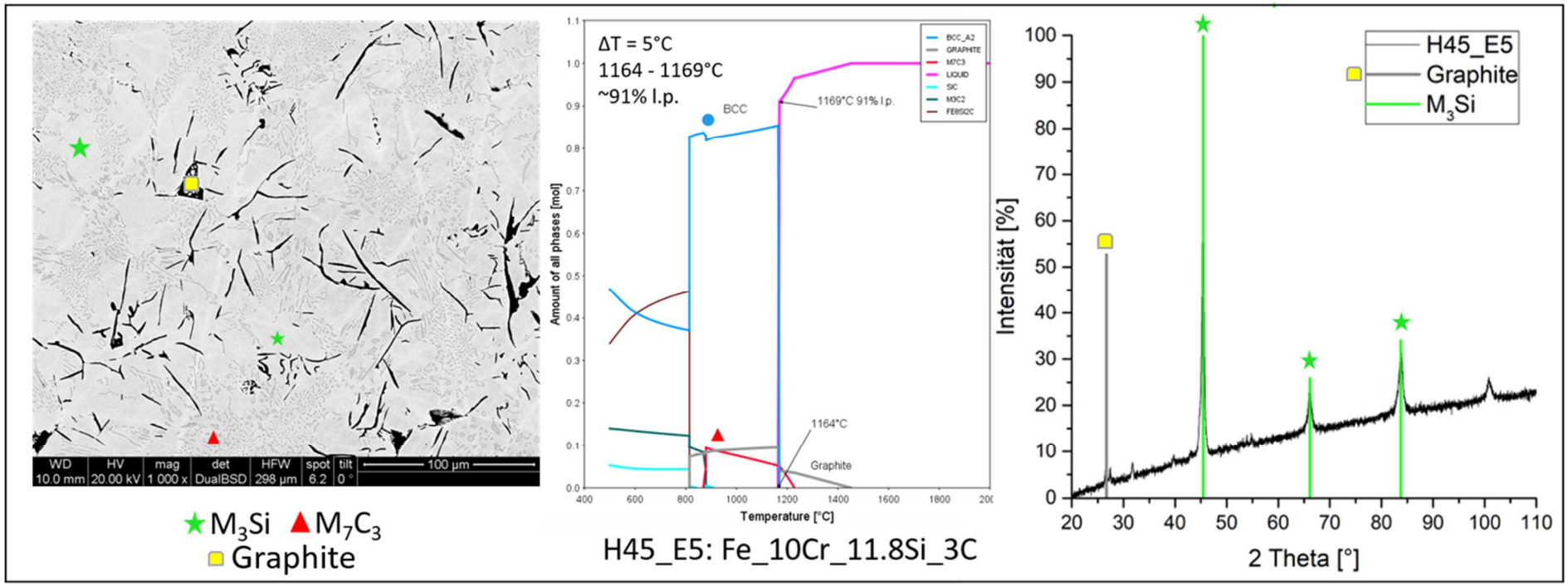

Figure 147 SEM x1000, EoP and XRD analysis from H45_E5 Ingot; ***Phase references*** *M_3Si =(Fe_3Si (04-003-3871) and/or $Cr_{0.6}Fe_{2.6}Si$ (04-006-7480), Graphit*

Die approbierte gedruckte Originalversion dieser Diplomarbeit ist an der TU Wien Bibliothek verfügbar.
The approved original version of this thesis is available in print at TU Wien Bibliothek.

H45_E6: Fe_11.7Cr_13.6Si_2.2C

Figure 148 shows the DTA measurement of H45_E6. This composition is fully molten under these conditions. The DTA curve shows one peak during the heating and one peak during the cooling stage. This system seems to fully melt in a relatively narrow melting range.

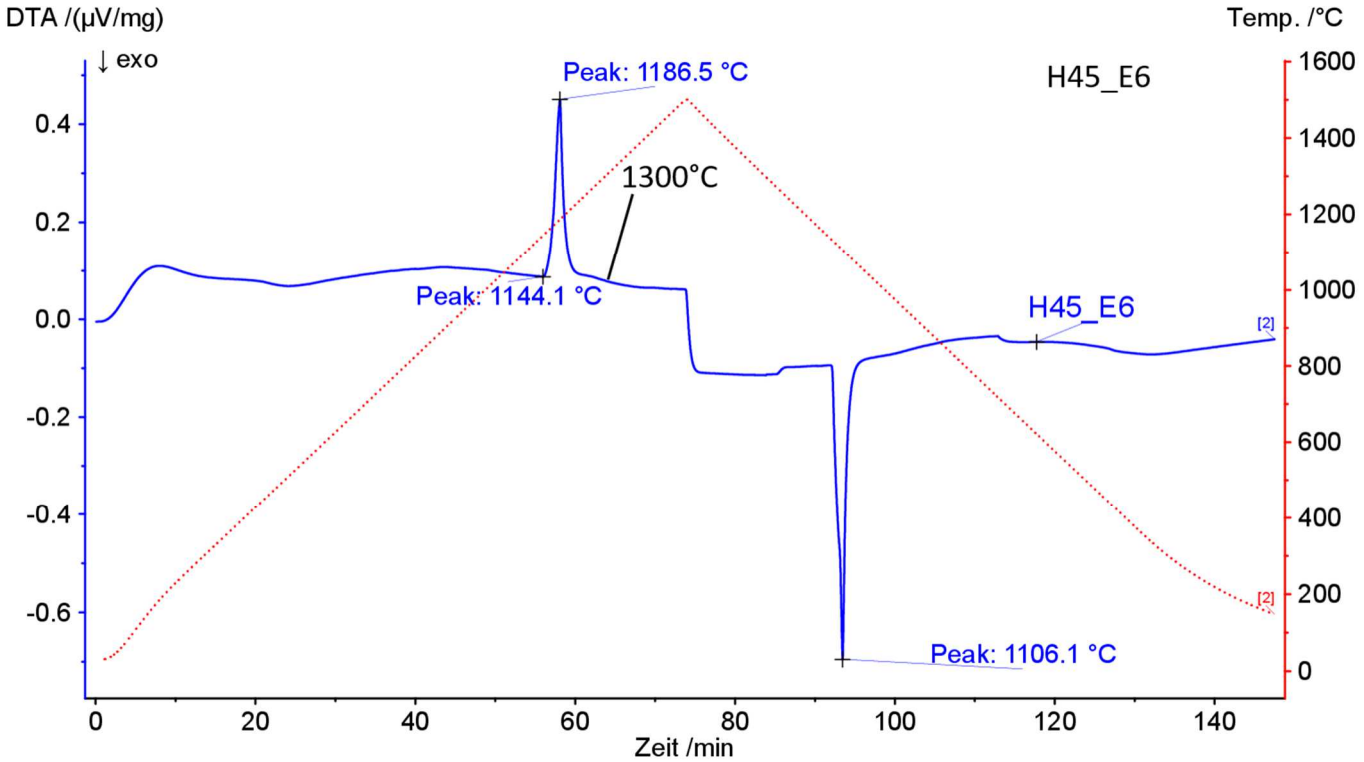

Figure 148 DTA analysis of H45_E6

Die approbierte gedruckte Originalversion dieser Diplomarbeit ist an der TU Wien Bibliothek verfügbar.
The approved original version of this thesis is available in print at TU Wien Bibliothek.

Phases: Figure 149 shows that with XRD and REM for H45_E5 three phases could be obtained. M_3Si, a ß-Mn structured phase and free graphite. Carbides or other structures could not be obtained in REM and are not showing up in XRD.

Composition: H45_E6 should have 72.5Fe_11.7Cr_13.6Si_2.2C. Combined EDX analysis and LECO measurement result in a composition **Fe72.7_13Cr_13Si_1.3C**. This system lost about half of the carbon, a mistake in powder preparation can be excluded.

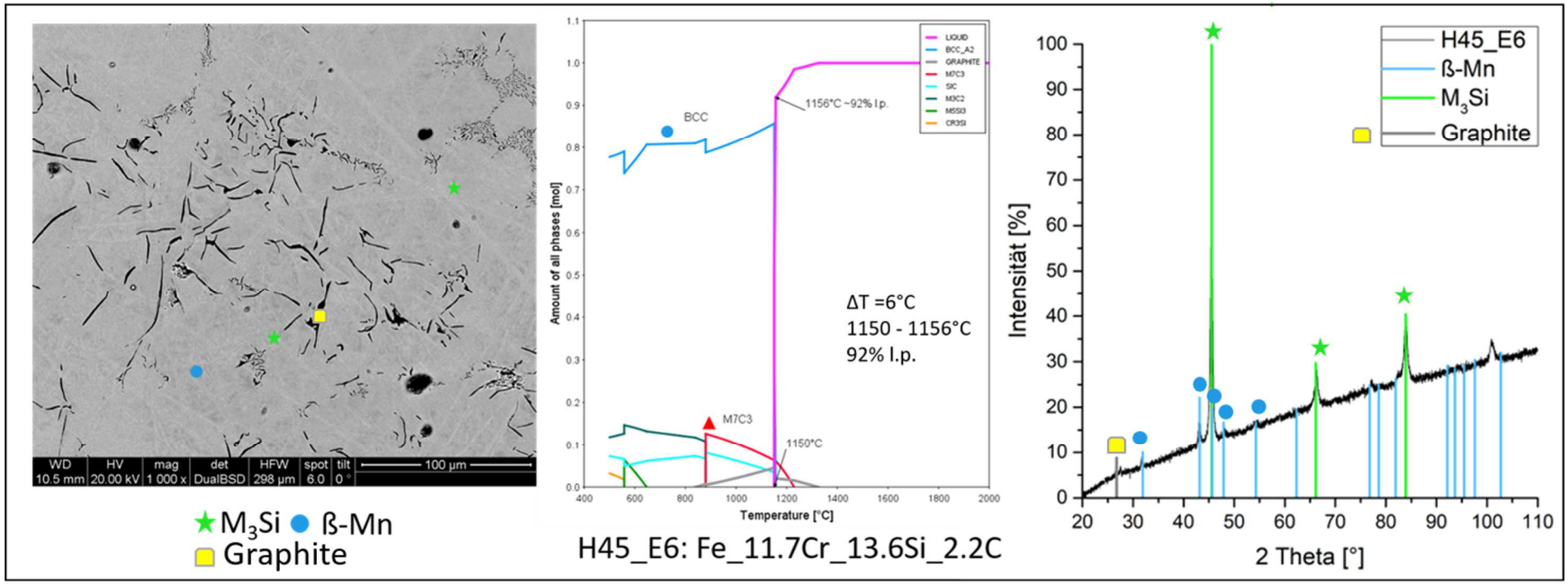

Figure 149 SEM x1000, EoP and XRD analysis from H45_E6 Ingot; ***Phase references*** *M_3Si =(Fe_3Si (04-003-3871) and/or $Cr_{0.6}Fe_{2.6}Si$ (04-006-7480), ß-Mn structured phase (04 007 2059)*

Die approbierte gedruckte Originalversion dieser Diplomarbeit ist an der TU Wien Bibliothek verfügbar.
The approved original version of this thesis is available in print at TU Wien Bibliothek.

H46: Fe_42Mn_6Si_0.4C

Figure 150 shows the DTA measurement of H46. This MA shows three different endothermal peaks during the heating stage. The last peak shows up below 1300°C, which means it did finish all reactions during the ingot melting. The cooling stage shows only two exothermal peaks.

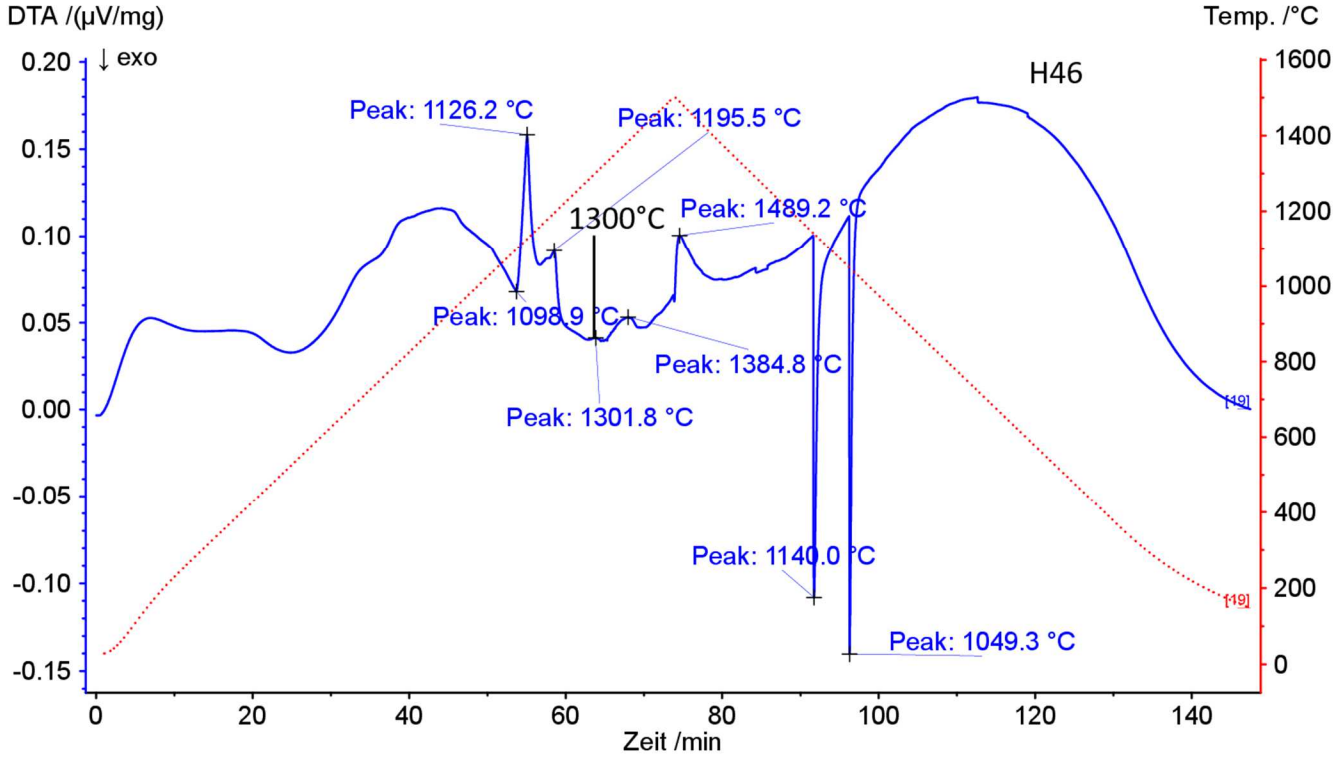

Figure 150 DTA analysis of H46

Die approbierte gedruckte Originalversion dieser Diplomarbeit ist an der TU Wien Bibliothek verfügbar.
The approved original version of this thesis is available in print at TU Wien Bibliothek.

Phases: Figure 151 shows that with XRD and REM for H46 two phases could be obtained. M_3Si and a ß-Mn structured phase are found.
Composition: H46 should have 51.6Fe_42Mn_6Si_0.4C. EDX analysis did detect Cr impurities in H46, resulting from the atomization process. The measured composition was **Fe58.6_29Mn_4Cr_8Si_0.4C**. Mn loss was huge for this system.

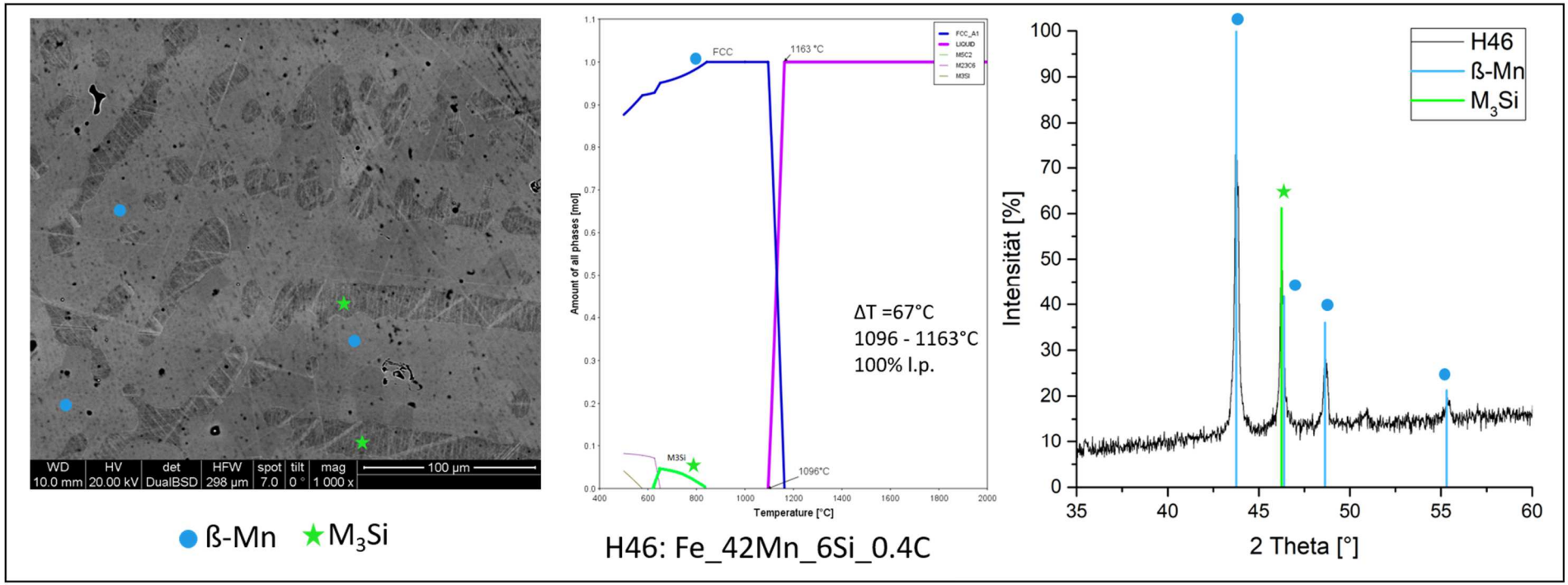

Figure 151 SEM x1000, EoP and XRD analysis from H46 DTA-Ingot; ***Phase references*** *M_3Si = (Fe_3Si (04-003-3871) and/or Fe_2MnSi (01-077-7953)), ß-Mn structured phase (04 007 2059)*

Die approbierte gedruckte Originalversion dieser Diplomarbeit ist an der TU Wien Bibliothek verfügbar.
The approved original version of this thesis is available in print at TU Wien Bibliothek.

H46_E1: Fe_41Mn_5.9Si_2C

Figure 152 shows the DTA measurement of H46_E1. This MA modification shows two prominent peaks during the heating stage. 1300°C seemed to be enough to fully melt this MA. The cooling stage shows three exothermal peaks.

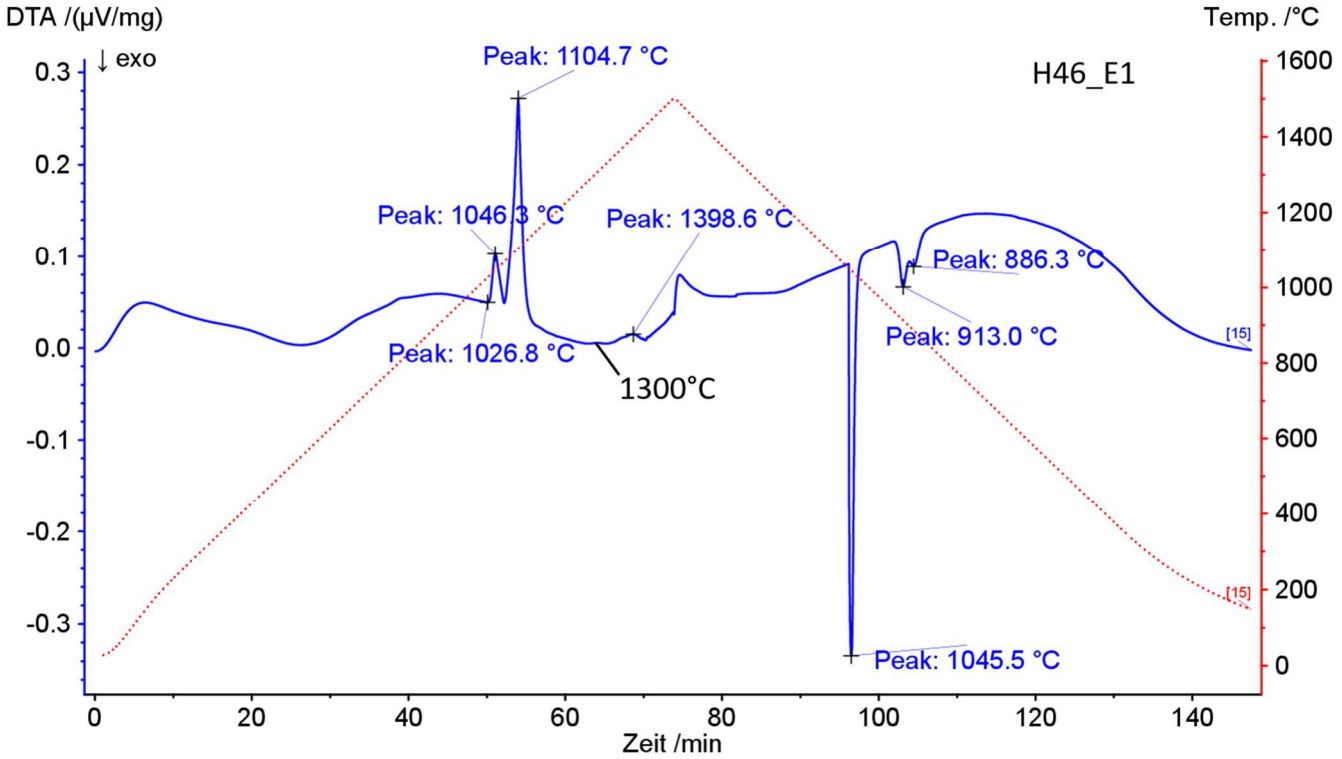

Figure 152 DTA analysis of H46_E1.

Die approbierte gedruckte Originalversion dieser Diplomarbeit ist an der TU Wien Bibliothek verfügbar.
The approved original version of this thesis is available in print at TU Wien Bibliothek.

Phases: Figure 153 shows that with XRD and SEM for H46_E1 four phases could be found. M_3Si and a ß-Mn structured phase, which is considered as a solid solution. M_7C_3 and M_5Si_3 could be identified as well in XRD and SEM.
Composition: H46_E1 should have 51.1Fe_41Mn_5.9Si_2C. Combined EDX analysis and LECO measurement result in a composition **Fe49_37Mn_5Cr_6Si_2.4C**. The Mn loss is relatively low compared to H46, so the system is supposed to keep the Mn very well.

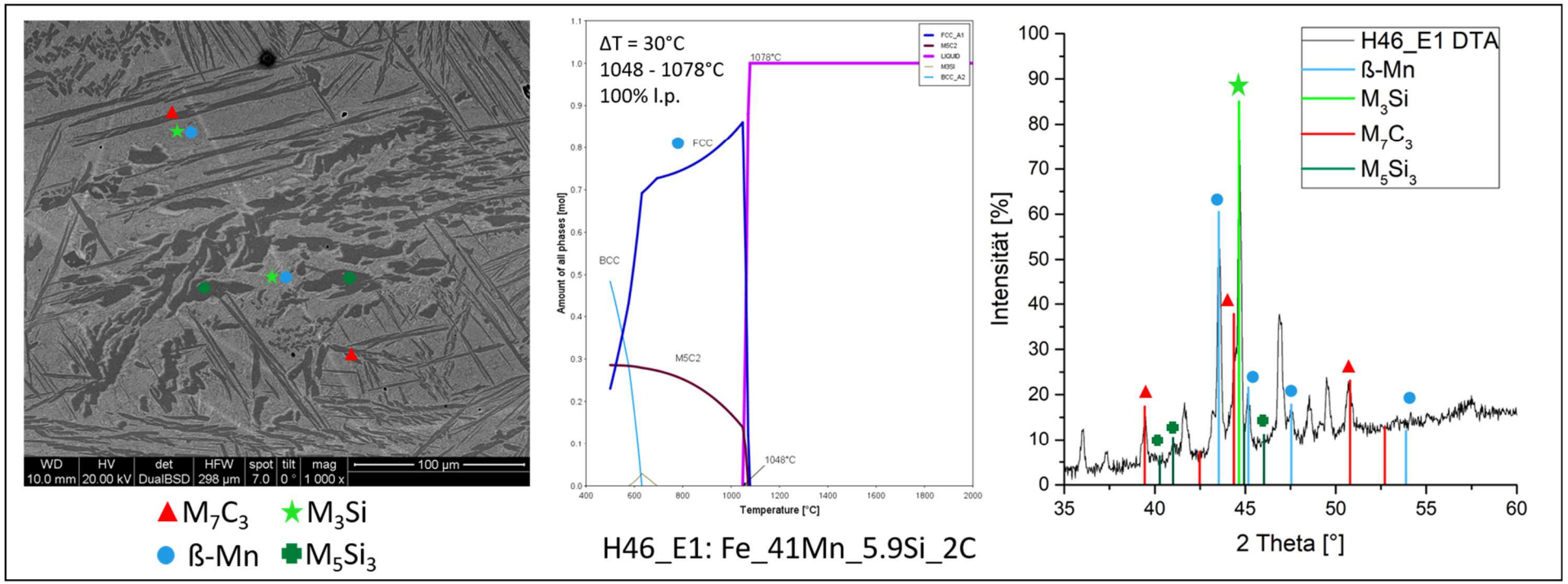

Figure 153 SEM x1000, EoP and XRD analysis from H46_E1 DTA-Ingot ***Phase references*** *M_7C_3 (04-017-0806), M_3Si = (Fe_3Si (04-003-3871) and/or Fe_2MnSi (01-077-7953)), ß-Mn (04-007-2059, M_5Si_3 (04-004-3035)*

Die approbierte gedruckte Originalversion dieser Diplomarbeit ist an der TU Wien Bibliothek verfügbar.
The approved original version of this thesis is available in print at TU Wien Bibliothek.

H46_E2: Fe_33Mn_7.5Si_3.4C

Figure 154 shows the DTA measurement of H46_E2. This MA modification fully melts below 1300°C, showing one peak during the heating stage and one peak during the cooling stage. This MA is supposed to melt in a relatively narrow melting window at comparatively low temperatures.

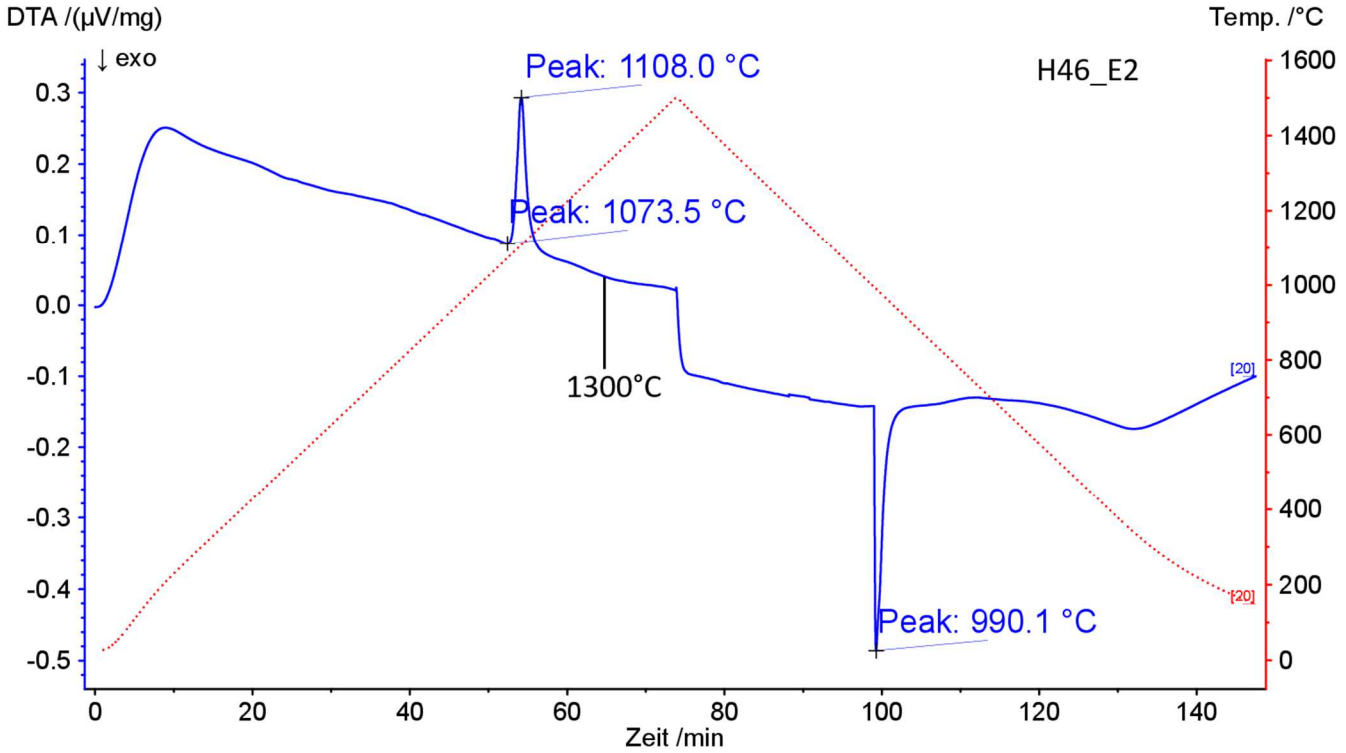

Figure 154 DTA analysis of H46_E2

Die approbierte gedruckte Originalversion dieser Diplomarbeit ist an der TU Wien Bibliothek verfügbar.
The approved original version of this thesis is available in print at TU Wien Bibliothek.

Phases: Figure 155 shows that with XRD and SEM for H46_E2 three phases could be obtained. A ß-Mn structured phase phase which is considered as a solid solution, M_3Si and M_7C_3. Not all peaks could be identified for this composition.
Composition: H46_E2 should have 51.1Fe_33Mn_7.5Si_3.4C. Combined EDX analysis and LECO measurement result in a composition **Fe59_29Mn_3Cr_6Si_2.8C**. The missing 1.5Si could be lost during the melting of the ingot, or more likely in an error during powder mix preparation. The Mn loss is relatively low, so the system is supposed to keep the Mn very well.

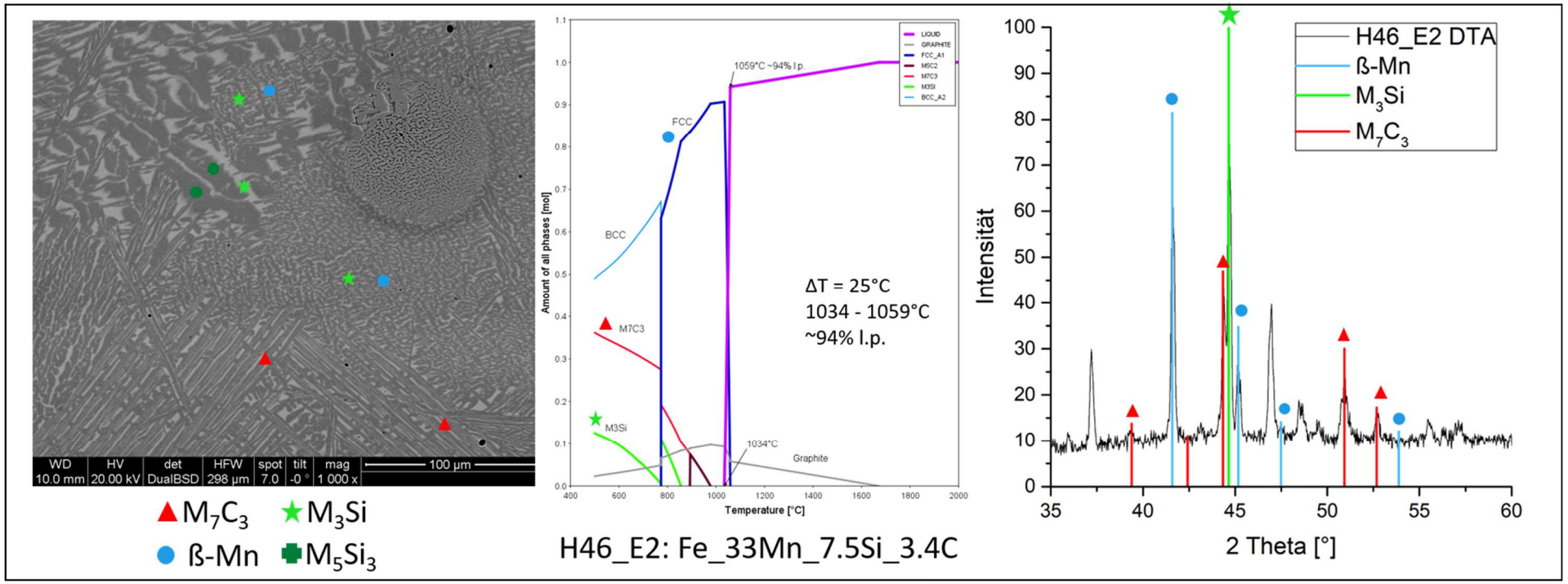

*Figure 155 SEM x1000, EoP and XRD analysis from H46_E1 DTA-Ingot; **Phase references** M_7C_3 (04-017-0806), M_3Si = (Fe_3Si (04-003-3871) and/or Fe_2MnSi (01-077-7953)), ß-Mn structured phase (04 007 2059)*

Die approbierte gedruckte Originalversion dieser Diplomarbeit ist an der TU Wien Bibliothek verfügbar.
The approved original version of this thesis is available in print at TU Wien Bibliothek.

H46_E3: Fe_30Mn_5Si_3.1C

Figure 156 shows the DTA measurement of H46_E3. It is clearly visible that this MA is fully molten under these conditions. The heating stage shows one endothermal reaction. Cooling stage shows two exothermal reactions for this MA.

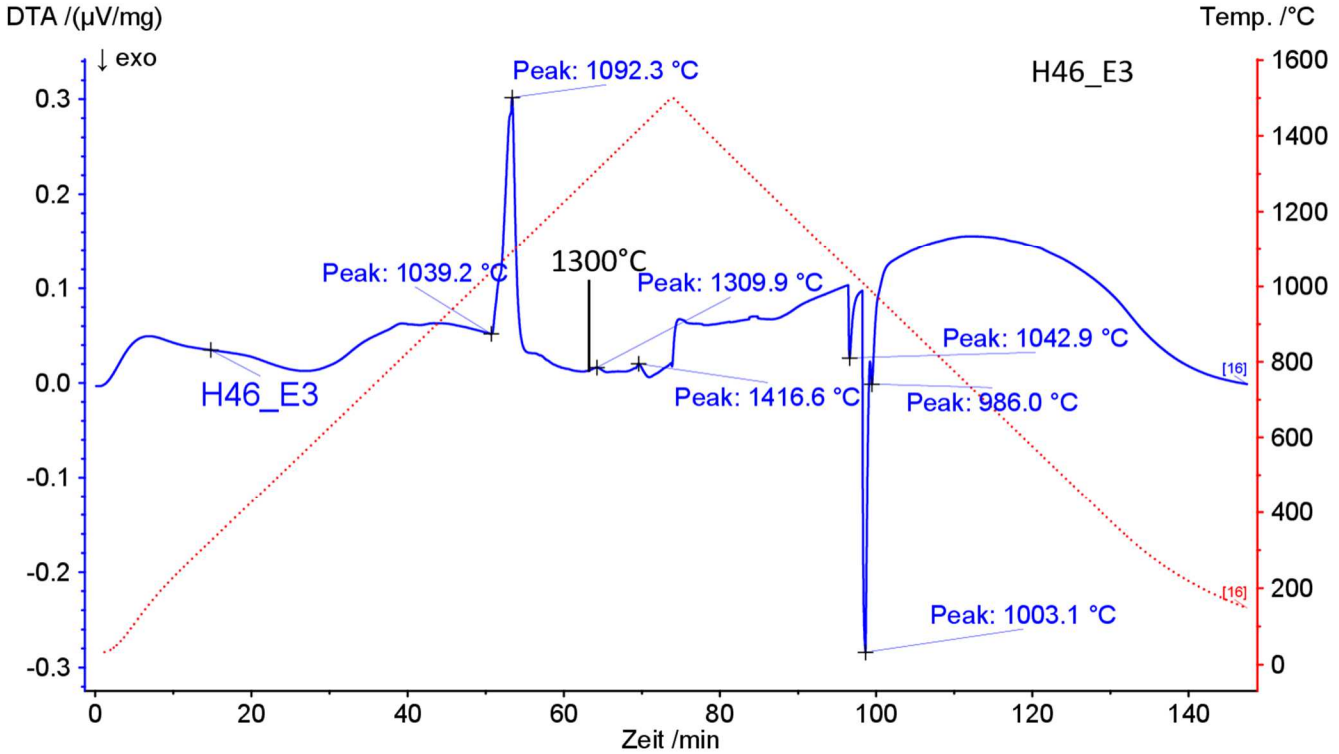

Figure 156 DTA analysis of H46_E3;

Die approbierte gedruckte Originalversion dieser Diplomarbeit ist an der TU Wien Bibliothek verfügbar.
The approved original version of this thesis is available in print at TU Wien Bibliothek.

Phases: Figure 157 shows that with XRD and REM for H46_E3 many phases could be obtained. Phases are distributed super fine in H46_E3 so it was not possible to do spot analysis or mappings in a reasonable time.

Composition: H46_E3 should have 61.9Fe_30Mn_5Si_3.1C. Combined EDX analysis and LECO measurement result in a composition **Fe64_25Mn_3Cr_5Si_3.3C**. The Mn is moderate for this composition.

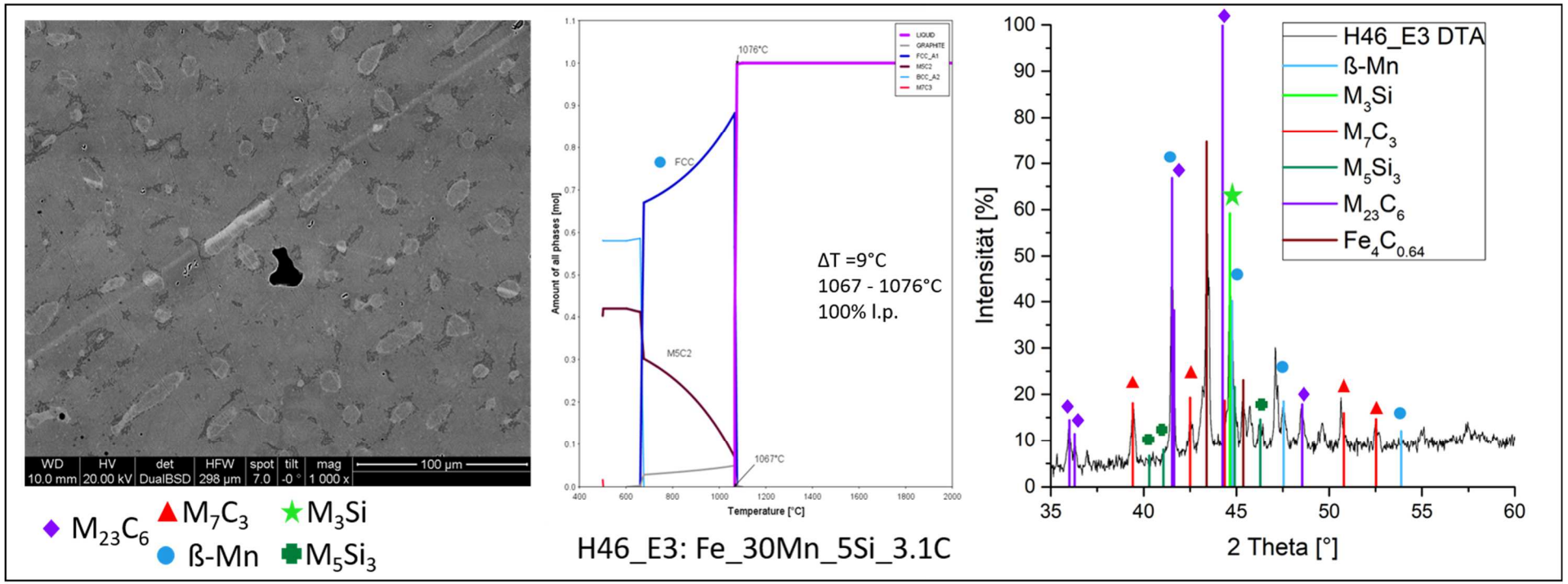

Figure 157 SEM x1000, EoP and XRD analysis from H46_E2 DTA-Ingot; ***Phase references*** *M_7C_3 (04-017-0806), M_3Si = (Fe_3Si (04-003-3871) and/or Fe_2MnSi (01-077-7953)), ß-Mn structured phase (04 007 2059), $M_{23}C_6$ (04-003-6076), M_5Si_3 (04-004-3035), $Fe_4C_{0.64}$ (01-071-1174)*

Die approbierte gedruckte Originalversion dieser Diplomarbeit ist an der TU Wien Bibliothek verfügbar.
The approved original version of this thesis is available in print at TU Wien Bibliothek.

H46_E4: Fe_40Mn_9Si_3C

Figure 158 shows the DTA measurement of H46_E4. This system is as well fully molten below 1300°C. The heating stage shows two endothermal peaks, while the cooling stage shows one exothermal peak. This system is supposed to be fully molten at comparatively low temperatures.

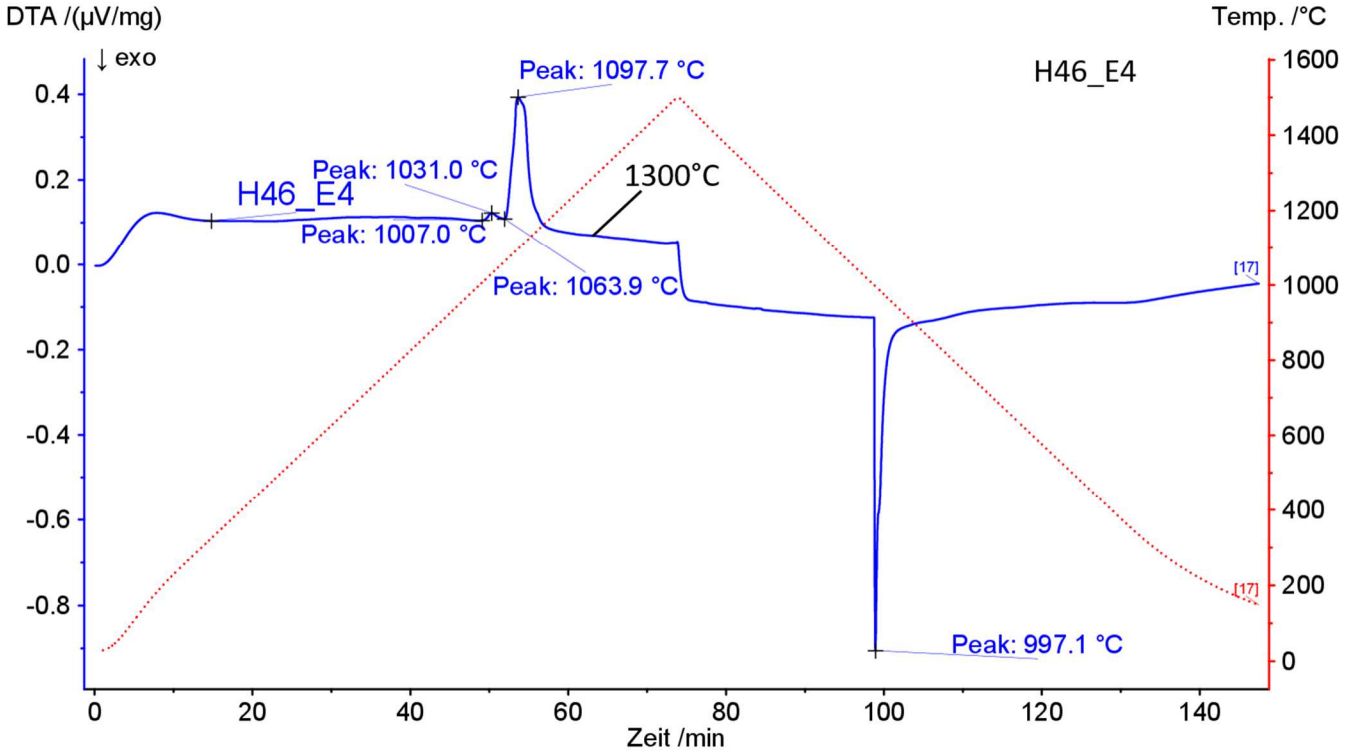

Figure 158 DTA analysis of H46_E4

Die approbierte gedruckte Originalversion dieser Diplomarbeit ist an der TU Wien Bibliothek verfügbar.
The approved original version of this thesis is available in print at TU Wien Bibliothek.

Phases: Figure 159 **s**hows that with XRD and SEM for H46_E4 three phases could be obtained. A Si containing carbide $M_{23}C_6$, a silicide M_3Si and a ß-Mn structured phase phase, considered as a solid solution.

Composition: H46_E4 should have 48Fe_40Mn_9Si_3C. Combined EDX analysis and LECO measurement result in a composition **Fe64_36Mn_3Cr_8Si_3.1C**. The Mn loss is relatively low, so the system is supposed to keep the Mn very well.

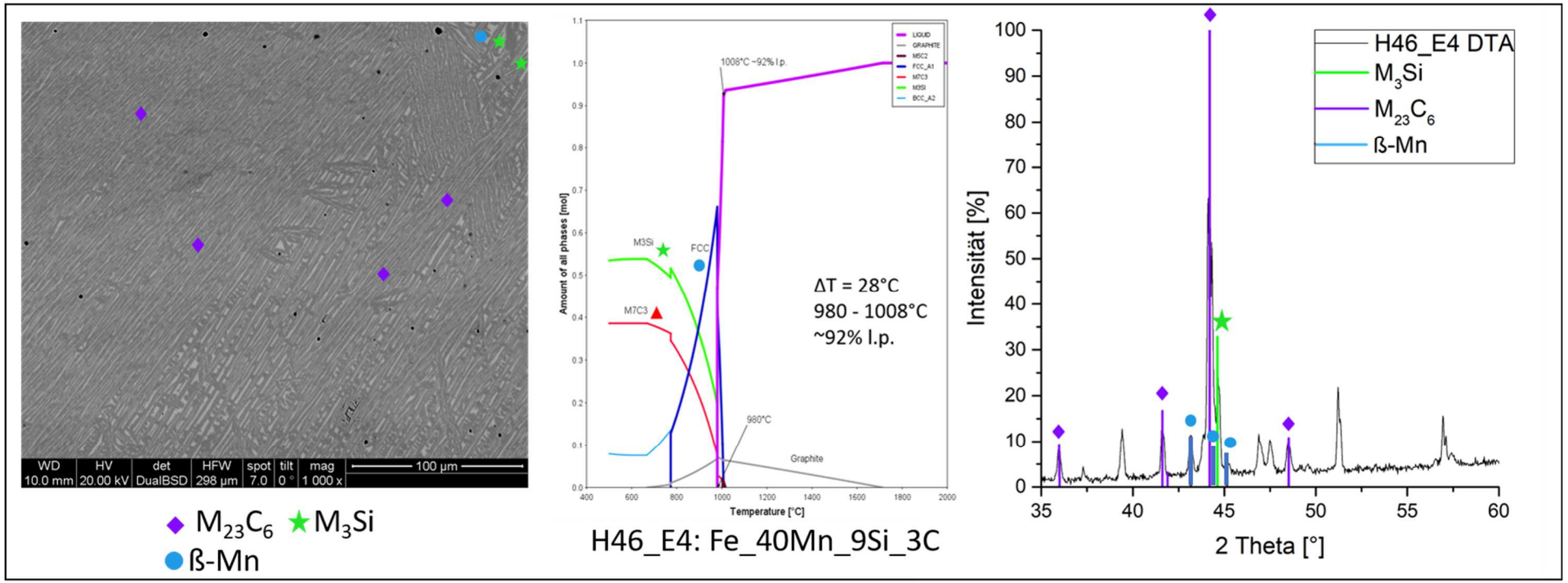

Figure 159 SEM x1000, EoP and XRD analysis from H46_E4 DTA-Ingot; ***Phase references*** *M_3Si = (Fe_3Si (04-003-3871) and/or Fe_2MnSi (01-077-7953)), ß-Mn structured phase (04 007 2059), $M_{23}C_6$ (04-003-6076)*

Die approbierte gedruckte Originalversion dieser Diplomarbeit ist an der TU Wien Bibliothek verfügbar.
The approved original version of this thesis is available in print at TU Wien Bibliothek.

H46_E5: Fe_30Mn_5Si_3.1C

Figure 160 shows the DTA measurement of H46_E5. This system is as well fully molten below 1300°C. The heating stage shows one endothermal peak, while the cooling stage shows one exothermal peak. This system is supposed to be fully molten at comparatively low temperatures.

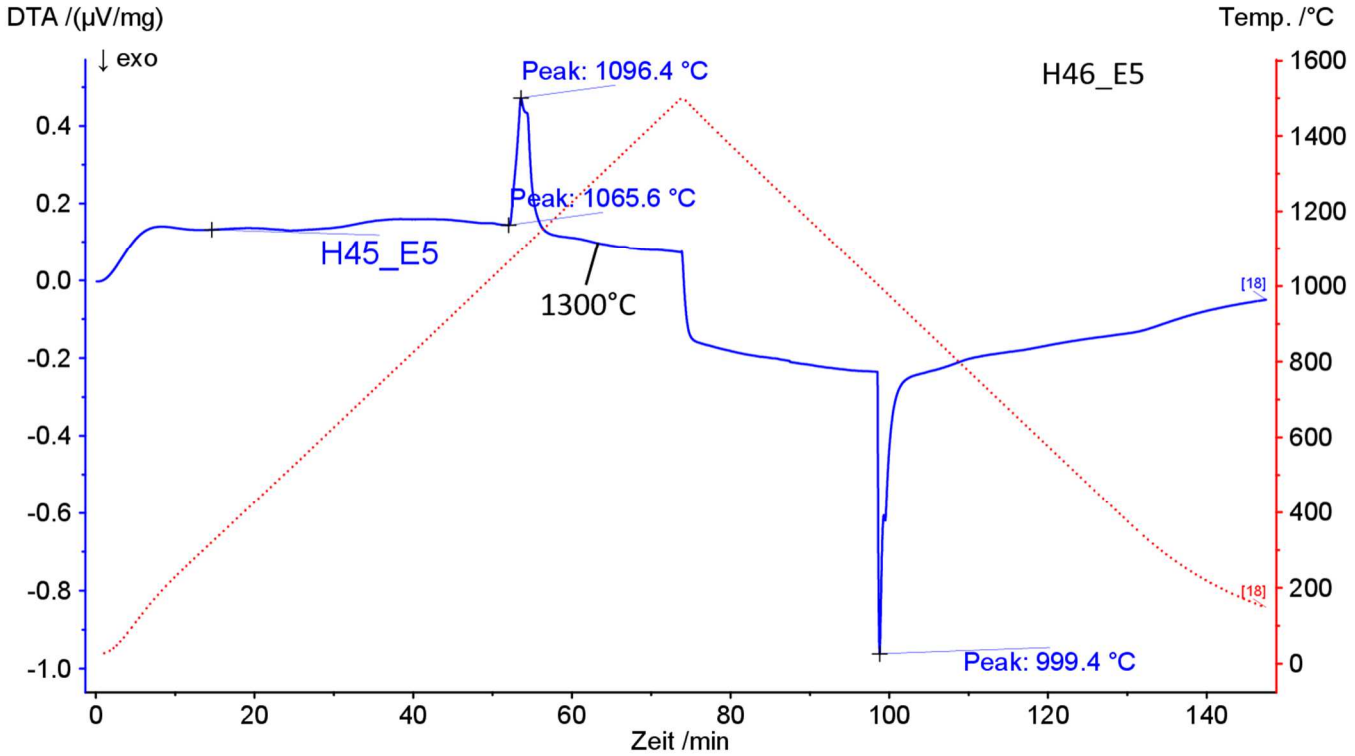

Figure 160 DTA analysis of H46_E5;

Die approbierte gedruckte Originalversion dieser Diplomarbeit ist an der TU Wien Bibliothek verfügbar.
The approved original version of this thesis is available in print at TU Wien Bibliothek.

Phases: Figure 161 shows that with XRD and REM for H46_E5 several phases could be obtained. Not all peaks in the XRD could be identified. Linking the found phases to the phases observed by SEM was difficult due to the fine structure of H46_E5.

Composition: H46_E5 should have 58Fe_30Mn_9Si_3C. Combined EDX analysis and LECO measurement result in a composition **Fe56_27Mn_3Cr_11Si_3C**. The Mn loss is relatively low, so the system is supposed to keep the Mn very well. The extra Si probably comes from an error during powder mix preparation.

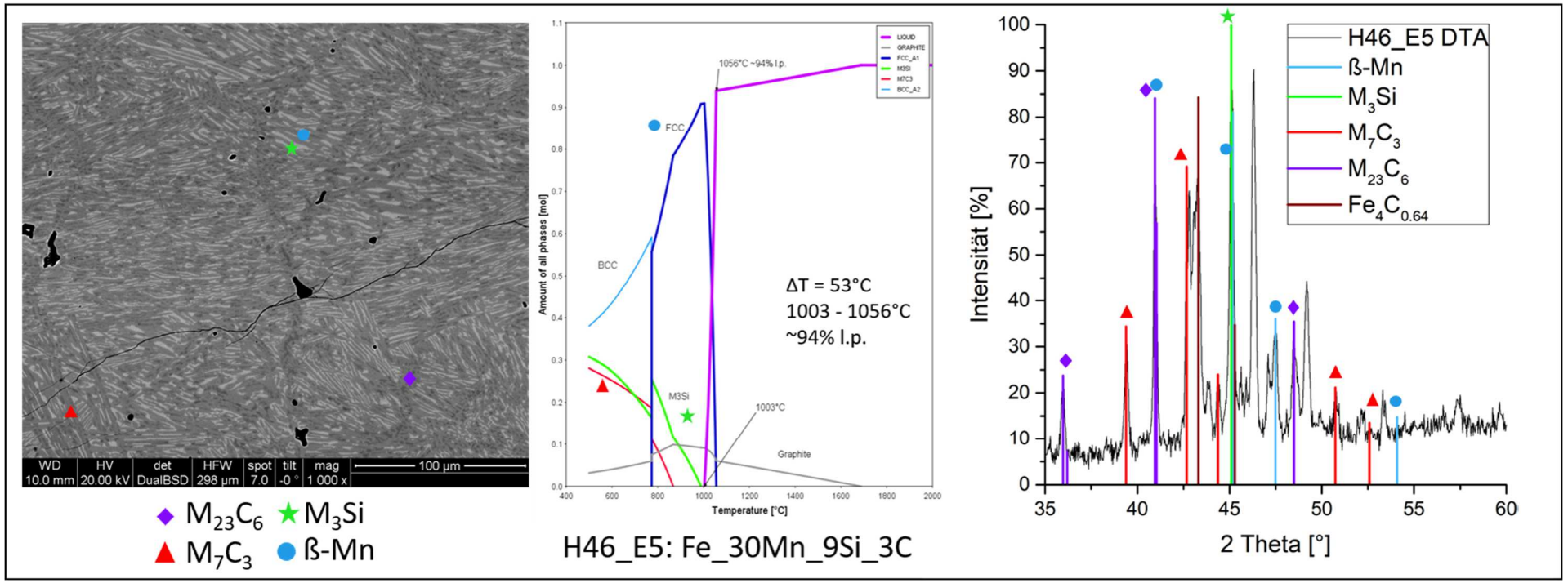

Figure 161 SEM x1000, EoP and XRD analysis from H46_E5 DTA-Ingot; ***Phase references*** *M_7C_3 (04-017-0806), M_3Si = (Fe_3Si (04-003-3871) and/or Fe_2MnSi (01-077-7953)), ß-Mn structured phase (04 007 2059), $M_{23}C_6$ (04-003-6076), $Fe_4C_{0.64}$ (01-071-1174)*

Die approbierte gedruckte Originalversion dieser Diplomarbeit ist an der TU Wien Bibliothek verfügbar.
The approved original version of this thesis is available in print at TU Wien Bibliothek.

H47: Fe_28Mn_27Cr_6Si_3.7C

Figure 162 shows the DTA measurement of H47. For this MA reactions seem to be almost finished below 1300°C. The heating stage shows two endothermal peaks. During the cooling stage three exothermal reactions could be obtained.

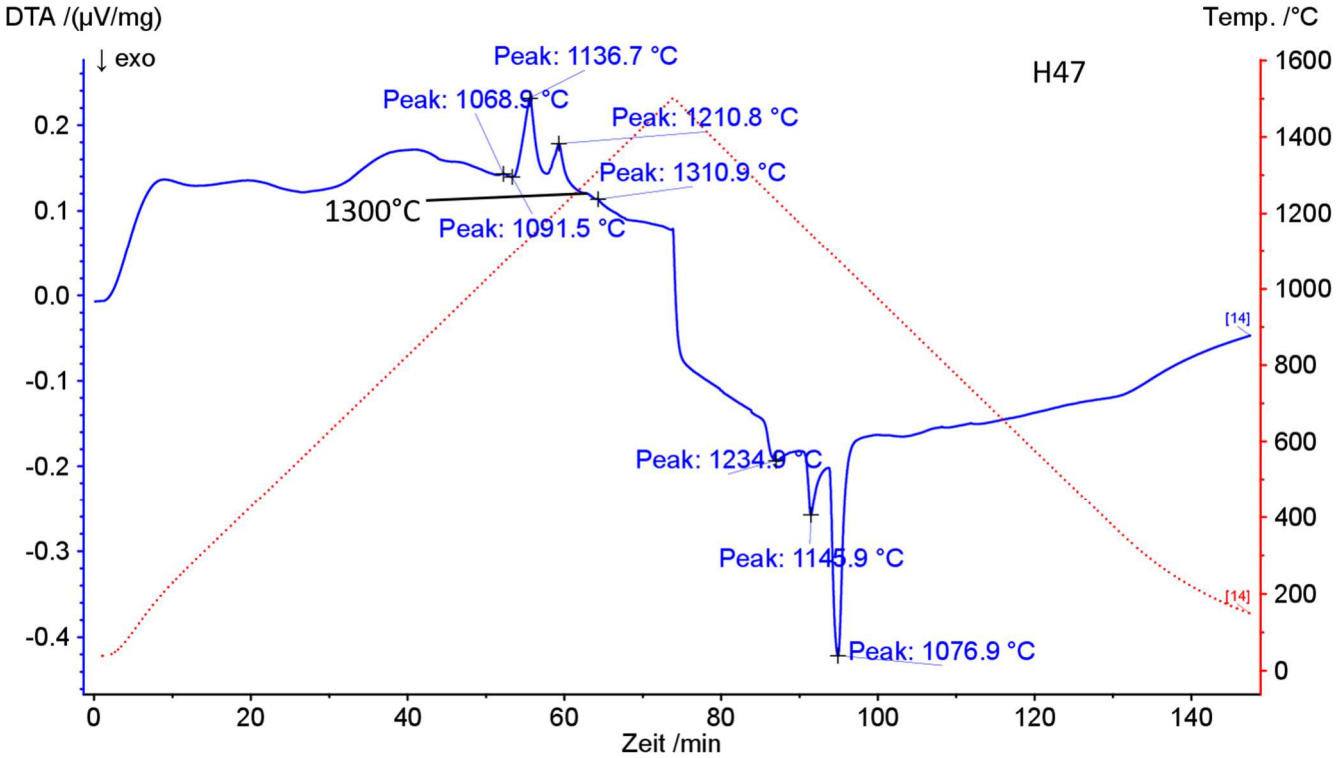

Figure 162 DTA analysis of H47 ingot;

Die approbierte gedruckte Originalversion dieser Diplomarbeit ist an der TU Wien Bibliothek verfügbar.
The approved original version of this thesis is available in print at TU Wien Bibliothek.

Phases: Figure 163 shows that with XRD and SEM for H45_E5 three phases could be obtained. M_3Si, a ß-Mn structured phase, considered as a solid solution and M_7C_3 predicted from ThermoCalc and found as well in XRD and SEM. The detected phases agree with theoretical calculations.
Composition: H47 should have 35.3Fe_28Mn_27Cr_6Si_3.7C. Combined EDX analysis and LECO measurement result in a composition **33.2Fe_29Mn_25Cr_9Si_3.8C**. In this sample no Mn loss could be obtained. This ingot was just molten from MA powder.

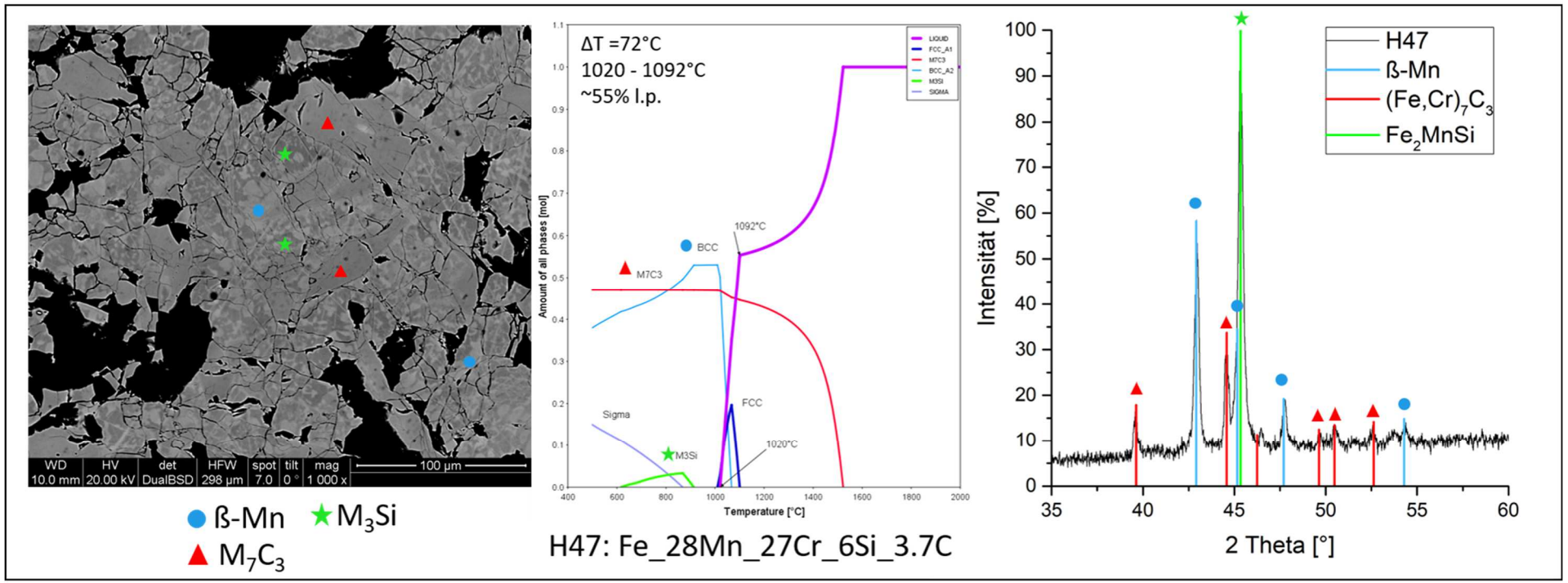

Figure 163 SEM x1000, EoP and XRD analysis from H47 ingot: ***Phase references*** *M_7C_3 (04-017-0806), M_3Si = (Fe_3Si (04-003-3871) and/or Fe_2MnSi (01-077-7953) and/or $Cr_{0.6}Fe_{2.4}Si$ (04-006-7480)), ß-Mn structured phase (04 007 2059),*

Die approbierte gedruckte Originalversion dieser Diplomarbeit ist an der TU Wien Bibliothek verfügbar.
The approved original version of this thesis is available in print at TU Wien Bibliothek.

H47_E1: Fe_35Mn_14Cr_11Si_3.8C

Figure 164 shows the DTA measurement of H47_E1. The heating stage shows two major peaks and a very slight reaction around 1034°C. The cooling stage shows two exothermal peaks.

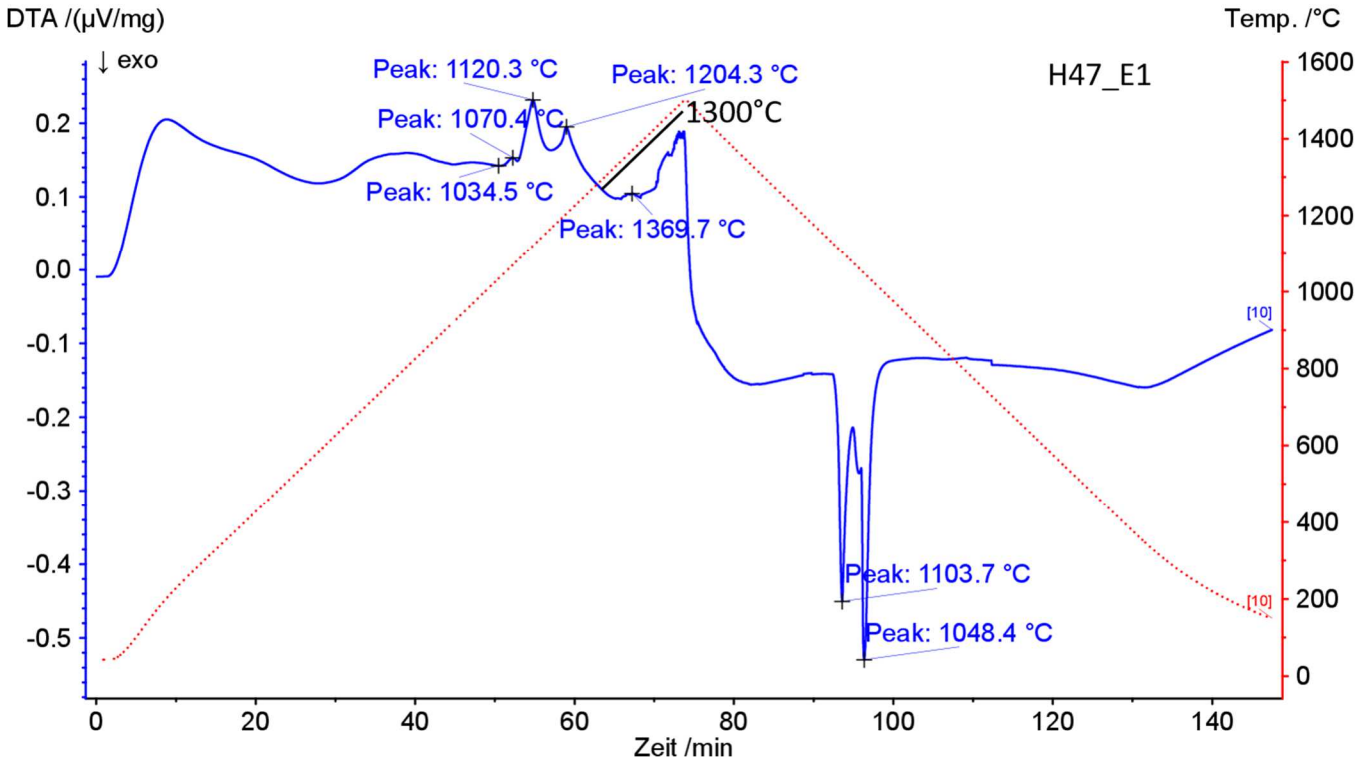

Figure 164 DTA analysis of H47_E1 ingot;

Die approbierte gedruckte Originalversion dieser Diplomarbeit ist an der TU Wien Bibliothek verfügbar.
The approved original version of this thesis is available in print at TU Wien Bibliothek.

Phases: Figure 165 shows that with XRD and SEM for H45_E5 three phases could be obtained. M_3Si, a ß-Mn structured phase, considered as a solid solution, and M_7C_3 predicted from ThermoCalc and found as well in XRD and SEM. The same phases as for H47 were found in SEM and XRD.
Composition: H47_E1 should have 36.2Fe_35Mn_14Cr_11Si_3.8C. Combined EDX analysis and LECO measurement result in a composition **40.2Fe_30Mn_16Cr_10Si_3.8C**. In comparison to H47 the Mn loss is huge, almost all Mn added as Mn powder to increase the content from 29% to 35% disappeared.

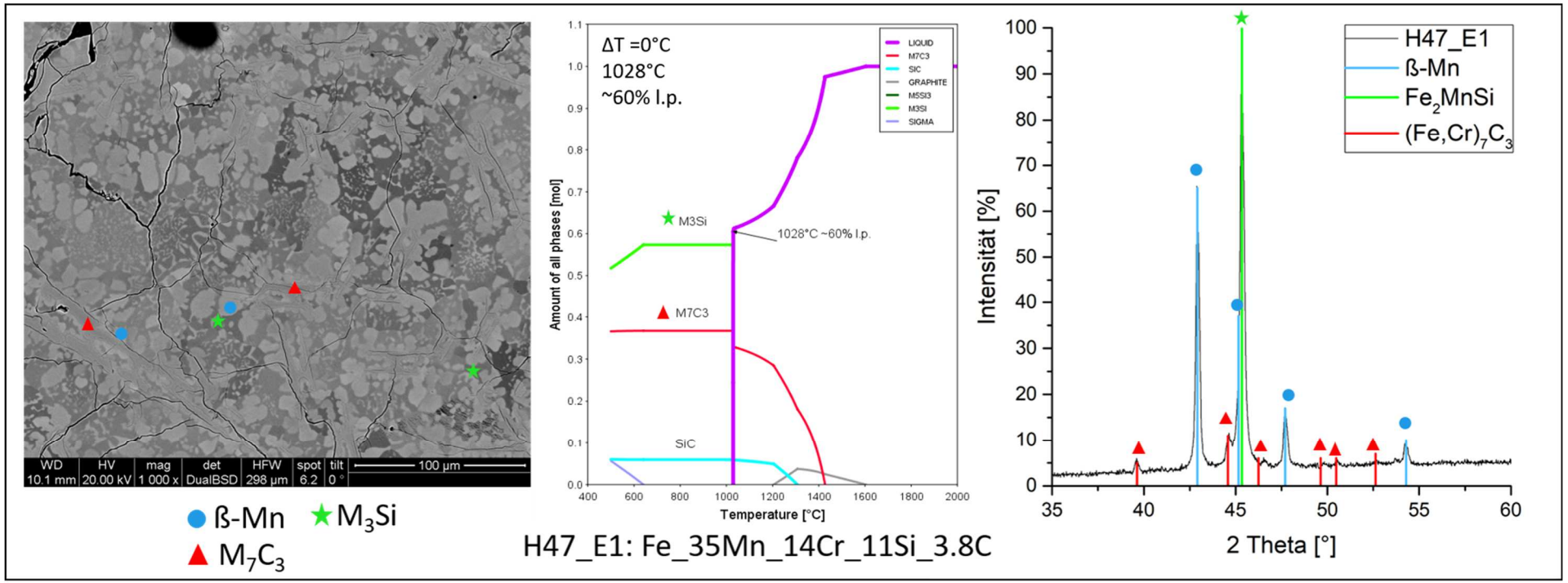

*Figure 165 SEM x1000, EoP and XRD analysis from H47_E1 Ingot; **Phase references** M_7C_3 (04-017-0806), M_3Si = (Fe_3Si (04-003-3871) and/or Fe_2MnSi (01-077-7953) and/or $Cr_{0.6}Fe_{2.4}Si$ (04-006-7480)), ß-Mn structured phase (04 007 2059)*

Die approbierte gedruckte Originalversion dieser Diplomarbeit ist an der TU Wien Bibliothek verfügbar.
The approved original version of this thesis is available in print at TU Wien Bibliothek.

H47_E2: Fe_38Mn_21Cr_8Si_3C

Figure 166 shows the DTA of H47_2, which is rather difficult. It is hard to tell if exothermal reactions take place during the heating phase. The MA seems to be almost molten at 1300°C. The cooling stage shows three sharp and defined exothermal reaction peaks.

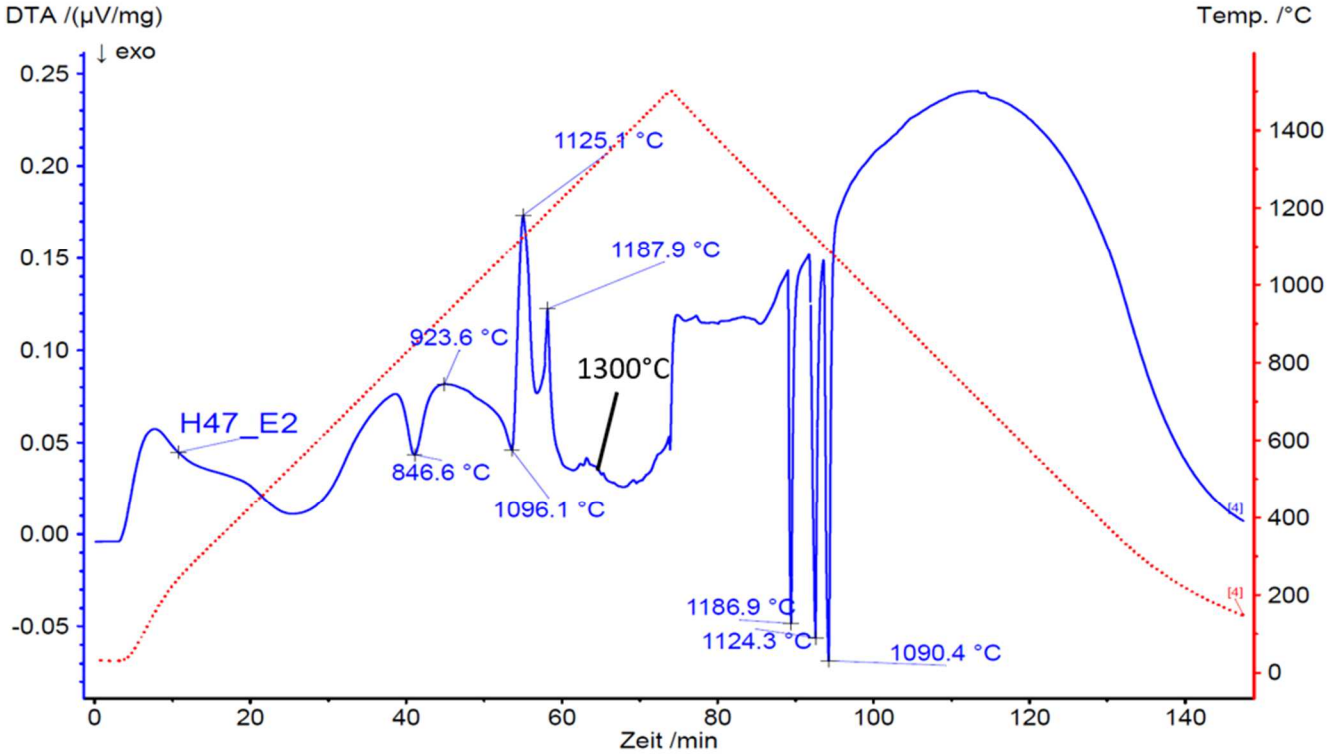

Figure 166 DTA analysis of H47_E2 ingot;

Die approbierte gedruckte Originalversion dieser Diplomarbeit ist an der TU Wien Bibliothek verfügbar.
The approved original version of this thesis is available in print at TU Wien Bibliothek.

Phases: Figure 167 shows that with XRD and REM for H45_E5 three phases could be obtained. M_3Si, a ß-Mn structured phase, considered as a solid solution phase, and M_7C_3 predicted from ThermoCalc and found as well in XRD and REM. The same phases as for H47 were found.
Composition: H47_E2 should have 30Fe_38Mn_21Cr_8Si_3C. Combined EDX analysis and LECO measurement result in a composition **33.3Fe_33Mn_22Cr_9Si_2.7C**. For this composition again a relatively high amount of Mn disappeared. This mix contained elemental Mn as well to increase to content from 29% to 38%.

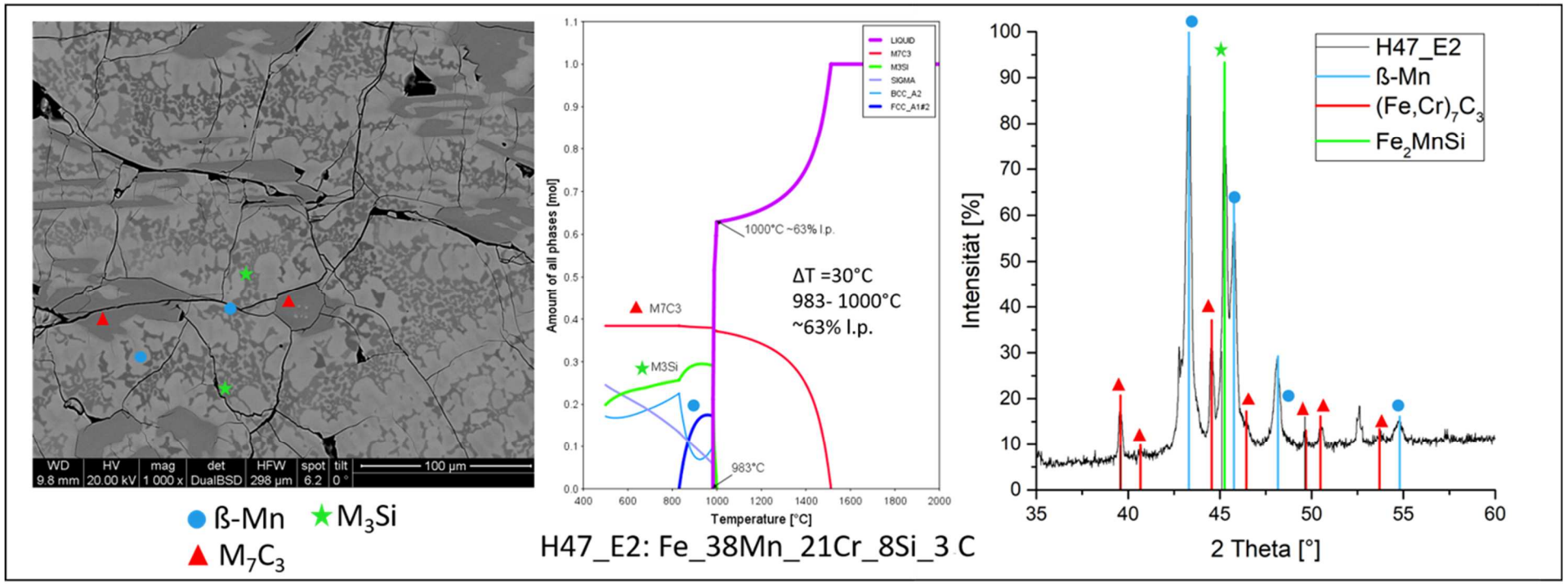

Figure 167 SEM x1000, EoP and XRD analysis from H47_E2 Ingot; ***Phase references*** *M_7C_3 (04-017-0806), M_3Si = (Fe_3Si (04-003-3871) and/or Fe_2MnSi (01-077-7953) and/or $Cr_{0.6}Fe_{2.4}Si$ (04-006-7480)), ß-Mn structured phase (04 007 2059)*

Die approbierte gedruckte Originalversion dieser Diplomarbeit ist an der TU Wien Bibliothek verfügbar.
The approved original version of this thesis is available in print at TU Wien Bibliothek.

H47_E3: Fe_38Mn_21Cr_8Si_3C

Figure 168 shows the DTA measurement of H47_E3. It is clearly visible that all reactions for this MA take place below 1300°C. During the heating stage two different endothermal peaks can be obtained. The cooling stage shows two exothermal peaks as well.

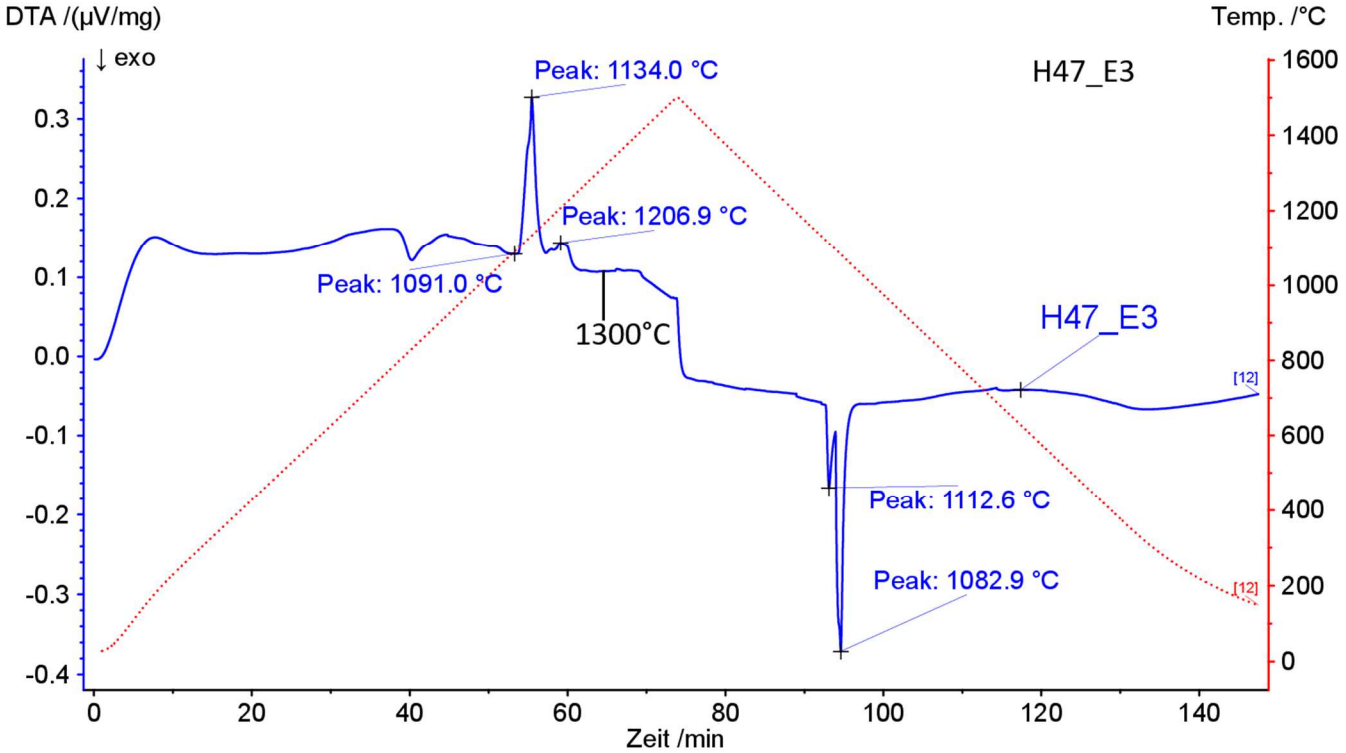

Figure 168 DTA analysis of H47_E3 ingot;

Die approbierte gedruckte Originalversion dieser Diplomarbeit ist an der TU Wien Bibliothek verfügbar.
The approved original version of this thesis is available in print at TU Wien Bibliothek.

Phases: Figure 169 shows that with XRD and REM for H45_E5 two phases could be obtained. M_3Si and a ß-Mn structured phase could be found in XRD as well as with SEM.

Composition: H47_E3 should have 39Fe_35Mn_12Cr_12Si_2C. Combined EDX analysis and LECO measurement result in a composition **43Fe_30Mn_14Cr_12Si_1.2C**. A rather high Mn loss was obtained for this composition as well. Elemental Mn was added to increase the Mn content from 29% to 35%. For this system C loss was huge as well.

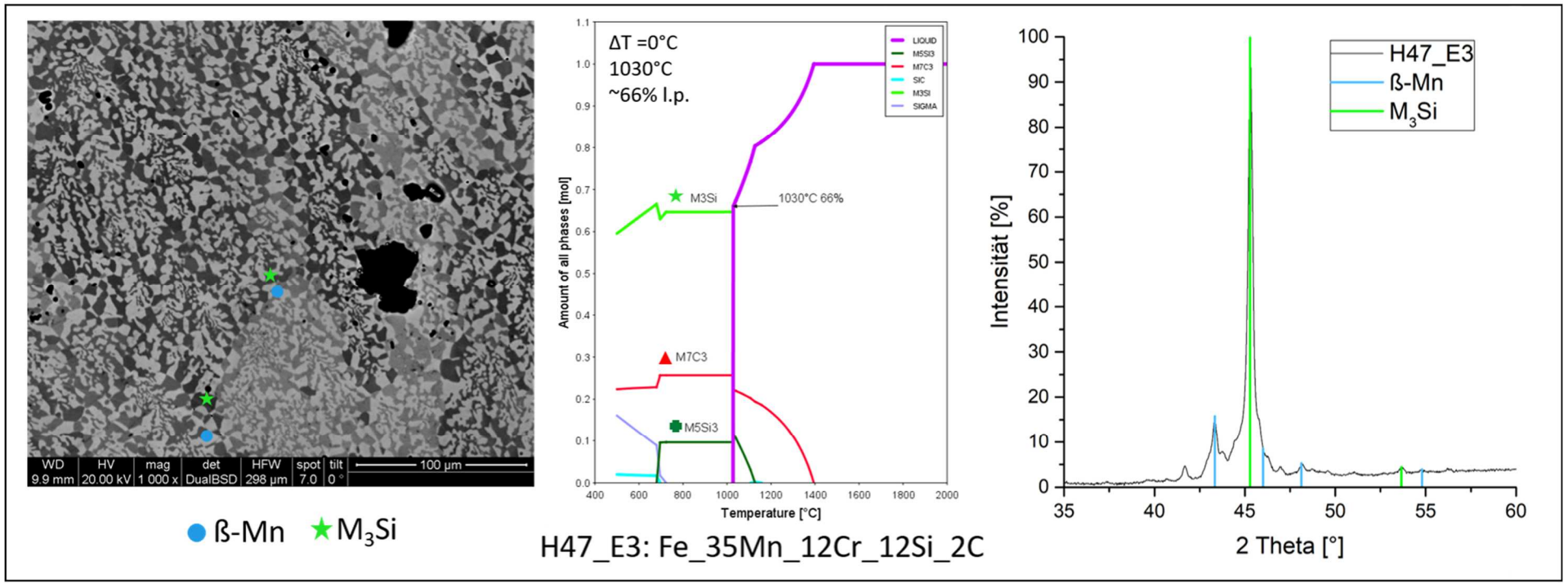

Figure 169 SEM x1000, EoP and XRD analysis from H47_E3 Ingot; ***Phase references*** *M_3Si = (Fe_3Si (04-003-3871) and/or Fe_2MnSi (01-077-7953) and/or $Cr_{0.6}Fe_{2.4}Si$ (04-006-7480)), ß-Mn structured phase (04 007 2059)*

Die approbierte gedruckte Originalversion dieser Diplomarbeit ist an der TU Wien Bibliothek verfügbar.
The approved original version of this thesis is available in print at TU Wien Bibliothek.

H47_E4: Fe_28Mn_27Cr_6Si_5C

Figure 170 shows the DTA measurement of H47_E4. Due to the high C content compared to the other modifications the reactions for this MA are clearly not finished at 1300°C, this might result in the formation of Cr-carbides as shown in Figure 171. The heating stage shows three endothermal reaction peaks. The dominant and last reaction does not seem to be finished at 1500°C. The cooling stage shows two different exothermal reaction peaks.

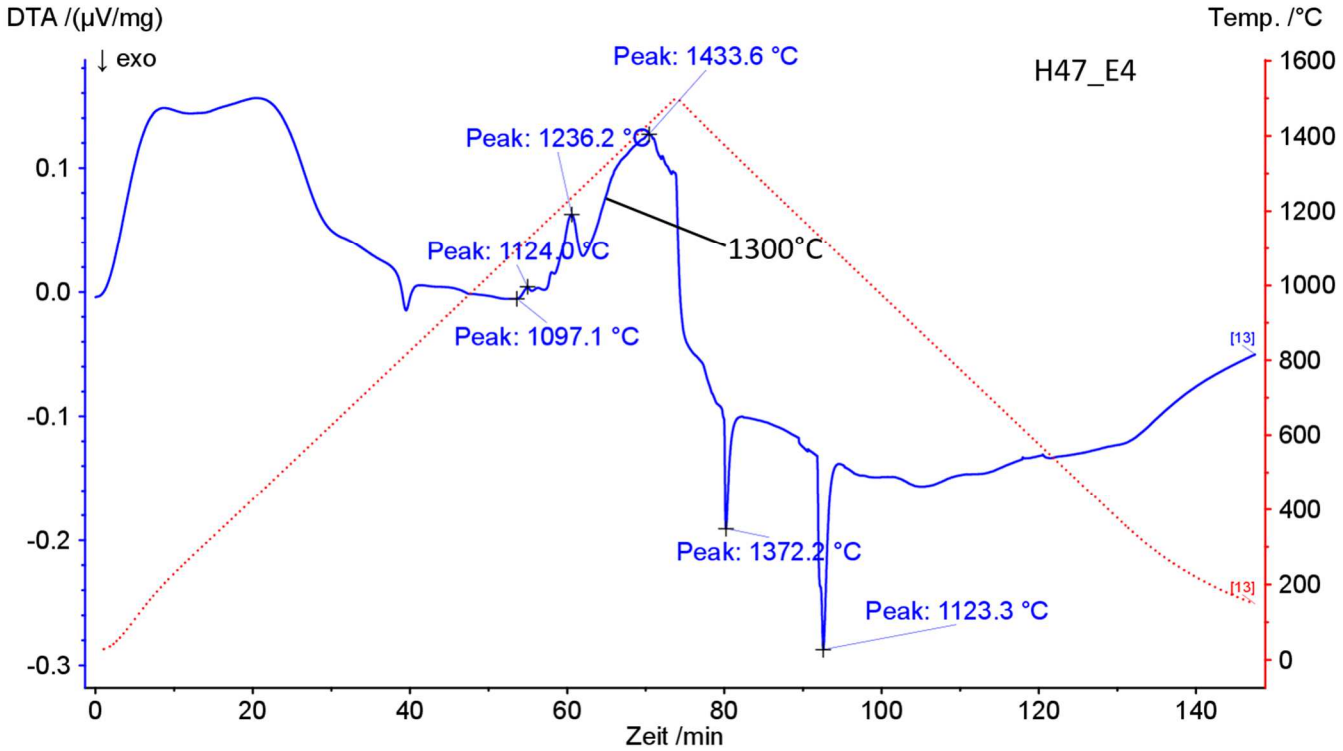

Figure 170 DTA analysis of H47_E4 ingot;

Die approbierte gedruckte Originalversion dieser Diplomarbeit ist an der TU Wien Bibliothek verfügbar.
The approved original version of this thesis is available in print at TU Wien Bibliothek.

Phases: Figure 171 shows that with XRD and SEM for H45_E4 three phases could be obtained. M_3Si, a ß-Mn structured phase and M_7C_3 phase. The M_7C_3 phase is the dominant phase for H47_E4 due to the much higher C content, which results in the high LT.

Composition: H47_E4 should have 34Fe_28Mn_27Cr_6Si_5C. Combined EDX analysis and LECO measurement result in a composition **37.8Fe_22Mn_29Cr_7Si_4.2C**.

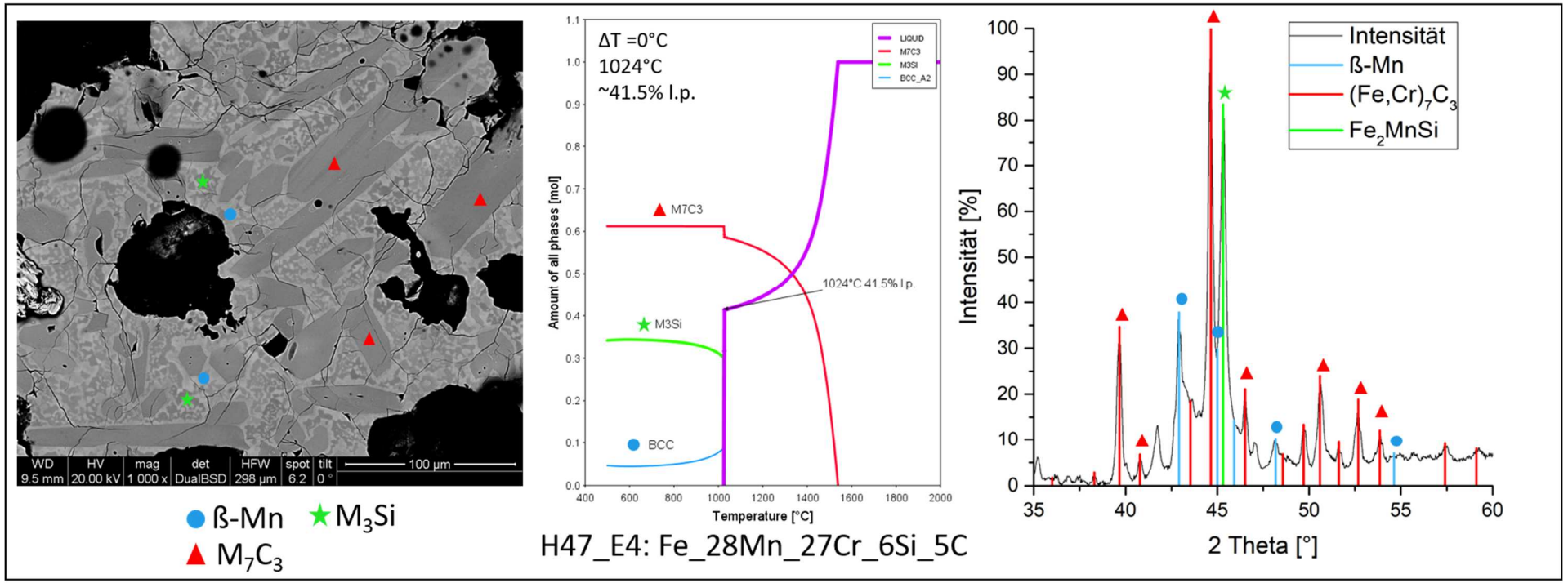

Figure 171 SEM x1000, EoP and XRD analysis from H47_E4 Ingot; ***Phase references*** *M_7C_3 (04-017-0806 M_3Si = (Fe_3Si (04-003-3871) and/or Fe_2MnSi (01-077-7953) and/or $Cr_{0.6}Fe_{2.4}Si$ (04-006-7480)), ß-Mn structured phase (04 007 2059)*

Die approbierte gedruckte Originalversion dieser Diplomarbeit ist an der TU Wien Bibliothek verfügbar.
The approved original version of this thesis is available in print at TU Wien Bibliothek.

H47_E5: Fe_40Mn_10Cr_12Si_0.5C

Figure 172 shows the DTA measurement of H47_E5. This MA modification is clearly molten below 1300°C. It shows a narrow melting range at comparatively low melting temperatures for this family. Heating stage and cooling stage show a single reaction peak.

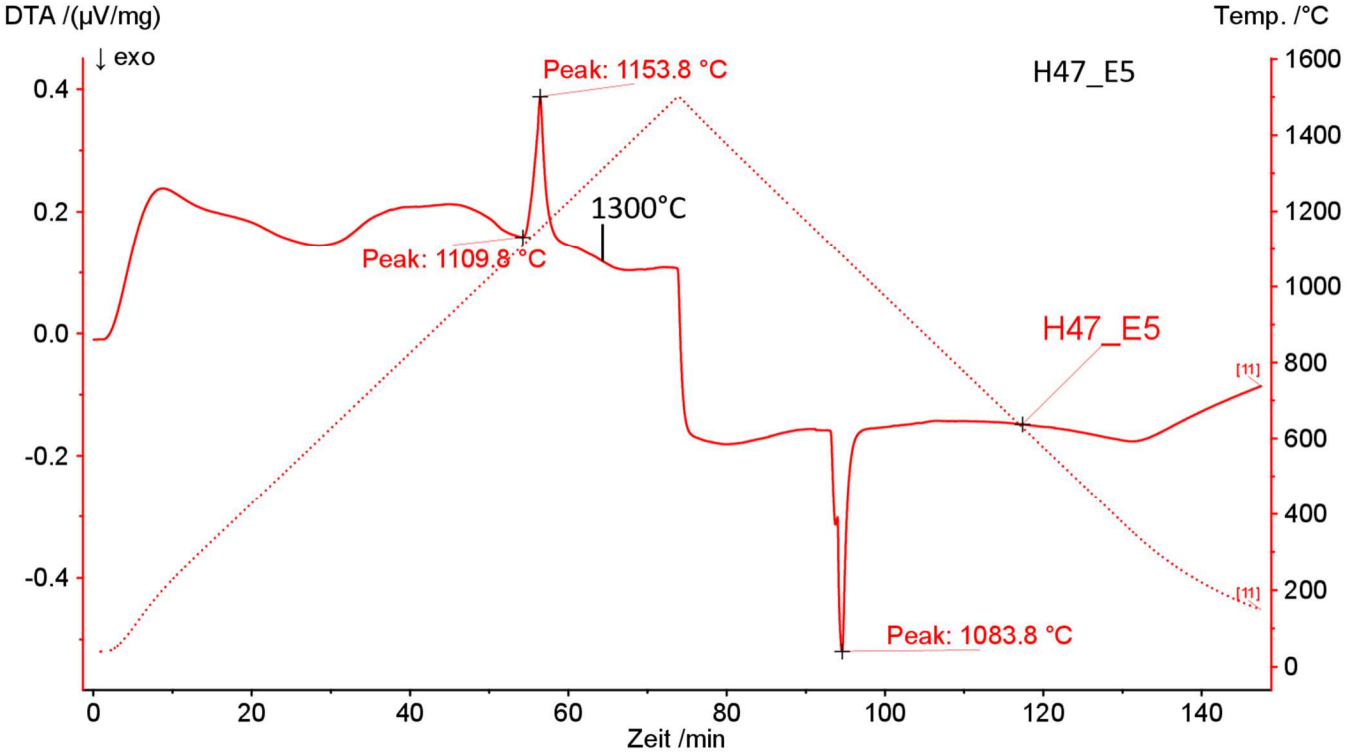

Figure 172 DTA analysis of H47_E5 ingot

Die approbierte gedruckte Originalversion dieser Diplomarbeit ist an der TU Wien Bibliothek verfügbar.
The approved original version of this thesis is available in print at TU Wien Bibliothek.

Phases: Figure 173 shows that with XRD and SEM for H45_E5 two phases could be obtained, M_3Si and a ß-Mn structured phase.
Composition: H47 should have 37.5Fe_40Mn_10Cr_12Si_0.5C. Combined EDX analysis and LECO measurement result in a composition **44.4Fe_32Mn_12Cr_11Si_0.6C**. The Mn loss of around 8wt% Mn during melting at 1300°C is relatively high. Elemental Mn was added to this composition to increase the Mn content from 29% to 40%.

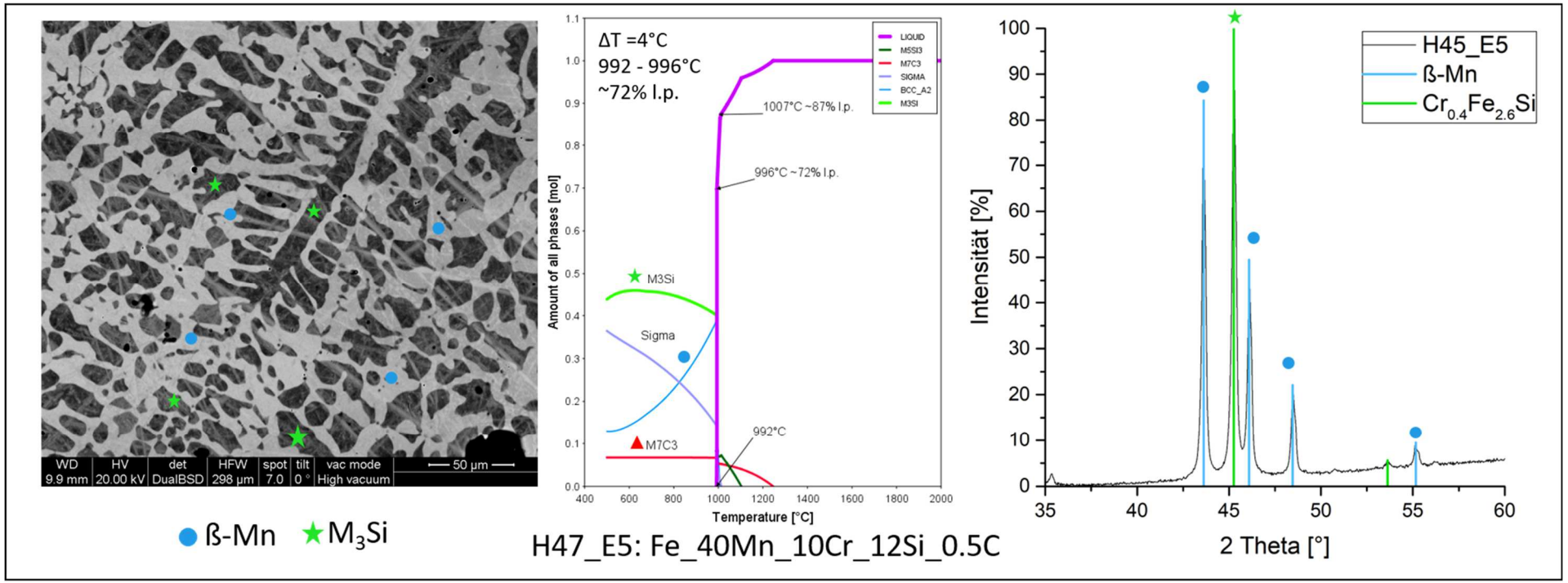

Figure 173 SEM x1000, EoP and XRD analysis from H47_E5 Ingot ***Phase references*** *M_3Si = (Fe_3Si (04-003-3871) and/or Fe_2MnSi (01-077-7953) and/or $Cr_{0.6}Fe_{2.4}Si$ (04-006-7480)), ß-Mn structured phase (04 007 2059)*

Die approbierte gedruckte Originalversion dieser Diplomarbeit ist an der TU Wien Bibliothek verfügbar.
The approved original version of this thesis is available in print at TU Wien Bibliothek.

6.4 Binary phase diagrams

Calculated binary systems were used as base for further calculations.

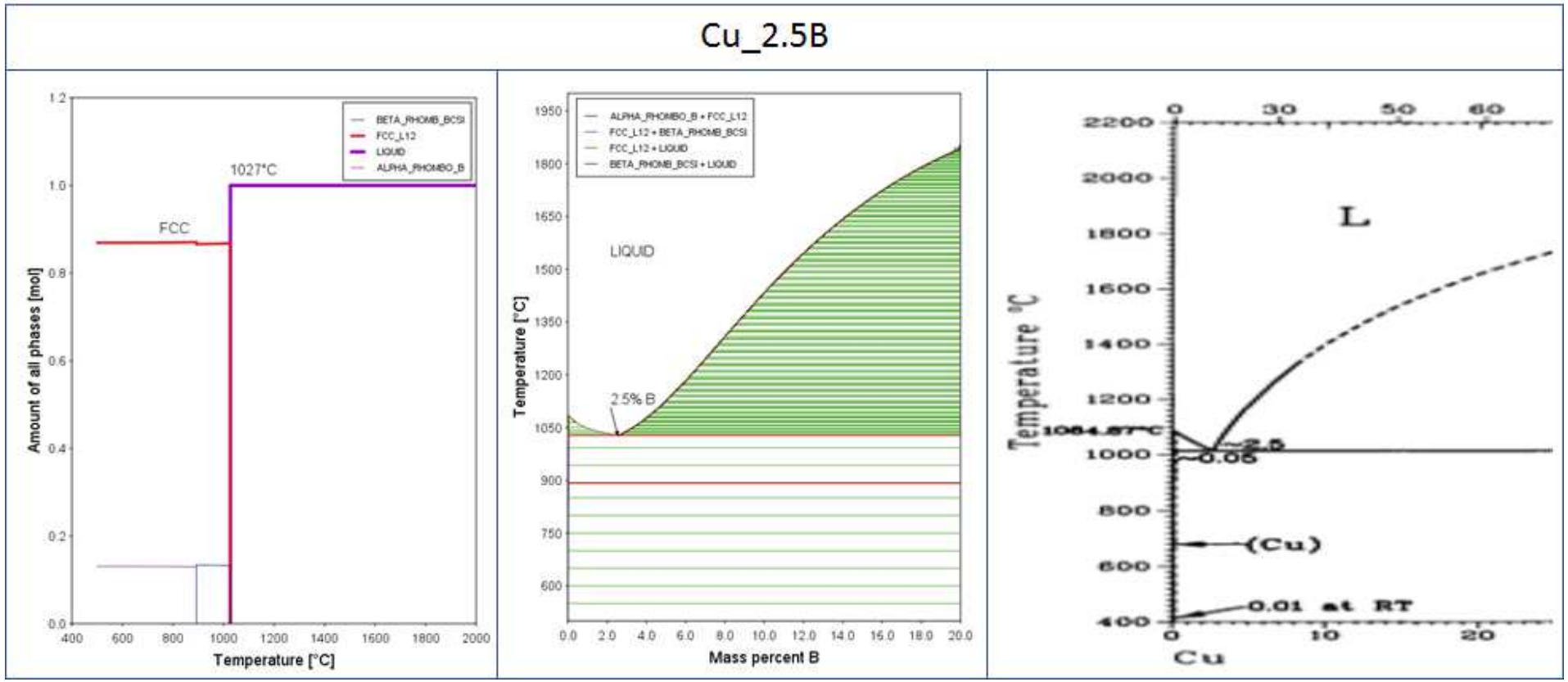

Figure 174 Cu – B; Evolution of phases, calculated phase diagram and phase diagram from ASM Handbook of metals Vol.3[59]

Figure 174 shows for Cu-B binary system calculated data and literature fit together. Both show a eutectic at 2.5 B and a melting point at ~1027°C

Die approbierte gedruckte Originalversion dieser Diplomarbeit ist an der TU Wien Bibliothek verfügbar.
The approved original version of this thesis is available in print at TU Wien Bibliothek.

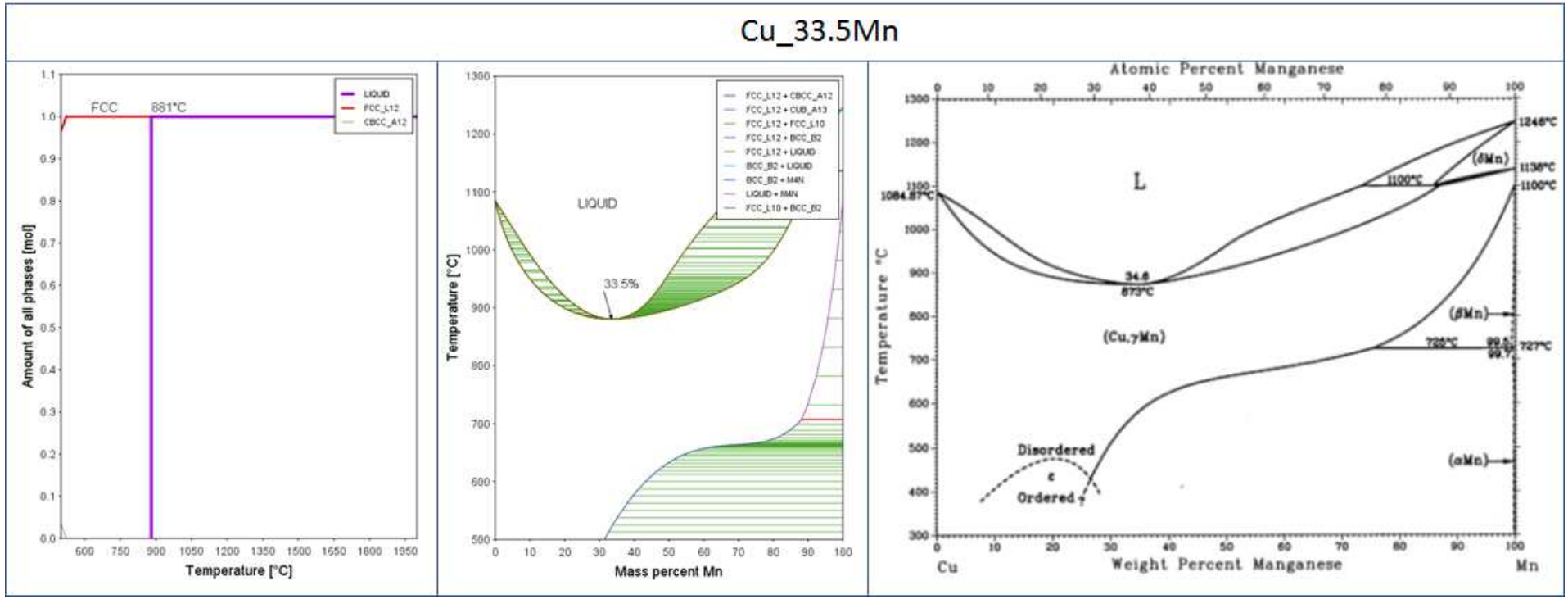

Figure 175 Cu – Mn; Evolution of phases, calculated phase diagram and phase diagram from ASM Handbook of metals Vol.3 [59]

Figure 175 compares the calculated and the measured phase diagram from the literature. Differing in eutectic composition calculated melting at 881°C with 33.5% Mn and melting at 872°C with 34.6% Mn which is in the range but a difference in comparison to the previous binary systems.

Die approbierte gedruckte Originalversion dieser Diplomarbeit ist an der TU Wien Bibliothek verfügbar.
The approved original version of this thesis is available in print at TU Wien Bibliothek.

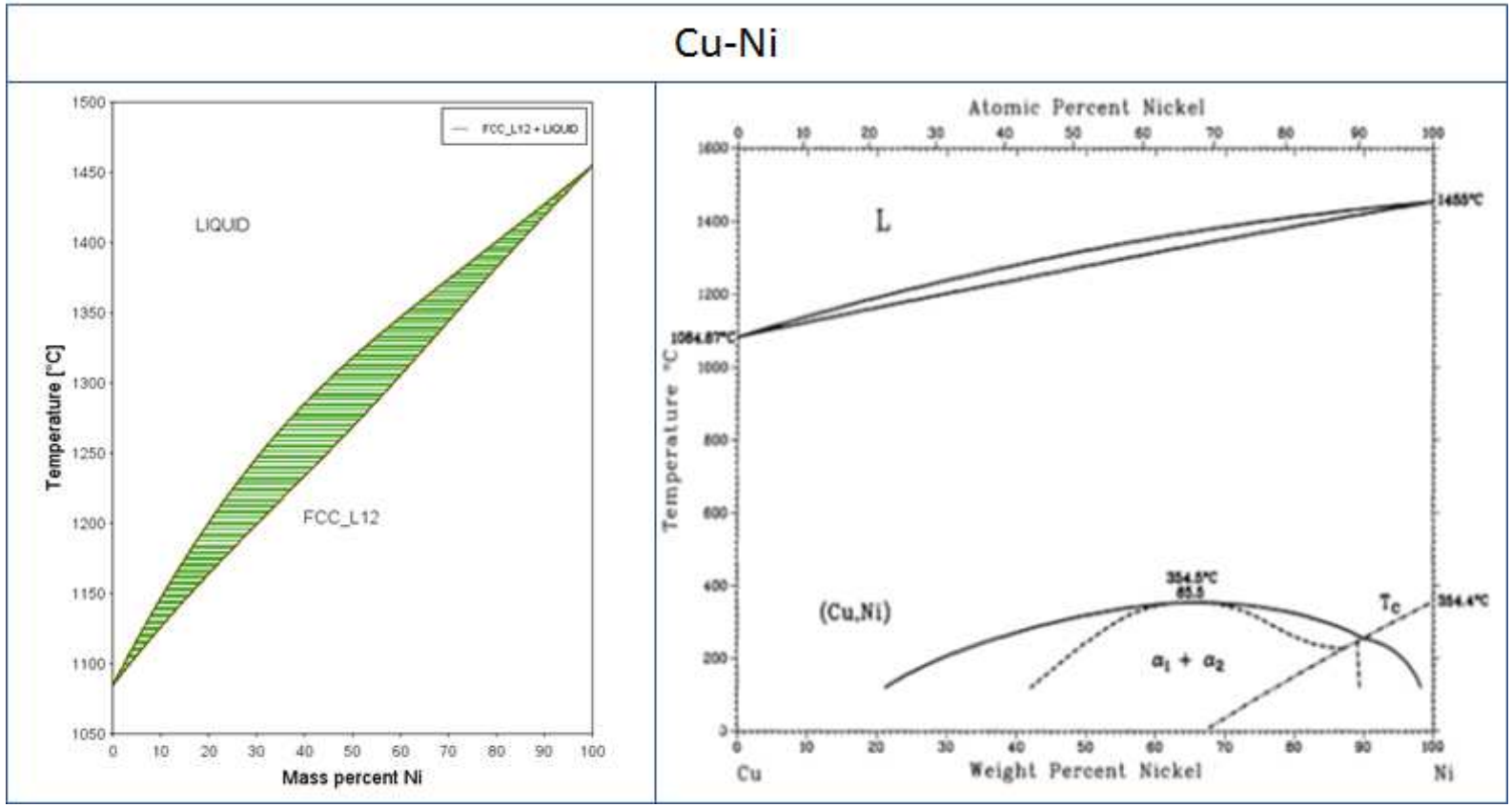

Figure 176 Cu – Ni; Calculated phase diagram and phase diagram from ASM Handbook of metals Vol.3 [59]

Figure 176 showing Cu-Ni system has no eutectic composition. Calculated phase diagram and literature fit together.

Die approbierte gedruckte Originalversion dieser Diplomarbeit ist an der TU Wien Bibliothek verfügbar.
The approved original version of this thesis is available in print at TU Wien Bibliothek.

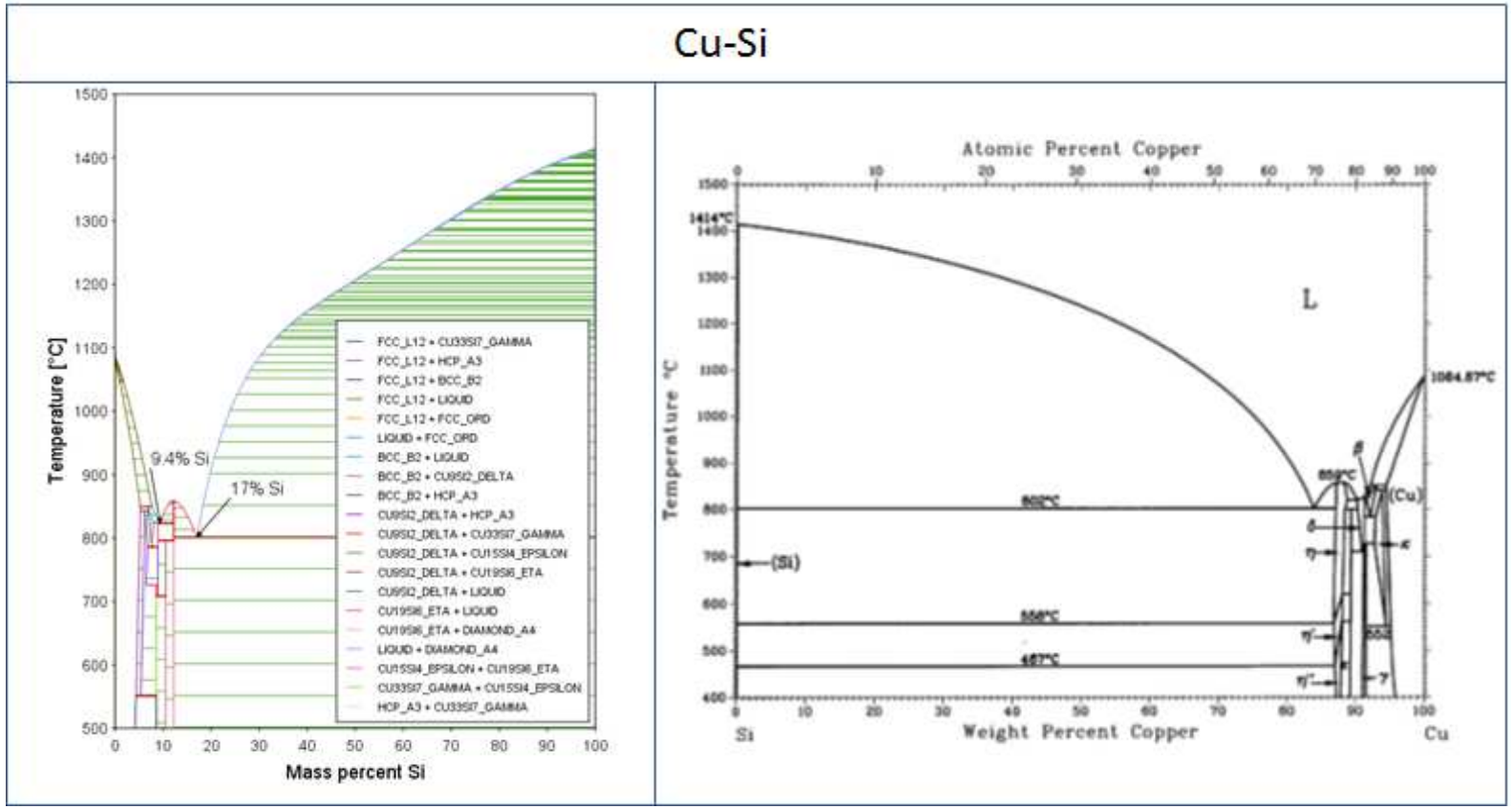

Figure 177 Cu – Si; Calculated phase diagram and phase diagram from ASM Handbook of metals Vol.3 [59]

Figure 177 showing Cu-Si system having 2 eutectic compositions at 9.4 and 17% Si. Both diagrams fit together.